NASA Technical Memorandum 102697
AVSCOM TR-90-B-006

Scaling Effects in the Static and Dynamic Response of Graphite-Epoxy Beam-Columns

Karen E. Jackson

July 1990

National Aeronautics and Space Administration

Langley Research Center
Hampton, Virginia 23665-5225

US ARMY AVIATION SYSTEMS COMMAND
AVIATION R&T ACTIVITY

SCALING EFFECTS IN THE STATIC AND DYNAMIC RESPONSE OF GRAPHITE-EPOXY BEAM-COLUMNS

ABSTRACT

Scale model technology represents one method of investigating the behavior of advanced, weight-efficient composite structures under a variety of loading conditions. Testing of scale models can provide a cost effective alternative to destructive testing of expensive composite prototypes and can be used to verify predictions obtained from finite element analyses. It is necessary, however, to understand the limitations involved in testing scale model structures before the technique can be fully utilized. The objective of this research is to characterize these limitations, or scaling effects, in the large deflection response and failure of composite beams. Scale model beams were loaded with an eccentric axial compressive load designed to produce large bending deflections and global failure.

A dimensional analysis was performed on the composite beam-column loading configuration to determine a model law governing the system response. An experimental program was developed to validate the model law under both static and dynamic loading conditions. Scale model beams ranging from 1/6 to full scale were constructed of high modulus graphite-epoxy composite material. Laminate stacking sequences including unidirectional, angle ply, cross ply, and quasi-isotropic were tested to examine a diversity of composite response and failure modes. The model beams were loaded under scaled test conditions until catastrophic failure. A large deflection beam solution was developed to compare with the static experimental results and to analyze beam failure. Also, the finite element code DYCAST (DYnamic Crash Analysis of STructures) was used to model both the static and impulsive beam response.

Static test results indicate that the unidirectional and cross ply beam responses scale as predicted by the model law, even under severe deformations. Some deviation from scaled response was

observed for the angle ply and quasi-isotropic beams due to damage development. The large deflection beam solution and DYCAST successfully predicted the static load versus end displacement response. In general, failure modes were consistent between scale models within a laminate family; however, a significant scale effect was observed in strength. Small scale beams failed at higher normalized end displacement levels than their full scale prototypes. Failure theories for composites such as maximum stress, maximum strain, and tensor polynomial, cannot predict this scale effect. Various statistical theories and fracture mechanics approaches offer promise in predicting the observed scale effect in strength since they incorporate measures of absolute size.

The scale effect in strength which was evident in the static tests was also observed in the dynamic tests. Scaling of load and strain time histories between the scale model beams and the prototypes was excellent for the unidirectional beams, but inconsistent results were obtained for the angle ply, cross ply, and quasi-isotropic beams. Again, failure modes were similar among the scale model beams within a laminate family. The DYCAST finite element model predicted accurately the dynamic beam response for the full scale unidirectional beam and provided detailed plots of deformation progression.

Results of this investigation show that valuable information can be obtained from testing on scale model composite structures, especially in the linear elastic response region. However, due to scaling effects in the strength behavior of composite laminates, caution must be used in extrapolating data taken from a scale model test when that test involves failure of the structure.

TABLE OF CONTENTS

LIST OF FIGURES

LIST OF TABLES

Chapter 1 - Introduction

1.1 Overview of Scaling Issues in Composite Structures

The high specific strength and stiffness characteristics of composite materials have led to their application in the development of advanced, weight-efficient military and commercial aircraft. Currently, government, industry and universities are working in cooperation on research programs designed to encourage the increased use of composite materials. The objective of one such program, the Advanced Composites Technology Program (ACT) sponsored by the National Aeronautics and Space Administration (NASA), is to develop and demonstrate the technology base needed to ensure the cost-effective use of advanced composite materials in primary structures of future aircraft [1]. The comprehensive data base of design information which exists for metals is not yet available for composite materials. This lack of information makes accurate analysis using conventional finite element techniques difficult. Consequently, composite prototypes must be fabricated and tested as part of design evaluation. Such testing, especially if it involves destruction of the design article, is expensive and time consuming.

An alternate method of understanding and predicting the response of aircraft structures under a variety of loading conditions is through the use of scale model testing. While the application of scale model testing is well known in fluid mechanics; for example, wind tunnel tests on models to determine flight loads, the method has not received as much attention as an experimental technique in solid mechanics. However, interest in scale model testing of fiber composite components is growing as the size and complexity of test articles increases. In fact, the ACT program contains research efforts to study scaling effects in the fundamental behavior of composite coupons. Later this research will be applied to construct scale models of innovative fuselage concepts using composite materials.

The problem of designing, building, and testing a scale model structure constructed of advanced, fiber-reinforced composite materials is a challenging one. Due to the complexity of the material itself, the problem of scaling a composite component may be examined on several levels. The most elemental approach is to scale the constituent materials, the fiber and matrix. This approach is similar to the technique used to fabricate reinforced concrete model structures in which the reinforcing bars and aggregate size are scaled [2-5]. For a typical graphite-epoxy composite material system, scaling of the microstructure on this level would involve scaling of fiber diameters and fiber shapes, and ensuring uniformity of fiber spacing. Fiber volume fractions should be the same for both model and prototype systems. However, for many structural problems, this degree of scaling becomes impractical and unnecessary.

The composite laminate represents the next level of complexity to examine. Scaling considerations for the laminate can be simplified if the individual lamina properties are smeared, i.e., the heterogeneous nature of the material is ignored on the microscopic level and the laminate is treated as a homogeneous, orthotropic sheet. This assumption is made when macroscopic structural aspects of the problem are more significant than material considerations for achieving scaled response. For example, to construct a scale model of a stiffened panel, issues like stiffener spacing, aspect ratios, and other construction details may influence the response to a higher degree than minor irregularities in the microstructure of a single ply in the laminated panel. Thus, each level of structural complexity has its own unique set of scaling difficulties and special concerns.

In addition, it is necessary to understand how changes in the material microstructure, including the initiation and growth of damage, accumulate in the material and affect the overall structural response determination at various dimensional scales. Haritos, et al [6] have introduced the term "mesomechanics" to describe the area of research which bridges the microstructure studies of fiber-reinforced composites with structural mechanics theories. Unfortunately, little

research has been conducted on this topic. Test data obtained in the laboratory on small coupon-type specimens are routinely assumed to be valid for full scale structures with no regard for possible distortions due to size or scale. This assumption is made even though a size effect in failure behavior of metallic structures has been well documented [7-10]. The limitations of scale modeling must be identified so that tests on sub-scale composite structures will generate valid data for predicting prototype behavior. Once the problems involved in testing scale models are identified and understood, the technique can be utilized as a valuable, cost-effective design tool.

1.2 Literature Review

The objective of dimensional analysis, or similitude, is to develop a set of dimensionless parameters which forms the scaling law governing the correlations between the model and the prototype. There are two basic concepts involved. First is the idea that a limited number of fundamental dimensions exist. Ehrlich [11] proposes that the six fundamental dimensions are distance, time, mass, temperature, light intensity, and electrical charge. The dimensions of all other variables are derived from these six. For example, the dimension of force is a well-known combination of mass, distance, and time determined by Newton's Second Law. Secondly, the equations which describe a phenomenon must be homogeneous; that is, the dimensions of every term in the equation must be the same. This statement is commonly called the law of dimensional homogeneity. The scale law may be determined either through non-dimensionalization of the governing equations or by dimensional analysis. Baker, Westine and Dodge [12] give an excellent presentation of both methods and provide several applications to solid and fluid mechanics problems. Other classical references on dimensional analysis and similitude theory are those of Langhaar [13], Murphy [14], Sedov [15], and Bridgman [16].

The first concepts of similitude theory had their origins in Greek civilization when Euclid imposed homogeneity restrictions on geometrical quantities. The theory was advanced by Galileo and Descartes in the Renaissance era. However, it was Fourier in 1822 who established the foundations of dimensional analysis. He understood the role of dimensions and the idea of dimensional homogeneity in deriving parameters or dimensionless groups which govern certain phenomena. After Fourier, no important development in dimensional analysis occurred for nearly half a century until work by Lord Rayleigh in England, Riabouchinsky in Russia, and Vaschy in France. Each of these individuals worked independently and in different fields of study, yet produced similar statements concerning dimensional analysis. However, the person most associated with model theory and dimensional analysis is E. Buckingham [17]. He published a series of articles from 1914 through 1916 on the basic principles of dimensional analysis including the statement of a theorem which is commonly known today as the Pi Theorem. Buckingham popularized dimensional analysis techniques by demonstrating the usefulness of the theory through practical applications. Unfortunately, development of the Pi theorem is often attributed to Buckingham because he failed to reference previous work by Vaschy and others. Macagno [18] has written an excellent article on the historical development of similitude theory and he outlines the contributions of each of the researchers mentioned previously.

Since the time of Buckingham, the principles of dimensional analysis have been applied in innovative ways to obtain solutions to mechanics problems. Baker, et al, [12] have stated that model analysis may be used to: (1) collect data to evaluate an analysis procedure, (2) obtain quantitative data for a prototype design, (3) generate a functional relationship to empirically solve a general problem, (4) evaluate limitations of an expensive system already in existence, (5) explore fundamental behavior of new phenomena, and (6) obtain results when no other method of analysis is possible.

Consequently, scale model technology has been used in space related applications [19-24]; dynamic modelling of civil engineering structures such as platforms, buildings, and bridges [25]; impact analysis of vehicles for safety and crashworthiness [26-30]; and simulations of structural response to blast loads [8,25,31,32]. The high cost and potentially dangerous test conditions associated with these applications make scale model testing an ideal alternative to performing experiments on prototypes.

Previous research on testing of scale model composite structures is limited. However, the available data generally fall into two categories. First is the application of scale model testing to large, complex structures. A few examples of research of this type will be discussed. Gustafson, et al, [28] constructed one-half scale helicopter fuselage subfloors of aluminum and graphite-epoxy composite material to investigate the nonlinear load-deflection behavior of the sections. The composite fuselage was designed as a one-for-one replacement of the metal structure using the same loads criteria. Few details of the construction of the composite section are provided in Reference [28], but the authors state that ultimate strengths of the metal and composite specimens were not identical due to differences in material properties. In addition, they noted a problem in selecting a rivet size which would provide scaling of the failure mode. Both static and impact tests were performed on the one-half scale fuselage sections. Although no comparisons were made to full scale data, the authors concluded that no economic benefits could be obtained from scale model testing due to increased labor costs associated with construction of the test article. They stated that results obtained from scale model impact tests would not accurately predict full-scale response because the gravity field was not scaled. However, no data were presented to support these conclusions.

McCullers and Naberhaus [33] describe an experimental and analytical research effort to fabricate a flexible wing model using composite materials. Design constraints required that the model meet a proof load condition of twice the maximum aerodynamic load

expected during wind tunnel tests. Since the full scale wing was constructed of isotropic materials, a goal of the project was to demonstrate the superior weight and stiffness advantages of composite materials. In addition, a design condition required that the skin material be stronger for the model than the full-scale wing, yet maintain the same scaled flexibility and meet compatibility requirements. Composite materials appeared to be an ideal choice for the skin design. Several composite material systems were evaluated, however no material met all of the scaling requirements exactly. As a compromise, a hybrid material of E-glass and graphite-epoxy was chosen. Excellent agreement between the experimental results and a finite element analysis were obtained for natural frequencies and mode shapes of the scale model composite wing. As in the previous example, it was not possible to study scaling effects since the model composite structures were compared directly to metal structures and not to full scale composite prototypes.

The problem of constructing and testing a scale model of the Filament Wound Case (FWC) of the solid rocket motor of the Space Shuttle was discussed by Verderaime [34]. An experimental program consisting of hydroburst tests on filament wound bottles, typically 20 inches in diameter, were conducted to simulate loading conditions in the prototype which has a diameter of 12 feet and is 100 feet long. Values of in-plane stiffness calculated from lamination theory and experimental results from the hydroburst tests were in gross disagreement. This inconsistency made it necessary to identify the winding parameters which significantly alter the construction. These were found to be fiber tow spacing and the ability of the resin to mend in the curing stage. It was concluded that resin dependent stiffnesses were significantly less on full-scale articles due to gaps and unmended resin areas caused by difficulty in scaling the winding process. Verderaime recommended that either the scaled stiffness be used with a corresponding weight penalty on full-scale, or the winding process be adjusted to eliminate the scale

effect and yield test articles with consistent elastic properties for all scaled sizes.

The second category of research which has been reported on scaling effects in composites concerns the influence of specimen size on failure. Often the term "scale effect" is used to describe the influence of varying specific geometrical parameters on the structural response. For example, Fairfull [35] studied scaling effects in the energy absorption behavior of axially crushed composite tubes. In his experiments the thickness-to-diameter (t/d) ratio of the tube was found to be a critical factor for determining the mode of crushing response, while tube length had no influence on the mean crush load for specimens of constant cross-sectional area. Consequently, his experimental approach concentrated on effects due to variations in t/d and not in determining scale effects involving material and geometric properties from replica model tests.

The scale effect in failure of composite structures has also been analyzed using statistical methods, particularly Weibull distributions, and fracture mechanics based theories. A review of the literature and discussion of these two approaches will be presented separately in Chapter 8 when the topic of scaling effects in failure behavior of composite beams is presented.

Finally, a series of tests have been conducted recently by Morton [36] to examine scaling effects in the dynamic response of transversely impacted composite beams. Results from his tests indicated that classical scaling laws apply for elastic dynamic response, but a size effect was observed as the beams became damaged under greater impact loads. Morton also discussed possible scaling conflicts due to rate dependent material properties and notch-sensitivity. A fracture mechanics hypothesis was presented to explain the size effect in strength, although a micromechanical damage study was not performed to verify the theory. The research performed by Morton is important in understanding scaling effects in composite structures because it focuses on an intermediate level problem. As such, it bridges the gap between detailed

microstructural studies on a material level and the testing of large, complicated structures on a macroscopic level.

1.3 Objective, Scope, and Approach of Research

The goal of this research is to demonstrate the validity of scale model testing in predicting the static and dynamic response of a typical aircraft substructure. In particular, the testing and analysis are performed on composite beam-columns subjected to an eccentric axial compressive load, as depicted in the schematic drawing in Figure 1-1. This loading configuration has been studied previously by Derian [37] and Sensmeier [38] to examine the large deflection response and failure of composite beams subjected to both static and impulsive loads. They chose to study the beam response because it represents the simplest generic aircraft-type structure, i.e., the beam could be a fuselage skin, stiffener flange, or stiffener cap. The beams are loaded dynamically in bending to simulate conditions observed during crash tests of aluminum fuselage sections [39]. It was observed from aluminum fuselage drop tests that much of the impact energy was absorbed through bending failures of the skins, stringers, and stiffeners. Thus, this loading configuration was chosen because it produces large flexural deformations and global failure of the beams away from the supported ends. Derian and Sensmeier used the eccentric beam-column configuration to study the energy absorption capabilities of composite materials with the ultimate goal of improving the crashworthiness of aircraft constructed of these materials.

Another objective of this research is to develop the scaling law which governs the static and dynamic response of the eccentrically loaded composite beam-column, and to verify the scaling law through an experimental program. For the static case, the nondimensional parameters, or Pi terms, which form the scaling law are found by nondimensionalizing the governing equations and boundary conditions for the small deflection beam-column problem.

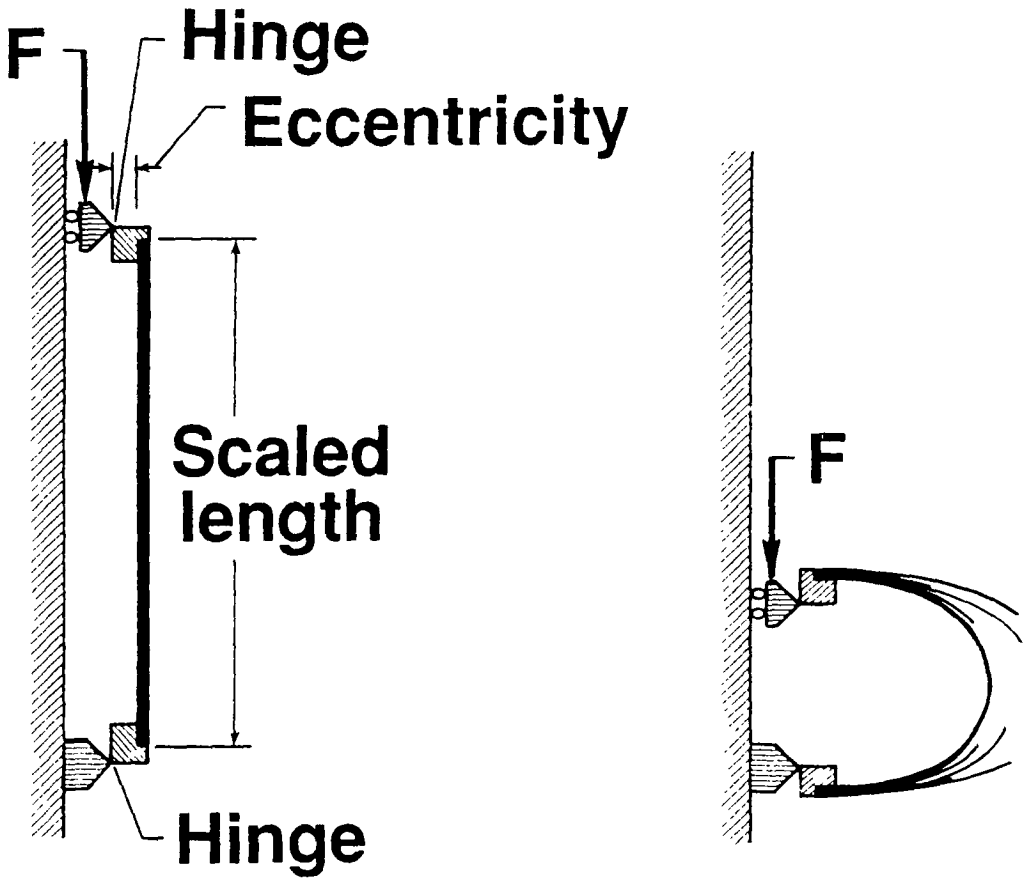

Figure 1-1. Schematic drawing of the test configuration.

A dimensional analysis based on the Pi Theorem is used to derive the scaling law for the beam-column subjected to impact loading conditions.

Since little previous data on scaling effects in composites have been reported, a comprehensive experimental program was implemented to verify the scaling law and to examine a variety of composite beam responses and failure mechanisms. Results for four laminate types including unidirectional, angle ply, cross ply, and quasi-isotropic are presented for graphite-epoxy composite beams having rectangular cross-sections. The approach taken in fabricating the scale model beams was to adjust the number of layers for each angular ply orientation to achieve scaling of the in-plane and bending properties on a laminate level. No attempt was made to scale individual fibers on a microstructural level. Replica model beams ranging in scaled size from 1/6, 1/4, 1/3, 1/2, 2/3, 3/4, 5/6, and full scale were tested under static load until failure. The static load-deflection data were used to determine the test parameters (drop height and impact mass) for the impact tests. Due to limitations in the drop tower used to perform the impact tests, only 1/2, 2/3, 3/4, 5/6, and full scale beams were tested dynamically. In each case, the impact tests were performed under scaled test conditions to produce failure of the beams.

Load and strain response of the beams under both static and dynamic loading conditions are examined to determine if significant deviations exist between the scale models and the prototypes when the responses are "scaled up". In addition, failure mechanisms between scale model and prototype beams are compared. Correlations of the test results between the scale model beams and the prototypes should validate the model law and prove whether full scale behavior can be predicted through inexpensive scale model testing.

Several analytical techniques were applied to the eccentrically loaded composite beam-column for comparison with the experimental data and to perform failure analyses. For the static

loading case, a one dimensional large rotation "elastica" type solution was developed to predict the beam-column response. The exact expression relating the moment and curvature was incorporated in the analysis, thus allowing the solution to predict large rotation response. In addition, the nonlinear finite element structural analysis computer program DYnamic Crash Analysis of STructures (DYCAST) [40] was used to model the beam response. Both the "elastica" beam solution and the DYCAST model are based on the assumption of linear elastic, isotropic material properties for the composite beam-column. Consequently, effective bending stiffnesses were derived for the composite beams. To investigate the effect of nonlinear material properties, a finite element code developed by Sensmeier [38] was also used. His code incorporated data from material characterization tests performed on the graphite-epoxy system used to fabricate the test specimens. It also included width-wise effects which become important for laminates with large bend-twist coupling terms. For the dynamic case, the composite beam-column impact problem was modeled using the DYCAST finite element code. These various analytical techniques provided insight into the beam-column response and were used to investigate scaling effects in the failure behavior.

1.4 Organization of the Report

An overview of the procedure used to derive the scaling parameters for the beam-column impact problem is presented in Chapter 2. In addition, the significance of some of the Pi terms in the scaling law and potential scaling conflicts are discussed. Details of the dimensional analysis procedure are somewhat tedious and are given in Appendix A.

Chapter 3 outlines the experimental program including beam specimens, testing apparatus, instrumentation, data acquisition, and test procedures. The chapter is divided into two main sections describing both the static and dynamic testing.

The various analytical techniques used to model the composite beam-column problem are described in Chapter 4. A small deflection, static beam analysis is developed and the governing equations and boundary conditions are nondimensionalized to illustrate this technique for determining scaling parameters. A large deflection beam analysis based on the "elastica" solution is described, with details of the development given in Appendix B. The nonlinear finite element code DYCAST model for both the static and dynamic loading conditions is presented. The finite element code developed by Sensmeier is also briefly described as applied to the eccentrically loaded beam-column problem.

The motivation and procedures used to determine values of the bending stiffness of the composite beams from experimental data are discussed in Chapter 5. Results are presented in Chapters 6 and 7 from the static and impact tests, respectively. Both chapters include descriptions of observed failure mechanisms, load and strain responses of the scaled beams, and comparisons of the static and dynamic experimental data with analysis. A discussion of failure analyses and the application of failure theories for predicting scaling effects in the strength of the composite beams are presented in Chapter 8. Finally, a summary of the results and recommendations for future work are highlighted in Chapter 9.

Chapter 2 - Dimensional Analysis

2.1 Development of Pi Terms

Two common methods are used to determine the nondimensional parameters which form the scaling law for a given phenomenon. These are (1) nondimensionalization of the governing equations, and (2) application of the Pi Theorem. The first technique is illustrated in Chapter 4 for the problem of a beam subjected to bending with small deflections. In general, the procedure involves expressing the governing partial or ordinary differential equations and boundary conditions in terms of dimensionless variables. The coefficients of terms in the resulting nondimensional equations form the Pi terms or scaling law. This technique has been applied extensively in the field of fluid mechanics to develop similarity conditions for fluid flows. Familiar parameters such as the Reynolds, Euler, Weber, and Froude numbers are Pi terms which result from dimensional analysis based on nondimensionalization of governing equations. For example, when the technique is applied to the Navier-Stokes equations for an incompressible, laminar flow, it is shown that fluid flows will be kinematically and dynamically similar if the Reynolds number is identical for the flows [41]. This example from fluid mechanics demonstrates that important information concerning a physical system can be obtained without solving the governing equations. However, one limitation of the method is that it requires sufficient knowledge of the problem so that the governing equations are known. Certain assumptions are implicit in the formulation of these equations (such as neglecting body forces, or frictional forces, or air resistance, etc.) which will limit the scope of a dimensional analysis based on this technique.

The Pi Theorem is the more general method of the two and it is used to develop the scaling law for the composite beam-column configuration illustrated in Figure 1-1. The technique consists of identifying the important physical variables relevant to the problem

under consideration. Each variable may be represented dimensionally in terms of a fundamental set of units, typically either the Force-Length-Time (F-L-T) system or the Mass-Length-Time (M-L-T) system. The Pi Theorem is used in conjunction with the law of dimensional homogeneity to derive the dimensionless parameters which form the scale law. The law of dimensional homogeneity states that an analytically derived equation which represents a physical phenomenon must be independent of the system of units. Consequently, the fundamental equations of physics are dimensionally homogeneous, and all relationships derived from them must also be dimensionally homogeneous. The Pi Theorem states that the behavior of any physical phenomenon can be represented in terms of independent dimensionless products, called Pi terms, which are derived from a complete set of relevant physical parameters [12].

The number of independent Pi terms which are formed to describe a physical system which involves n variables is equal to the number n-q, where q is the rank of the dimensional matrix formed by the dimensions of each variable. In general, the number q is equal to the number of fundamental dimensions needed to describe each of the variables, or three. The nondimensional Pi terms which are formed by application of the Pi Theorem are products and quotients of the original variables. The Pi terms are independent, but not unique, and may be multiplied together to form new combinations which are equally acceptable. In the development of a scale model experiment, attempts are made to ensure that the Pi terms are identical for the model and the prototype. This may or may not be possible given the set of variables chosen to describe the problem. Scaling conflicts arise when Pi terms are not satisfied in an experiment. Typically, the geometric scale factor, λ, is first chosen for the experiment. The scale factors for all other variables are then derived in terms of the geometric scale factor from the Pi terms and other conditions set by the experiment.

Listed in Table 2-1 are the parameters which were chosen for the composite beam-column problem shown in Figure 1-1. Variables

were chosen to describe the geometry of the beam, its constitutive behavior, and the impact conditions of the experiment. Additionally, variables were selected to characterize the response of the beam such as position, transverse displacement, and frequency of vibration. A total of 24 parameters are listed in Table 2-1 and three fundamental units (M-L-T system) are used to express their dimensions. Thus, a total of 21 nondimensional Pi terms will be formed by application of the Pi Theorem. Details of the procedure used to develop the Pi terms are outlined in Appendix A and are based on the methods presented in Reference [12]. Easier and more elegant methods exist for developing the Pi terms in addition to the one presented in Appendix A. For example, Barr presents an excellent survey of several techniques in References [42-45].

The Pi terms for the beam-column impact problem are:

$$\pi_1 = b/l \qquad \pi_2 = h/l \qquad \pi_3 = l^2\eta/D_{eff}t^2 \qquad \pi_4 = l^2A_{11}/D_{eff}$$

$$\pi_5 = \nu \qquad \pi_6 = e/l \qquad \pi_7 = Fl/D_{eff} \qquad \pi_8 = vt/l$$

$$\pi_9 = E/D_{eff} \qquad \pi_{10} = \sigma l^3/D_{eff} \qquad \pi_{11} = \varepsilon \qquad \pi_{12} = M/D_{eff} \qquad (2.1)$$

$$\pi_{13} = \Delta/t \qquad \pi_{14} = gt^2/l \qquad \pi_{15} = x/l \qquad \pi_{16} = \omega t$$

$$\pi_{17} = w/l \qquad \pi_{18} = at^2/l \qquad \pi_{19} = \dot{\varepsilon}t \qquad \pi_{20} = \tau l^3/D_{eff}t$$

$$\pi_{21} = K_Q l^{5/2}/D_{eff}$$

Ideally, to perform a scale model experiment, each of the Pi terms must be the same for the model and the prototype. A variable is designated for model or prototype by the subscripts m or p, respectively. It is possible to form relationships among the variable

Table 2-1. List of parameters for the dimensional analysis of the composite beam impact problem.

VARIABLE NAME	SYMBOL	DIMENSIONS (M-L-T)
Beam Length	l	L
Width	b	L
Thickness	h	L
Beam Mass	η	M
Beam Axial Stiffness	A_{11}	M/T^2
Bending Stiffness	D_{eff}	ML^2/T^2
Poisson Ratio	ν	1
Eccentricity of Load	e	L
Force of Impact	F	ML/T^2
Velocity of Impactor	v	L/T
Energy of Impact	E	ML^2/T^2
Stress in Beam	σ	M/LT^2
Strain in Beam	ε	1
Applied End Moment	M	ML^2/T^2
Time	t	T
Duration of Pulse	Δ	T
Gravity	g	L/T^2
Position along Beam	x	L
Frequency of vibration	ω	1/T
Transverse Displacement	w	L
Acceleration	a	L/T^2
Strain Rate	$\dot{\varepsilon}$	1/T
Strain Rate Parameter	τ	T
Critical Stress Intensity Factor	K_Q	$M/T^2L^{1/2}$

scale factors by equating Pi terms for the model and prototype. For example, the third Pi term yields the relation:

$$\pi_3 = (l^2\eta/D_{eff}t^2)_m = (l^2\eta/D_{eff}t^2)_p \tag{2.2}$$

Writing this expression in terms of the variable scale factors gives,

$$\lambda_{Deff}\lambda_t^2 = \lambda_l^2\lambda_\eta \tag{2.3}$$

where the symbol λ with its subscript designates the scale factor for that particular variable. For example,

λ_l = length of the model/length of the prototype.

The relations derived from π_1 through π_{21} form the basis of the scaling law. To completely develop the law, certain assumptions are made from the experiment. First, the geometric scale factors, λ_l, are chosen to be 1/6, 1/4, 1/3, 1/2, 2/3, 3/4, 5/6, and 1. Since λ_l is fixed for the models, it is designated $\lambda_l = \lambda$, the geometric scale factor. Also, the same material is used to construct both the models and the prototype. This requires that

$$\lambda_{D_{eff}} = \lambda^3$$

$$\lambda_{A_{11}} = \lambda \tag{2.4}$$

$$\lambda_\eta = \lambda^3$$

Now, based on the relationships derived from the Pi terms together with the scaling parameters chosen from the experiments, it is possible to complete the scaling law.

$$\lambda_b = \lambda \qquad \lambda_h = \lambda \qquad \lambda_t = \lambda \qquad \lambda_v = 1$$

$$\lambda_e = \lambda \qquad \lambda_F = \lambda^2 \qquad \lambda_v = 1 \qquad \lambda_E = \lambda^3$$

$$\lambda_\sigma = 1 \qquad \lambda_\varepsilon = 1 \qquad \lambda_M = \lambda^3 \qquad \lambda_\Delta = \lambda \tag{2.5}$$

$$\lambda_g = 1/\lambda \qquad \lambda_x = \lambda \qquad \lambda_\omega = 1/\lambda \qquad \lambda_W = \lambda$$

$$\lambda_a = 1/\lambda \qquad \lambda_{\dot{\varepsilon}} = 1/\lambda \qquad \lambda_\tau = \lambda \qquad \lambda_{K_Q} = \lambda^{1/2}$$

2.2 Discussion of the Pi Terms

The concept of similarity between two systems implies that homologous positions and homologous times are related by a constant value. When the constants of proportionality between variables used to describe a system are known, then results from model tests can be "scaled up" to predict prototype response. Various types of similarity may be defined between systems including geometric, dynamic, kinematic, and constitutive similarity. These will be discussed in light of the dimensional analysis performed on the composite beam-column impact problem which was outlined in the previous section.

2.2.1 Geometric Similarity

A model is said to be geometrically similar to its prototype if the dimensions have been scaled by the same factor. In the extreme, geometric similarity requires that all geometric dimensions of a system be scaled to produce an exact replica model. However, in most cases this is impractical or impossible to achieve. For the composite beam-column problem, geometric similarity is ensured by fabricating beams with scaled lengths, widths, and thicknesses. In addition, the boundary conditions are scaled by applying the same geometric scale factor to the hinge supports which provide the offset for the axial load. However, not all geometric dimensions involved are scaled in proportion to the geometric scale factor. For example, the drop height for the impact tests is distorted geometrically. It

should be noted that this variable is not included in the list of relevant parameters for the problem. As seen in Eq. 2.5, the impact velocity scales as unity which implies that the velocity of the drop mass must be the same for both the model and prototype beam experiments. The velocity at impact is determined by the drop height ($v^2 = 2gH$). Consequently, to ensure scaled velocity, the same drop height is used for both the model and prototype tests. This distortion is permitted since the gravitational field is not scaled.

Baker, et al [12] discuss the scaling of impact problems in terms of two separate processes which may be decoupled. The first is the drop mass falling in a gravitational field and the second is the impact event and subsequent dynamic response of the beam. The beam deformation is solely dependent on the kinetic energy of the striking mass. The use of a free-fall drop mass is simply a convenient technique to obtain the correct incident velocity for impact. The fact that the structural problem is scaled in one manner and the free-fall mass in another is due to the distortion in the gravitational field. The scaling law given by Eq. 2.5 indicates that gravity should scale as $1/\lambda$. This requirement is not satisfied since the gravity field was unaltered and, thus, scales as unity. One way to interpret the gravity distortion is to consider that if a 1/6 scale model is tested in 1-g, the influence of the gravity force is equivalent to testing the full scale model in 1/6-g. Obviously, as the scale factor of the model is reduced, the gravitational effect is similar to testing the full-scale model in zero-g. This result has important implications for testing of scale model structures for space applications as discussed in Reference [20].

2.2.2 Dynamic and Kinematic Similarity

Kinematic similarity has been defined by Langhaar [13] as follows: "The motions of two systems are similar if homologous particles lie at homologous points at homologous times." Thus, kinematic similarity implies similarity between the motions of two

systems. For the composite beam-column problem, the scale factors for position, time, velocity, acceleration, and frequency define kinematic similarity between model and prototype systems. It is noted that time scales in the same proportion as the geometric scale factor, λ. Thus, for a 1/2 scale model, events happen twice as fast in real time as for the prototype.

Dynamic similarity between two systems exists if homologous parts of the systems experience homologous forces. It can be shown that if kinematic similarity exists for systems which have similar mass distributions, then dynamic similarity is easily inferred from Newton's Second Law. If a model and prototype are also geometrically similar, then the scale law predicts that the forces will scale as λ^2. Likewise, the applied moment and energy parameters will scale as λ^3, as indicated in Eq. 2.5.

2.2.3 Constitutive Similarity

Models are not always constructed of the same material as the prototype, often for reasons of cost or difficulties in fabrication. Dissimilar material models are usually designed to have constitutive similarity, or homologous stress-strain curves, within the loading range of interest. All of the composite beam specimens tested in the experimental portion of this investigation were manufactured from the same pre-preg material system and were constructed to ensure constitutive similarity. Details of the fabrication technique are given in Chapter 3. Since the material density is constant for both the model and prototype beams, it scales as unity. Then, geometric similarity between the model beams implies that beam masses will scale as λ^3. Inplane stiffness and effective bending stiffness will scale as λ and λ^3, respectively, as indicated in Eq. 2.4.

The strain rate parameter, τ, was included in the list of relevant parameters to illustrate the effect of rate-sensitivity in material behavior. Morton [36] has discussed the scaling conflicts which arise when time-dependent material properties are introduced

into a dimensional analysis. To illustrate the problem, suppose a material constitutive response is given by the relation

$$\sigma = E(\varepsilon + \tau\dot{\varepsilon}) \tag{2.6}$$

From the dimensional analysis presented in the previous section it was found that τ scales in proportion with the geometric scale factor, λ (This is reasonable since τ has the dimension of time and time scales as λ.) However, when the same material is used to construct both the model and prototype, the strain rate constant is identical for both systems and scales as 1.0. This scaling distortion implies that strain rates in the model will be greater than those in the prototype. For high strain rates, this result could cause brittle behavior in the model while the prototype exhibits ductile behavior at corresponding times during the loading. However, in his investigation, Morton [36] concluded that rate effects were insignificant for the composite material system and laminates that he tested, but noted that these effects may become important for matrix-dominated laminates.

The scaling law, Eq. 2.5, indicates that stress conditions are the same in the model as in the prototype, i.e., stress scales as unity. Ideally, then, failure should occur at the same stress level and at homologous times for the model and full scale beams. However, deviations from this elementary approach to strength scaling have been commonly observed. It has been well documented that small scale models exhibit higher failure loads than full-scale prototypes. A general discussion of this phenomenon is given by Jones [9]. One explanation for the size effect in fracture has been developed based on principles of linear elastic fracture mechanics. To illustrate how a fracture mechanics model introduces a scaling conflict, the critical stress intensity factor, K_Q , is included in the dimensional analysis. K_Q is defined as the value of the stress intensity factor for which crack growth becomes unstable. Since composite materials often exhibit brittle fracture, it is reasonable to include a parameter such as the critical stress intensity factor to model the failure mechanism. K_Q is

assumed to be a material property and, thus, is not dependent on loading conditions, initial crack geometry or size, or any other parameter. As such, K_Q will have the same value for both model and prototype beams. The dimensional analysis, however, indicates that K_Q scales in proportion to $\lambda^{1/2}$. To determine how this scaling conflict effects stress, π_{21} is divided by π_{10}, to yield a new nondimensional parameter which must be satisfied for both model and prototype beams.

$$\left[\frac{K_Q}{\sigma l^{1/2}}\right]_m = \left[\frac{K_Q}{\sigma l^{1/2}}\right]_p \tag{2.7}$$

Rewriting this expression in terms of the variable scale factors gives:

$$\lambda_\sigma = \lambda_{K_Q} \lambda_l^{-1/2} \tag{2.8}$$

If K_Q is assumed to scale as unity and the length scale factor scales in proportion to the geometric scale factor, λ, then, the stress scale factor becomes $\lambda^{-1/2}$. This means that the stress required to propagate a crack in a linear elastic model will be greater by a factor of $\lambda^{-1/2}$ than the stress needed to propagate a crack in a geometrically and constitutively similar prototype. As an example, the stress for crack propagation in a 1/4 scale structural model will be twice the value required for the full-scale structure. Consequently, the model will appear to be twice as strong. This effect has been studied in detail by Atkins and Caddell [10] and a more complete discussion of this issue, especially as applied to the composite beam-column problem, is provided in Chapter 8.

Chapter 3 - Experimental Program

Details of the experimental program which was implemented to investigate scaling effects in the large deflection response of composite beams are outlined in this chapter. The static and dynamic programs are separated into two main sections of the chapter. Within each section, the fabrication and instrumentation of beam specimens, test apparatus and procedure, and data acquisition systems are discussed.

3.1 Static Testing

The static test program was developed to examine a wide variety of composite behavior ranging from a very stiff to a more flexible beam response. The four laminate types chosen for study were unidirectional, angle ply, cross ply, and quasi-isotropic. In addition to the variation in beam response due to stiffness differences among these laminate families, a variation in failure modes or mechanisms was expected. The comprehensive experimental program outlined in the following sections was designed to provide a broad-based foundation of information on scaling effects in composites.

3.1.1 Beam Specimens

Beams having unidirectional, angle ply, cross ply, and quasi-isotropic laminate stacking sequences were constructed of a Hercules* high modulus graphite fiber and epoxy system designated as AS4/3502 for the static and dynamic tests. Complete material characterization tests were performed on this material system by

---

* Identification of commercial products and companies is used to describe adequately the test materials. The identification of these commercial products does not constitute endorsement, expressed or implied, of such products by the U.S. Army or the National Aeronautics and Space Administration.

Sensmeier [38]. The response of the material in both the fiber and transverse material directions in tension and compression and the inplane shear response were obtained and reported in Reference [38]. The material exhibited varying degrees of both nonlinear and bimodular material response. For the current research project only the initial material moduli were considered. A summary of the material properties as determined from material characterization tests is given in Table 3-1.

The full scale beam dimension was chosen to be 3.0 inches wide with a 30.0 inch gage length, and 48 plies thick with an average ply thickness of 0.0054 inches. The total length of the full scale beam was 34.5 inches, including the distance of the beam supported in the hinges. The scale model beams were constructed by applying seven different geometric scale factors including 1/6, 1/4, 1/3, 1/2, 2/3, 3/4, and 5/6 to the full scale dimensions. A set of scaled beams is illustrated in Figure 3-1 and the dimensions and lay-ups of each beam are listed in Table 3-2. The thickness dimension was scaled by reducing the number of layers in each angular ply group of the full scale laminate stacking sequence by the appropriate factor. Using this approach, it was not possible to construct a 1/4 or 3/4 scale quasi-isotropic beam. This technique of constructing the scale model beams by adjusting the number of θ_i-plies achieves scaling on a macroscopic level. The inplane stiffnesses, A_{ij} , are scaled by λ, and the bending stiffnesses, D_{ij}, are scaled by λ^3. Ideally, to construct a true replica model of the prototype beam, the microstructure should be scaled as well as the macroscopic dimensions. This would entail having composite manufacturers fabricate prepreg tape with scaled fiber diameters and thicknesses. In fact, scaling on this level is accomplished in the construction of model structures made from reinforced concrete [2,3]. In that application both the reinforcing bar diameter and the size of the aggregate are sized accordingly to build models which are scaled for strength and stiffness. Practically, however, scaling of the microstructure for advanced composites is not feasible at this time. Since the thickness dimension for the

Table 3-1. Material properties of AS4/3502 high modulus graphite-epoxy.

TEST	VALUE
Longitudinal Tension, E_1	19.85 (Msi)
Transverse Tension, E_2	1.43 (Msi)
Inplane Shear, G_{12}	0.82 (Msi)
Poisson Ratio, ν_{12}	0.293

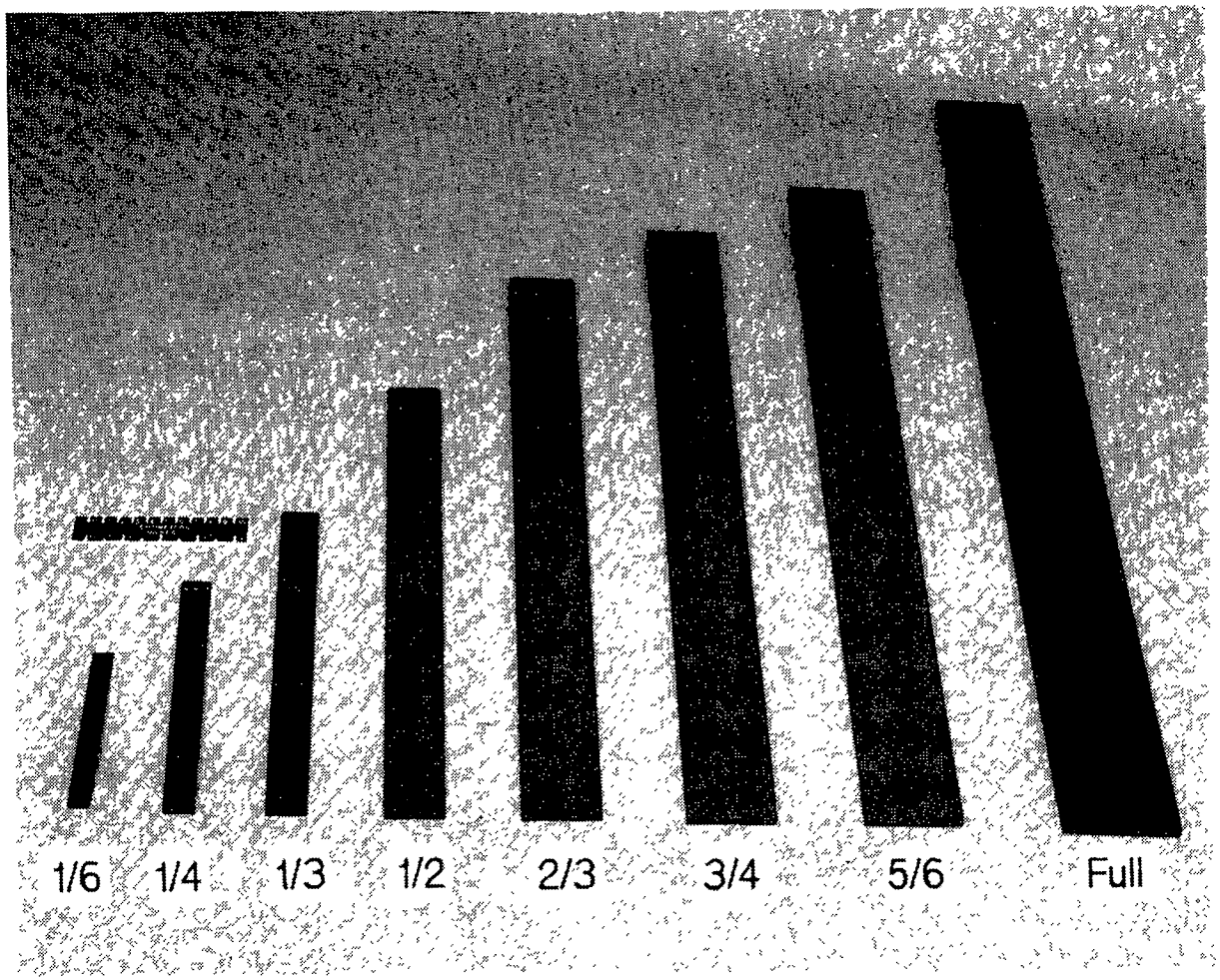

Figure 3-1. Photograph of a set of scale model beams for static testing.

TABLE 3-2. Scale model beam dimensions and lay-ups.

SCALE	BEAM DIMENSION	UNIDIRECTIONAL	ANGLE PLY	CROSS PLY	QUASI-ISOTROPIC
1 / 6	0.5" X 5.0"	$[0]_{8T}$	$[45_2/-45_2]_S$	$[0_2/90_2]_S$	[-45/0/45/90]s
1 / 4	0.75" X 7.5"	$[0]_{12T}$	$[45_3/-45_3]_S$	$[0_3/90_3]_S$	----------
1 / 3	1.0" X 10.0"	$[0]_{16T}$	$[45_4/-45_4]_S$	$[0_4/90_4]_S$	$[-45_2/0_2/45_2/90_2]_S$
1 / 2	1.5" X 15.0"	$[0]_{24T}$	$[45_6/-45_6]_S$	$[0_6/90_6]_S$	$[-45_3/0_3/45_3/90_3]_S$
2 / 3	2.0" X 20.0"	$[0]_{32T}$	$[45_8/-45_8]_S$	$[0_8/90_8]_S$	$[-45_4/0_4/45_4/90_4]_S$
3 / 4	2.25" X 22.5"	$[0]_{36T}$	$[45_9/-45_9]_S$	$[0_9/90_9]_S$	----------
5 / 6	2.5" X 25.0"	$[0]_{40T}$	$[45_{10}/-45_{10}]_S$	$[0_{10}/90_{10}]_S$	$[-45_5/0_5/45_5/90_5]_S$
6 / 6	3.0" X 30.0"	$[0]_{48T}$	$[45_{12}/-45_{12}]_S$	$[0_{12}/90_{12}]_S$	$[-45_6/0_6/45_6/90_6]_S$

smallest size beam is approximately two orders of magnitude greater than the fiber diameter, the idea of scaling on the macroscopic level is justified.

Panels having the laminate stacking sequences listed in Table 3-2 were fabricated at the Composite Model Shop of the NASA Langley Research Center using prepreg tape. The panels were cured according to manufacturer's specifications and C-scanned to detect any gross defects. From the panels, six beams having the appropriate scaled dimensions listed in Table 3-2 were machined. Of these six, three beam specimens were designated and instrumented for static testing and three were designated and instrumented for dynamic testing. Slight variations were observed in the thickness dimensions of the cured beam specimens. Generally, the 1/6 scale beam was thicker on a per ply basis than the full scale beam for all laminate types. The maximum deviation in normalized thickness was approximately six percent. The measured thicknesses were used in all calculations for each beam specimen.

A labeling system was devised for the beam specimens. The first letter in the beam label identifies the lay-up of the beam. Unidirectional beams begin with 'U', angle ply with 'A', cross ply with 'C', and quasi-isotropic with 'Q'. The next three to four letters designate the scale factor of the beam. The following key shows the nomenclature which was used:

SIX	- 1/6 scale
FOR	- 1/4 scale
THR	- 1/3 scale
HALF	- 1/2 scale
2THR	- 2/3 scale
3FOR	- 3/4 scale
5SIX	- 5/6 scale
FULL	- full scale

Finally, the last digit in the beam name is the number of the specimen. These numbers range from 1 through 6, since six beam

specimens were fabricated for each laminate type and size. An example of a typical beam name would be: U2THR4. Thus, this beam is a unidirectional, 2/3 scale beam, specimen number 4. This beam identification system will be employed for the remainder of this report.

3.1.2 Test Apparatus

The basic loading configuration for the scaled beams is depicted in Figure 1-1. Each beam specimen was gripped in a set of hinges which offset the axial load with a moderate eccentricity. A detailed drawing of the hinge and beam attachment is shown in Figure 3-2. Eight sets of hinges were constructed (one for each of the eight scale factors) to ensure that the end condition was properly scaled. For each hinge, the eccentricity, the grip length, and the total distance from the center of the pin to the unsupported or free portion of the beam were scaled. The hinges and face plates were fabricated from aluminum.

The hinges were pinned to the platens of a standard load test machine which applied the compressive vertical load. The hinged-pinned connection allowed the beam to undergo large rotations during deformation. Beam specimens were loaded in this manner until catastrophic failure, defined as complete loss of load-carrying capability. The beam-column loading configuration was chosen, in part, because failures occur in a global fashion at the center of the beam where the maximum bending moment occurs. Thus, failures tend not to be introduced by local effects at the grip supports. Although the beam was loaded as a beam-column, the bending strains were several orders of magnitude greater than those due to axial compression. Therefore, the beam was, essentially, in a state of pure bending.

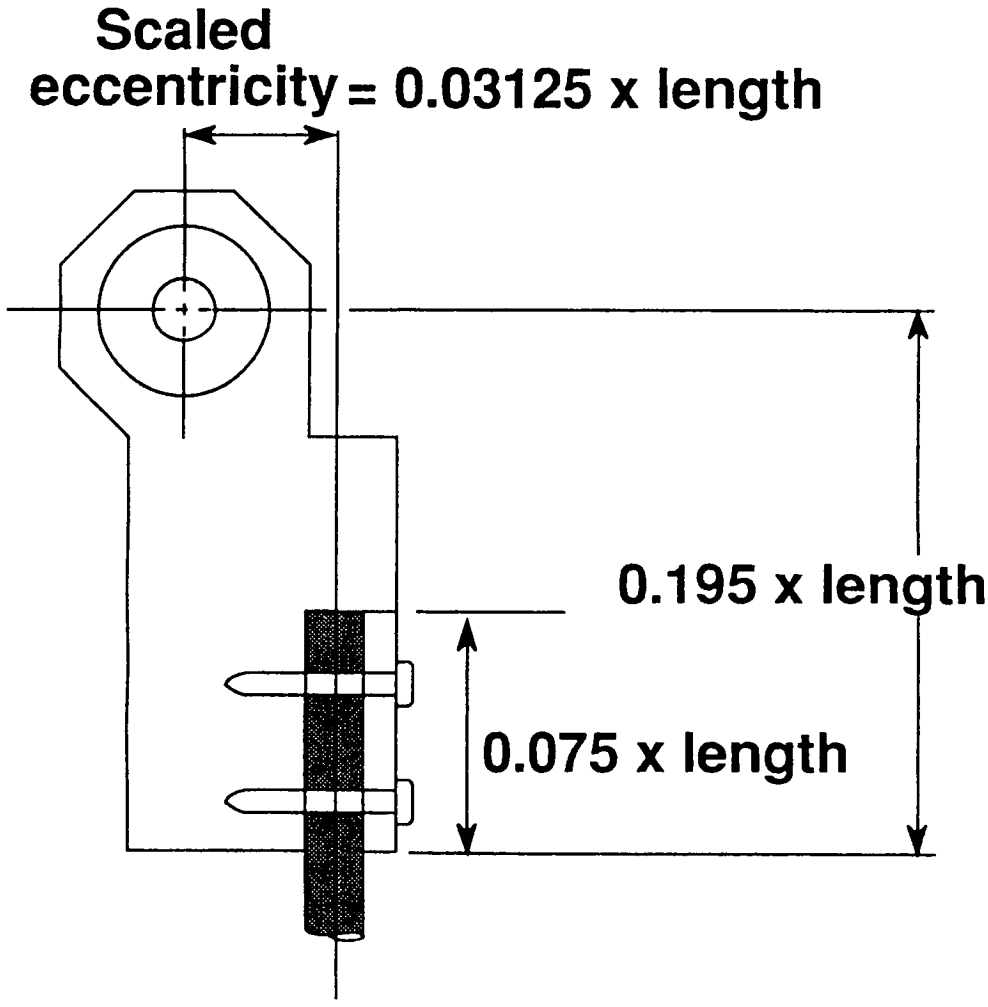

Figure 3-2. Detailed drawing of the hinge-beam attachment.

3.1.3 Instrumentation

Each beam was instrumented with back-to-back strain gages located at distances one-quarter and two-thirds along the length of the beam and with strain gage rosettes at the midpoint, as illustrated in Figure 3-3. Two sizes of strain gages were employed to accommodate the large differences in size among the beam specimens. The 1/6 and 1/4 scale beams were instrumented with gages having smaller effective gage lengths than those used for the 1/3 through full scale beams. All gages were standard 350 ohm resistance gages with gage factors ranging from 2.09 to 2.17.

Vertical load was measured by a load platform located at the base of the bottom hinge, as illustrated in Figure 3-4. The bottom hinge was securely fastened to the load platform which was mounted to the bottom platen of the load test machine. Two load platforms were designed and built for measuring the vertical load applied to the beam-column through the test machine. One had a maximum load capacity of 100 pounds and was used for the smaller scaled beam tests and for those tests in which small loads were expected, i.e., the majority of the angle ply beam tests. The second load platform had a capacity of 1000 pounds and was used for the larger scaled beam tests. The design of the load platforms was based on a bonded strain gage configuration. This configuration was wired such that any side loads or bending moments which might be present due to slight misalignments or bearing friction in the hinges would not influence the vertical load measurement.

The distance traveled by the platens of the load test machine during a test is defined as the end displacement for that test. End displacement was measured by a displacement transducer attached to the lower platen of the load test machine. A string type potentiometer (string pot) having a maximum range of 40 inches was used. The string was extended and attached to the upper platen of the load test machine prior to a test. During deformation, the upper platen was lowered and the string was drawn into the device

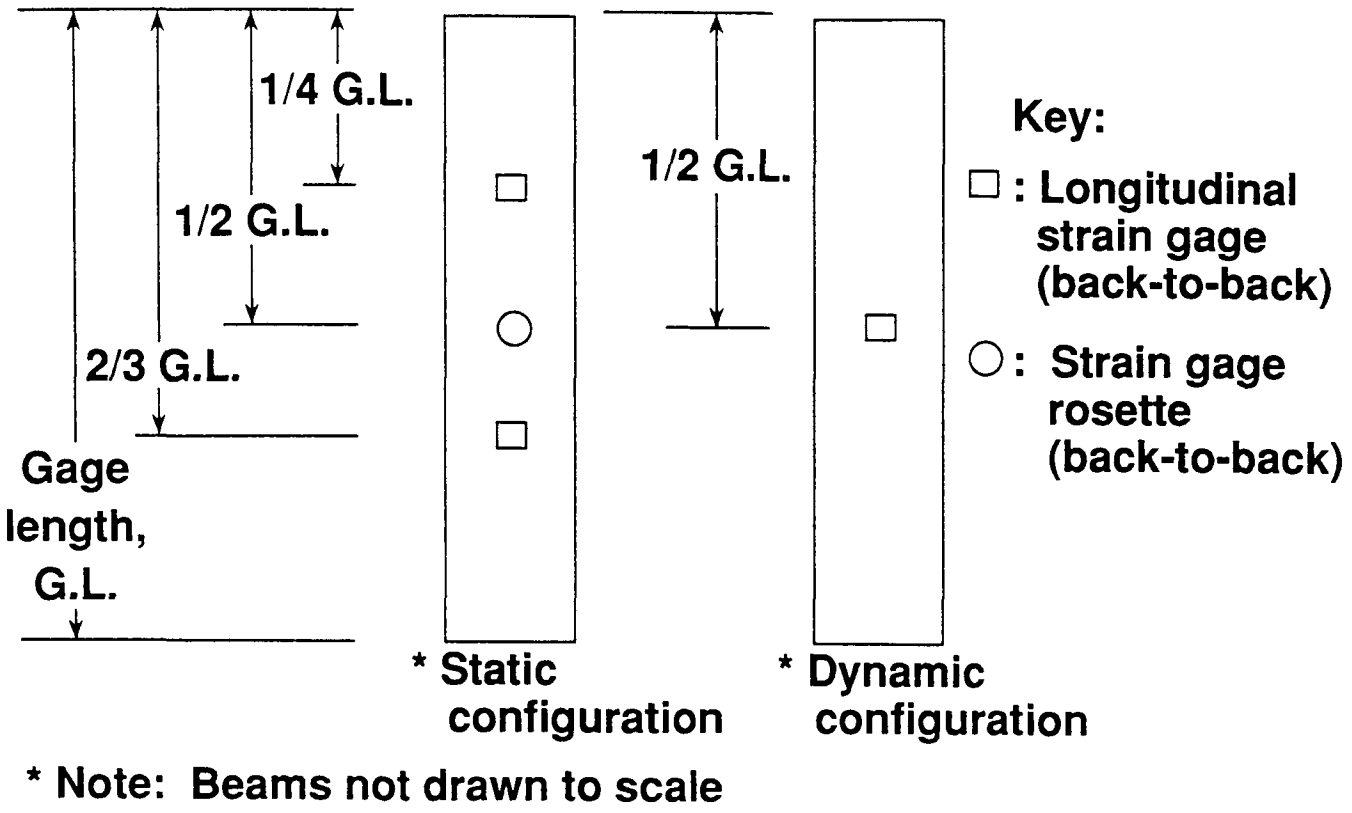

Figure 3-3. Strain gage layout for static and dynamic beam specimens.

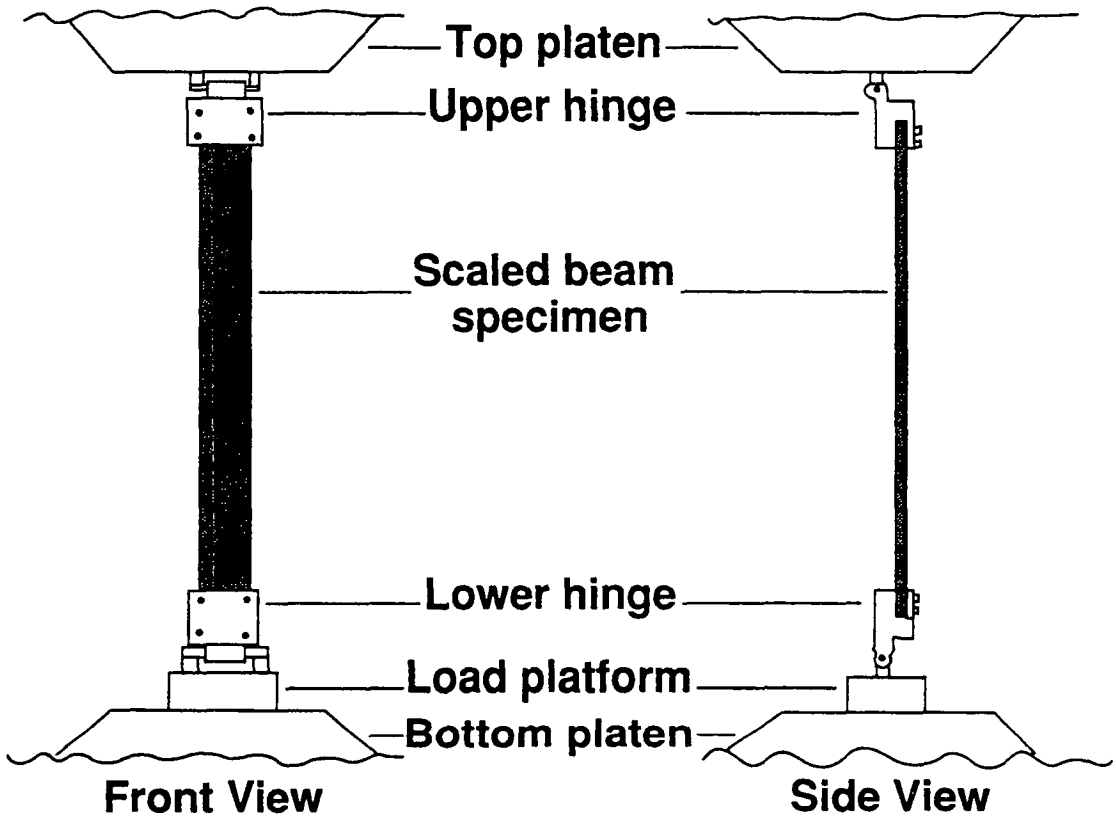

Figure 3-4. Schematic drawing of front and side views of the static test configuration.

producing an output voltage which could be converted into a displacement measurement. The string pot had a resolution of +/- 0.25% of full scale in the range of 2 to 5 inches, and a resolution of +/- 0.1% of full scale for displacements greater than 20 inches.

3.1.4 Data Acquisition

A personal computer based data acquisition system was used to collect 12 channels of data for each static beam test. The 12 channels were: load from the load platform; end displacement from the string pot; tensile and compressive longitudinal strains at a position located one quarter along the beam length from back-to-back strain gages; tensile and compressive longitudinal strains at a position located two-thirds along the beam length from back-to-back strain gages; and tensile and compressive longitudinal, transverse, and diagonal (along a 45 degree angle) strains from back-to-back strain gage rosettes located at the midpoint of the beam. The analog signals for each channel were amplified and filtered prior to being digitized by a MetraByte model DASH-16F multifunction high speed analog/digital I/O expansion board. The DASH-16F uses an industry standard 12 bit successive approximation, 8 microsecond converter. The DASH-16F board is supported by the STREAM-16 high speed data transfer utility program and by the LOTUS Measure data acquisition software package. LOTUS Measure software was used to collect calibration data and initial readings for the load, end displacement, and strain signals prior to a test. Test data were collected at a rate of 1 Khz (83.3 Hz per channel) using the STREAM-16 software. Digitized test data were converted to engineering units using the calibration factors and zero readings obtained before the test. Because of the high sampling rate of the STREAM-16 software, a large amount of data was generated for each test making the data files intractable. As a result, a program was written to process the data and reduce the size of the files. Typically, the data files were manipulated such that an initial portion of the file was unaltered, but

the remainder was thinned by a factor appropriate for the size of the file being considered.

3.1.5 Procedure

The test procedure consisted of the following steps. The beam specimen was securely fastened to the bottom hinge support and loosely supported in the top hinge. All instrumentation was set up and zero condition signals were obtained on the data acquisition system for all channels. Next, the beam was securely fastened in the top hinge while the load was monitored. This was done to ensure that the beam was not prestressed by a load introduced due to torque applied to the face plates of the top hinge.

Vertical compressive load was applied to the beam specimen by lowering the top platen of the load test machine. The platen traveled at a constant rate of 0.2277 in/sec. The test was completed when the beam specimen fractured catastrophically. Three replicate beams of each scale and laminate type were tested.

3.2 Dynamic Testing

An experimental program was developed to investigate scaling effects in the response and failure of composite beams subjected to impact loads. An application of this research is in the area of crashworthiness and energy absorption of generic composite structures. The U.S. Army and NASA have initiated a comprehensive research program to study the response of composite structures to impact or crash-type loads [46]. The objective of the joint program is to demonstrate the energy absorption capability of composite aircraft components by testing increasingly complex structures. A potentially large payoff can be realized if scale model composite structures can be tested instead of large composite prototype structures. The dynamic testing program outlined in the following sections was designed and implemented to determine the validity of

using scale model testing for studying the impact response of composite structural elements.

3.2.1 Beam Specimens

The scale model beams described in Section 3.1.1 were also tested under impact loading. Due to limitations of the drop tower which was used to conduct the impact tests, only the full, 5/6, 3/4, 2/3, and 1/2 scale unidirectional, angle ply, cross ply, and quasi-isotropic beams were tested dynamically. Table 3-2 lists the lay-ups and dimensions of the scale model beams. Figure 3-5 is a photograph of a set of scale model beams which were tested under impact loads.

3.2.2 Test Apparatus

The same loading configuration shown in Figure 1-1 was employed for the dynamic tests except that the compressive vertical load was applied impulsively. The beam specimens were gripped in scaled hinges, shown in Figure 3-2, which offset the axial load and produced the large rotations and deflections in bending. A schematic drawing of the drop tower used to perform the impact tests is shown in Figure 3-6, and a corresponding photograph is shown in Figure 3-7. The tower consists of four vertical steel rods ten feet long and one inch in diameter. The rods were fastened at the bottom to a channel section fixed to the floor and, at the top to a structural support beam of the building. The upper hinged end of the beam was supported by a slider which was free to move vertically along the two innermost rods through low friction bearings. The mass car slid down the two outermost rods on similar bearings and provided the impact force. Contact was made between the mass car and the slider through spherical steel impact points. High acceleration spikes at impact were moderated by placing a section of hard rubber covered by small lead plates on the slider/mass car impact point as shown in Figure 3-8. The lower hinge was fastened to a load platform which

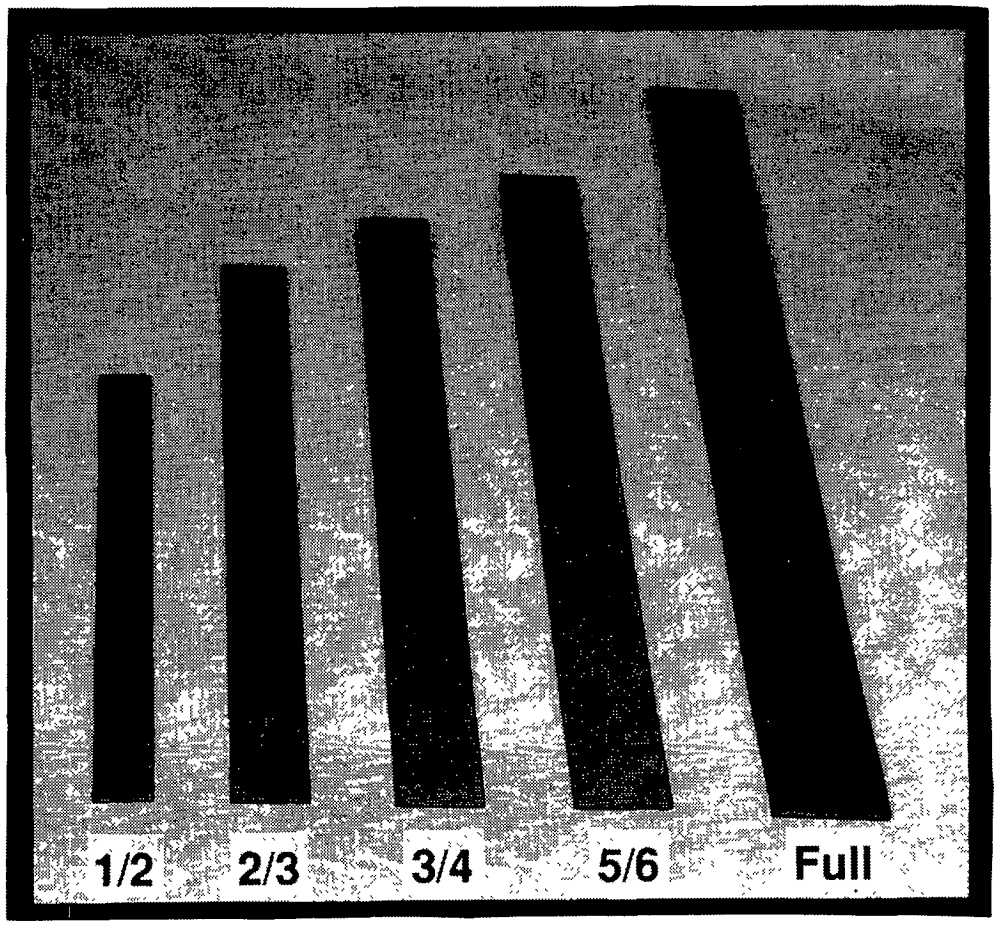

Figure 3-5. Photograph of a set of scale model beams for dynamic testing.

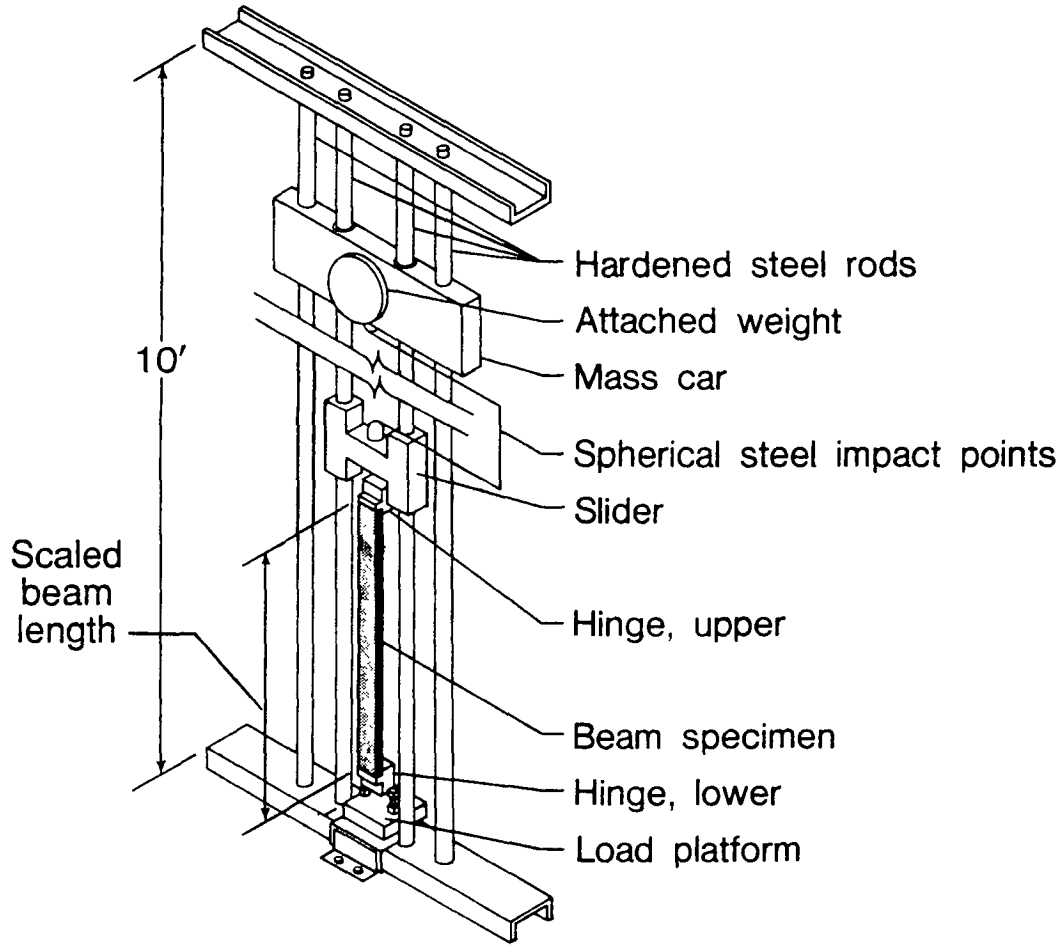

Figure 3-6. Schematic drawing of the drop tower used for impact testing of scale model composite beams.

ORIGINAL PAGE
BLACK AND WHITE PHOTOGRAPH

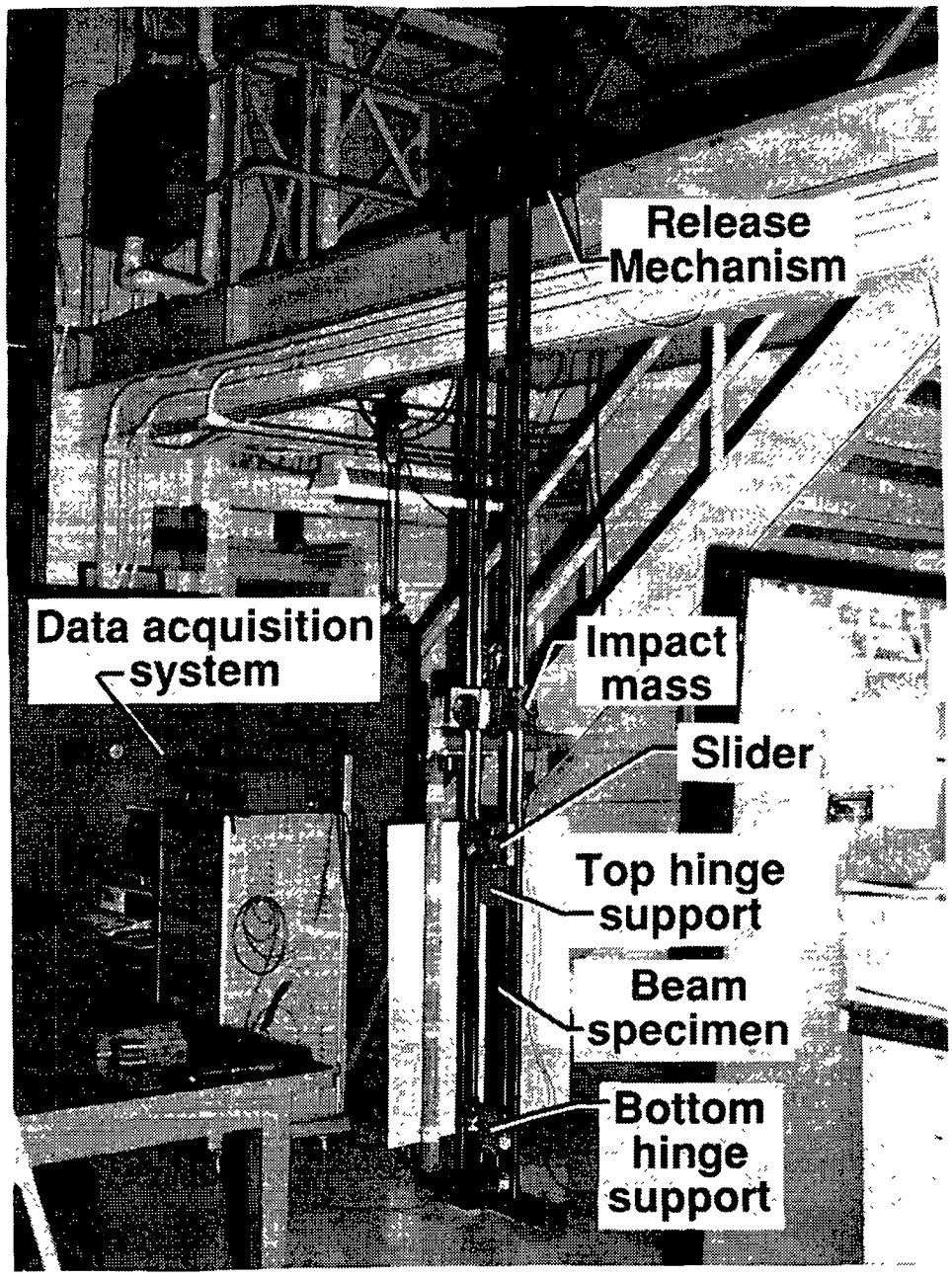

Figure 3-7. Photograph of the drop tower used to conduct impact tests on scale model composite beams.

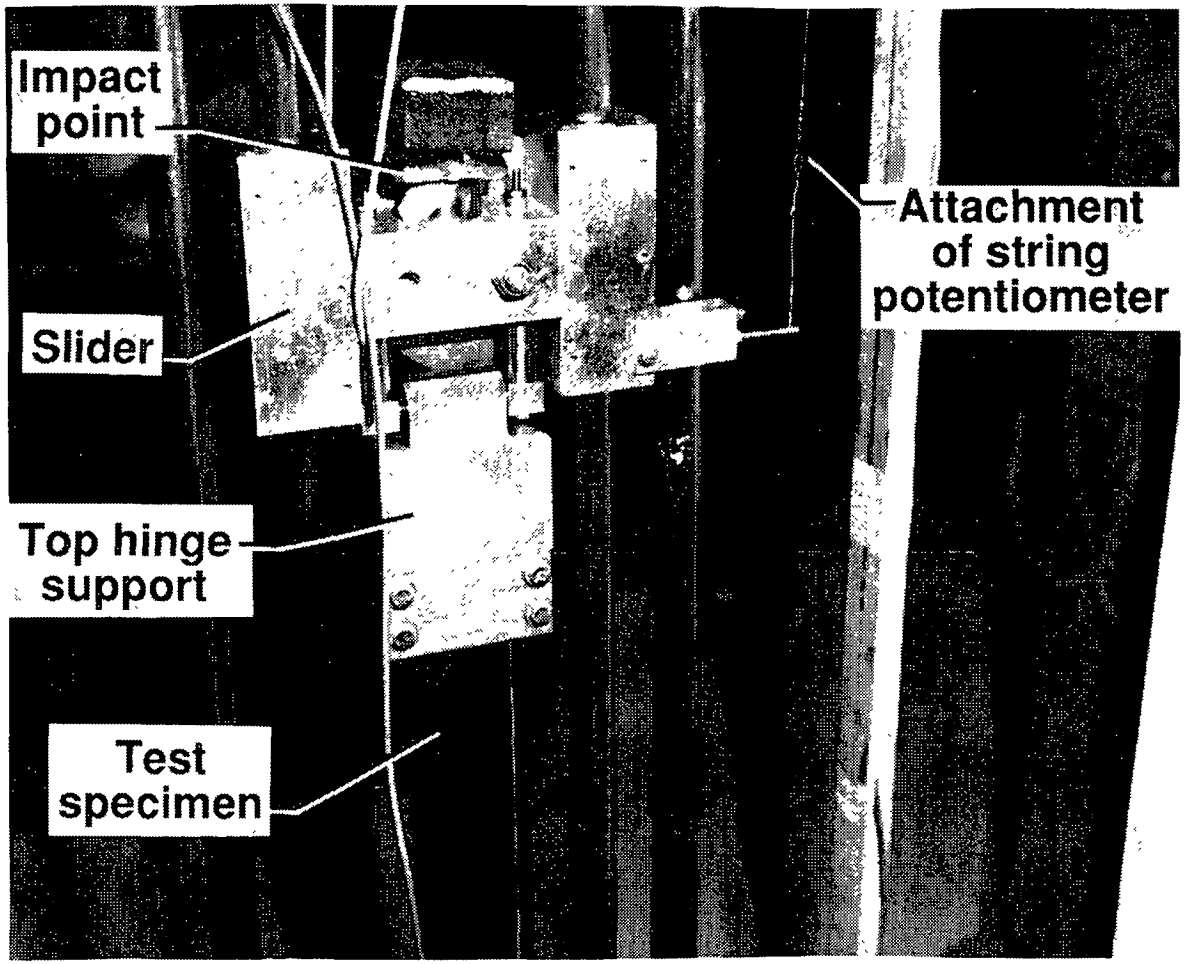

Figure 3-8. Photograph of the slider and top hinge attachment.

was supported by four vertical force transducers mounted to the lower channel section. A picture of the lower hinge connection and load platform is depicted in Figure 3-9.

The drop tower has evolved into its current configuration after being used by two previous researchers, Derian [37] and Sensmeier [38], to investigate the dynamic response and energy absorption capabilities of composite beams. Several modifications have been made to the tower since its original construction to improve its performance and to correct minor problems. The various upgrades and changes to the tower are reported in References [37,38].

3.2.3 Instrumentation

Five channels of dynamic data were recorded for each test. Tensile and compressive surface strains were recorded from back-to-back longitudinal strain gages located at the midpoint of each beam, as shown in Figure 3-3. End displacement of the beam was measured using a string potentiometer displacement transducer attached to the slider, as depicted in Figure 3-8. The string pot was extended as the beam deformed under the impact of the dropped mass. According to manufacturer's specifications, the string pot had an operating range up to 300 inches/second which was greater than any of the impact velocity test conditions. An accelerometer was attached to the mass car to measure vertical acceleration. Vertical load was obtained from four piezoelectric force transducers located between the load platform and the lower channel support. The four load cells, Kistler Model 9212, are compact, sensitive, fast-response transducers for measuring dynamic and short-term static forces. Each load cell was rated for a maximum load of 5000 pounds. A load cell was placed at each corner of a four inch square underneath the load platform. The output from each cell was summed electronically to obtain the total vertical force reacted through the load platform.

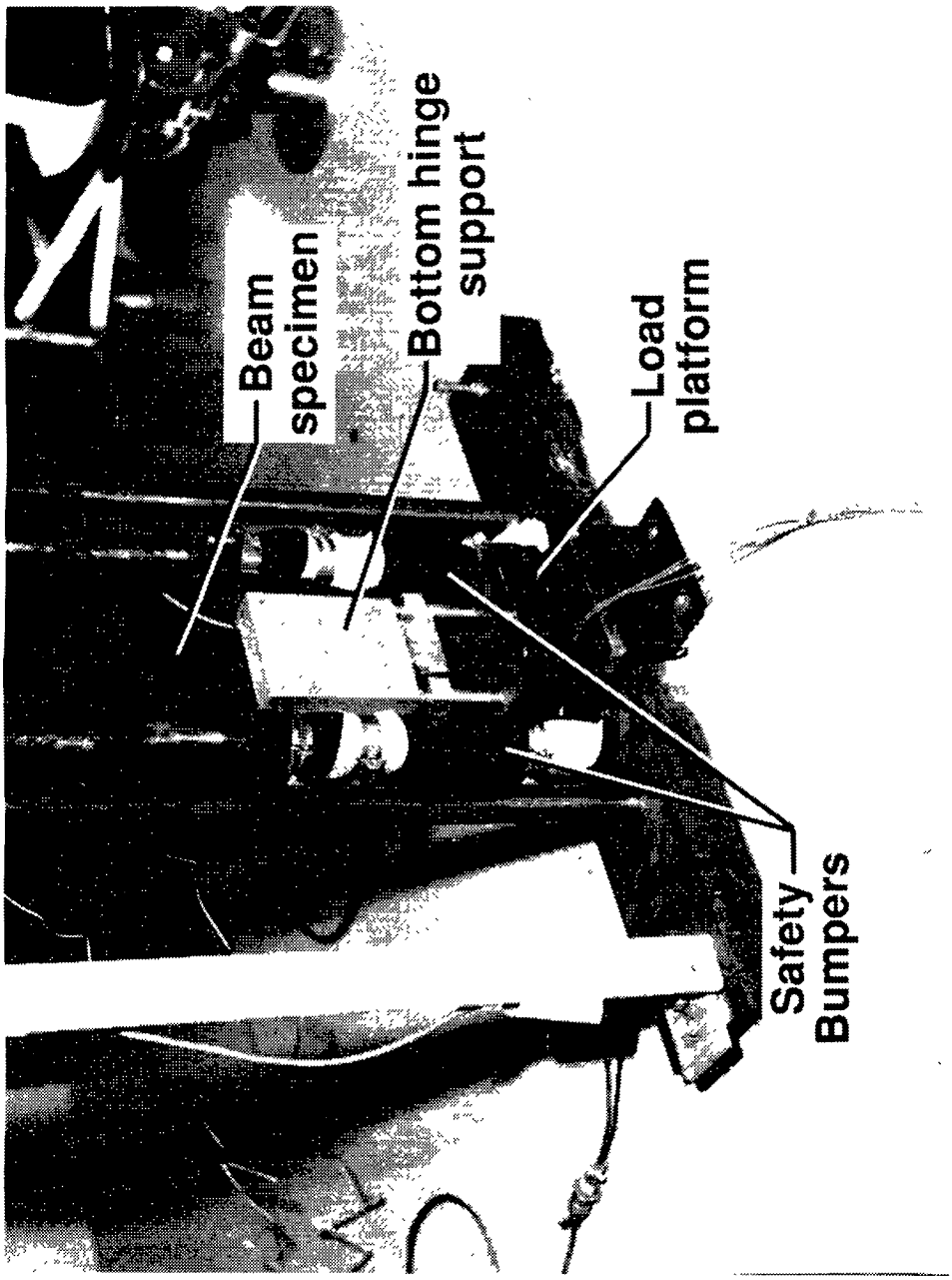

Figure 3-9. Photograph of the lower hinge attachment and load platform.

3.2.4 Data Acquisition

All data were recorded using the same personal computer based data acquisition system as described in Section 3.1.4. LOTUS Measure software was used to obtain calibration and zero readings prior to a test. The STREAM-16 dynamic data acquisition software package was used to collect the impact data. The analog signals were amplified and filtered prior to sampling at a rate of 2000 Hz. Resolution of the analog-to-digital system was 12 bits. The digital data were converted to engineering units using the previously determined calibrations and zero readings.

3.2.5 Procedure

The test conditions for each of the four laminate types were determined, in part, by the results obtained from the static tests as reported in References [47,48]. The static energy-to-failure values were calculated from load versus end displacement plots for the full scale unidirectional, angle ply, cross ply, and quasi-isotropic beams. These values were then used as a guide for determining the test conditions required to ensure failure of the beams in the impact tests. Tables 3-3 through 3-6 present the loading parameters for the four laminate types tested. In each case, the drop height was held constant for all of the model beams within a laminate family. For the angle ply, cross ply, and quasi-isotropic laminates the impact energy was scaled by the scale factor, λ^3, as indicated in Eq. 2.5. This value was divided by the drop height to determine the amount of weight to be added to the mass car for each scale model test. For the unidirectional laminates the impact force was scaled directly by the factor, λ^2. In all cases, more weight was added to the mass car than was actually necessary to produce beam failure.

In addition to scaling the impact mass, it was necessary to scale the weight of the slider which supported the top hinge attachment. This piece of hardware weighed 5.55 lbs and added a small preload

TABLE 3-3. Impact test conditions for unidirectional scale model beams.

UNIDIRECTIONAL

Scale Factor	full	5/6	3/4	2/3	1/2
Drop Height (in)	60	60	60	60	60
Impact Energy (in-lbs)	8825.6	6120	4962	3924	2208
Impact Weight (lbs)	147.1	102.1	82.7	65.4	36.8
Impact Velocity (in/sec)	215.3	215.3	215.3	215.3	215.3

TABLE 3-4. Impact test conditions for angle ply scale model beams.

ANGLE PLY

Scale Factor	full	5/6	3/4	2/3	1/2
Drop Height (in)	36	36	36	36	36
Impact Energy (in-lbs)	3355.2	1941.7	1415.5	994.1	419.4
Impact Weight (lbs)	93.2	53.9	39.3	27.6	11.65
Impact Velocity (in/sec)	166.8	166.8	166.8	166.8	166.8

TABLE 3-5. Impact test conditions for cross ply scale model beams.

	CROSS PLY				
Scale Factor	full	5/6	3/4	2/3	1/2
Drop Height (in)	48	48	48	48	48
Impact Energy (in-lbs)	4473.6	2588.9	1887.3	1325.5	559.2
Impact Weight (lbs)	93.2	53.9	39.3	27.6	11.65
Impact Velocity (in/sec)	192.6	192.6	192.6	192.6	192.6

TABLE 3-6. Impact test conditions for quasi-isotropic scale model beams.

QUASI-ISOTROPIC

Scale Factor	full	5/6	3/4	2/3	1/2
Drop Height (in)	48	48	--	48	48
Impact Energy (in-lbs)	7046.4	4077.8	--	2087.8	880.8
Impact Weight (lbs)	146.8	84.95	--	43.5	18.35
Impact Velocity (in/sec)	192.6	192.6	--	192.6	192.6

to the beam specimen prior to impact. At impact the inertia of the slider had to be considered, as well. Consequently, to ensure scaled conditions, the slider was used alone for the 1/2 scale specimens and mass was added to the slider for 2/3 scale specimens through full scale.

The test procedure consisted of the following steps. First, the correct impact and slider masses were attached to the mass car and slider for the particular scale and type of beam to be tested. Next, the beam was mounted in the top and bottom hinge supports and calibration signals were recorded with no applied load. The impact mass was raised to the correct drop height and secured. The data acquisition system was prepared to collect data at a manual trigger from the test operator. At time equal zero, the drop mass was released from rest and the data system was enabled to record the load, strain, displacement, and accelerometer time histories. In general, two or three replicate beams of the same laminate type and scaled size were tested dynamically.

Chapter 4 - Beam Analysis

Several analysis techniques were used to predict the response of the eccentrically loaded composite beam-column under both static and dynamic loads. For the static tests, a small deflection beam solution and a large deflection, "elastica" type beam analysis were derived. The small deflection beam solution was used in conjunction with experimentally determined values of load versus transverse displacement to calculate an effective beam bending stiffness. This work is described in more detail in Chapter 5, but the development of the analysis is presented in this section. The small deflection solution also provided a first approximation, linear comparison with the nonlinear beam analysis. The large deflection beam solution predicted the end displacement, transverse midpoint displacement, and rotation at the hinged ends of the beam as functions of applied load.

In addition to the beam solutions, the nonlinear finite element structural analysis computer program DYCAST (DYnamic Crash Analysis of STructures) [40] was used to model the composite beam-column. DYCAST is a commercially available code developed by Grumman Aerospace Corporation under partial support from NASA Langley Research Center. The program incorporates material and geometric nonlinear structural response for analyzing impact problems. It has been used successfully to model the dynamic response of simple structures, such as a single circular composite frame [49], as well as large complex structures such as an entire section of a full scale transport aircraft [50]. A static DYCAST model was developed and correlated with the large deflection exact beam analysis. Once verified, the model was then used for predicting the beam response under impact loading conditions.

The beam analyses and DYCAST models mentioned previously are one-dimensional beam solutions. To investigate the importance of including widthwise effects and nonlinear material behavior, a finite element code developed by Sensmeier [38] was used to model

the composite beam-column. This code will be referred to as the MDS2DB program for the remainder of the report.

Details of the analytical development and the finite element modeling will be presented in the following sections.

4.1 Small Deflection Beam Analysis

4.1.1 Analytical Development

A small deflection beam analysis is derived in this section based on the governing equilibrium equations for the problem of elastic buckling of bars. The nomenclature used in the development is listed in Table 4-1 and some of the important geometrical variables are depicted in Figure 4-1. The derivation is based on the Euler-Bernoulli assumptions, as listed in Reference [51]. Some of the major assumptions include (1) the material is Hookean, isotropic, and homogeneous; (2) plane sections normal to the neutral surface remain plane and normal to the neutral surface after bending; (3) the effect of transverse shear is negligible; and (4) the deflections are small compared to the cross-sectional dimensions. The equilibrium equation may be developed from the stationary value of the potential energy, as outlined in Reference [51], or by setting the sum of the moments on a differential beam element equal to zero. If the energy method is used, the resulting equilibrium equation is fourth order. The equation may be reduced to second order since the moment and shear are prescribed at the ends of the beam. Two successive integrations yield the resulting equation

$$\frac{d^2w}{dx^2} + k^2w = 0 \qquad (4.1)$$

where k^2, the buckling coefficient, is equal to P/EI. The general solution of this equation is

$$w(x) = A \sin(kx) + B \cos(kx) \qquad (4.2)$$

Table 4-1. Nomenclature for the Small Deflection Beam Analysis

Variable Name	Description
x	axial coordinate measured along the length of the beam, in
w	transverse displacement, in
P	axial load, lb
E	Young's modulus, psi
I	moment of inertia, in^4
e	initial eccentricity, in
δ	horizontal projection of the distance from the pin to the free portion of the beam, in
α	rotation angle at the end of the beam due to applied load, rad
ϕ	hinge angle, rad
k	buckling coefficient = $\sqrt{P/EI}$, in
m	subscript denoting a model variable
p	subscript denoting a prototype variable

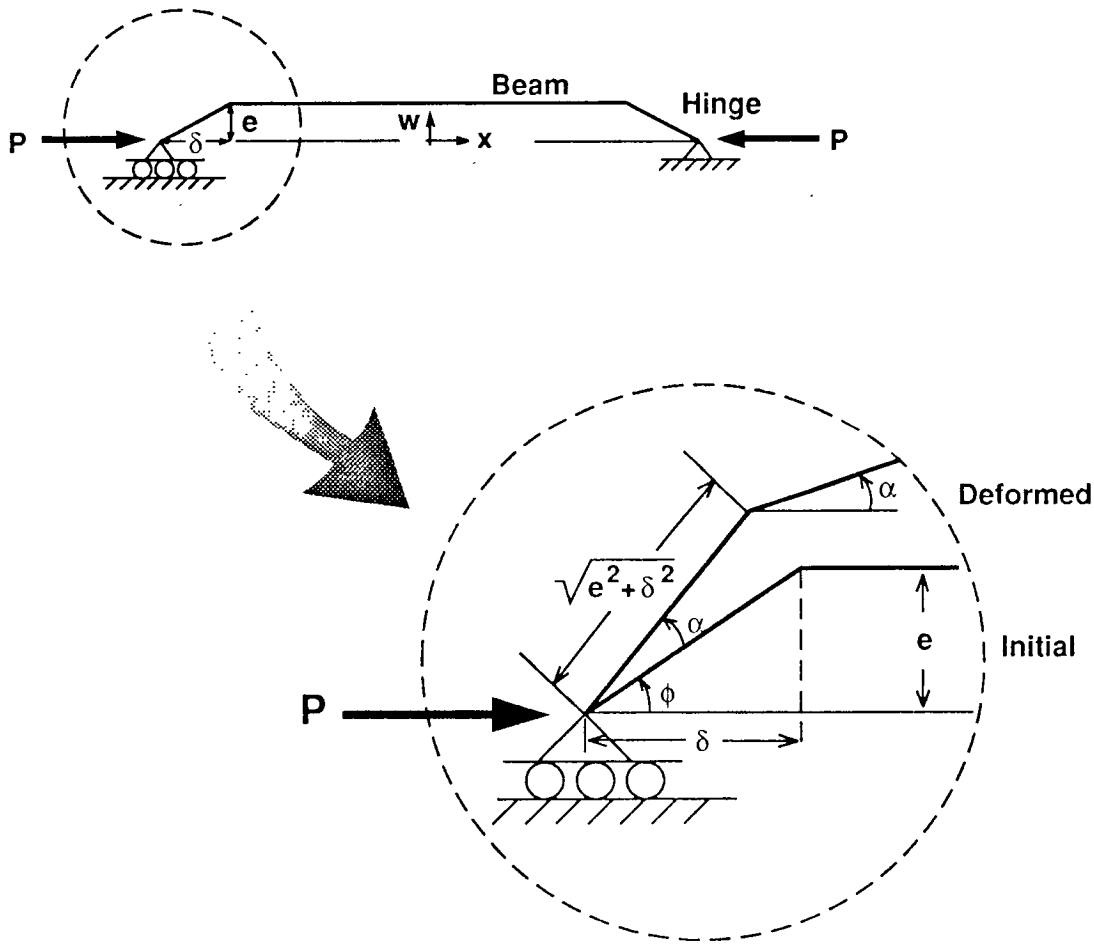

Figure 4-1. Schematic drawing of the static load configuration for small deflection analysis.

where A and B are unknown constants to be found by application of boundary conditions.

Figure 4-1 shows the eccentrically loaded beam-column, the geometry of the hinged end connection, and coordinate system. The variables 'x' and 'w' define position along the length of the beam and transverse displacement, respectively. The initial eccentricity is denoted by 'e' and the horizontal projection of the distance from the pin to the free portion of the beam is 'δ'. The variable 'α' is the rotation angle of the end of the beam relative to the horizontal caused by load applied to the beam-column. The angle ϕ is defined by the hinge geometry, i.e.,

$$\sin(\phi) = e/\sqrt{e^2+\delta^2}$$
$$\cos(\phi) = \delta/\sqrt{e^2+\delta^2} \qquad (4.3)$$

Boundary conditions for the beam-column are found by solving for the vertical displacement of the ends of the beam in the deformed position. For the end at x = -L/2 this condition is

$$w(-L/2) = \sin(\alpha + \phi)\sqrt{e^2+\delta^2} \qquad (4.4)$$

and a similar expression is written for the end of the beam at x = L/2. Expanding the sine term using the formula for the sine of the sum of two angles and using the small rotation assumption to approximate the sine and cosine of α by

$$\sin(\alpha) \approx \alpha = \frac{dw}{dx} \qquad \text{and} \quad \cos(\alpha) \approx 1 \qquad (4.5)$$

yields the boundary conditions at x = -L/2

$$w(-L/2) = e + \delta\left[\frac{dw}{dx}\right]_{x=-L/2} \qquad (4.6)$$

and at x = L/2

$$w(L/2) = e - \delta \left[\frac{dw}{dx}\right]_{x=L/2} \tag{4.7}$$

Applying the boundary conditions, Eqs. 4.6 and 4.7, to the general solution, Eq. 4.2, and solving for the unknown constant coefficients gives the solution for the transverse displacement of the beam as a function of position,

$$w(x) = \frac{e\ \cos(kx)}{\cos(kL/2) - k\delta \sin(kL/2)} \tag{4.8}$$

Some checks on the small deflection, small rotation solution were made including: (1) midpoint slope of the deflection curve is zero at the center of the beam, x=0, (2) rotation at either end of the beam is the same numerical value with opposite signs, (3) for $\delta = 0$, the solution degenerates to the pure eccentrically loaded beam-column problem which has been solved in Reference [51], and, (4) for zero applied load, k=0, the deflection curve is w(x) = e.

4.1.2 Scaling Considerations

The small deflection analysis presented in the previous section can be used to illustrate the procedure for deriving the scaling parameters from the governing differential equation and boundary conditions for a simple problem. This procedure is discussed in detail in Reference [12] and the method will be highlighted here. The first step requires that the physical system be described adequately by a set of equations and boundary conditions. In general this step necessitates some insight into the physics of the problem, more than simply a knowledge of the important parameters involved. In writing the governing equation certain assumptions and simplifications are incorporated which generally limit the scope of

the problem. For the eccentrically loaded beam-column, assuming small rotations and deflections, the governing equation is Eq. 4.1, as derived in the previous section, and the boundary conditions are Eqs. 4.6 and 4.7.

The second step is to advance a hypothesis for obtaining a model law based on the variables in the differential equation. This is done by assuming relationships between the scale factors for each of the variables. Recall from Chapter 2 that a scale factor λ is defined as the ratio of a physical quantity in the model divided by the same property in the prototype. For example, $\lambda_x = x_m/x_p$. The hypothesis proposed for the beam-column problem is

$$\begin{aligned} \lambda_x &= \lambda_L \\ \lambda_w &= \lambda_L \\ \lambda_c &= \lambda_L \\ \lambda_\delta &= \lambda_L \\ \lambda_k &= 1/\lambda_L \end{aligned} \tag{4.9}$$

where λ_L is the length scale factor. This hypothesis forms a model law for the problem; however, it is not unique. In general, other relationships among the scale factors could have been chosen which would also give a consistent and valid model law. It is reasonable to choose the geometries associated with the problem to scale in the same proportion as the length scale factor, especially when the experiment has been designed in this manner. However, the choice of scaling the buckling coefficient as $1/\lambda_L$ may not seem obvious. A logical choice might have been to scale the buckling coefficient as unity, since the geometries are scaled in proportion to λ and the same material system is be used for both the model and prototype. Only after following the next two steps would this choice have been found in error.

Step three involves writing the governing equation and boundary conditions in terms of a model system and a prototype system with a goal of testing the hypothesis. This is accomplished by

direct substitution. For the model system, the governing equation becomes,

$$\frac{d^2w_m}{dx_m^2} + k_m^2 w_m = 0 \tag{4.10}$$

and the boundary conditions become,

at $x_m = -L_m/2$

$$w_m(-L_m/2) = e_m + \delta_m\left[\frac{dw_m}{dx_m}\right]_{x_m = -L_m/2} \tag{4.11}$$

at $x_m = L_m/2$

$$w_m(L_m/2) = e_m - \delta_m\left[\frac{dw_m}{dx_m}\right]_{x_m = L_m/2} \tag{4.12}$$

Likewise, for the prototype system, the governing equation becomes,

$$\frac{d^2w_p}{dx_p^2} + k_p^2 w_p = 0 \tag{4.13}$$

and the boundary conditions become,

at $x_p = -L_p/2$

$$w_p(-L_p/2) = e_p + \delta_p\left[\frac{dw_p}{dx_p}\right]_{x_p = -L_p/2} \tag{4.14}$$

at $x_p = L_p/2$

$$w_p(L_p/2) = e_p - \delta_p\left[\frac{dw_p}{dx_p}\right]_{x_p = L_p/2} \tag{4.15}$$

The final step is to verify the model law by using the hypothesis to check the invariance of the substitution given above. To simplify the notation, the length scale factor, λ_L , will be written as λ. The model law given in Eq. 4.9 becomes,

$$\begin{aligned} x_m &= \lambda x_p \\ w_m &= \lambda w_p \\ e_m &= \lambda e_p \\ \delta_m &= \lambda \delta_p \\ k_m &= k_p/\lambda \end{aligned} \tag{4.16}$$

Substituting these expressions for the model variables into Eq. 4.10 gives

$$\frac{\lambda\, d^2 w_p}{\lambda^2 dx_p^2} + \frac{k_p^2 \lambda\, w_p}{\lambda^2} = 0 \tag{4.17}$$

Cancelling values of λ from this equation yields

$$\frac{d^2 w_p}{dx_p^2} + k_p^2 w_p = 0 \tag{4.18}$$

which is identical to Eq. 4.13. If this procedure is applied to the boundary conditions, Eqs. 4.11 and 4.12 for the model system, the result will be that Eqs. 4.14 and 4.15 are recovered identically. This verifies that the model law as given in Eqs. 4.9 and 4.16 is valid. The Pi terms generated by this procedure are:

$$\pi_1 = x/L \qquad \pi_2 = w/L \qquad \pi_3 = e/L \qquad \pi_4 = \delta/L \qquad \pi_5 = kL \tag{4.19}$$

Additional information can be obtained by examining π_5 in more detail. The relationship between the model and prototype systems based on this Pi term is

$$k_m L_m = k_p L_p \tag{4.20}$$

Substituting for the buckling coefficient gives,

$$L_m \sqrt{P_m/E_m I_m} = L_p \sqrt{P_p/E_p I_p} \tag{4.21}$$

Rewriting this expression in terms of the scale factors gives,

$$\lambda_P \lambda^2 = \lambda_E \lambda_I \tag{4.22}$$

If the beam geometry is scaled by the linear factor λ , then the moment of inertia, I, will scale as λ^4. If the same material is used to construct both the model and the prototype, then Young's modulus will scale as unity. Using this information in Eq. 4.22 gives the result that

$$\lambda_P = \lambda^2 \tag{4.23}$$

or, load will scale in proportion to the length scale factor squared.

4.1.3 Derivation of an Equivalent Bending Stiffness

The small deflection beam analysis derived in section 4.1.1 was developed assuming homogeneous, isotropic, and Hookean material properties, and used the familiar beam bending stiffness, EI. The bending stiffness is an important parameter for this problem since it is used to calculate the Euler buckling load of the beam-column. The Euler load has been defined as a characteristic load and it is used to normalize both the analytical and experimental load data. This section outlines the procedure to derive an equivalent bending

stiffness for symmetric laminated composite beams in which the beam is treated as a special case of a laminated plate. The procedure is based on a technique presented in Reference [52] which provides a more complete discussion on the one-dimensional analysis of laminated composite plates.

The constitutive relations for symmetric laminated plates may be reduced to the form

$$\begin{bmatrix} M_x \\ M_y \\ M_{xy} \end{bmatrix} = \begin{bmatrix} D_{11} & D_{12} & D_{16} \\ D_{12} & D_{22} & D_{26} \\ D_{16} & D_{26} & D_{66} \end{bmatrix} \begin{bmatrix} \kappa_x \\ \kappa_y \\ \kappa_{xy} \end{bmatrix} \tag{4.24}$$

where the moments (M_i), bending stiffnesses (D_{ij}), and curvatures (κ_j) are derived from lamination theory in Reference [53]. In order to derive a beam theory the following assumption is made:

$$M_y = M_{xy} = 0 \tag{4.25}$$

This assumption is analogous to the plane stress assumption of classical elasticity. It is also assumed that the beams have a high length-to-width ratio and that the transverse displacement, w, is a function of the axial coordinate, x, only. Applying these assumptions to Eq. 4.24 gives

$$M_x = D_{11}\kappa_x + D_{12}\kappa_y + D_{16}\kappa_{xy} \tag{4.26}$$

$$0 = D_{12}\kappa_x + D_{22}\kappa_y + D_{26}\kappa_{xy} \tag{4.27}$$

$$0 = D_{16}\kappa_x + D_{26}\kappa_y + D_{66}\kappa_{xy} \tag{4.28}$$

Eqs. 4.27 and 4.28 are used to solve for κ_y and κ_{xy} in terms of κ_x and the bending stiffnesses D_{ij},

$$\kappa_y = -\frac{D_{12}}{D_{22}} - \frac{D_{26}}{D_{22}}\left(\frac{a}{b}\right)\kappa_x \tag{4.29}$$

and

$$\kappa_{xy} = \left(\frac{a}{b}\right)\kappa_x \tag{4.30}$$

where $a = D_{12}D_{26} - D_{16}D_{22}$ and $b = D_{66}D_{22} - D_{26}^2$.

The expressions for κ_y and κ_{xy} derived in Eqs. 4.29 and 4.30 above are substituted into Eq. 4.26 to give the final result:

$$M_x = D_{eff}\kappa_x \tag{4.31}$$

where,

$$D_{eff} = D_{11} - D_{12}\left[\frac{D_{12}}{D_{22}} + \frac{D_{26}}{D_{22}}\left(\frac{a}{b}\right)\right] + D_{16}\left(\frac{a}{b}\right) \tag{4.32}$$

The effective bending stiffness, D_{eff}, incorporates the bending and twist coupling terms, D_{16} and D_{26}, which are important for angle ply and quasi-isotropic laminates.

4.2 Large Deflection Beam Analysis

A large deflection beam analysis was developed to predict the response of the composite beam-column subjected to eccentric axial load. The analysis is based on the "elastica" problem initially solved by Euler during 1770-1773 for the large deflections of a tip loaded cantilever beam. A detailed historical account of the problem is presented in Reference [54]. The term "elastica" refers to the shape of the elastic curve of a buckled bar when the exact differential equation is solved. The equation is derived using the exact expression for the curvature of a beam segment. The solution of the "elastica" has been applied to a number of physical problems and some examples of these are reported in References [55-58]. The text

by Frisch-Fay [59] provides a thorough treatment of the large deflections of flexible beams under a variety of loading conditions and end restraints. A brief outline of the solution procedure for the "elastica" problem is given in Timoshenko [60] along with numerical results for a slender rod fixed at one end and free at the other.

Sathyamoorthy [61] presents an excellent overview paper in which he surveys recent advances in the nonlinear analysis of beams including both exact solutions and finite element analyses. In general, the incorporation of material and geometric nonlinearities has increased to meet the demand for more realistic physical models. This is especially true for advanced fiber reinforced composite structures. The high stiffness and strength behavior of composite material systems allows structural designs which routinely perform under conditions of large deformations. For the eccentrically loaded beam-column problem, the inclusion of the geometric nonlinearity is required due to the large end rotations experienced by the beam. However, material nonlinearity and bimodularity are neglected. This assumption is based on results of Sensmeier's analysis which found that including nonlinear material effects produced little improvement in load and strain predictions.

Highlights of the development of the large deflection solution including the derivation of the governing equation and boundary conditions are presented in the following section. More complete details are presented in Appendix B. The solution was coded into a FORTRAN computer program to analyze the various laminate stacking sequences and sizes of the model beams and to perform a stress analysis for failure prediction.

4.2.1 Analytical Development

A schematic drawing of the beam-column loading configuration is depicted in Figure 4-2 and a list of the nomenclature used in the large deflection beam analysis is listed in Table 4-2. The governing differential equation is derived by writing an expression for the

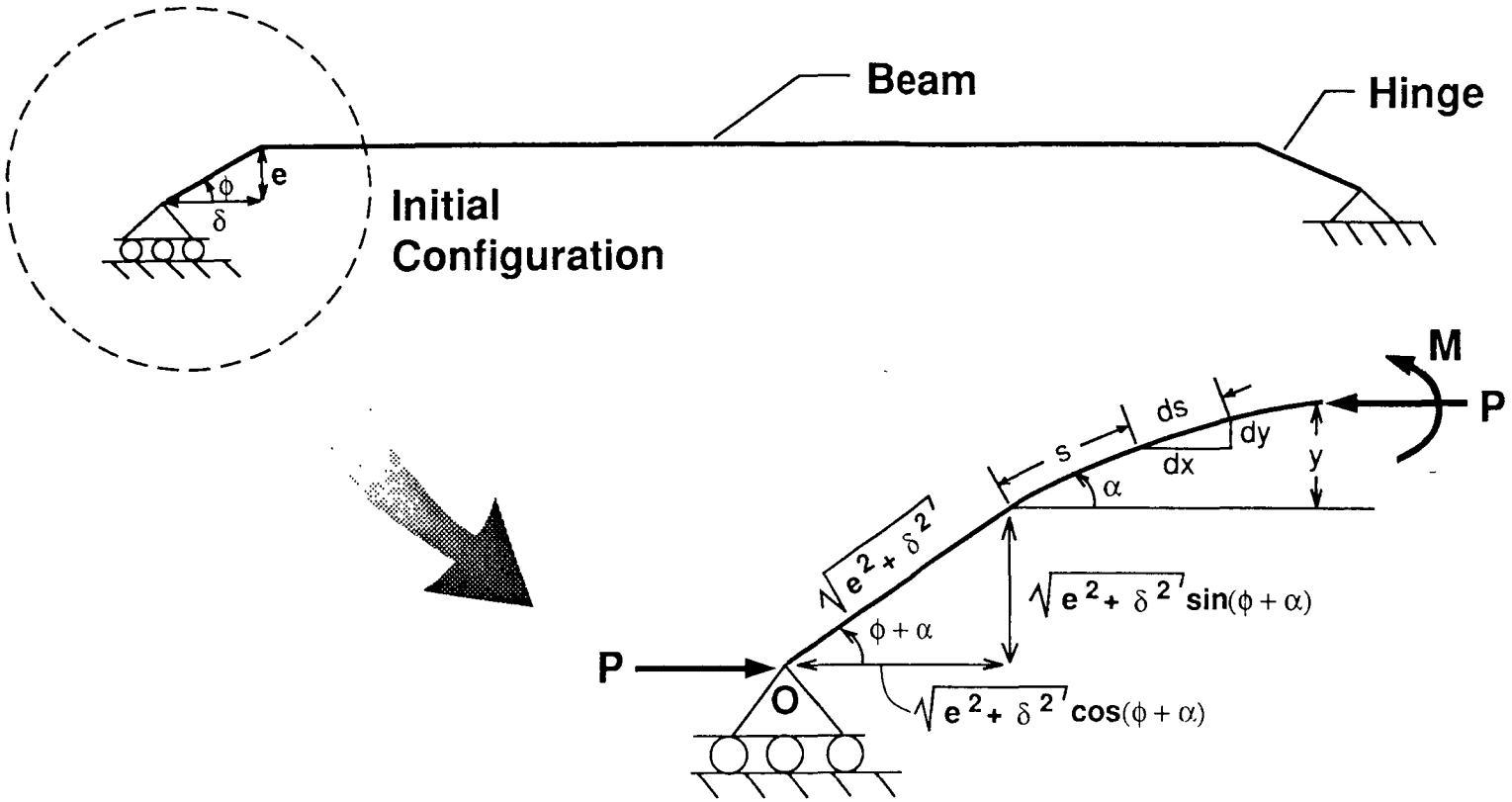

Figure 4-2. Schematic drawing of the static load configuration for large deflection analysis.

Table 4-2. Nomenclature for the Large Deflection Beam Analysis

Variable Name	Description
x	axial coordinate
y	transverse coordinate
s	distance along the beam length
θ	rotation angle at any point along the beam
P	axial load
E	Young's modulus
I	moment of inertia
e	initial eccentricity
δ	horizontal projection of the distance from the pin to the free portion of the beam
α	rotation angle at the end of the beam due to applied load
ϕ	hinge angle
M	moment
L	total beam length

equilibrium of moments about the hinge pin, shown as point O in Figure 4-2.

$$\sum M_0 = M + Py + P\sqrt{e^2 + \delta^2}\,\sin(\phi + \alpha) = 0 \tag{4.33}$$

The moment at an arbitrary point along the length of the beam is equal to the flexural rigidity times the curvature,

$$M = EI\,\frac{d\theta}{ds} \tag{4.34}$$

where $d\theta/ds$ represents the exact expression for the curvature of a beam segment. Substituting the constitutive equation, Eq. 4.34, into Eq. 4.33 gives

$$EI\,\frac{d\theta}{ds} + Py + P\sqrt{e^2 + \delta^2}\,\sin(\phi + \alpha) = 0 \tag{4.35}$$

Differentiating Eq. 4.35 with respect to s and assuming that the load and end rotation are independent of s gives

$$EI\,\frac{d^2\theta}{ds^2} + P\,\frac{dy}{ds} = 0 \tag{4.36}$$

From the geometry of a differential beam segment, it is seen that

$$\frac{dy}{ds} = \sin\theta \tag{4.37}$$

Substituting Eq. 4.37 into 4.36 and using the notation for the buckling coefficient, $k^2 = P/EI$, gives the governing differential equation,

$$\frac{d^2\theta}{ds^2} + k^2\sin\theta = 0 \tag{4.38}$$

This equation has the same form as the governing differential equation for the oscillations of a pendulum. The analogy between the large deflections of a bar loaded only at its ends and the rotation of a rigid body about a fixed point is called the Kirchhoff dynamical analogy. A discussion of this analogy is presented in Reference [58].

The order of the differential equation is reduced by integrating Eq. 4.38

$$\int \frac{d^2\theta}{ds^2}\left(\frac{d\theta}{ds}\right) ds = - \int k^2 \sin\theta \, d\theta \tag{4.39}$$

resulting in a first-order differential equation:

$$\frac{d\theta}{ds} = \pm\sqrt{2(k^2\cos\theta + C)} \tag{4.40}$$

Because the order of the differential equation has been reduced, only one boundary condition is required to solve for the constant, C. The boundary condition is found by solving for the moment at the hinge-beam connection point where s=0.

$$M(0) = -P \sin(\theta + \alpha)\sqrt{e^2 + \delta^2} \tag{4.41}$$

Using the identity for $\sin(\theta + \alpha)$ and incorporating the hinge geometry gives the resulting boundary condition,

$$M(0) = -P\, e \cos\alpha - P\, \delta \sin\alpha \tag{4.42}$$

The moment at s=0 is equal to the flexural rigidity times the curvature evaluated at that point,

$$M(0) = EI\left[\frac{d\theta}{ds}\right]_{\theta=\alpha} = -P\, e \cos\alpha - P\, \delta \sin\alpha \tag{4.43}$$

or,

$$\left[\frac{d\theta}{ds}\right]_{\theta=\alpha} = -k^2\, e\cos\alpha - k^2\,\delta\sin\alpha \tag{4.44}$$

The unknown constant in Eq. 4.40 can now be evaluated by applying the boundary condition, Eq. 4.44. The constant is found to be

$$C = 1/2\left[k^2(e\cos\alpha + \delta\sin\alpha)\right]^2 - k^2\cos\alpha \tag{4.45}$$

Substituting for C into the governing differential equation, Eq. 4.40, yields,

$$\frac{d\theta}{ds} = -k\sqrt{2\left[\cos\theta - \cos\alpha + 1/2\, k^2(e\cos\alpha + \delta\sin\alpha)^2\right]} \tag{4.46}$$

Note that since $d\theta/ds$ is always negative, as seen in Figure 4-2, the positive sign has been dropped from the equation. The solution of Eq. 4.46 is accomplished by introducing a change of variable in the following manner,

$$\sin(\theta/2) = A\sin\psi \tag{4.47}$$

where

$$A = \sqrt{\sin^2\alpha/2 + 1/4\, k^2(e\cos\alpha + \delta\sin\alpha)^2} \tag{4.48}$$

Utilizing a series of trigonometric relationships, Eq. 4.46 can be expressed in terms of the new variable in the following form;

$$ds = -\frac{d\psi}{k\sqrt{1 - A^2\sin^2\psi}} \tag{4.49}$$

This equation may be integrated to give the total length of the beam,

$$L = \int_{\theta=\alpha}^{\theta=-\alpha} ds = 2/k \int_{\psi=0}^{\psi=\psi_\alpha} \frac{d\psi}{\sqrt{1 - A^2 \sin^2 \psi}} \tag{4.50}$$

where the upper limit on the integration of Ψ is given by,

$$\psi_\alpha = \sin^{-1}\left[\frac{\sin(\alpha/2)}{A}\right] \tag{4.51}$$

The integral appearing in Eq. 4.50 is known as the complete elliptic integral of the first kind and is designated as $F(A,\Psi\alpha)$. Thus,

$$kL/2 = F(A,\psi_\alpha) \tag{4.52}$$

Values of the elliptic integral are tabulated in mathematical handbooks for monotonically increasing values of the parameters A and $\Psi\alpha$. In addition, numerical integration techniques can be used to determine the value of the elliptic integral for known values of A and $\Psi\alpha$.

The transverse midpoint deflection of the beam is found from the definition,

$$\frac{dy}{ds} = \sin\theta = 2 \sin(\theta/2) \cos(\theta/2) \tag{4.53}$$

Introducing the change of variable given by Eq. 4.47 and using Eq. 4.48, it is possible to write Eq. 4.53 as,

$$\frac{dy}{ds} = 2A \sin\psi \sqrt{1 - A^2 \sin^2 \psi} \tag{4.54}$$

The expression derived for ds in Eq. 4.49 is substituted into Eq. 4.54 to give the resulting equation,

$$dy = -2A/k \sin\psi \, d\psi \tag{4.55}$$

Integrating this equation and applying the appropriate boundary conditions gives the solution for the transverse midpoint displacement of the beam as

$$y_{mid} = \frac{2A}{k}\left[1 - \cos\psi_\alpha\right] \tag{4.56}$$

In a similar manner, the total axial shortening of the beam can be found from

$$\frac{dx}{ds} = \cos\theta = -1 + 2\cos^2(\theta/2) \tag{4.57}$$

This equation is transformed by the same variable transformation given by equations 4.47 and 4.48 and by a series of trigonometric relationships to give the integral equation

$$x_{total} = -2/k\int_0^{\psi_\alpha} \frac{d\psi}{\sqrt{1 - A^2\sin^2\psi}} + 4/k\int_0^{\psi_\alpha} \sqrt{1 - A^2\sin^2\psi}\, d\psi \tag{4.58}$$

The first integral in Eq. 4.58 is simply the complete elliptic integral of the first kind which was found previously in Eq. 4.50. The second integral which appears in Eq. 4.58 has the form of the complete elliptic integral of the second kind and is designated as $E(A,\psi_\alpha)$. Values of the complete elliptic integral of the second kind are also tabulated in mathematical handbooks for discrete values of the parameters A and ψ_α. Substituting results from Eq. 4.50 and using the notation for the elliptic integral in Eq. 4.58 gives the final result

$$x_{total} = -L + 4/k\, E(A,\psi_\alpha) \tag{4.59}$$

The transverse midpoint displacement, total axial shortening, and end rotation form the solution for the eccentrically loaded beam-

column problem. The rotation angle, α, and the total axial shortening, x_{total} , were used to predict the end displacement of the beam for comparison with the experimental results. As shown in Figure 4-3, the end displacement of the beam is defined as the axial distance traveled by the hinge pin and is denoted in the figure as Δ_{exp}. This distance was measured by displacement transducers during the experiments. The end displacement is given by the equation,

$$\Delta_{exp} = L - x_{total} + 2\left[\delta(1-\cos\ \alpha) + e\ \sin\ \alpha\right] \tag{4.60}$$

In a similar manner, the rotation of the hinges must be accounted for in comparing the small deflection and large deflection predictions for transverse midpoint displacement. When referred to the undeformed axis as shown in Figure 4-3, the transverse midpoint displacement is given by the following equation,

$$y_{exp} = y_{mid} + e(\cos\ \alpha - 1) + \delta\ \sin\ \alpha \tag{4.61}$$

4.2.2 Solution Algorithm

An examination of the solution developed in the previous section indicates that three unknowns exist. These are the rotation angle, α; the midpoint transverse displacement, y_{mid}; and, the total axial shortening, x_{total}. A solution algorithm was programmed to determine these unknowns given the beam length, beam bending stiffness, hinge geometry, and the loading conditions applied to the beam. A flowchart of the solution algorithm is presented in Figure 4-4. The program is divided into three main sections. The first section allows the user to input material properties, the angular ply orientations, and the geometry of the particular laminated beam to be studied. The program calculates an equivalent beam bending stiffness as derived in Eq. 4.32 from a laminate analysis. The Euler

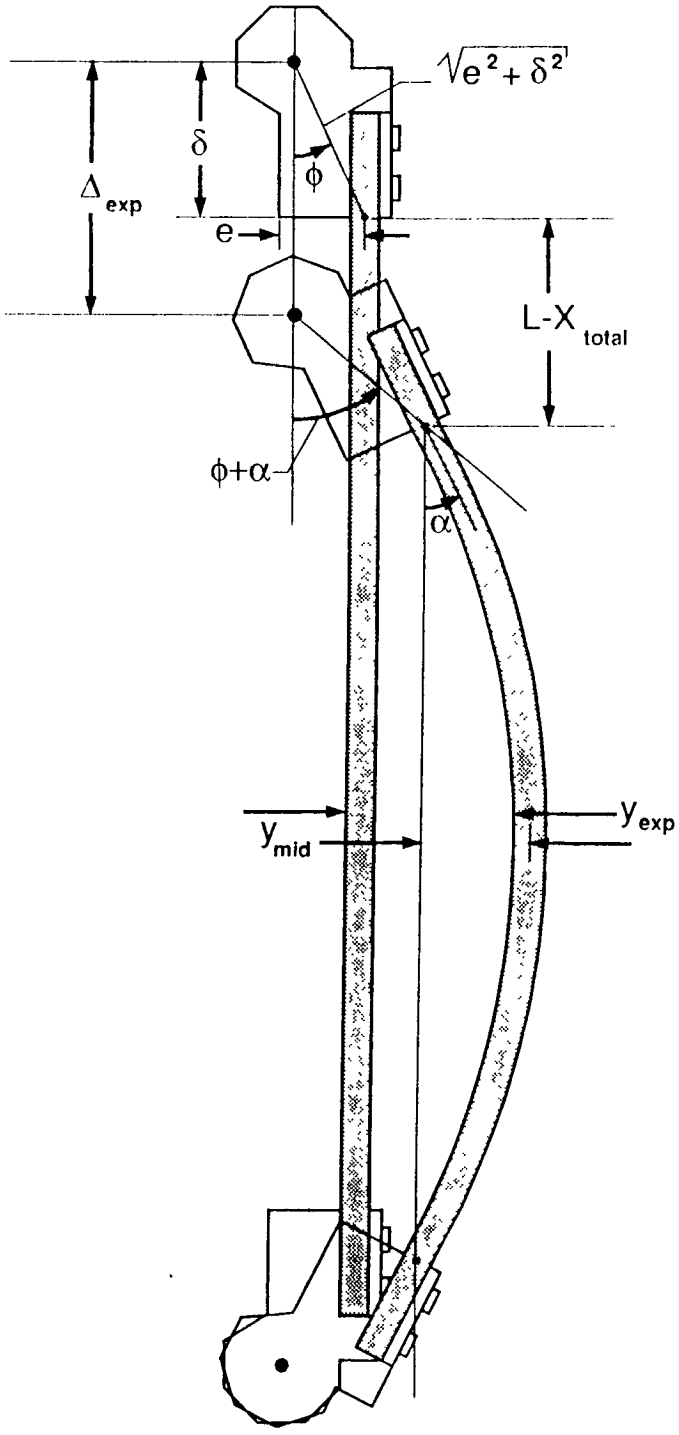

Figure 4-3. Schematic drawing of the hinge-beam configuration.

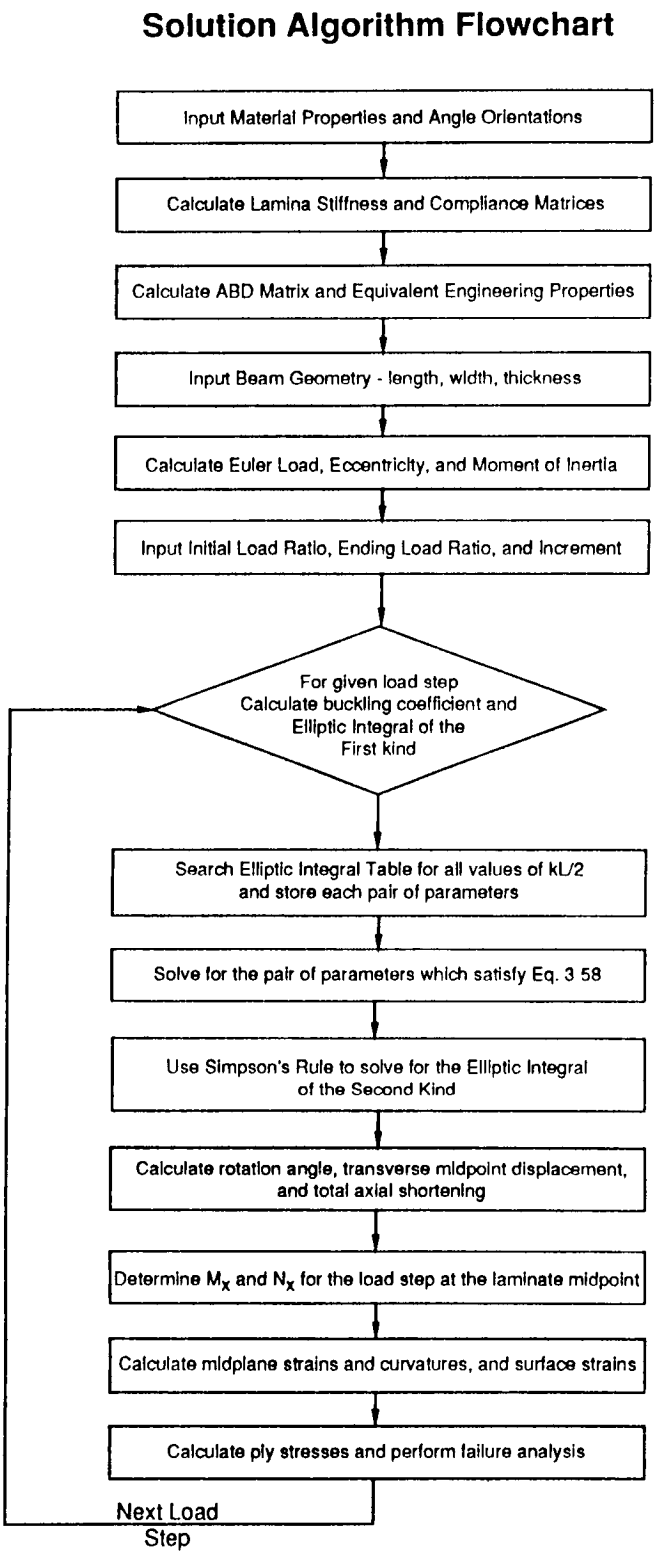

Figure 4-4. Solution algorithm flowchart.

load is determined and the initial load ratio, final load ratio, and load increment are input.

The next section of the program calculates the rotation angle, midpoint transverse displacement, and total axial shortening for the initial value of the load ratio, and for each load increment following until the final load ratio is achieved. For the particular value of the load at a given load step, the program calculates the value of the buckling coefficient, k, and the value of the elliptic integral of the first kind, as derived in Eq. 4.52. A routine is employed to search the table of values of elliptic integrals of the first kind for all parameters A and ψ_α which contain the known value of the elliptic integral for the particular load step. Interpolation between values in the table is necessary to get the correct parameters. The program next determines which of the pairs of parameters (A,ψ_α) are the correct ones for the problem by substituting each pair into Eq. 4.48. The pair which best solves this equation is chosen. Once the values of A and ψ_α are known, the midpoint transverse displacement, y_{mid}, is found from Eq. 4.56. The total axial shortening, x_{total} is found from Eq. 4.59 where the elliptic integral of the second kind, $E(A,\psi_\alpha)$, is determined by numerical integration using Simpson's Rule since the limits of integration and the parameter A are known. The rotation angle, α, is found simply by substituting the values of A and ψ_α into Eq. 4.51 and solving. Having determined α, y_{mid}, and x_{total}, the end displacement given by Eq. 4.60 and the midpoint displacement given by Eq. 4.61 are now solved for direct comparison with the experimental results.

The final portion of the program performs a stress and failure analysis based on the load and displacement results determined previously. For each load step an equivalent applied moment, M_X, and axial thrust, N_X, are calculated at the midpoint of the beam. From lamination theory, the midplane strains and curvatures are determined as well as surface strains for comparison with the strain gage experimental data. Again, using lamination theory, ply stresses

are determined and failure criteria including maximum strain, maximum stress, and Tsai-Wu are applied on a layer-by-layer basis.

The solution algorithm depends heavily on the table of values for the elliptic integral of the first kind. A separate routine was written to calculate the values in the table using Simpson's Rule of numerical integration. Initially, the table was determined for angle increments of 1 degree, resulting in a table of 90 x 90 values, which is typical of the tables printed in mathematical handbooks. However, it was found that the solution appeared to "stair-step" for low values of the load due to the crudeness of the table and the interpolation techniques. The table of elliptic integrals was recalculated for 1/2 degree increments, resulting in a table of 180 x 180 values, which smoothed the solution considerably, but greatly increased the running time of the program. Finally, the table was further refined for every 1/10 degree increments from zero to 90 degrees and the stair-step effect was virtually eliminated. Figures 4-5 and 4-6 illustrate the effect of refining the elliptic integral table on the load versus midpoint displacement and end displacement response, respectively. The stair step effect is negligible, even for the most course elliptic integral table for load ratios greater than 0.4. However, it was necessary to remove the stair-step effect for low values of load ratio since the analysis was used to derive equivalent beam bending stiffnesses empirically. More details of the bending stiffness determination are presented in Chapter 5.

4.2.3 Agreement Between the Large Deflection Beam-Column Solution Algorithm and "Elastica" Solution

In order to verify the large deflection beam-column solution derived in section 4.2.1 and programmed in section 4.2.2, a case was considered in which the hinged end conditions were simplified to solve the problem of a pinned beam-column. This was accomplished by setting the eccentricity and delta parameters of Figure 4-1 equal to zero. The large deflection solution for this problem is presented in

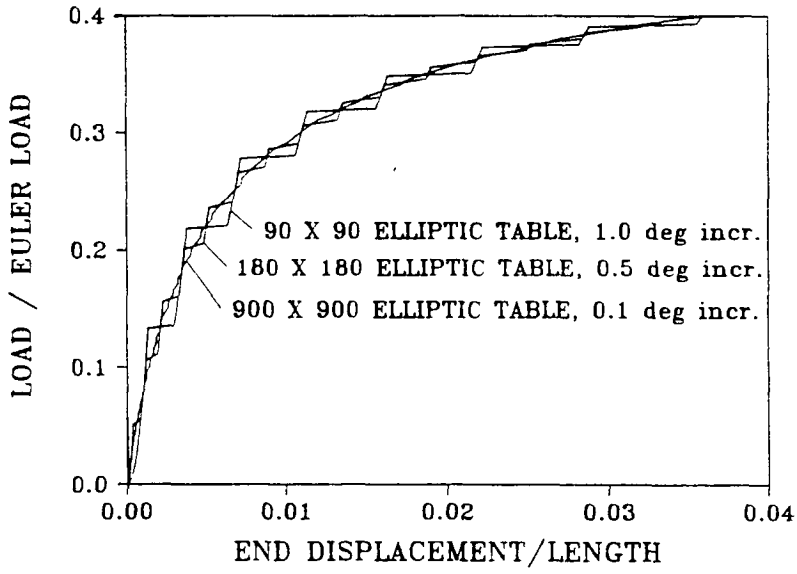

Figure 4-5. Effect of refined elliptic integral table on analytic predictions of normalized load versus end displacement response.

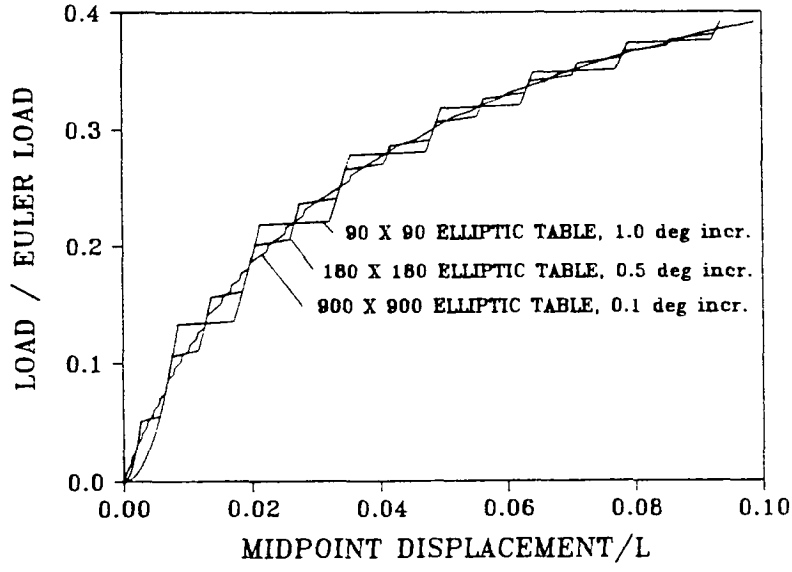

Figure 4-6. Effect of refined elliptic integral table on analytic predictions of normalized load versus midpoint displacement response.

Timoshenko [60]. Figures 4-7, 4-8, and 4-9 are, respectively, comparisons of the normalized load versus end displacement, load versus midpoint displacement, and load versus rotation angle results from the large deflection beam analysis and the data presented in Timoshenko for a pinned beam-column. The large deflection beam analysis predicts exactly the solution for the pinned beam-column problem, thus validating the solution algorithm for this simplified case.

4.2.4 Agreement with Small Deflection Beam Solution

Figure 4-10 is a plot of the normalized midpoint transverse displacement versus load ratio for the small deflection beam solution and the large deflection "elastica" solution. The small and large deflection analyses agree exactly for load ratios (defined as load divided by Euler load) less than 0.4. However, for higher load ratios, the small deflection solution increases rapidly and becomes unbounded at a load ratio of approximately 0.5. The large deflection solution remains bounded and continues to predict the midpoint displacement response. For the eccentrically loaded beam-column problem under consideration, the maximum normalized midpoint displacement is approximately 0.5 which represents the point at which the ends of the beam touch. The value is actually slightly greater than 0.5, since the geometry of the hinges during rotation adds to the midpoint displacement as measured from the initial unloaded configuration.

4.3 Finite Element Analysis

4.3.1 DYCAST Static and Dynamic Model

In addition to the small and large deflection beam analyses presented in the previous sections, the nonlinear finite element structural analysis computer program DYCAST was used to model the composite beam-column. The DYCAST code was used to model both

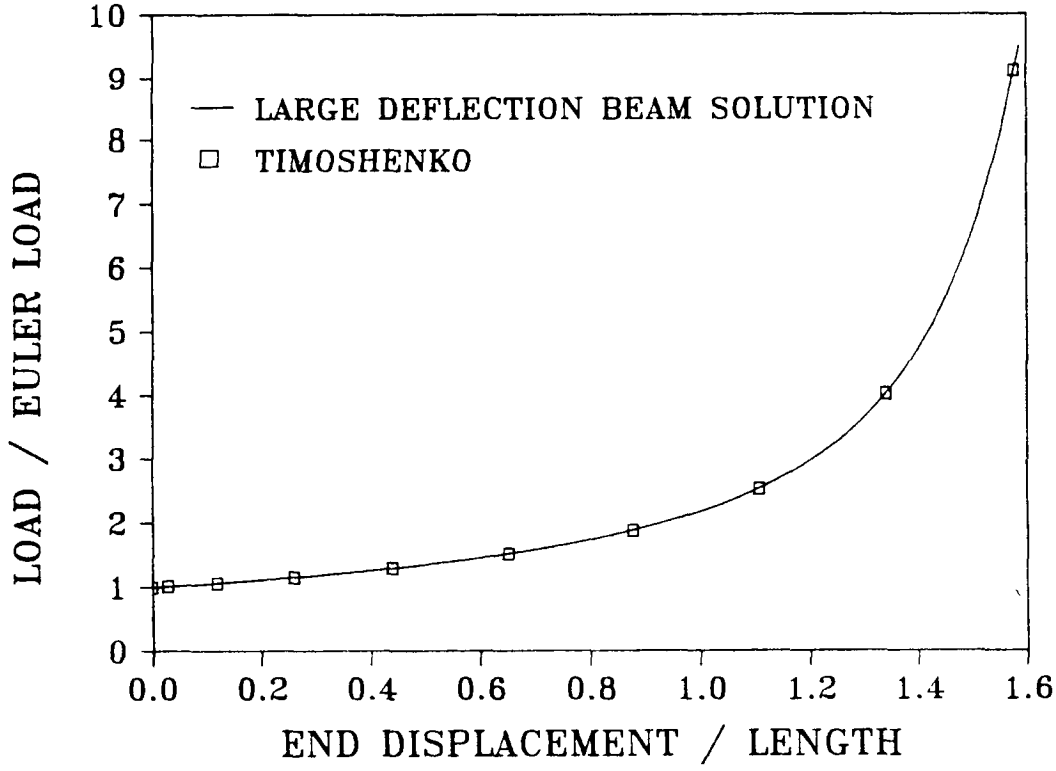

Figure 4-7. Comparison of Timoshenko solution and large deflection beam analysis of normalized load versus end displacement.

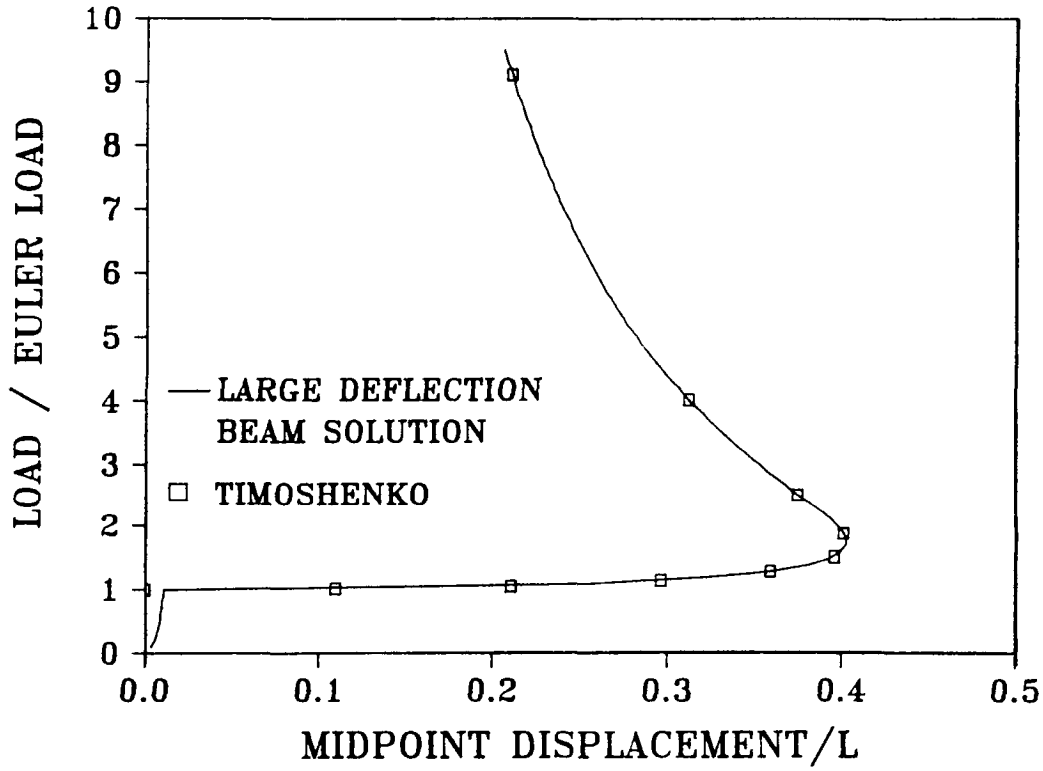

Figure 4-8. Comparison of Timoshenko solution and large deflection beam analysis of normalized load versus midpoint displacement.

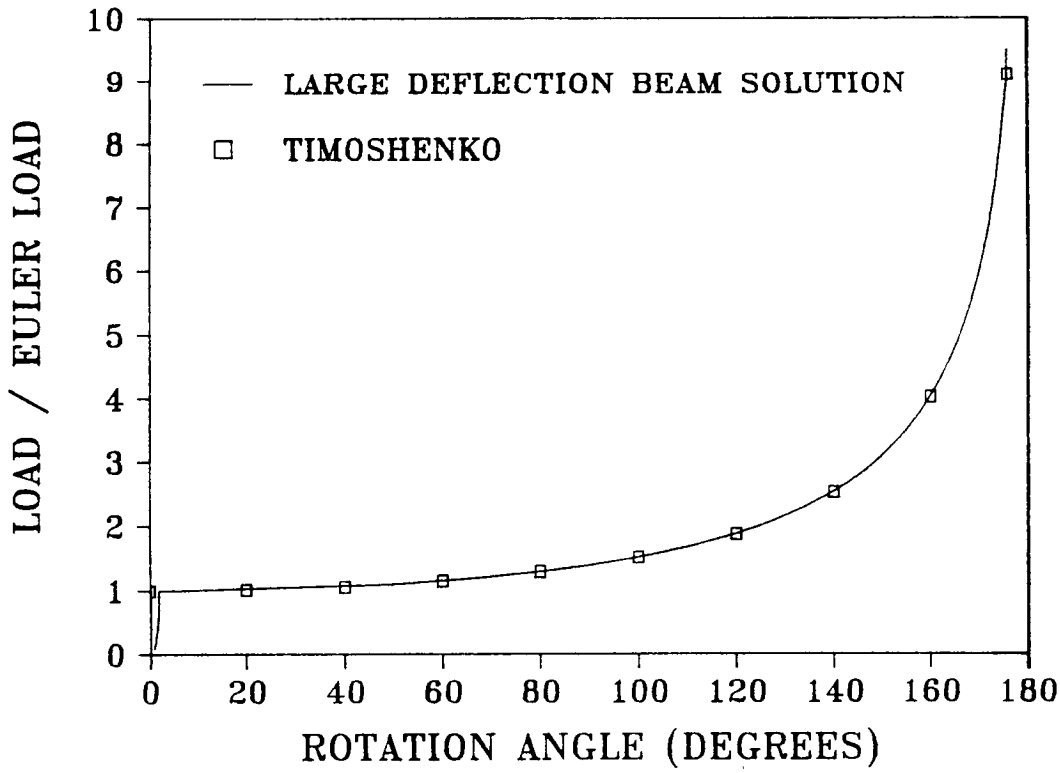

Figure 4-9. Comparison of Timoshenko solution and large deflection beam analysis of normalized load versus rotation angle.

the static and dynamic beam response. The composite laminate was discretized into 60 beam elements which were constrained to permit only planar deformations, i.e., no twisting or warping of the cross section was allowed. The hinges at the top and bottom of the beam were modeled by two rigid beam elements each. The model assumed pinned conditions at the attachment point between the hinge and the load machine, and clamped conditions between the hinge and beam. DYCAST allows only isotropic material properties for beam elements, therefore equivalent isotropic properties were determined for each of the composite laminates tested using lamination theory as outlined in Section 4.1.3. Thus, the bending stiffness used in the DYCAST model was the same as that used in the small and large deflection beam analyses. The complete model including the hinge supports had 192 degrees of freedom.

For the static loading condition, the applied load was increased incrementally at the top of the beam using a static full Newton iterative technique in which the stiffness matrix was updated in each iteration. The full Newton procedure was required since the modified Newton method which updated the stiffness matrix for each load step failed to converge in the nonlinear region of the response curve. Figure 4-11 is a plot comparing the static normalized load versus end displacement response from a DYCAST and large deflection exact beam analysis. The DYCAST beam model and the large deflection beam analysis agree for all values of load ratio thus validating the finite element model.

For the dynamic loading condition, the impact was modeled by applying an initial velocity to a lumped mass representing the mass car and slider at the top of the beam. The value of the initial velocity was calculated from conservation of linear momentum principles. To validate that the velocity value used for the model was correct, the end displacement experimental data were differentiated with time. The velocity after impact obtained in this manner was subsequently used as the initial velocity to improve the model and to give better correlation with experimental strain data. The implicit Newmark-

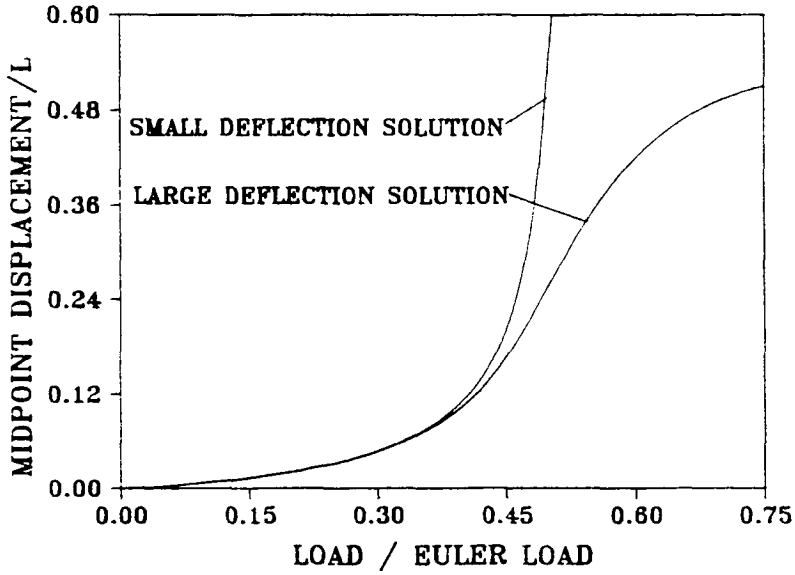

Figure 4-10. Comparison of normalized midpoint displacement versus load for the small and large deflection beam solutions.

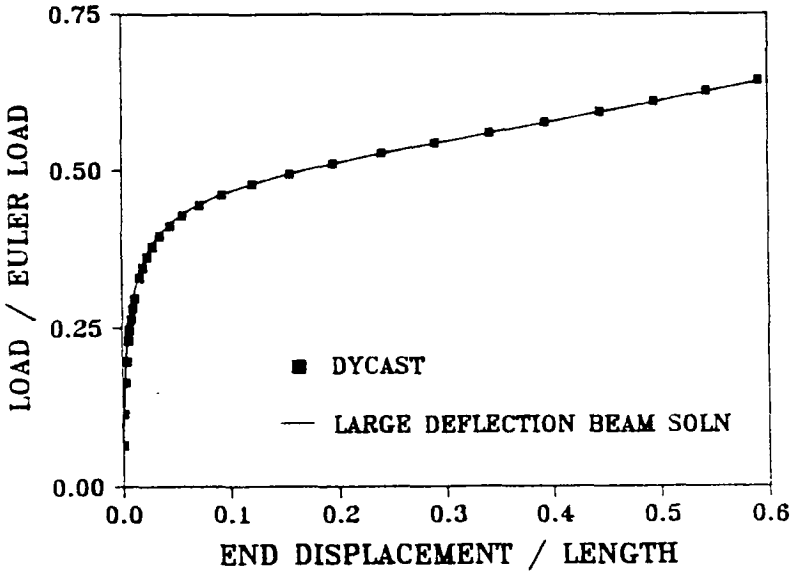

Figure 4-11. Comparison of normalized load versus end displacement between DYCAST and large deflection beam solution.

Beta time integration method was used and the stiffness matrix was updated for each time step.

4.3.2 Geometric and Material Nonlinear Beam Analysis (incorporating width-wise effects)

Sensmeier [38] developed a geometric and materially nonlinear finite element analysis to model the large deflection flexural response of eccentrically loaded beam-columns. The composite beam configuration he tested and for which he developed the analysis represents the two-thirds scale model beam of this investigation. His analysis will be referred to as the MDS2DB program and it was developed using an incremental, noniterative finite element based on the Kantrovich method. A co-rotational solution technique was employed. Width-wise effects were included by assuming specific forms of the displacements across the width of the beam. In addition, the model included nonlinear material behavior as determined from material characterization tests on the AS4/3502 graphite-epoxy system. The eccentrically loaded composite beam-columns were modeled using the MDS2DB program to investigate the importance of material nonlinearity and width-wise effects for the laminates included in this investigation.

Sensmeier found that inclusion of nonlinear material behavior was important in predicting the load-deflection response of unidirectional laminates, while width-wise effects were determined to be more important for laminates with off-axis plies. The finite element model also successfully predicted the difference in strain magnitudes on the tensile and compressive sides of the beams. He found that the strain difference was due to a combination of material nonlinearity and width-wise effects. The width-wise effects were highly dependent on the amount of bend-twist coupling present in the composite laminate under consideration.

Figures 4-12 through 4-15 are plots of the normalized load-displacement responses for 2/3 scale unidirectional, angle ply, cross

ply, and quasi-isotropic beams comparing the MDS2DB and large deflection beam solutions, respectively. Since the large deflection beam analysis does not permit nonlinear material properties, the MDS2BD analysis for each laminate was performed using the linear material properties. Thus, the plots illustrate the the importance of including width-wise effects for each of the four laminate types under consideration. Excellent agreement is obtained for the unidirectional and cross ply laminates, as shown in Figures 4-12 and 4-14, which is expected since these laminates have no D_{16} or D_{26} bend- twist coupling stiffnesses. However, the angle ply laminate, as shown in Figure 4-13, exhibits a large bend-twist coupling term and the inclusion of width-wise effects gives a significantly stiffer load-deflection response than the large deflection beam analysis. The inclusion of width-wise effects leads to a slightly stiffer response for the quasi-isotropic laminate, as seen in Figure 4-15, since the bend-twist coupling stiffness is not large. The tendency of the MDS2DB solution to stiffen and deviate from the large deflection beam analysis, as evident in Figures 4-12 and 4-13, for end displacement/length values greater than 0.80 is due to a numerical instability and does not represent a physical phenomenon.

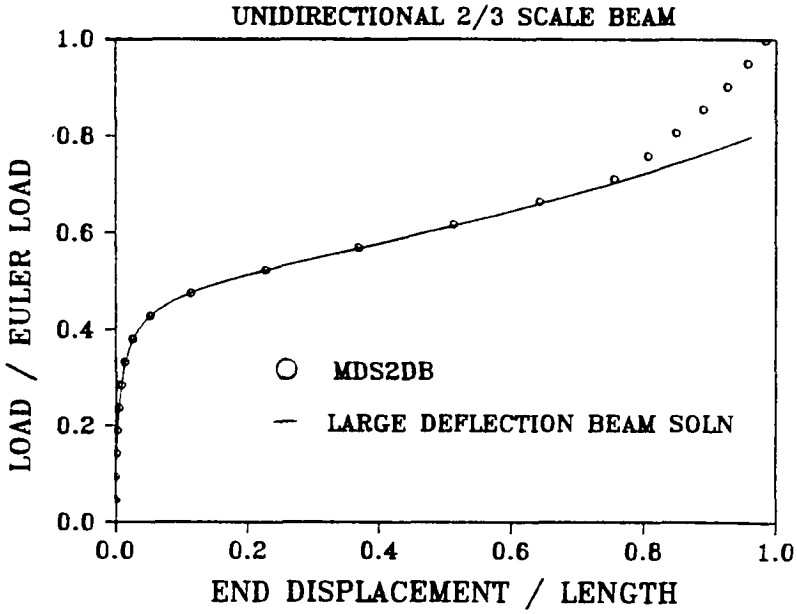

Figure 4-12. Comparison of normalized load versus end displacement predictions for a unidirectional 2/3 scale beam using MDS2DB analysis and the large deflection beam solution.

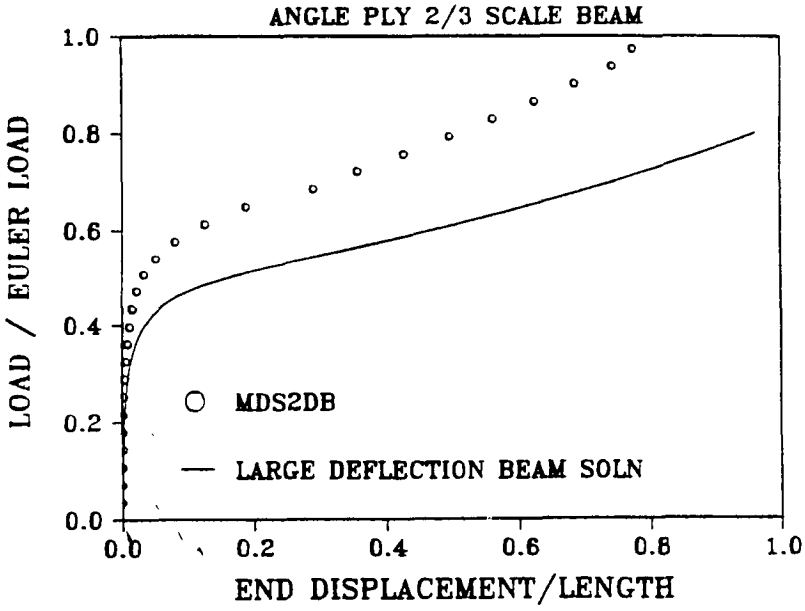

Figure 4-13. Comparison of normalized load versus end displacement predictions for an angle ply 2/3 scale beam using MDS2DB analysis and the large deflection beam solution.

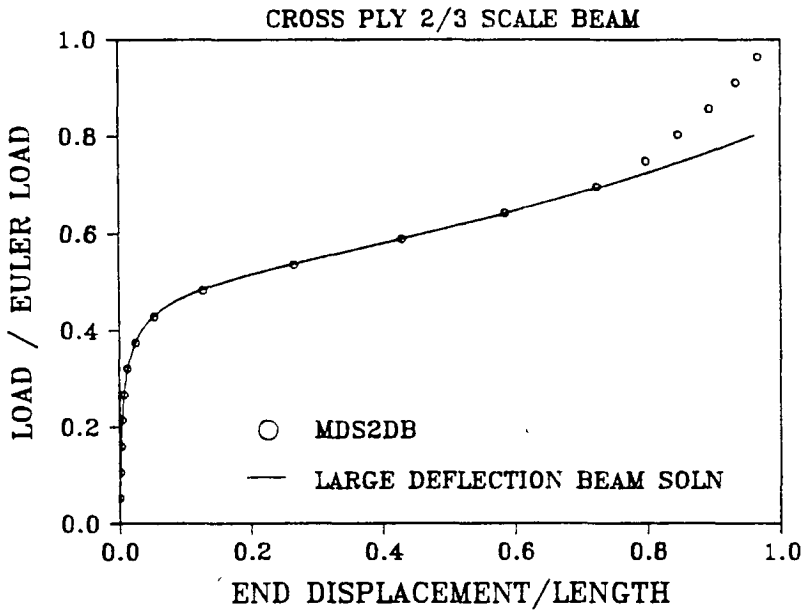

Figure 4-14. Comparison of normalized load versus end displacement predictions for a cross ply 2/3 scale beam using MDS2DB analysis and the large deflection beam solution.

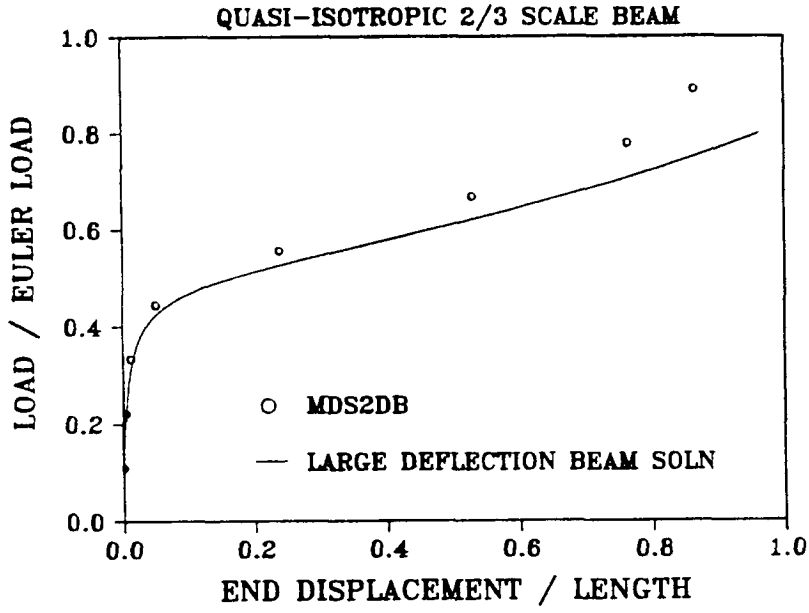

Figure 4-15. Comparison of normalized load versus end displacement predictions for a quasi-isotropic 2/3 scale beam using MDS2DB analysis and the large deflection beam solution.

Chapter 5. Investigation of Beam Bending Stiffness

5.1 Motivation

The Euler load has been chosen as a characteristic load of the eccentrically loaded beam-column problem and is used to normalize the load data for both the experiment and the various analytical techniques. The Euler load is given by:

$$P_{eu} = \pi^2 D_{eff} \frac{b}{L^2} \tag{5.1}$$

where b is the beam width and L is the beam length. The effective bending stiffness, D_{eff}, may be derived from Eq. 4.32 for any laminate if the angular ply orientations, laminate thickness, and the material moduli are known. Once the bending stiffness is calculated, the Euler load is found from Eq. 5.1.

Figure 5-1 shows the experimental normalized load versus end displacement results for a set of scaled unidirectional beams. For each beam specimen the Euler load was determined from Eq. 5.1 using the effective bending stiffness as calculated from lamination theory. The material moduli used to calculate the bending stiffnesses were obtained from material characterization tests and are given in Table 3-1. The plot of Figure 5-1 indicates that the response of the model beams scales for low values of the load ratio. However, as the deflections become large, the beam load-deflection behavior deviates from a scaled response. The slopes of the response curves are similar, yet some beams appear stiffer than others. No recognizable pattern is observed in the response curves, i.e., the smaller beams are not necessarily stiffer than the larger ones or vise versa.

Figure 5-2 is a plot of the 1/6 and full scale unidirectional beam normalized load-displacement response plotted with the large deflection beam analysis and the DYCAST model results. Good agreement is obtained between the experimental data and the two analyses for low load values. But, the analyses overpredict the beam

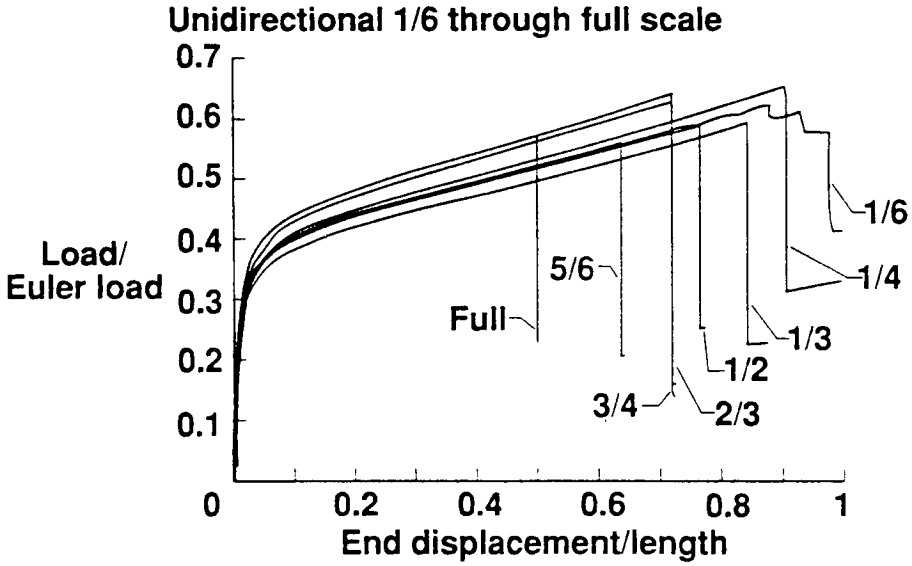

Figure 5-1. Experimental load versus end displacement results for unidirectional 1/6 through full scale. (Euler load is calculated using lamination theory predictions of beam bending stiffness.)

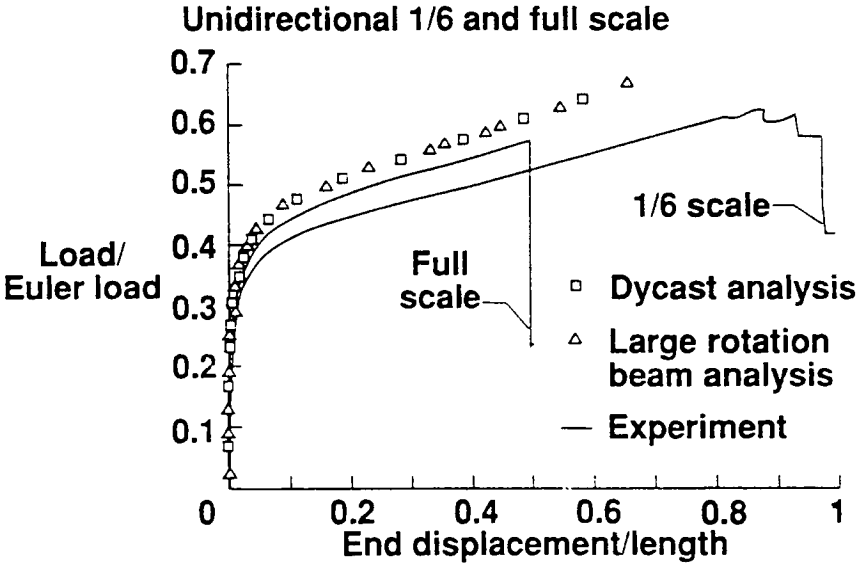

Figure 5-2. Unidirectional 1/6 and full scale beam normalized load versus end displacement data with DYCAST and large deflection beam analyses. (Euler load is calculated using lamination theory prediction of beam bending stiffness.)

response by as much as twenty per cent for higher load ratios, even though the analyses predict the character of the response curve well.

The trends indicated in Figures 5-1 and 5-2 for the unidirectional beams are typical of the angle ply, cross ply, and quasi-isotropic beams as well. Similar plots for these laminates are provided in Reference [62]. The Euler load is the only nonempirical quantity used to construct these plots. If the Euler load as determined from lamination theory is incorrect, it could explain the deviation from scaled response seen in Figure 5-1 and the poor agreement between the analyses and the experimental data seen in Figure 5-2. Since the effective bending stiffness, D_{eff}, is the only component of the Euler load which could be in error, an experimental program was initiated to verify that the effective bending stiffness based on lamination theory is, in fact, the bending stiffness exhibited by the scale model beams in the lab. A brief description of the experimental program and results of that investigation are presented in this chapter.

5.2 Experimental Program to Determine Effective Beam Bending Stiffness

Tests were performed on a set of 1/6, 1/4, and 1/3 scale model beams of unidirectional, angle ply, cross ply, and quasi-isotropic laminate stacking sequences to determine the effective beam bending stiffness. The beams were supported in scaled hinges, as described in Chapter 3, which offset the axial load and produced bending deformations. The upper hinge was fixed to a rigid support. A load cell was mounted under the lower hinge support which was attached to a high-precision stage for accurate position adjustments. From an initially straight configuration, a small end displacement was applied to the beam specimen. Measurements of vertical load and transverse midpoint displacement were recorded. The end displacement was increased and new readings were made for a total of approximately 25 measurements. The maximum load never

exceeded 0.2 times the Euler load of the beam as calculated from lamination theory. Thus, all measurements were taken in the load-deflection regime where small deflection beam assumptions were valid.

The equation for the transverse displacement of a beam assuming small displacements has been derived in Section 4.1.1 and is written as Eq. 4.8. In this equation, the out-of-plane displacement at any location along the beam may be found for a specific hinge geometry, load, beam length, and beam bending stiffness (EI). This equation was rearranged such that the bending stiffness could be found for a given load, transverse midpoint displacement, beam length, and hinge geometry. An equivalent bending stiffness was determined for each set of data points (load and transverse midpoint displacement) from a beam test and the values were averaged to give the experimentally determined bending stiffness for that beam.

5.3 Comparison of Experimentally Determined Beam Bending Stiffness with Lamination Theory Prediction

The experimentally determined bending stiffnesses of each of the beams tested are listed in Table 5-1 along with their dimensions, laminate stacking sequences, and the value of the bending stiffness determined from lamination theory. The percentage differences between lamination theory and experiment are listed in the last column of Table 5-1. These results show that the bending stiffness derived from lamination theory can differ from the experimentally determined value by as much as 25 per cent. Predictions of bending stiffness were not consistently better or worse for a particular laminate family (unidirectional, angle ply, cross ply, and quasi-isotropic) or for a particular scale factor (1/6, 1/4, and 1/3). In general, lamination theory does not give reliable predictions of beam bending stiffness when compared to the measured values. It is reasonable to conclude that discrepancies between the lamination theory predictions for bending stiffness and the actual values are

Table 5-1. Experimentally Determined Beam Bending Stiffness

Scale Factor	Lay-up	Beam Length in	Beam Width in	Beam Thickness in	Bending Stiffness Lamination Theory lb-in^2	Bending Stiffness Experiment lb-in^2	Percent Difference
1/6	[0]	5	0.5	.049	97.89	95.28	2.7
1/6	[45/-45]	5	0.5	.044	9.28	7.14	23.1
1/6	[0/90]	5	0.5	.048	81.15	64.28	20.8
1/6	[-45/0/45/90]	5	0.5	.045	30.03	34.20	-13.9
1/4	[0]	7.5	0.75	.071	444.03	353.23	20.5
1/4	[45/-45]	7.5	0.75	.0715	59.71	61.46	-2.9
1/4	[0/90]	7.5	0.75	.066	316.42	289.97	8.4
1/3	[0]	10	1.0	.087	1089.30	911.26	16.3
1/3	[45/-45]	10	1.0	.086	138.53	173.13	-25.0
1/3	[0/90]	10	1.0	.086	933.39	823.99	11.7
1/3	[-45/0/45/90]	10	1.0	.086	419.15	425.60	-1.5

responsible for the anomalies seen in the load-deflection response curves of Figures 5-1 and 5-2.

The disparity between lamination theory prediction for bending stiffness and the experimentally determined values is not unusual. Whitney [63] has published data comparing the elastic modulus determined from 4-point bending tests with theoretical values for graphite-epoxy quasi-isotropic laminates. Tests were conducted on laminates with various stacking sequences of 0°, ±45°, and 90° orientations. The difference between experiment and theory for modulus measurements of symmetric, 8 ply beams ranged from 13 to 21 per cent error, a variation typical of the results seen in the bending stiffness determination experiments reported here. In contrast, modulus values obtained from tensile tests of the same laminates showed good agreement with lamination theory predictions.

5.4 Empirical Determination of Effective Bending Stiffness of Scaled Composite Beams from Static Load Response

Results of the bending stiffness experiments indicate that it is necessary to use empirical means to solve for the bending stiffness of each scale model beam tested. Since transverse midpoint displacement measurements were not made during the tests, the small deflection analysis could not be used to solve for the bending stiffness. Instead, a technique was employed in which the large deflection beam analysis was matched graphically to the experimental load versus end displacement response. The normalizing factor for the load, the Euler load, was adjusted until the analysis and experiment agreed for small values of load ratio, i.e., less than load ratios of 0.4. The effective beam bending stiffness was found by solving Eq. 5.1 using the Euler load value determined from the matching technique.

The experimentally determined values of bending stiffness and the lamination theory predictions are given in Table 5-2 for each of

Table 5-2. Bending Stiffness Values Determined from Lamination Theory and Experiment for Scaled Composite Beams

BEAM LABEL	LAY-UP	SCALE FACTOR	Deff*b (LAM)	Deff*b (EXP)
USIX1		1/6	82.27	65.75
USIX3	$[0]_8$	1/6	84.06	66.00
USIX5		1/6	80.51	65.85
AVERAGE			82.28	65.87
UFOR1		1/4	370.47	319.50
UFOR3	$[0]_{12}$	1/4	375.92	326.45
UFOR5		1/4	395.87	333.38
AVERAGE			380.75	326.44
UTHR1		1/3	1003.70	855.00
UTHR3	$[0]_{16}$	1/3	1033.90	860.00
UTHR5		1/3	1121.10	910.00
AVERAGE			1052.90	875.00
UHALF1		1/2	5368.65	4650.00
UHALF3	$[0]_{24}$	1/2	5686.05	4980.00
UHALF5		1/2	5123.55	4785.00
AVERAGE			5392.75	4805.00
U2THR1		2/3	17082.20	15460.00
U2THR3	$[0]_{32}$	2/3	17428.40	16020.00
U2THR5		2/3	16834.20	15800.00
AVERAGE			17114.93	15760.00
U3FOR1		3/4	27175.50	22860.00
U3FOR3	$[0]_{36}$	3/4	27742.50	26005.50
U3FOR5		3/4	27956.25	26416.50
AVERAGE			27624.75	25094.00
U5SIX1		5/6	43830.00	37750.00
U5SIX3	$[0]_{40}$	5/6	40335.00	39937.50
U5SIX5		5/6	41870.00	38875.00
AVERAGE			42011.67	38854.17
UFULL1		1	83256.00	68970.00
UFULL3	$[0]_{48}$	1	87888.00	82200.00
UFULL5		1	80040.00	81300.00
AVERAGE			83728.00	77490.00

Table 5-2. Continued

BEAM LABEL	LAY-UP	SCALE FACTOR	Deff*b (LAM)	Deff*b (EXP)
ASIX1		1/6	10.60	11.00
ASIX3	$[45_2/-45_2]_S$	1/6	10.39	11.00
ASIX5		1/6	10.74	11.10
AVERAGE			10.58	11.03
AFOR1		1/4	56.03	54.00
AFOR3	$[45_3/-45_3]_S$	1/4	56.03	56.33
AFOR5		1/4	55.31	57.08
AVERAGE			55.79	55.80
ATHR1		1/3	137.08	150.00
ATHR3	$[45_4/-45_4]_S$	1/3	143.42	144.82
ATHR5		1/3	140.96	148.00
AVERAGE			140.49	147.61
AHALF1		1/2	680.31	630.00
AHALF3	$[45_6/-45_6]_S$	1/2	747.96	690.00
AHALF5		1/2	721.05	667.50
AVERAGE			716.44	662.50
A2THR1		2/3	2247.60	1934.00
A2THR3	$[45_8/-45_8]_S$	2/3	2362.60	2410.00
A2THR5		2/3	2306.60	2430.00
AVERAGE			2305.60	2258.00
A3FOR1		3/4	3522.83	3375.00
A3FOR3	$[45_9/-45_9]_S$	3/4	4079.03	3926.25
A3FOR5		3/4	3727.58	3757.50
AVERAGE			3776.48	3686.25
A5SIX1		5/6	5487.00	4275.00
A5SIX3	$[45_{10}/-45_{10}]_S$	5/6	5890.50	5087.50
A5SIX5		5/6	5771.50	5375.00
AVERAGE			5716.33	4912.50
AFULL1		1	10833.90	9150.00
AFULL3	$[45_{12}/-45_{12}]_S$	1	11307.90	10170.00
AFULL5		1	11395.80	9795.00
AVERAGE			11179.20	9705.00

Table 5-2. Continued

BEAM LABEL	LAY-UP	SCALE FACTOR	Deff*b (LAM)	Deff*b (EXP)
CSIX1		1/6	70.65	55.17
CSIX3	$[0_2/90_2]_S$	1/6	68.21	54.39
CSIX5		1/6	70.65	57.50
AVERAGE			69.83	55.69
CFOR1		1/4	299.93	243.75
CFOR3	$[0_3/90_3]_S$	1/4	295.33	243.38
CFOR5		1/4	309.27	233.87
AVERAGE			301.51	240.33
CTHR1		1/3	949.79	814.50
CTHR3	$[0_4/90_4]_S$	1/3	949.79	772.50
CTHR5		1/3	944.26	785.60
AVERAGE			947.95	790.87
CHALF1		1/2	4526.55	3937.50
CHALF3	$[0_6/90_6]_S$	1/2	4854.60	4104.75
CHALF5		1/2	4725.30	4125.95
AVERAGE			4702.15	4056.07
C2THR1		2/3	15108.20	13274.00
C2THR3	$[0_8/90_8]_S$	2/3	14856.20	13950.00
C2THR5		2/3	15021.00	13700.00
AVERAGE			14995.13	13641.33
C3FOR1		3/4	23421.50	21960.00
C3FOR3	$[0_9/-90_9]_S$	3/4	23674.50	22461.21
C3FOR5		3/4	23798.25	22050.00
AVERAGE			23634.75	22157.07
C5SIX1		5/6	39062.50	34242.50
C5SIX3	$[0_{10}/90_{10}]_S$	5/6	40502.50	35875.00
C5SIX5		5/6	39062.50	34875.00
AVERAGE			39542.50	34997.50
CFULL1		1	10833.90	61860.00
CFULL3	$[0_{12}/90_{12}]_S$	1	11307.90	71250.00
CFULL5		1	11395.80	68400.00
AVERAGE			11179.20	67170.00

Table 5-2. Continued

BEAM LABEL	LAY-UP	SCALE FACTOR	Deff*b (LAM)	Deff*b (EXP)
QSIX1		1/6	29.36	24.00
QSIX3	$[-45/0/45/90]_S$	1/6	29.04	23.25
QSIX5		1/6	29.69	24.88
AVERAGE			29.36	24.04
QHR1		1/3	441.48	395.00
QHR3	$[-45_2/0_2/45_2/90_2]_S$	1/3	438.94	402.50
QHR5		1/3	441.48	389.00
AVERAGE			440.63	395.50
QHALF1		1/2	2256.30	1942.50
QHALF3	$[-45_3/0_3/45_3/90_3]_S$	1/2	2299.35	1981.50
QHALF5		1/2	2239.20	1980.00
AVERAGE			2264.95	1968.00
Q2THR1		2/3	7267.00	6100.00
Q2THR3	$[-45_4/0_4/45_4/90_4]_S$	2/3	7043.20	6600.00
Q2THR5		2/3	7474.80	6400.00
AVERAGE			7261.67	6366.67
Q5SIX1		5/6	16602.50	15125.00
Q5SIX3	$[-45_5/0_5/45_5/90_5]_S$	5/6	15476.00	15802.50
Q5SIX5		5/6	14990.25	15412.50
AVERAGE			16356.25	15446.67
QFULL1		1	33558.00	30600.00
QFULL3	$[-45_6/0_6/45_6/90_6]_S$	1	35016.00	32550.00
QFULL5		1	35421.00	32850.00
AVERAGE			34665.00	32000.00

the scaled composite beams which were tested statically. When the experimentally determined values of bending stiffness are used to calculate the Euler load and normalize the load-end displacement response, the anomalies seen in Figures 5-1 and 5-2 for the unidirectional beams disappear. This is evident in Figure 5-3 which is a plot of the normalized load versus end displacement data of 1/6 through full scale unidirectional beams, similar to Figure 5-1 except that the experimental bending stiffness was used to calculate the Euler load. As seen in the figure, the load response curves scale until failure occurs. Figure 5-4 is a plot of the large deflection beam solution and DYCAST beam analysis with the normalized 1/6 and full scale unidirectional beam load response. This figure indicates that the two analyses predict the load response well when the experimental data are normalized by the Euler load which is determined empirically.

The effective bending stiffness values determined for each scaled beam can be used to investigate scaling effects in the elastic response. In Figures 5-5 through 5-8, the bending stiffness values from Table 5-2 have been multiplied by the appropriate scale factor ($1/\lambda^4$) and normalized by the full scale value and plotted versus scale factor for the unidirectional, angle ply, cross ply, and quasi-isotropic laminates, respectively. Any significant deviations from the straight line at one in each figure may be interpreted as a scale effect. Results for the unidirectional, cross ply and quasi-isotropic laminates (Figures 5-5, 5-7, and 5-8) show deviations of less than 10% from scaled response. This variation can be explained through minor differences in thicknesses of the fabricated beams and experimental error. However, the angle ply laminates, shown in Figure 5-6, exhibit a large scale effect in the bending stiffness response. The smaller beams are significantly stiffer than the full scale beams. This finding reinforces the importance of using the empirical bending stiffness in normalizing the load-displacement data for the angle ply laminates, and indicates that more research is

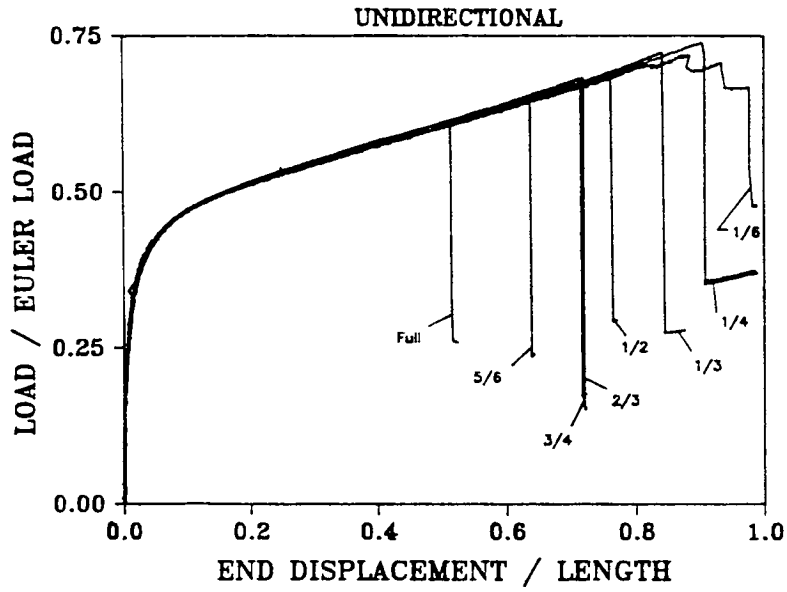

Figure 5-3. Experimental load versus end displacement results for unidirectional 1/6 through full scale beams. (Euler load is determined empirically using matching technique.)

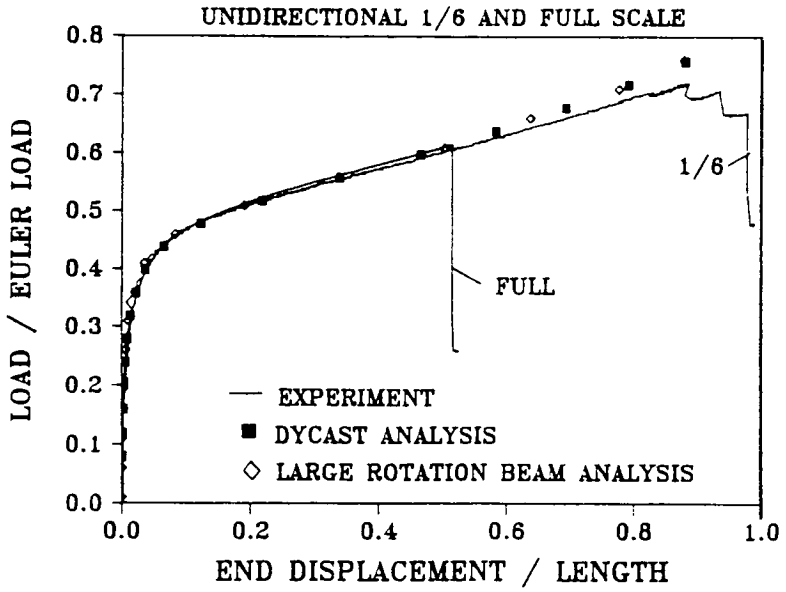

Figure 5-4. Unidirectional 1/6 and full scale beam normalized load versus end displacement data with DYCAST and large deflection beam analyses. (Euler load is determined empirically using the matching technique.)

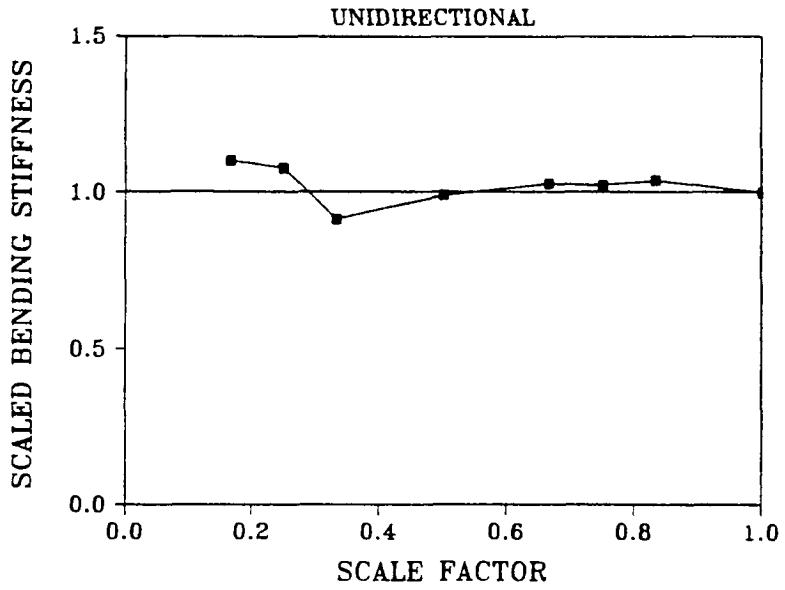

Figure 5-5. Normalized scaled bending stiffness ($[(EI)_{model} /(EI)_{prototype}]*1/\lambda^4$) versus scale factor for unidirectional beams.

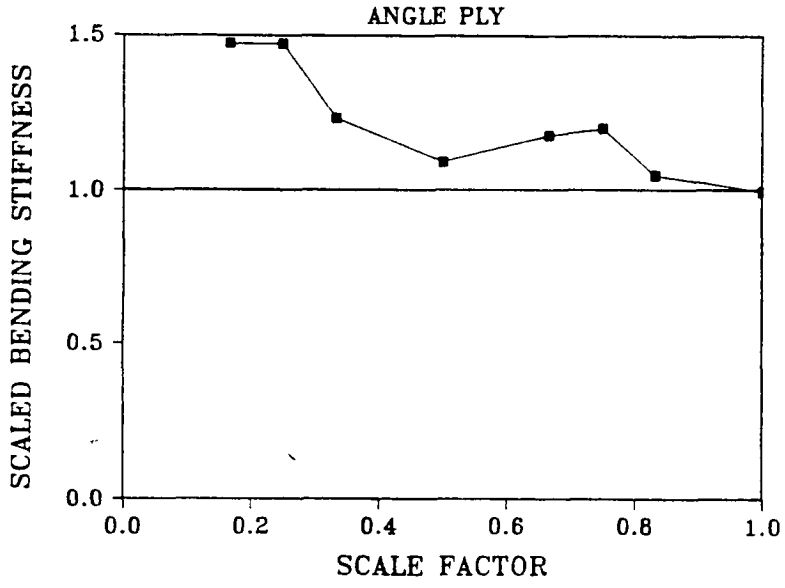

Figure 5-6. Normalized scaled bending stiffness ($[(EI)_{model} /(EI)_{prototype}]*1/\lambda^4$) versus scale factor for angle ply beams.

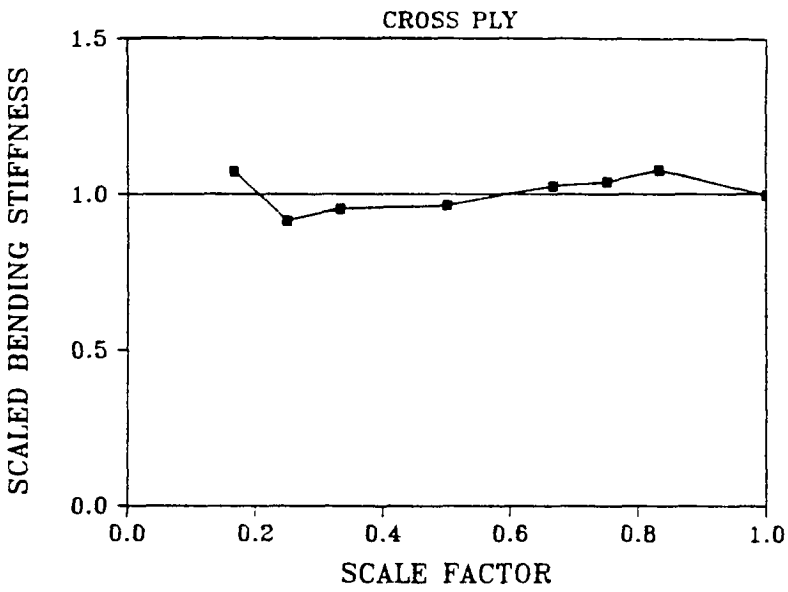

Figure 5-7. Normalized scaled bending stiffness ($[(EI)_{model} /(EI)_{prototype}]*1/\lambda^4$) versus scale factor for cross ply beams.

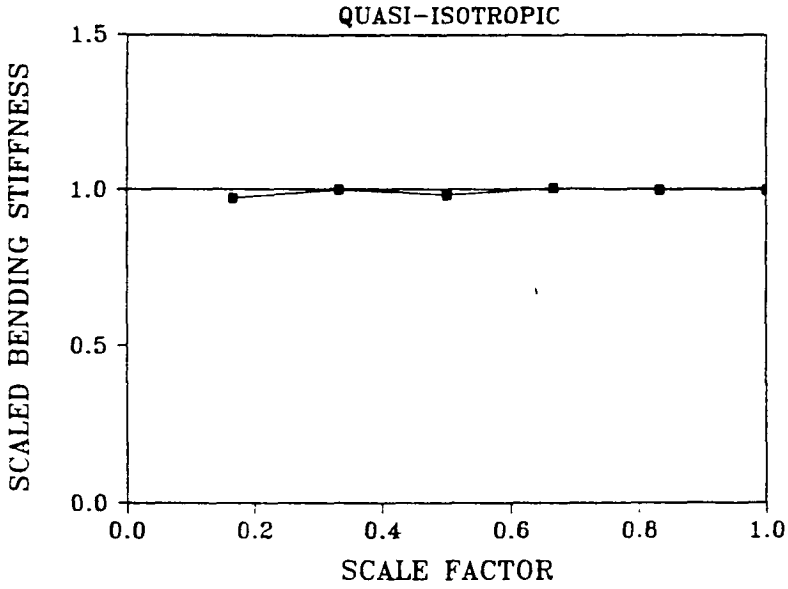

Figure 5-8. Normalized scaled bending stiffness ($[(EI)_{model} /(EI)_{prototype}]*1/\lambda^4$) versus scale factor for quasi-isotropic beams.

needed to verify the observed scale effect in elastic response for this family of laminates.

Because Derian [37] and Sensmeier [38] performed similar tests on eccentrically loaded composite beams using the same graphite-epoxy material system, it is useful to examine their approach to the composite beam constitutive behavior. Derian [37] conducted a series of static tests and observed a significant difference between tensile and compressive surface strain magnitudes at the midpoint of the beams. This finding led him to hypothesize that the material exhibited either a nonlinear elastic or bimodular elastic material behavior. He performed static tests to determine empirically the bending tensile and compressive moduli. Results of these tests indicated that the laminates he tested exhibited, to a first approximation, a bimodular material response. Comparisons between lamination theory predictions of bending stiffnesses derived from tensile and compressive moduli and the empirically determined values showed significant differences, especially for the compression modulus. Derian used the empirically determined flexural moduli in a finite element program to predict the deformation response of the beams with moderate success. Derian concluded that classical lamination theory cannot be used with confidence for the prediction of the large deformation response of laminated beams.

In contrast to Derian's empirical approach, Sensmeier [38] performed material characterization tests on the graphite-epoxy system (AS4/3502) which was used to fabricate the beam specimens. His purpose was to determine if the material did, indeed, exhibit nonlinear or bimodular stress-strain behavior and to incorporate the material constitutive response into a finite element model. The experimental curves were approximated by polynomials, and the algebraic expressions were programmed into the finite element model. The material constitutive behavior was implemented for each load step by determining the current strain state in each ply of each beam element. Once the ply strain state is known, the tangent modulus of the stress-strain curve was found for that strain level.

The ply stiffnesses were then used to calculate a laminate stiffness matrix for each element. The updated element stiffness matrix was used for the next load increment. Thus, in this step-wise fashion, the model incorporated the stress-strain response in both tension and compression as determined from material characterization tests. Using this approach, Sensmeier achieved excellent agreement for unidirectional thick (30 ply) laminates for both load and strain response. The model also predicted the large difference in tensile and compressive surface strain for a $((30/0/-30)_5)_S$ laminate. However, in general, the finite element model overpredicted the load-end displacement response, in one case by as much as 20%. Sensmeier concluded that the most critical factor in predicting both the load and strain response was not the nonlinear constitutive behavior, but the inclusion of width-wise degrees of freedom. This was particularly true for laminates with off-axis plies exhibiting large bend-twist coupling behavior.

In conclusion, the effective bending stiffness which was found by applying the matching technique to the static load-displacement data may be thought of as a structural stiffness. As such, it incorporates the effects of (1) microcracking and other defects in the beam, (2) width-wise responses, (3) nonlinear and bimodular material behavior, and (4) misalignments and minor variations in the test conditions. The empirical approach is a means of determining the beam stiffness since none of the effects mentioned previously can be isolated from the problem.

Chapter 6 - Static Test Results

Experimental results from the static testing program are presented for the four laminate types and range of scaled sizes of composite beam-columns. Scale effects in the load and strain response of the beams are investigated and the damage mechanisms are discussed for each of the laminate families. The various analytical models described in Chapter 4 are compared to the experimental results.

The normalized load versus end displacement response is discussed for the unidirectional, angle ply, cross ply, and quasi-isotropic scale model beams. The vertical load is normalized by the Euler column buckling load for each beam. The Euler load was calculated using an effective bending stiffness which was determined by matching the large deflection beam analysis to the experimental data for each beam. The procedure used to find the effective beam bending stiffnesses is described more fully in Chapter 5 and the values are listed in Table 5-2. It was necessary to find the effective bending stiffness empirically since values determined from lamination theory were not sufficiently accurate. The end displacement data are normalized by the gage length of the beam specimens which are listed in Table 3-2.

Static tests were performed on three replicate beams for each laminate type and scaled size. In general, the unidirectional, cross ply, and quasi-isotropic beams showed little deviation in the load-deflection responses among the replicate beams. More variation was seen in the load-deflection response of the angle ply beams; however, this was not unexpected since the response of these laminates is sensitive to initial damage in the form of matrix cracks, and the response is affected by damage sustained during loading. The load and strain response of all the replicate beams are plotted in Appendix C. These plots illustrate the deviations in beam response and failure among the replicates. The results from a single,

representative test are presented for each laminate type and size of beam.

6.1 Unidirectional Beams

6.1.1 Load-Deflection Response

Normalized load versus end displacement results are shown in Figure 6-1 for the unidirectional beams. The data for beams ranging in scale from 1/6 through full scale appear to fall on a single curve. For small values of the load ratio, typically less than 0.4, this indicates that the beam response scales for small deflections. As the load ratio increases, the response becomes nonlinear and the beams undergo large rotations and deflections. In fact, the 1/6 scale beam fails at an end displacement ratio of 0.95 which means that the ends of the beam are close to touching one another when failure occurs. Yet, even under these severe deformations, no deviations from scaled response are observed. However, a scale effect in strength is evident in the plot of Figure 6-1. The small scale beams fail at higher normalized load and end displacement levels than the full scale beam. For the unidirectional beams, the 1/6 scale beam fails at an end displacement ratio two times greater than that of the full scale beam and at a significantly higher load ratio. The data indicate that as the beam size decreases from the full scale prototype, the failure loads increase correspondingly. In addition, the failures occur at higher values of end displacement and are dispersed at fairly regular intervals for the 5/6, 3/4, 2/3, 1/2, 1/3, 1/4, and 1/6 scale beams. The average failure load ratios, loads, end displacement ratios, and strains are listed in Table 6-1 for the scale model unidirectional beams.

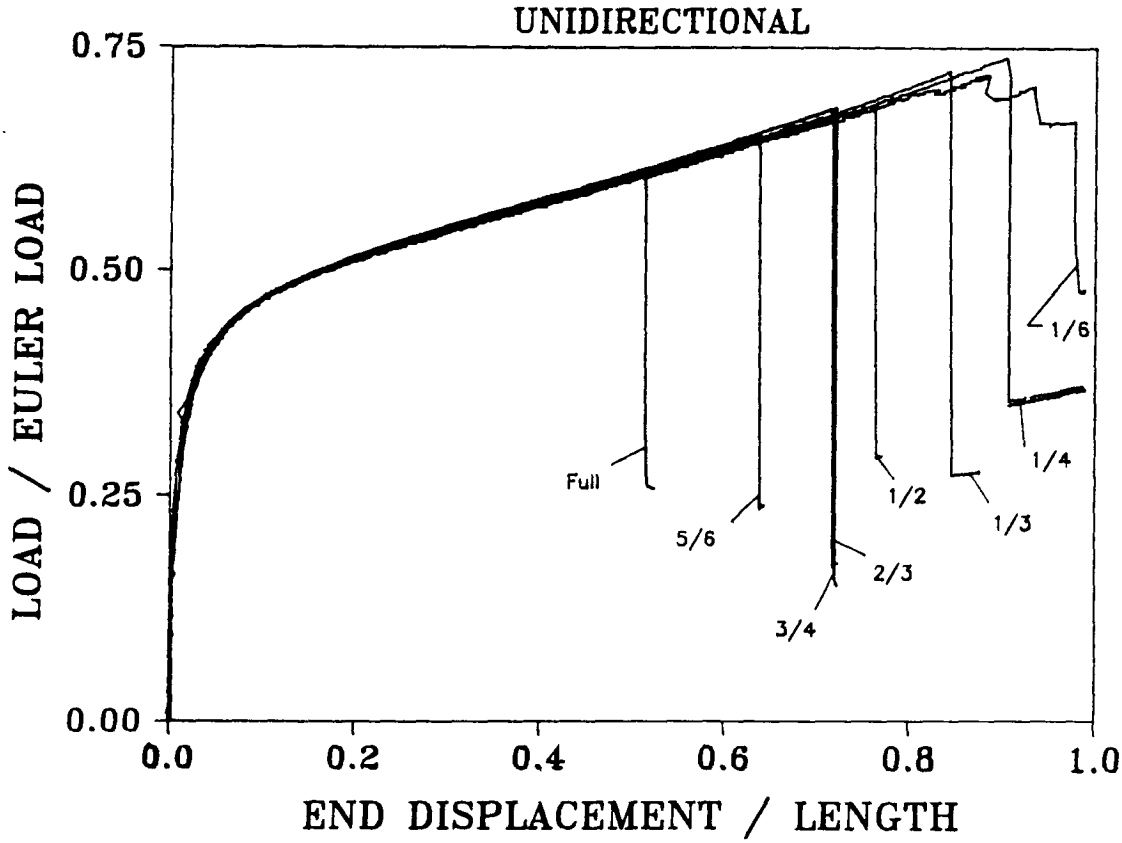

Figure 6-1. Normalized load versus end displacement experimental results for unidirectional 1/6 through full scale model beams

Table 6-1. Average failure loads, displacements, and strains for scaled unidirectional beams.

UNIDIRECTIONAL					
Scale Factor	Failure Load (lbs)	Failure Load Ratio	End Disp. Ratio	Failure Strain Tension (microin/in)	Failure Strain Compression (microin/in)
1/6	17.4	.67	.98	gage failures	gage failures
1/4	42.0	.73	.91	17169.9	-20097.8
1/3	62.6	.72	.86	15624.9	-18160.7
1/2	142.4	.68	.74	14080.5	-17006.8
2/3	271.8	.69	.75	13481.9	-16684.1
3/4	351.8	.69	.74	14436.3	-16610.3
5/6	406.4	.67	.68	13498.2	-15402.5
Full	524.1	.62	.54	11315.5	-12387.8

6.1.2 Strain-Deflection Response

Tensile and compressive midpoint strain versus normalized end displacement are plotted for the unidirectional scale model beams in Figure 6-2. The strain measurements were recorded directly from strain gages applied to the tensile and compressive surfaces of the beams at their midspan. Since strain is a dimensionless quantity, no normalizing factor is required to make comparisons between data for the different scale model beams. Only a slight variation from scaled response is evident in the plot of Figure 6-2. The strain response is bounded by the 1/4 scale beam data which exhibits the highest strain magnitude, and by the full scale beam data which exhibits the lowest strain magnitude. However, the maximum deviation between the strain responses for these two beams is approximately five per cent. Failure strains are listed in Table 6-1 and indicate that as beam size decreases the failure strain increases. In fact, the tensile and compressive failure strains for the 1/4 scale unidirectional beams are 52% and 62% higher, respectively, than the full scale failure strains. The strain response for the 1/6 scale beam, as shown in Figure 6-2, is a gage failure and does not represent failure of the beam.

It is also observed from Figure 6-2 and Table 6-1 that the compressive strain response and failure strains for the various scale model beams are greater in magnitude than the corresponding tensile strains. To illustrate the difference in strain magnitudes, the absolute value of the compressive strain is plotted with the tensile strain for the 1/4 scale unidirectional beam in Figure 6-3(a). The percentage difference between strain magnitudes is plotted in Figure 6-3(b) as a function of end displacement ratio. The difference between compression and tensile strain magnitudes was also observed by Derian [37] and Sensmeier [38]. Sensmeier reported that the difference in strain magnitudes increased linearly with end displacement until failure for the unidirectional beams he tested. He also noted that the percentage difference in failure strain magnitudes

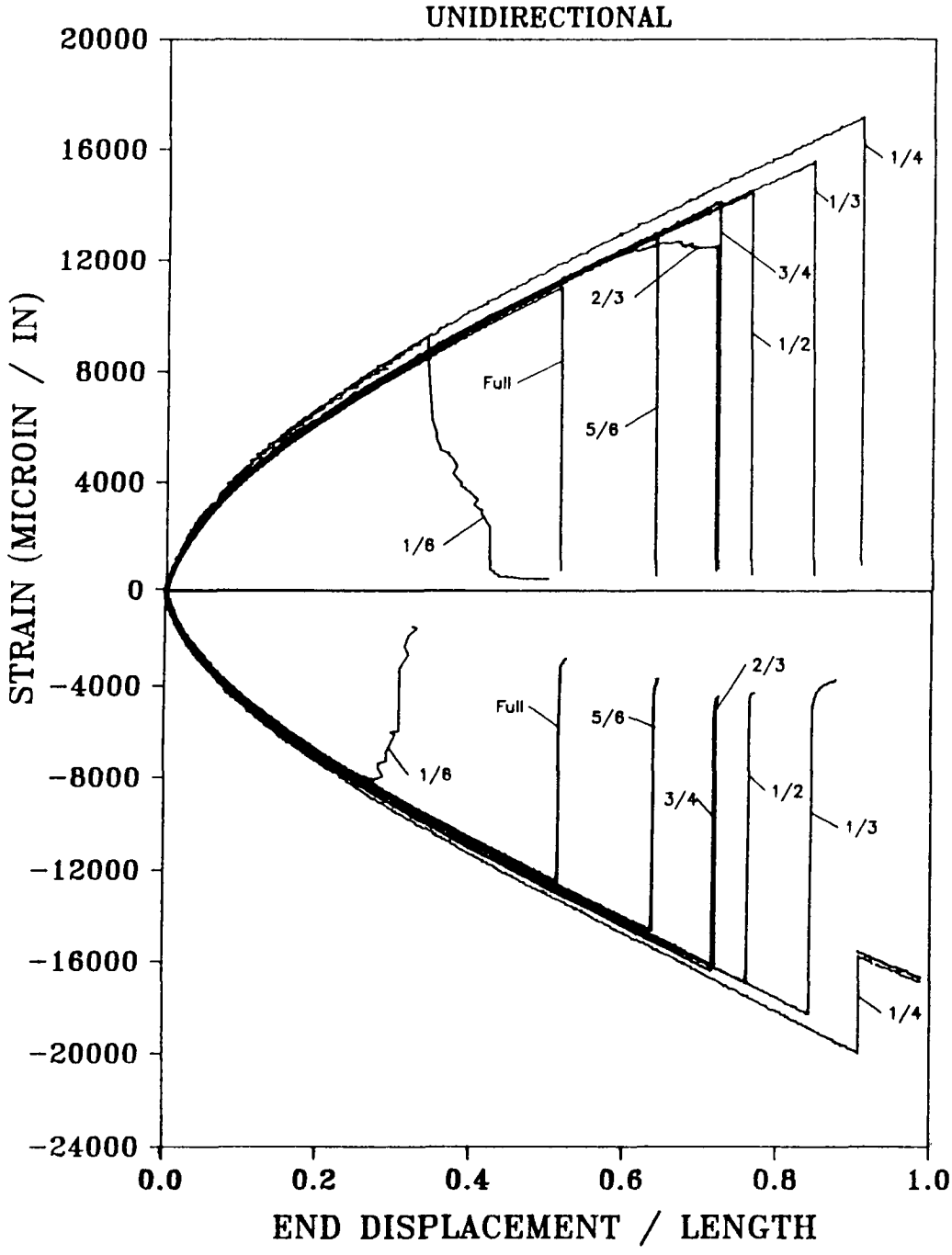

Figure 6-2. Midpoint strain versus end displacement/length experimental results for unidirectional 1/6 through full scale model beams.

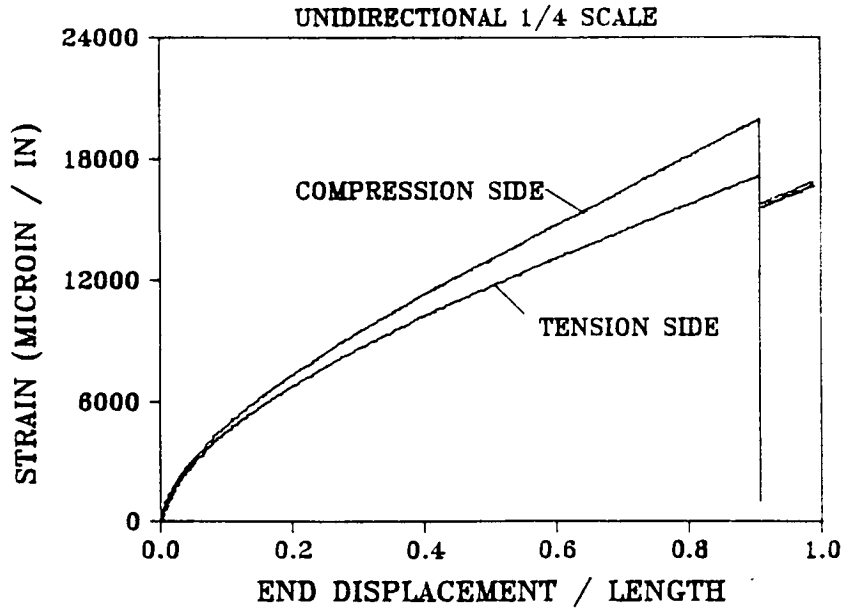

(a) Compressive and tensile midpoint strain-displacement data for 1/4 scale unidirectional beam.

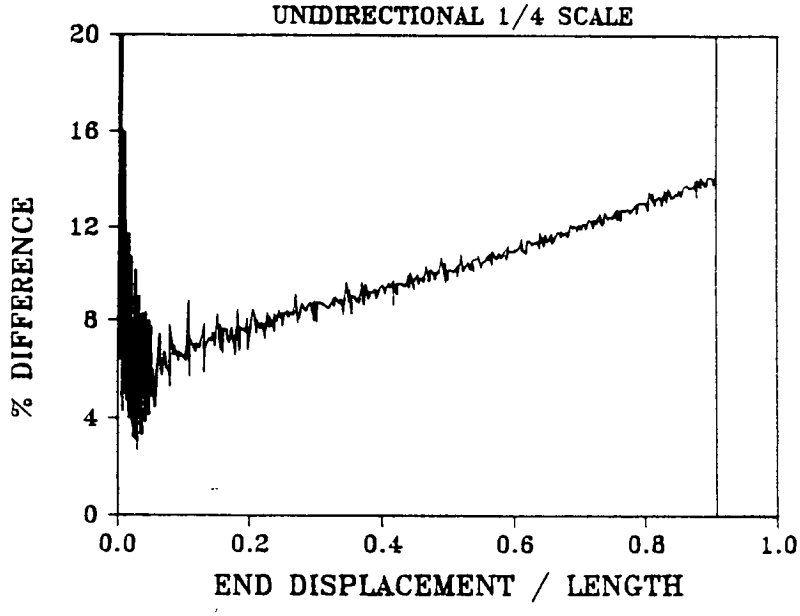

(b) Percent difference in compressive and tensile strain magnitudes versus end displacement ratio.

Figure 6-3. Midpoint strain-displacement data for unidirectional 1/4 scale model beam.

for a 30-ply unidirectional laminate was approximately 13%. Figure 6-3 indicates that the strain response of the unidirectional 1/4 scale beam yields consistent results with those of Sensmeier.

On first examination, it seems reasonable to assume that the difference in compressive and tensile strain magnitudes may be attributed to the axial load which produces a strain component that effectively adds to the compressive strain and subtracts from the tensile strain. However, the strain component due to the axial load is two orders of magnitude less than the measured surface strains and cannot account for the large observed differences. Sensmeier examined nonlinear material properties and width-wise effects as factors which contribute to the strain phenomenon. He found that for a unidirectional 30-ply laminate the incorporation of nonlinear material properties was essential for predicting the difference in strain magnitudes, while width-wise effects appeared to have little influence. These factors will be studied in more detail in the next section when the Sensmeier finite element analysis (MDS2DB) is compared to the experimental data from this investigation.

6.1.3 Comparison of Experiment with Analysis

Predictions of the normalized load-deflection response from the large deflection "elastica" beam analysis and the DYCAST finite element model are plotted with experimental data from the 1/4 and full scale unidirectional beams in Figure 6-4. Excellent agreement between both analysis techniques and the experimental data is achieved. The analytical response predictions are slightly stiffer than the 1/4 scale beam experimental data for end displacement ratios greater than 0.5. For large end displacement ratios, a loss of stiffness due to matrix cracking and fiber breakage is expected. However, the material properties in the analyses are not degraded to account for this effect and remain linear elastic until failure. For the unidirectional beams, this assumption does not introduce a significant error in the model.

It is also interesting to note that the matching technique which was used to derive an effective bending stiffness for the beams was performed for load ratios less than 0.4 and end displacement ratios less than 0.05. Yet, the Euler load calculated from this procedure was used to normalize all of the load data for the specific beam. The excellent agreement obtained over the entire loading range indicates that the technique is an effective means of finding the bending stiffness empirically.

Based on the results of Figure 6-4, it appears that a one dimensional, linear elastic model which accounts for large deflections is adequate to model the eccentrically loaded beam-column problem for unidirectional laminates. The key issue for successfully modeling the response of the unidirectional laminates is to use the correct bending stiffness for the beam. The importance of this factor is illustrated in Figure 6-5. The MDS2DB finite element program was used to model the 1/4 scale unidirectional beam. Results of the load-deflection response are plotted in Figure 6-5 along with the experimental data. Since the MDS2DB code incorporates width-wise effects and can include nonlinear material properties, the analytical and experimental load data were not normalized by the Euler load to avoid confusion. The MDS2DB model using linear material properties overpredicted the experimental data by 21% at an end displacement ratio of 0.6. The model was rerun using the nonlinear material property capabilities of the code with no measurable improvement.

The strain response predictions from the large rotation beam analysis and DYCAST are plotted in Figure 6-6 with the experimental strain data from the 1/4 and full scale unidirectional beams. Agreement between the two analyses is excellent. The analyses tend to overpredict the tension side strain slightly for large end displacement ratios, and tend to underpredict the response on the compression side. This trend is expected since the difference between tensile and compression strain magnitudes increases as the end displacement ratio increases, as indicated in Figure 6-3(b). Neither the large rotation beam analysis or DYCAST can predict the

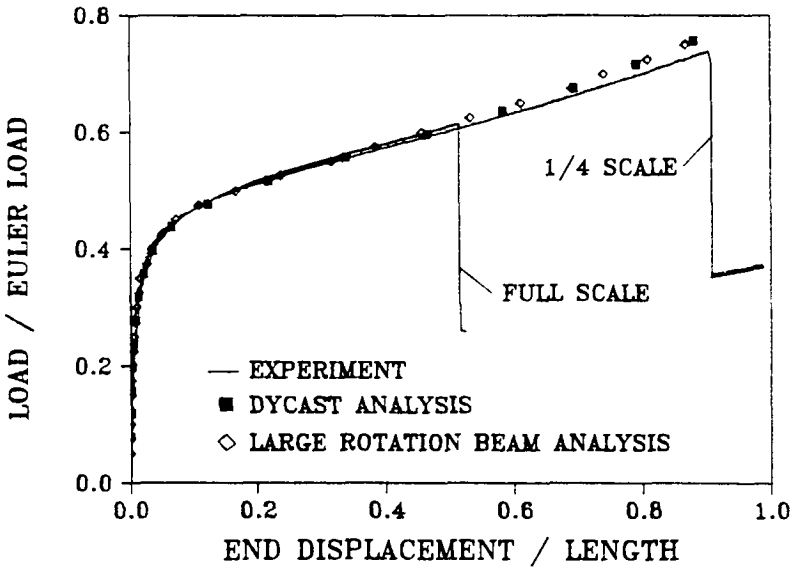

Figure 6-4. Comparison of large deflection beam analysis and DYCAST load-displacement predictions with unidirectional 1/4 and full scale beam experimental response.

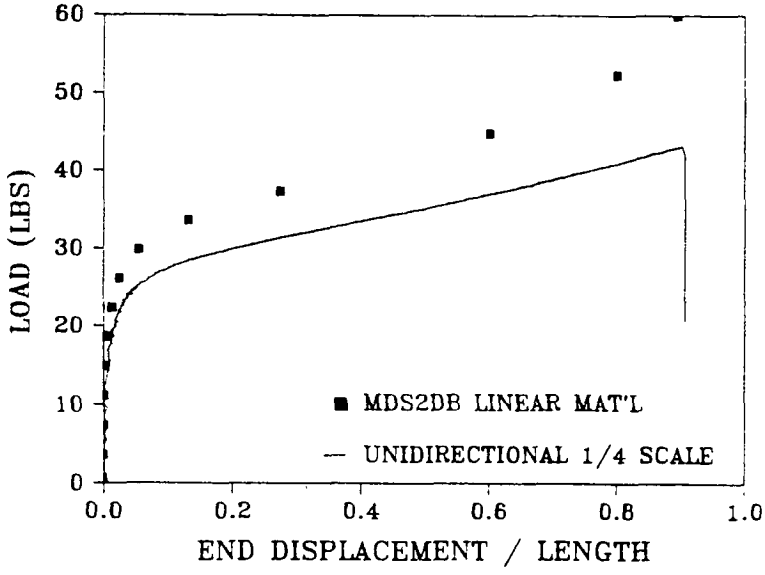

Figure 6-5. Comparison of MDS2DB analysis with unidirectional 1/4 scale model beam load-displacement experimental response.

difference in tensile and compressive strains which may be attributed to nonlinear material behavior or width-wise effects. Figure 6-7 is a plot of the 1/4 scale unidirectional strain data with a MDS2DB analysis using linear material properties. The MDS2BD finite element model had better success at predicting the compressive strains than the beam solution or DYCAST, but also slightly overpredicted the tensile strain. The MDS2DB model was also run using nonlinear material properties with no significant change in the strain response. A comparison of the results from Figures 6-6 and 6-7 indicates that including width-wise effects leads to a slight improvement in predicting the strain response for unidirectional laminates. It is anticipated that this effect will become more important for laminates containing off-axis plies which exhibit bend-twist interaction behavior.

6.1.4 Failure Mechanisms

The unidirectional beams failed through fiber fractures near the midpoint of the beam and by splitting along the longitudinal axis of the beam. This failure mode is illustrated in Figure 6-8 which is a photograph of the three 1/3 scale unidirectional beams tested under static load. Damage was occurring during loading since audible events could be heard; however, final fracture occurred catastrophically at the midspan of the beam and resulted in complete loss of load carrying capability. Figure 6-8 shows that this failure mode is consistent between replicate beams of the same size and lay-up. Figure 6-9 indicates that the failure mode is typical of all the unidirectional beams 1/6 through full scale. Consequently, failure modes appear to be independent of specimen size for the unidirectional laminates.

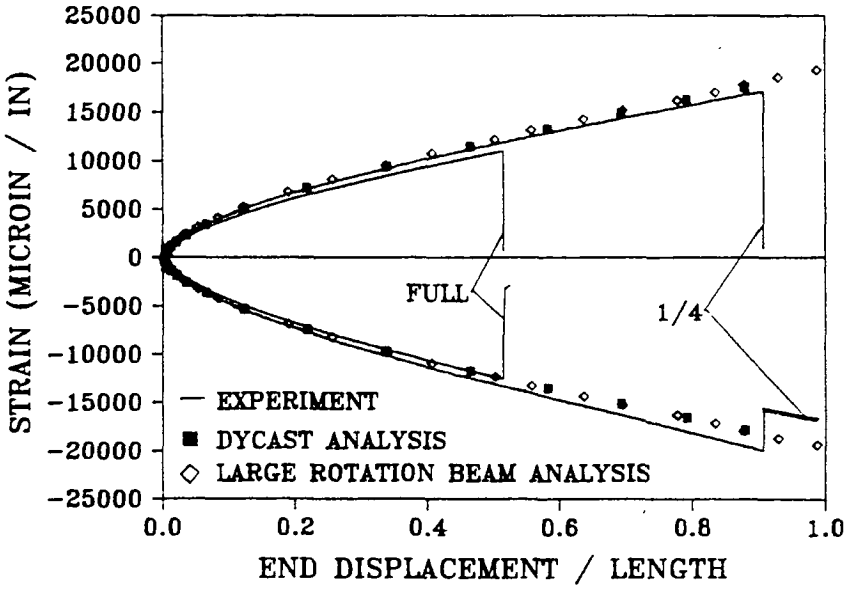

Figure 6-6. Comparison of large deflection beam analysis and DYCAST strain-displacement predictions with unidirectional 1/4 and full scale beam experimental response

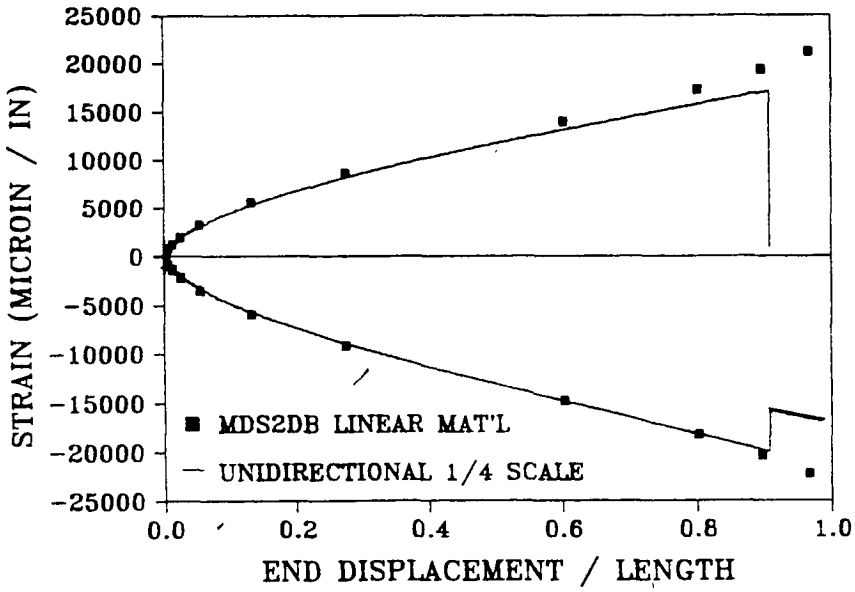

Figure 6-7. Comparison of MDS2DB analysis with unidirectional 1/4 scale model beam strain-displacement experimental response.

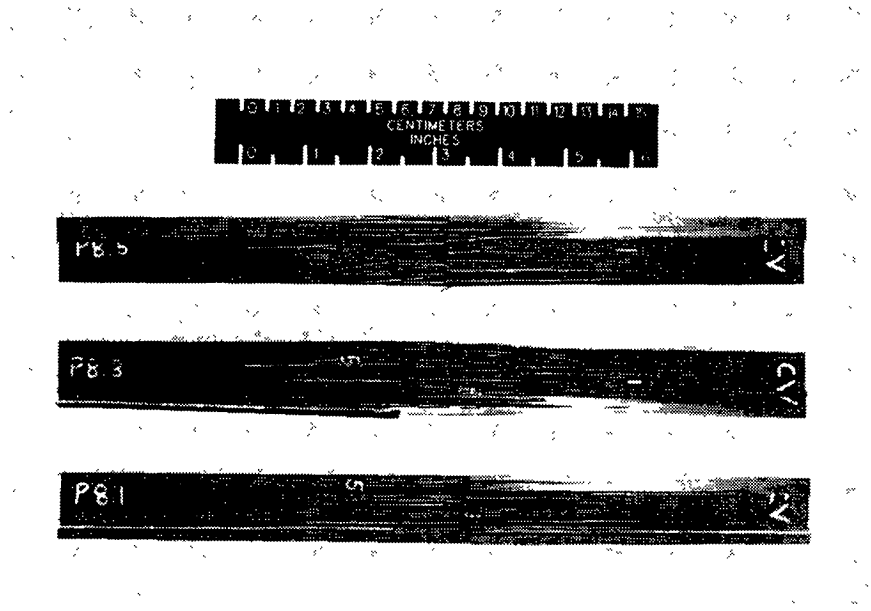

Figure 6-8. Photograph of failed unidirectional 1/3 scale beams, three replicates.

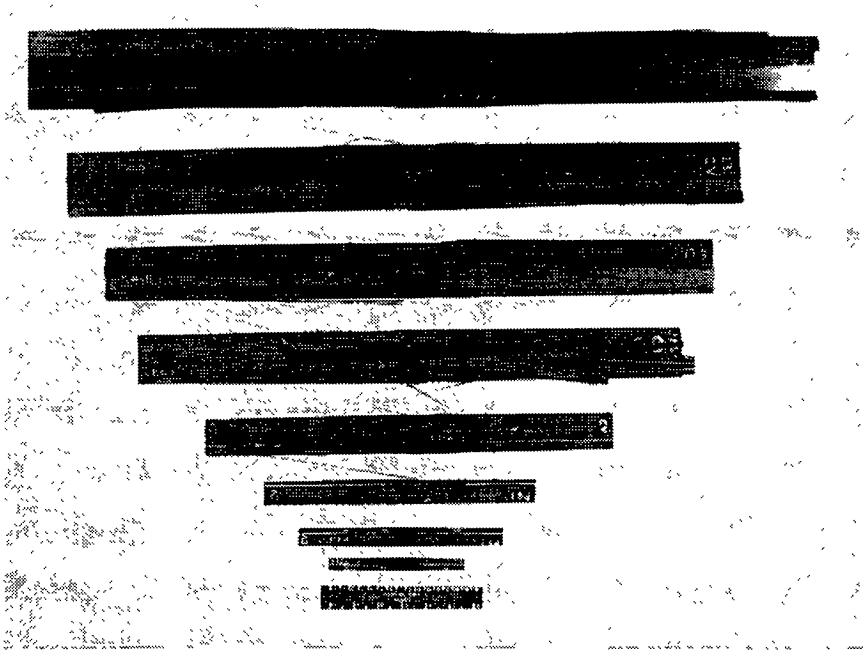

Figure 6-9. Photograph of a set of failed unidirectional beams 1/6 through full scale.

6.2 Angle Ply Beams

6.2.1 Load-Deflection Response

The normalized load versus end displacement response for each of the scale model angle ply beams (1/6 through full scale) is plotted in Figure 6-10. For load ratios less than 0.4, the load responses of the scale model beams fall on the same curve as expected based on the technique used to determine the beam bending stiffness. As indicated in Figure 4-10, the load ratio value of 0.4 marks the load level where small deflection beam theory is no longer valid. For load ratios higher than 0.4 the beams undergo large deflections and end rotations. At this point, the large scale angle ply beams (full, 5/6 and 3/4 scale) developed matrix cracks which resulted in a severe loss of stiffness and early failure. These failures occurred at an end displacement ratio of approximately 0.1. In general, as the size of the beams decreased, the load level at which matrix cracking initiated increased slightly. Consequently, the smaller scale beams supported higher loads with less stiffness reduction and failed at greater end displacement ratios. In fact, the 1/6 scale angle ply beam failed at an end displacement ratio six times greater than the full scale beam. The unevenness of the load response seen in Figure 6-10 for the 1/6 and 1/4 scale beams is an artifact of the data collection system and instrumentation used to measure the test parameters, and is not an experimental phenomenon. Failure loads, load ratios, end displacement ratios, and tensile and compressive strains are listed in Table 6-2 for each of the scale model angle ply beams.

6.2.2 Strain-Deflection Response

The experimental strain-deflection response is plotted in Figure 6-11 for the scale model angle ply beams. Strain measurements were recorded from gages attached on the tensile and compressive

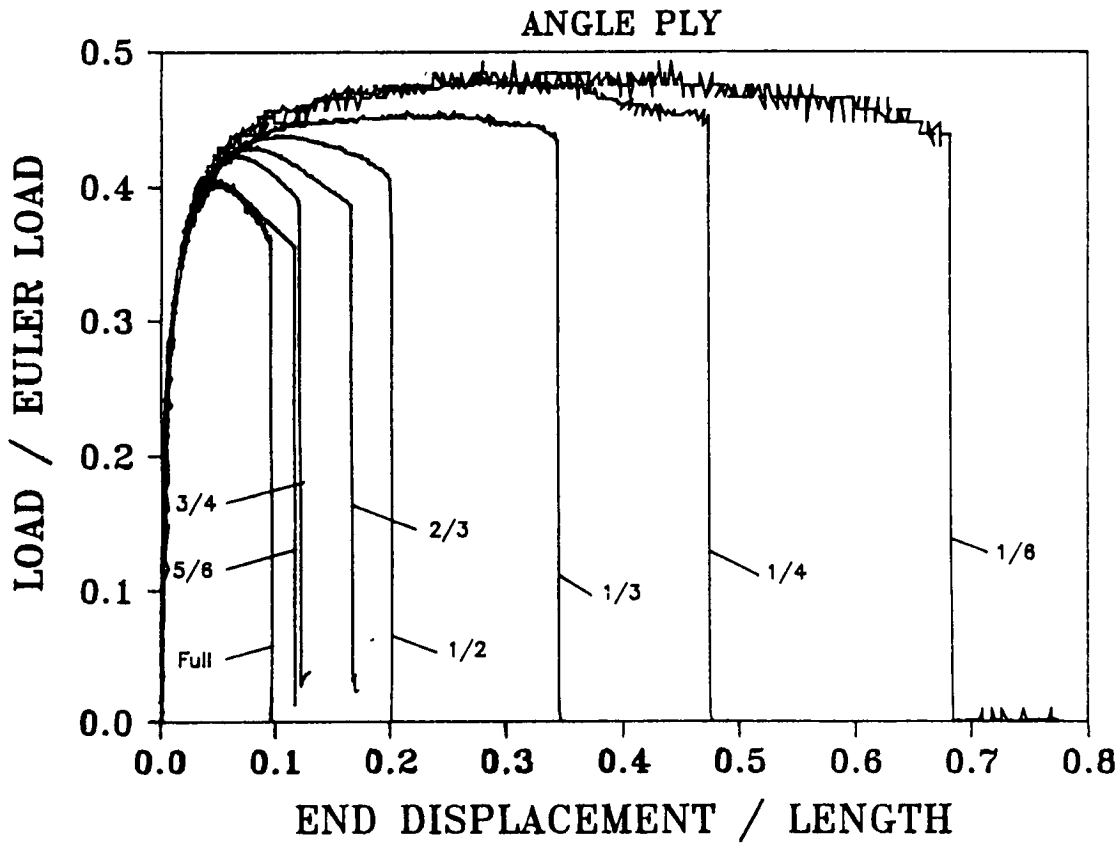

Figure 6-10. Normalized load versus end displacement experimental results for angle ply 1/6 through full scale model beams.

Table 6-2. Average failure loads, displacements, and strains for scaled angle ply beams.

ANGLE PLY					
Scale Factor	Failure Load (lbs)	Failure Load Ratio	End Disp. Ratio	Failure Strain Tension (microin/in)	Failure Strain Compression (microin/in)
1/6	1.96	.45	.67	17448.0	-16618.6
1/4	4.35	.44	.47	12236.8	-13636.6
1/3	6.43	.44	.36	9592.9	-11266.8
1/2	11.8	.41	.21	6243.2	-7916.6
2/3	19.5	.35	.16	8360.9	-7424.9
3/4	28.3	.39	.11	4592.6	-5177.4
5/6	26.0	.34	.15	6570.4	-7731.4
Full	37.5	.35	.11	5453.8	-4556.1

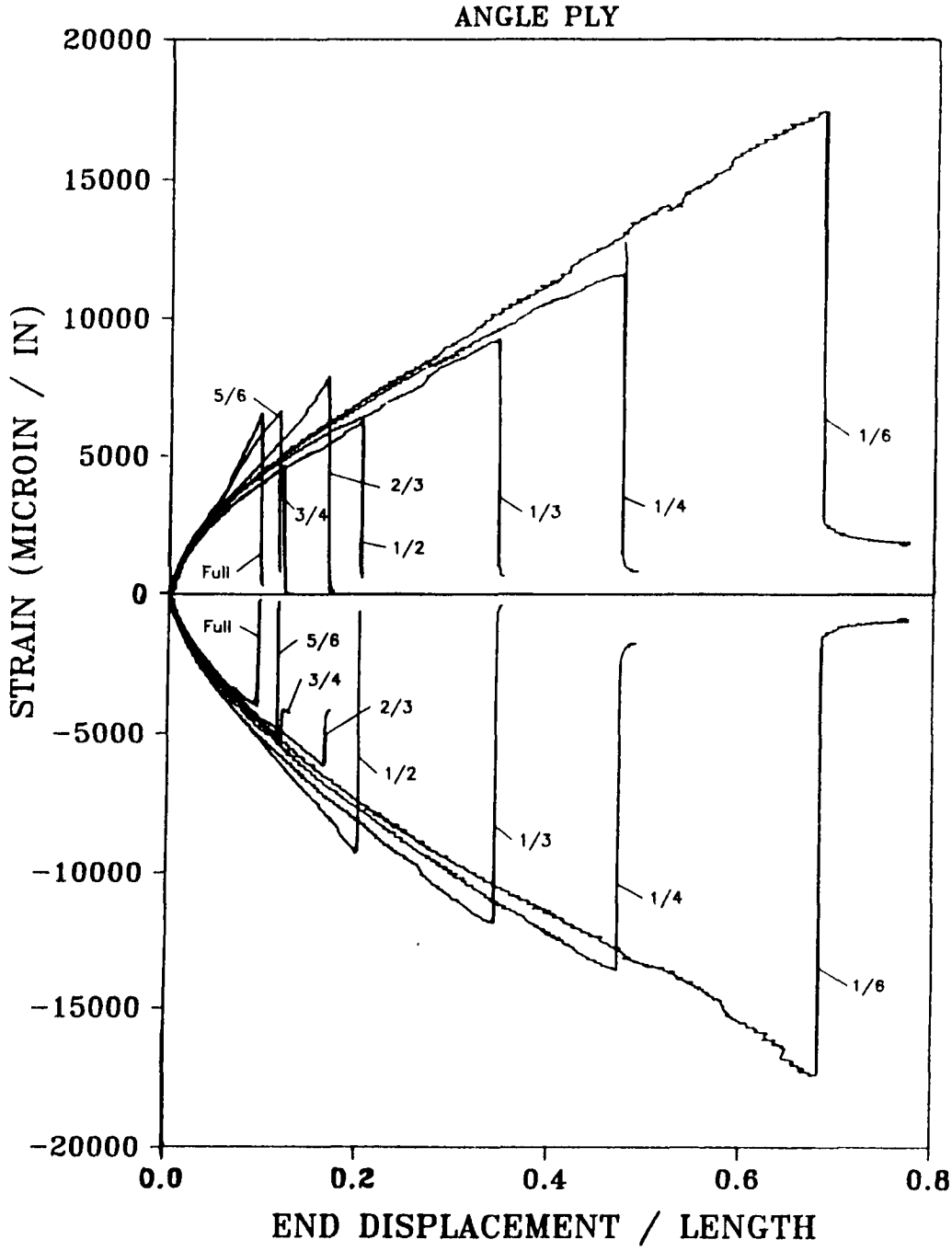

Figure 6-11. Midpoint strain versus end displacement/length experimental results for angle ply 1/6 through full scale model beams.

sides of each beam at midspan. The data shown in Figure 6-11 indicate that the strain response of angle ply beams does not scale in a consistent manner for large deflections. The tensile strain readings for the full, 5/6, and 2/3 scale beams suggest a sudden increase in beam stiffness which is not observed for the other scale model beams. This stiffening effect occurs at end displacement ratios where the load data indicate a loss of beam stiffness (Figure 6-10). The effect is not seen in the compression side strain for those same beams. Strain data from compression side gages for the 1/6, 1/4, 1/3, and 1/2 scale beams indicate that strain magnitudes increase as the size of the beam increases. However, the compressive strain data for the 2/3, 3/4, 5/6, and full scale beams do not follow this trend. The tensile strain data from the 1/6, 1/4, 1/3, and 1/2 scale beams show the opposite behavior. Strain magnitudes tend to increase as the size of the beams decreases. However, the tensile strain data for the 2/3, 3/4, 5/6, and full scale beams indicate that this trend is not consistent for the larger scale model beams.

Although the data are not as consistent, the failure strains listed in Table 6-2 show that the angle ply laminates exhibit the same trend as the unidirectional beams that failure strains increase as beam size decreases. However, unlike the unidirectional beams, the large difference in compression and tensile side strain magnitudes was not observed. To illustrate this, Figure 6-12(a) contains a plot of the tensile strain and the absolute value of the compressive side strain versus end displacement ratio for the 1/6 scale angle ply beam. Little difference in strain magnitudes is seen. Figure 6-12(b) shows that the maximum difference in strain magnitudes is about 5 per cent and that the compression strain magnitude is actually less than the tensile strain magnitude for end displacement ratios greater than 0.4.

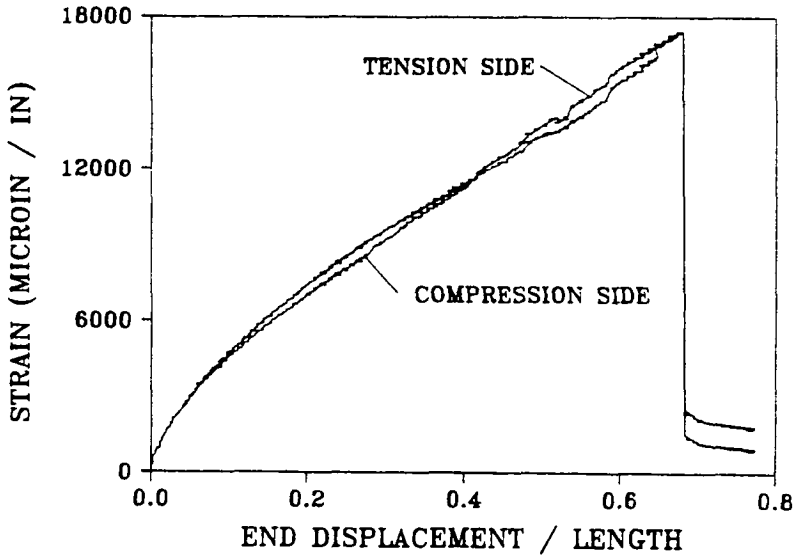

(a) Compressive and tensile midpoint strain-displacement results for a 1/6 scale angle ply beam.

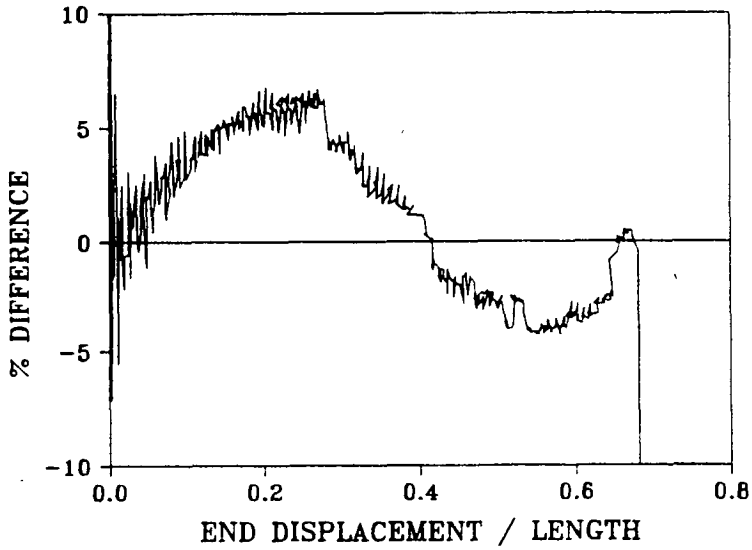

(b) Percent difference in compressive and tensile strain magnitudes versus displacement ratio for a 1/6 scale angle ply beam.

Figure 6-12. Midpoint strain-displacement data for angle ply 1/6 scale model beam.

6.2.3 Comparison of Experiment with Analysis

The large deflection "elastica" beam solution and the DYCAST finite element analysis are compared with the normalized load response for the 1/6 and full scale angle ply beams in Figure 6-13. Agreement between analysis and experiment is excellent up to a load ratio of 0.4. At this point, the full scale beam experiences a loss in stiffness which is reflected in the load response. The same effect occurs for the 1/6 scale beam, but at a slightly higher load ratio. Also, the reduction in stiffness is not as severe in the 1/6 scale beam and the load response flattens until ultimate beam failure occurs at an end displacement ratio of 0.67. Since neither the beam solution or DYCAST possessed the capability to predict and model the effect of matrix cracking on beam stiffness, the analytical results yielded a much stiffer response for load ratios higher than 0.4.

It is possible that the load response behavior of the angle ply laminates is influenced by width-wise effects which are not accounted for in the beam solution or DYCAST analysis. Sensmeier [38] found that it was necessary to include width-wise degrees-of-freedom in his finite element model to successfully predict the load and strain response of laminates with large bend-twist coupling terms. Since the angle ply laminates have large D_{16} and D_{26} bending stiffnesses, a model of the eccentrically-loaded 1/6 scale angle ply beam was developed for the MDS2DB finite element code. Load-deflection results are presented in Figure 6-14 from the analysis using linear material properties and experiment. It is evident from the plot that the MDS2DB model grossly overpredicts the load response of the 1/6 scale angle ply beam. The possible influence of width-wise effects on the load response is masked by the loss of beam stiffness due to matrix cracks. A MDS2DB model of the angle ply beam was run using nonlinear material properties and initial results showed that the load response was less stiff than the linear case. However, due to computation difficulties the model would not produce results for end displacement ratios greater than 0.1.

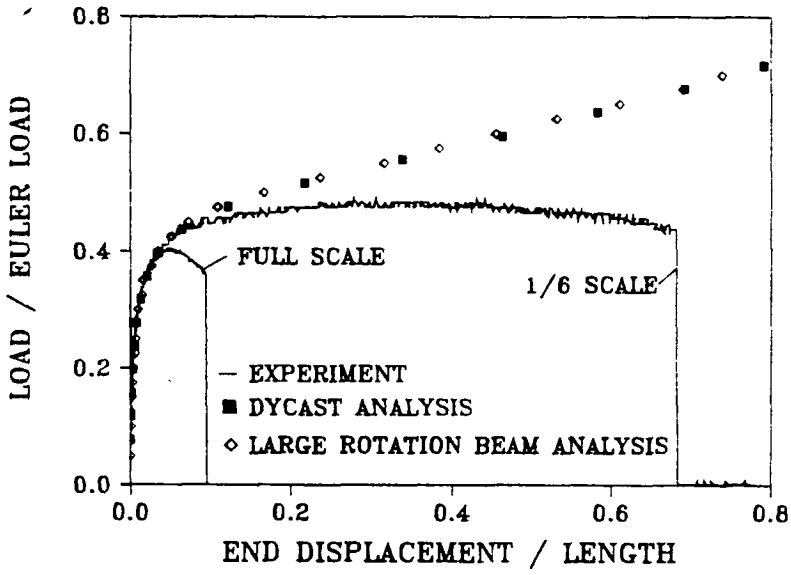

Figure 6-13. Comparison of large deflection beam analysis and DYCAST load-displacement predictions with angle ply 1/6 and full scale beam experimental response.

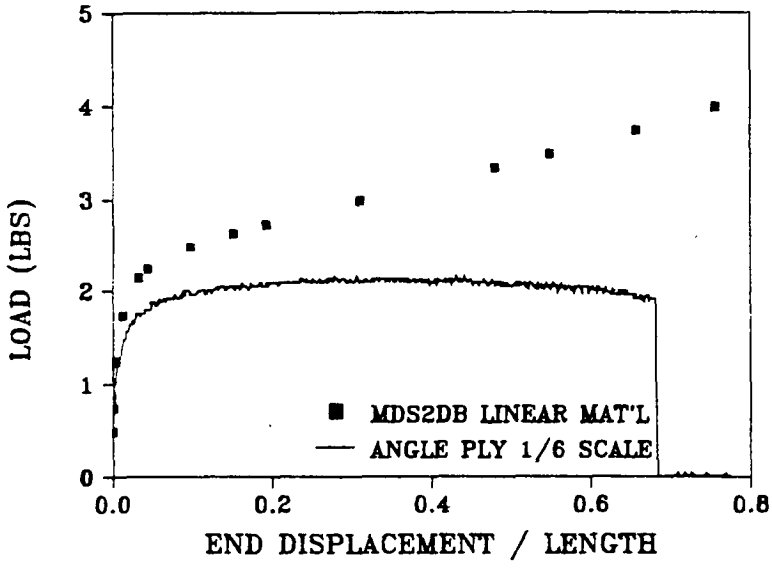

Figure 6-14. Comparison of MDS2DB analysis with angle ply 1/4 scale model beam load-displacement experimental response.

A comparison of the large deflection beam solution and DYCAST analytical predictions for midpoint surface strain with the experimental data from the 1/6 and full scale angle ply beams is presented in Figure 6-15. The analyses do not predict the stiffening effect seen in the full scale tensile gage. It is assumed that this behavior is anomalous and due to partial failure of the gage. In general, excellent agreement is obtained between the analyses and experimental data. The analyses tend to overpredict the tensile side strain and underpredict the compressive side strain for end displacement ratios greater than 0.3 by approximately 15%. It is interesting to compare this result with the load-deflection data shown in Figure 6-13. It is observed that the stiffness of the beam is significantly degraded for end displacement ratios greater than 0.05 resulting in poor agreement between the analyses and experimental data. However, the analyses predict the strain response well. This contradiction may be explained by the local nature of strain gage measurements compared to the global nature of the load data. A strain gage measures the response of the local region of material where it is attached. The gage measures changes in location of points on the surface of the material and is affected by the integrity of the material only if a crack or material flaw is near to the point of attachment of the gage. However, the load data is influenced by any change in stiffness in the beam. The integrated effect of local variations in stiffness along the length of the beam is reflected in the load-deflection response.

Figure 6-16 shows the comparison of the midpoint strain results from the MDS2DB analysis of the 1/6 scale angle ply beam with the experimental data. The MDS2DB analysis overpredicts the compression side strain and underpredicts the tension side strain slightly. The inclusion of width-wise degrees of freedom in the MDS2DB model does improve the prediction of compressive strain for the angle ply laminate.

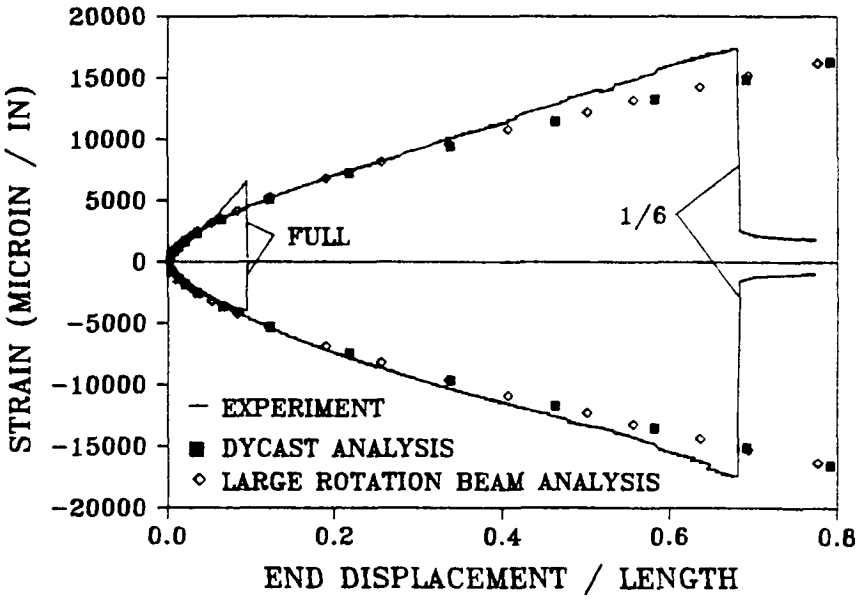

Figure 6-15. Comparison of large deflection beam analysis and DYCAST strain-displacement predictions with angle ply 1/6 and full scale beam experimental response.

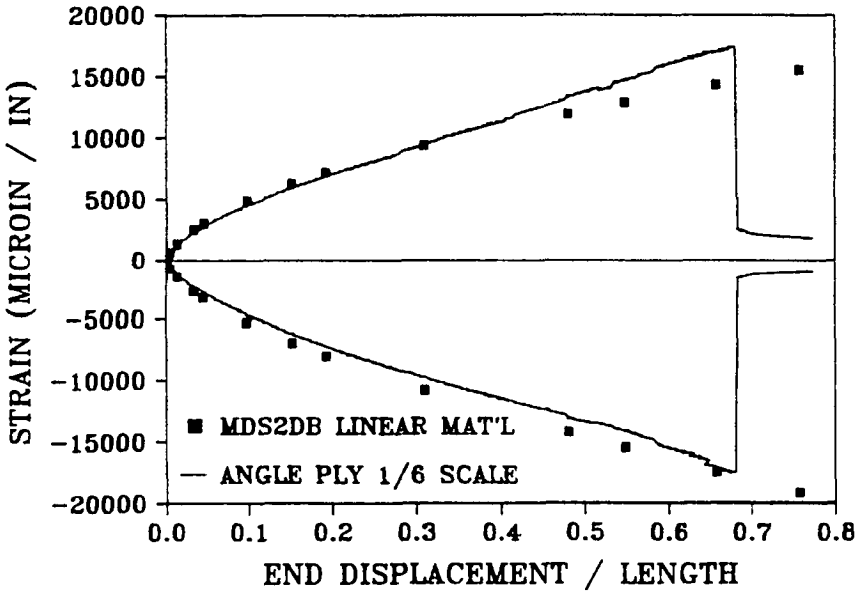

Figure 6-16. Comparison of MDS2DB analysis with angle ply 1/6 scale model beam strain-displacement experimental response.

6.2.4 Failure Mechanisms

Figure 6-17 contains a photograph of the three replicate 1/3 scale angle ply beams tested statically to failure under eccentric axial load. Failure occurred by transverse matrix cracking along 45 degree fiber directions. There was no evidence of fiber fracture in any of the failed beams. In general, the major fracture event which resulted in separation of the beam was located just below the midpoint of the beam, as indicated in Figure 6-17. Since the magnitude of the bending moment is greatest at the midpoint of the beam, the failure location was expected there. The deviation may be due to a local stiffening effect at the center of the beam caused by the attachment of strain gage rosettes on both sides of the beam. Failure mechanisms are consistent between each of the replicate beams as shown in Figure 6-17. Figure 6-18 shows that the same failure mechanism was evident for all of the scale model angle ply beams. Thus, even though the failure mechanisms are much different for the angle ply and unidirectional beams, for both laminates the mode of failure is not dependent on specimen size.

6.3 Cross Ply Beams

6.3.1 Load-Deflection Response

The normalized load-deflection data for the scale model cross ply beams is shown in Figure 6-19. The load response curves for each of the beams (1/6 through full scale) fall on a single curve. This implies that the response scales for both small and large deflections. In fact, the load-deflection response for the cross ply laminates is nearly identical to the unidirectional response. This is expected since the 90 degree core plies carry little load and do not contribute significantly to the bending stiffness of the beams. However, the scale effect in the failure behavior of this family of laminates is dramatic. The effect is even more severe for the cross ply laminates

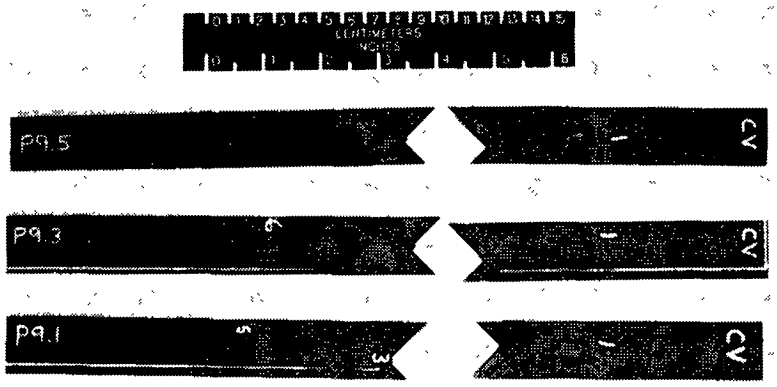

Figure 6-17. Photograph of failed angle ply 1/3 scale beams, three replicates.

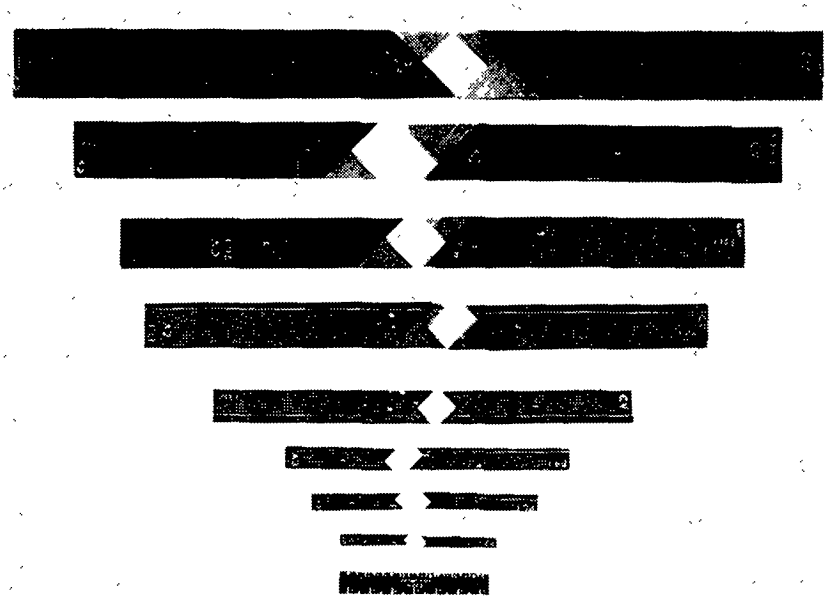

Figure 6-18. Photograph of a set of failed angle ply beams 1/6 through full scale.

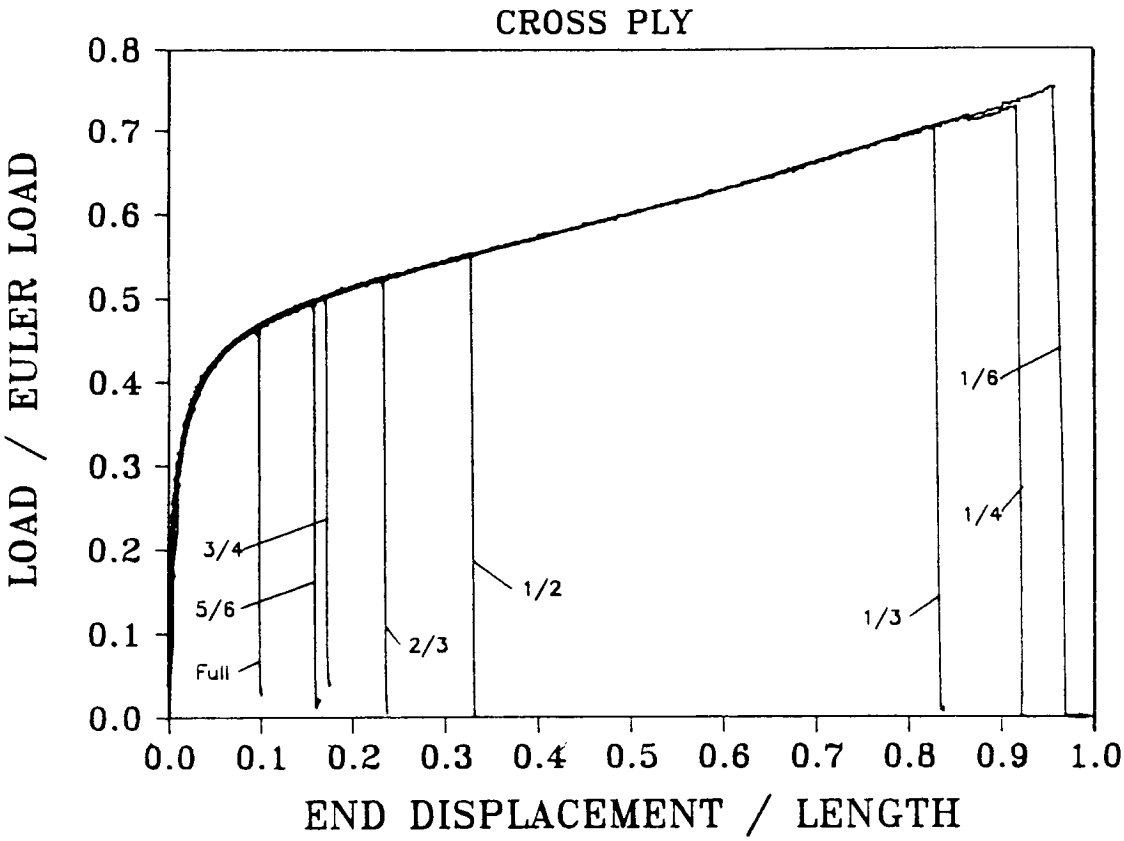

Figure 6-19. Normalized load versus end displacement experimental results for cross ply 1/6 through full scale model beams.

than for the unidirectional laminates. The 1/6 scale cross ply beam fails at an end displacement ratio of 0.96 which is approximately 10 times the value for the full scale beam. Unlike the unidirectional beams where the failure locations were fairly evenly spaced between the 1/6 and full scale beams, a large gap is observed in the failure locations for the cross ply beams. The gap occurs between the 1/3 and 1/2 scale model beams. It is obvious from the large difference in failure loads and locations between the 1/6 and full scale beams shown in Figure 6-19 that the 90 degree plies in the cross ply laminates cause a severe reduction in strength as the size of the beam increases. Table 6-3 lists the average values of failure load, load ratio, end displacement ratio, and strain for the scale model cross ply beams. In general, the failure load ratios, end displacement ratios, and strains increase as the size of the beam decreases.

6.3.2 Strain-Deflection Response

The scaled response seen in the load-deflection curves is also reflected in the strain-deflection data for the scale model cross ply beams, as shown in Figure 6-20. The strain responses do not fall on a single curve, but the variation in strain magnitudes is less than 6% for any value of end displacement ratio. Ultimate failure of the 1/6 scale beam is indicated by the compression gage since the tensile gage failed prematurely. Otherwise, the large scale effect in failure behavior which is observed in the load-deflection response is also evident in the strain behavior. The 1/6 scale beam fails at a strain level 5 times higher than the failure strain of the full scale beam.

The failure strain data listed in Table 6-3 indicate that the cross ply laminates exhibit a difference in compression side and tensile side strain magnitudes similar to the unidirectional beams. Figure 6-21(a) contains a plot of the absolute value of the compression strain and the tensile strain versus end displacement ratio for the 1/4 scale cross ply beam. The percentage difference in strain magnitudes is plotted in Figure 6-21(b). These figures show

Table 6-3. Average failure loads, displacements, and strains for scaled cross ply beams.

CROSS PLY					
Scale Factor	Failure Load (lbs)	Failure Load Ratio	End Disp. Ratio	Failure Strain Tension (microin/in)	Failure Strain Compression (microin/in)
1/6	17.1	.76	.96	gage failures	-21946.5
1/4	31.3	.75	.95	16729.6	-20963.3
1/3	54.9	.71	.84	15026.6	-18940.5
1/2	99.6	.56	.35	8637.6	-10136.7
2/3	177.6	.53	.26	7207.7	-8305.4
3/4	219.3	.51	.19	5925.6	-6762.2
5/6	274.9	.50	.16	5370.6	-6149.3
Full	345.1	.47	.10	3901.0	-4223.6

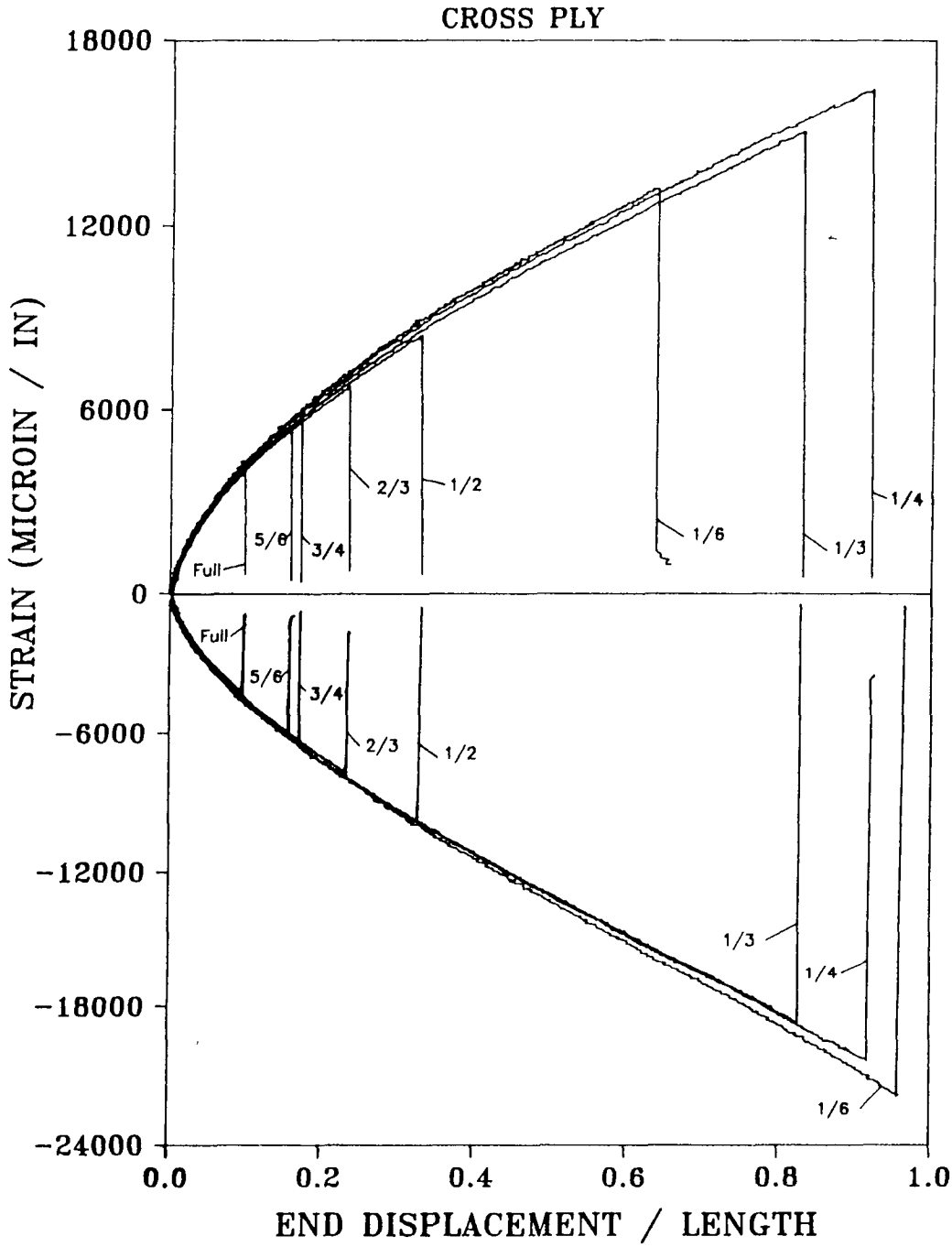

Figure 6-20. Midpoint strain versus end displacement/length experimental results for cross ply 1/6 through full scale model beams.

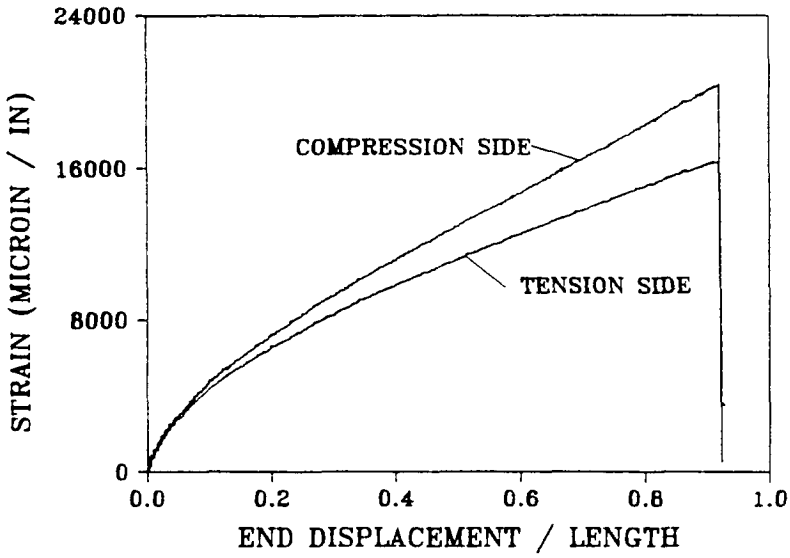

(a) Compressive and tensile midpoint strain-displacement results for a 1/4 scale cross ply beam.

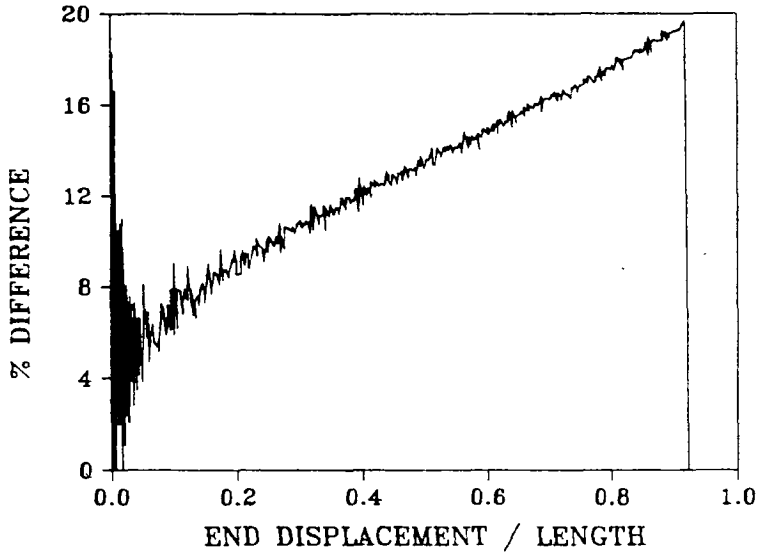

(b) Percent difference in compressive and tensile strain magnitudes versus end displacement ratio.

Figure 6-21. Midpoint strain-displacement data for cross ply 1/4 scale model beam.

that the difference between compression and tensile strain magnitudes increases linearly as the end displacement increases, and, at the point of failure, is approximately 20%. Sensmeier [38] attributed the difference between compression and tensile side strain magnitudes to nonlinear effects, possibly nonlinear material properties or the influence of transverse or "anticlastic" curvature. Using his analysis code, Sensmeier showed that laminates which have a large D_{12} bending stiffness term which couples longitudinal and transverse curvature exhibit a high degree of anticlastic curvature. Unfortunately, no transverse gages were applied across the width of the beams studied in this investigation to confirm these predictions. However, the cross ply 1/4 scale beam does show a greater difference in strain magnitudes than the 1/4 scale unidirectional beam. It also has a larger D_{12} bending stiffness than the unidirectional beam. This observation tends to support the conclusion that width-wise effects contribute to the difference in strain magnitudes between the compression and tension sides of the beams.

6.3.3 Comparison of Experiment with Analysis

Figure 6-22 contains the 1/4 and full scale load-deflection experimental data plotted with the load predictions from the large deflection beam analysis and DYCAST. Agreement between the analyses and experiment is excellent, especially for end displacement ratios less than 0.5. For ratios higher than 0.5, the analyses tend to slightly overpredict the load response. As the deformations become increasingly large, the 90 degree core plies tend to develop transverse matrix cracks which degrade the stiffness of the beam. Neither the large deflection beam solution or the DYCAST finite element analysis can model the reduction in beam stiffness due to matrix cracks. Consequently, the analyses overpredict the load response when damage of this type occurs in the beam.

Load response predictions from the MDS2DB finite element code are presented in Figure 6-23 along with the 1/4 scale cross ply load-displacement experimental data. Both linear and nonlinear material cases were modeled to examine the effect of constitutive behavior on the load response. Both the linear and nonlinear models significantly overpredict the load-displacement curve. The incorporation of nonlinear material properties alters the load response only slightly. The discrepancy between the MDS2DB analysis and experiment is difficult to explain. However, if the MDS2DB load data are normalized by the Euler load (54.26 lbs) which is calculated using lamination theory, and the experimental data are normalized by the Euler load (41.03 lbs) which is found empirically using the matching technique, then the analysis and experiment show excellent agreement. This observation implies that the bending stiffnesses derived for the beam based on lamination theory are not accurate.

Figure 6-24 shows the comparison between the large deflection beam and DYCAST analyses and the 1/4 and full scale strain-deflection experimental data. The agreement is generally quite good, especially for end displacement ratios less than 0.4. As the deflections become large, both analyses tend to overpredict the tensile side strain and underpredict the compression side strain. This is not unexpected since the compression and tension side strain magnitudes diverge for increasing end displacement ratios, as depicted in Figure 6-21(a) and (b). Better agreement is found when the MDS2DB finite element model is compared with the experimental results from the 1/4 scale cross ply beam, as shown in Figure 6-25. The MDS2DB model which utilized nonlinear material properties predicted both tensile and compressive side strain magnitudes well, even for very large end displacement ratios. Agreement is only slightly poorer for the model using linear material properties. A comparison of the data presented in Figures 6-24 and 6-25 illustrates the importance of including width-wise effects for successfully predicting the strain response of cross ply laminates.

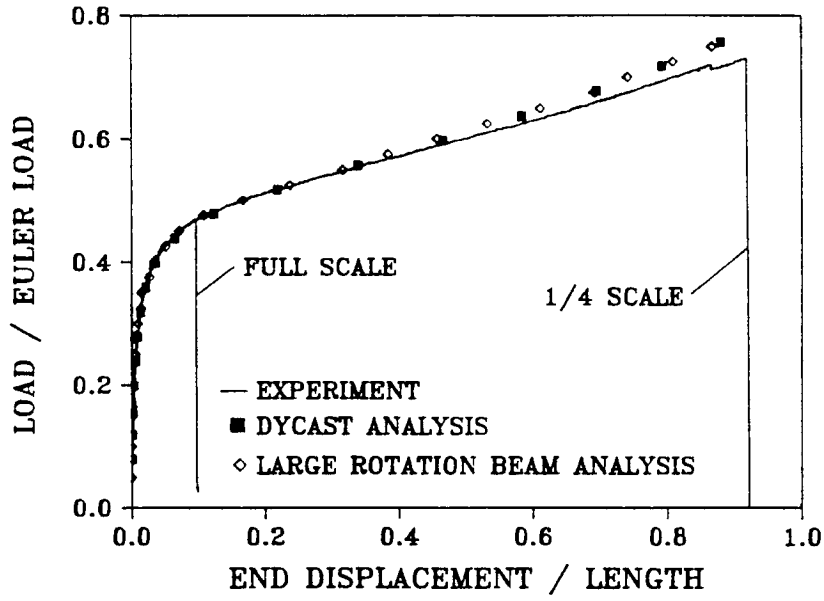

Figure 6-22. Comparison of large deflection beam analysis and DYCAST load-displacement predictions with cross ply 1/4 and full scale beam experimental response

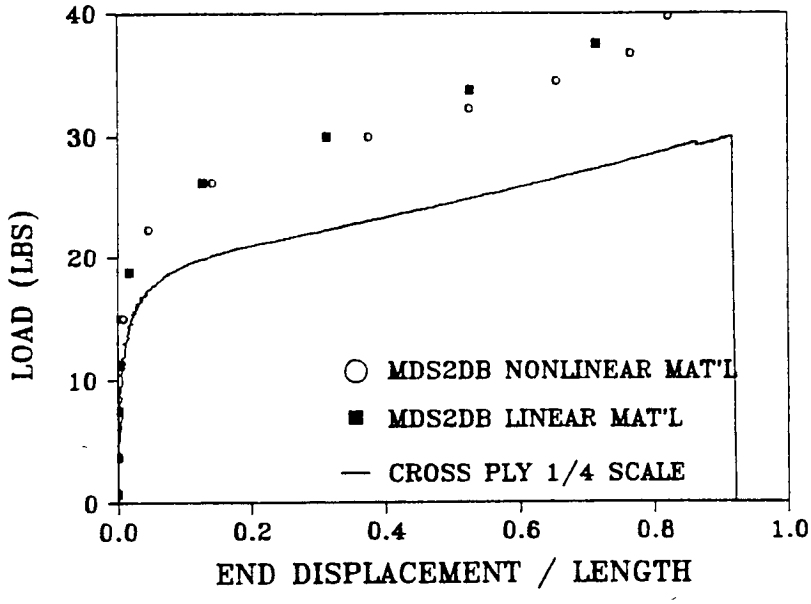

Figure 6-23. Comparison of MDS2DB analysis with cross ply 1/4 scale model beam load-displacement experimental response.

6.3.4 Failure Mechanisms

The cross ply laminates exhibited combined failure mechanisms of transverse matrix cracking, delamination, and fiber fracture, as shown in Figure 6-26 which contains a photograph of the three 1/3 scale cross ply beams tested statically to failure. As the cross ply beams experience large deflections and rotations, the 90 degree plies located at the center of the laminate developed matrix cracks. These cracks were evenly spaced along the length of the beam and resulted in uniform pieces of debris, some of which are shown in Figure 6-27 for the 5/6 scale beam. Ultimate failure of the cross ply beams was caused either by fiber fractures in the 0 degree plies at the midspan of the beam, or by a large delamination which developed between the 0 and 90 degree layers. Figure 6-26 shows that failure modes were consistent between replicates of beams having the same size and lay-up. However, photographs of a complete set of scale model cross ply beams (Figure 6-27) indicate that the smaller scaled beams showed more damage than the full scale beam. The 1/6, 1/4 and 1/3 scale beams failed by matrix cracking, longitudinal splitting, delamination, and ultimately fiber fractures at the center of the beam. Starting with the 1/2 scale beam, no fiber fractures were observed for the larger scale model beams. This finding implies that the large gap between failure locations which was seen in Figures 6-19 and 6-20 between the 1/3 and 1/2 scale beams represents a transition in failure mechanisms. Consequently, there is a size effect in the failure mode of cross ply laminates.

6.4 Quasi-Isotropic Beams

6.4.1 Load-Deflection Response

The load-deflection response of the scale model quasi-isotropic beams is shown in Figure 6-28. The data fall on a single curve for

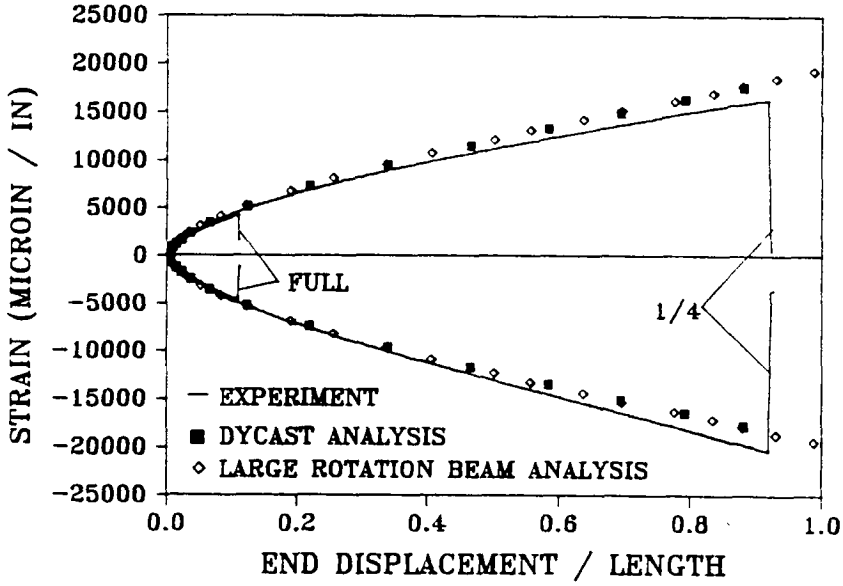

Figure 6-24. Comparison of large deflection beam analysis and DYCAST strain-displacement predictions with cross ply 1/4 and full scale beam experimental response.

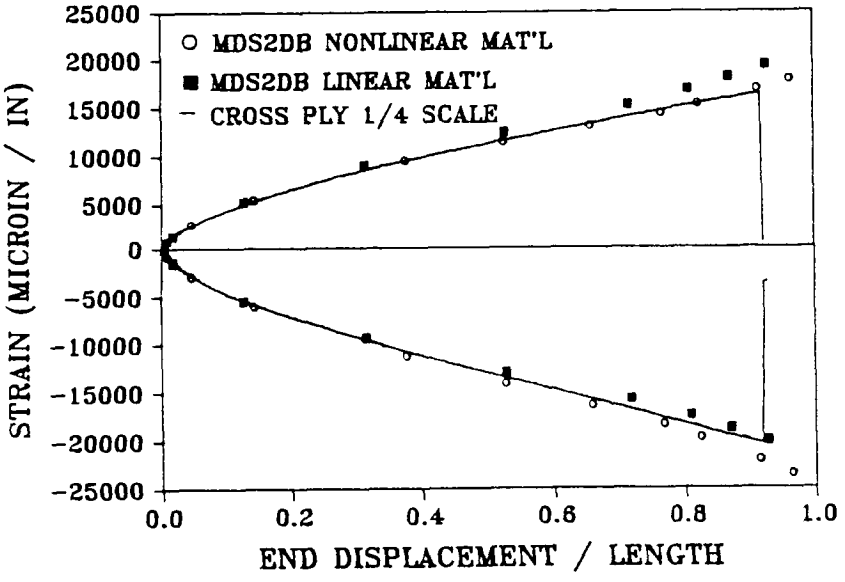

Figure 6-25. Comparison of MDS2DB analysis with cross ply 1/4 scale model beam strain-displacement experimental response

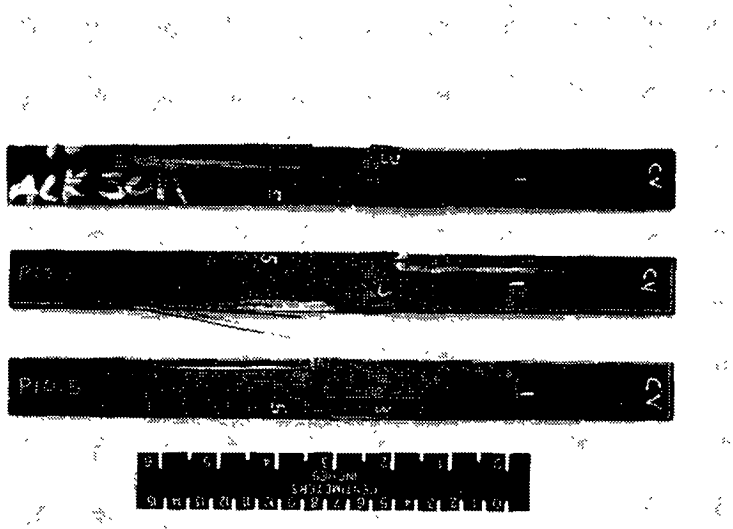

Figure 6-26. Photograph of failed cross ply 1/3 scale beams, three replicates.

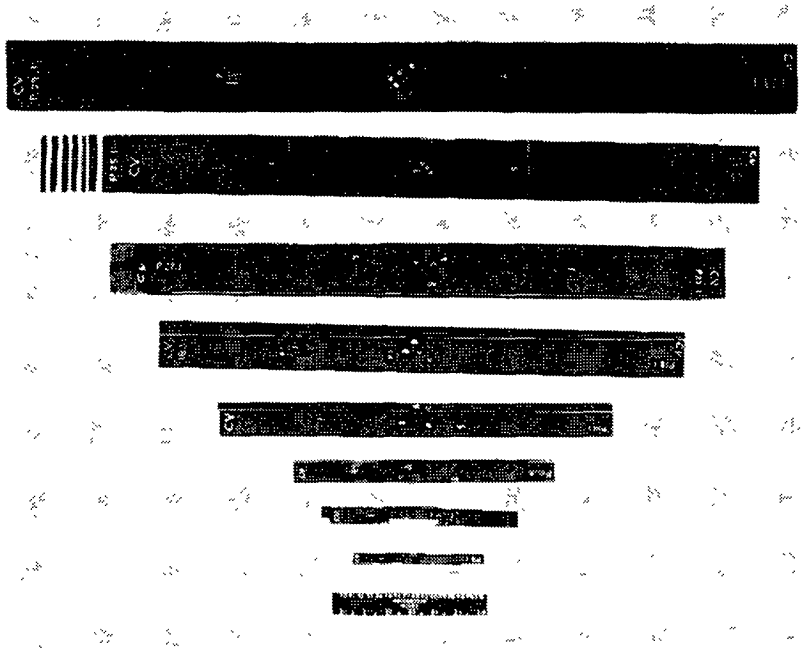

Figure 6-27. Photograph of a set of failed cross ply beams 1/6 through full scale.

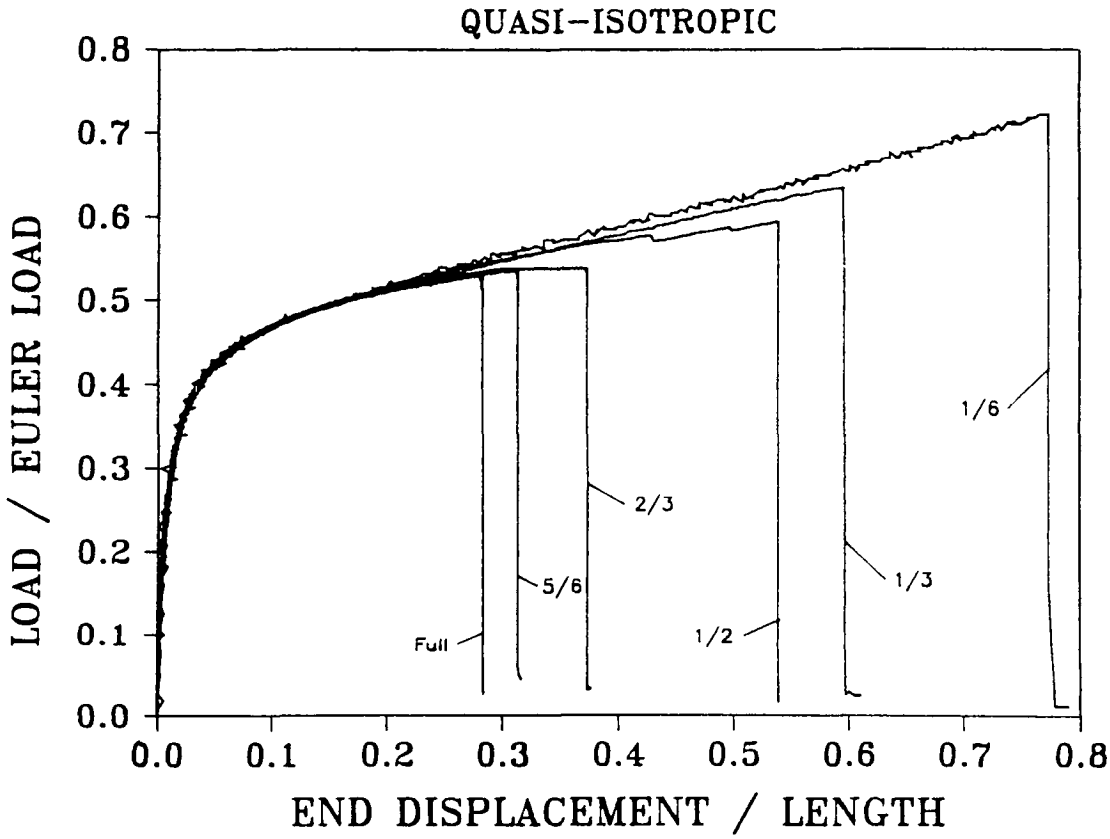

Figure 6-28. Normalized load versus end displacement experimental results for quasi-isotropic 1/6 through full scale model beams.

end displacement ratios less than 0.2 and load ratios less than 0.5 which indicates that the load response scales in this region. For greater values of load and displacement, the smaller scale model beams exhibit a stiffer load-deflection response than the larger scale beams. The deviation from scaled response is not as dramatic as that observed for the angle ply beams and appears to be caused by damage which develops in the larger beams and results in a reduction in beam stiffness. The average failure loads, load ratios, end displacement ratios, and strains are listed in Table 6-4 for the quasi-isotropic beams. The scale effect in strength which was noted for the unidirectional, angle ply, and cross ply laminates is also seen for the quasi-isotropic beams. The 1/6 scale beam fails at a load ratio which is 40% higher than the full scale beam value and at an end displacement ratio approximately three times the value for the full scale beam. The failures for the scale model beams are fairly evenly spaced between the 1/6 and full scale, i.e., there is no apparent gap in failure locations as was observed for the cross ply beams.

6.4.2 Strain-Deflection Response

The strain-deflection response of the quasi-isotropic beams is shown in Figure 6-29 for one of each of the scale model beams tested statically to failure. The results indicate that the strain response does not scale. The curves of the different scale model beams deviate from one another for end displacement ratios greater than 0.1. On the tensile side, the strain response is bounded by the 5/6 scale beam which exhibits the greatest strain magnitude for a particular value of end displacement ratio, and the full scale beam which exhibits the least strain magnitude. At failure, the variation in strain is 15% between the 5/6 scale beam and the full scale beam. On the compression side, the strain response is bounded by the 2/3 and full scale beam responses which show the greatest strain magnitude for a given end displacement ratio, and by the 1/6 scale

Table 6-4. Average failure loads, displacements, and strains for scaled quasi-isotropic beams.

QUASI-ISOTROPIC					
Scale Factor	Failure Load (lbs)	Failure Load Ratio	End Disp. Ratio	Failure Strain Tension (microin/in)	Failure Strain Compression (microin/in)
1/6	7.0	.73	.80	14349.1	-17039.8
1/3	24.1	.62	.53	10583.2	-14516.3
1/2	51.9	.60	.59	gage failures	-14853.7
2/3	84.4	.54	.37	9114.3	-11578.6
5/6	131.1	.54	.31	7759.9	-9964.2
Full	187.3	.53	.29	6875.9	-9511.7

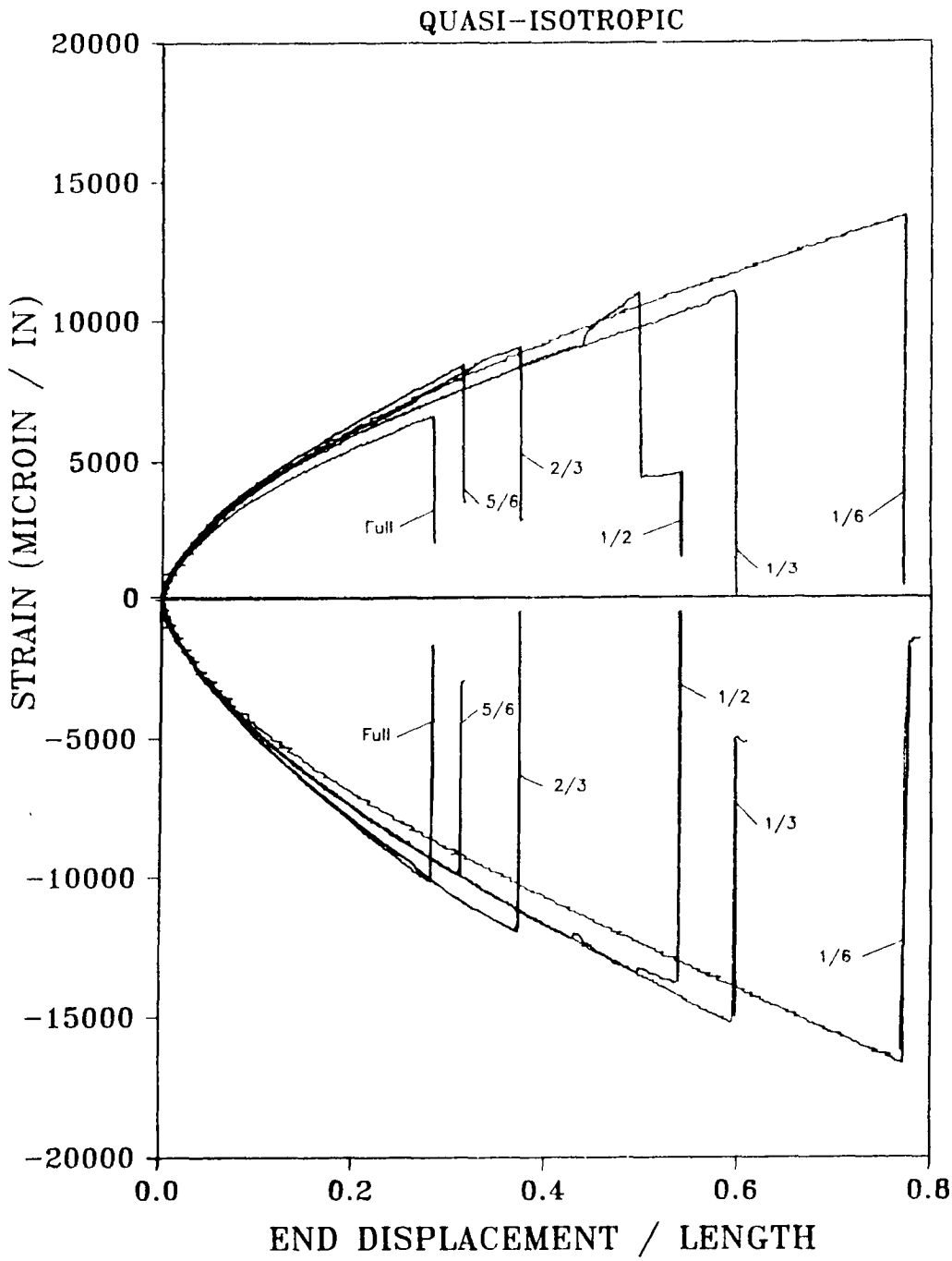

Figure 6-29: Midpoint strain versus end displacement/length experimental results for quasi-isotropic 1/6 through full scale model beams.

beam response which has the least strain magnitude. At failure, the difference in strain magnitudes between the full scale beam and the 1/6 scale beam is 18%. In general the strain data do not indicate that the larger scale model beams are experiencing any damage, as was indicated in the load-deflection responses shown in Figure 6-28. However, the strain response of the 1/2 scale beam does show that a partial failure of the beam occurs on the tensile side near the attachment of the gage. The scale effect in strength which is seen in the load-deflection response of Figure 6-28 is also reflected in the strain-deflection response of Figure 6-29 and in the failure data listed in Table 6-4. The 1/6 scale quasi-isotropic beam fails at a strain magnitude which is twice the value for the full scale beam.

The strain data listed in Table 6-4 also indicate that tensile strain magnitudes are less than compression strain magnitudes at the midspan of the beam. To illustrate the difference, the absolute value of the compression strain is plotted with the tensile strain in Figure 6-30 (a) for the 1/6 scale quasi-isotropic beam. The percentage difference in strain magnitudes is plotted as a function of end displacement ratio in Figure 6-30 (b). These figures show that the tensile and compression strain magnitudes begin to deviate from one another at an end displacement ratio of 0.1, and they continue to diverge in a linear fashion until ultimate beam failure. At that point the difference is approximately 17%.

6.4.3 Comparison of Experiment with Analysis

Figure 6-31 contains a plot of the load-deflection data from the 1/6 and full scale quasi-isotropic beams with analytical predictions from the large deflection beam solution and DYCAST finite element model. Excellent agreement is obtained between the analyses and experiment, even for very large end displacement ratios. The full scale beam load response begins to deviate from the analyses and the 1/6 scale beam response at an end displacement ratio of 0.2, near the ultimate failure location of the beam. This flattening of the

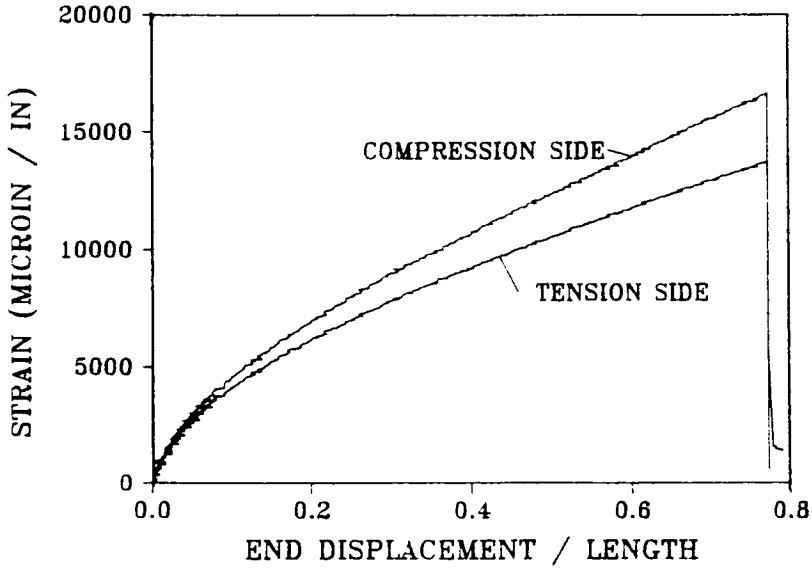

(a) Compressive and tensile midpoint strain-displacement results for a 1/6 scale quasi-isotropic beam.

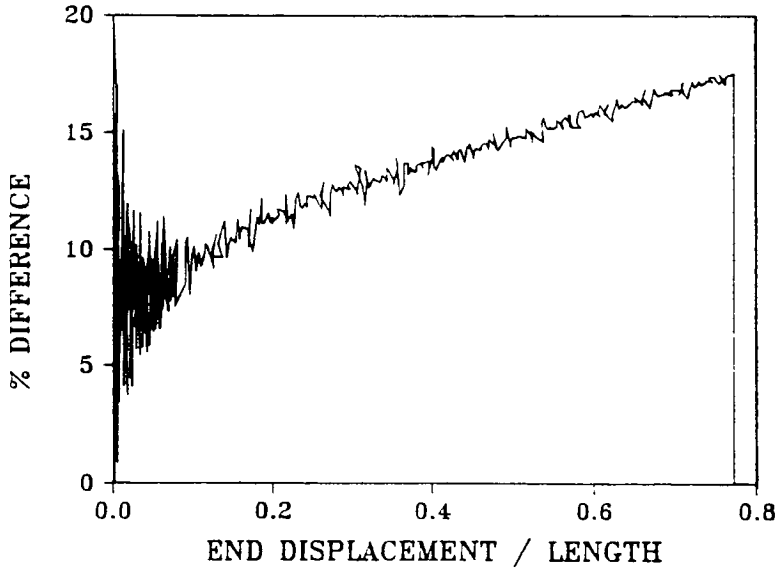

(b) Percent difference in compressive and tensile strain magnitudes versus end displacement ratio.

Figure 6-30. Midpoint strain-displacement data for unidirectional 1/6 scale model beam.

load response is attributed to damage which is occurring in the beam prior to failure. A similar effect is not seen in the 1/6 scale quasi-isotropic beam load response which is slightly stiffer than predicted by the analyses. No reduction in stiffness is observed in the 1/6 scale beam prior to failure. This observation implies that a scale effect in failure mechanism may occur for the quasi-isotropic laminates.

The quasi-isotropic laminates chosen for this investigation exhibit a moderate amount of bend-twist coupling through the D_{16} and D_{26} bending stiffness terms. Consequently, the influence of width-wise effects was investigated by modeling the 1/6 scale quasi-isotropic beam using the MDS2DB code with both linear and nonlinear material properties. Results from the MDS2DB analysis are plotted with the load data from the 1/6 scale beam experiment in Figure 6-32. The load response is not normalized by the Euler load for this comparison. The MDS2DB analysis overpredicts the load response by approximately 20%. Interestingly, this is the same difference observed between the Euler load calculated from linear material properties and lamination theory (11.72 lbs) and the Euler load based on the empirically determined bending stiffness (9.82 lbs) for the 1/6 scale quasi-isotropic beam. In fact, if the experimental load data are normalized by the empirically determined Euler load and the MDS2DB load data are normalized by the value determined from lamination theory, then the experimental curve falls between the two analytical predictions using linear and nonlinear material properties. Again, this implies that the bending stiffness of the beam as calculated from lamination theory is too high to accurately predict the large deflection response.

The strain response predictions from the large deflection beam solution and DYCAST are plotted in Figure 6-33 with the 1/6 and full scale quasi-isotropic strain data. Both analyses show excellent agreement with the compression strain of the 1/6 scale beam. However, the analyses overpredict the tensile strain. This is not unexpected since the quasi-isotropic beams exhibited a large

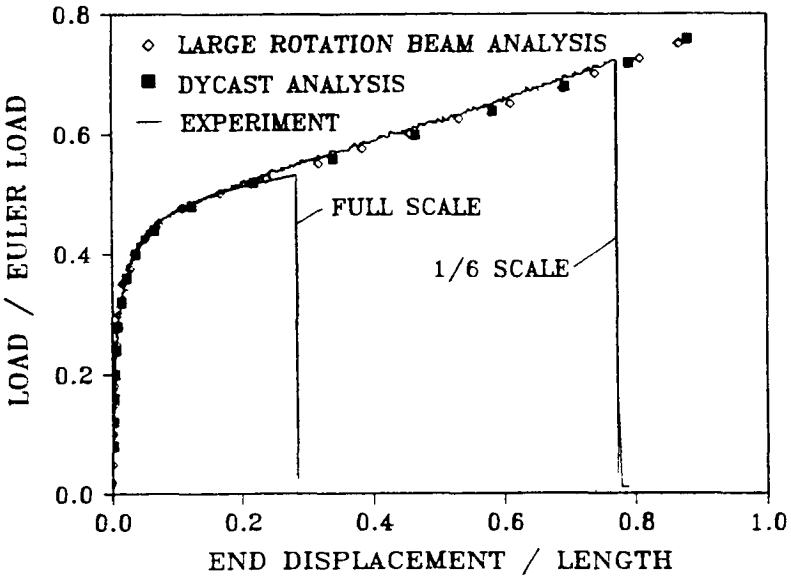

Figure 6-31. Comparison of large deflection beam analysis and DYCAST load-displacement predictions with quasi-isotropic 1/6 and full scale beam experimental response.

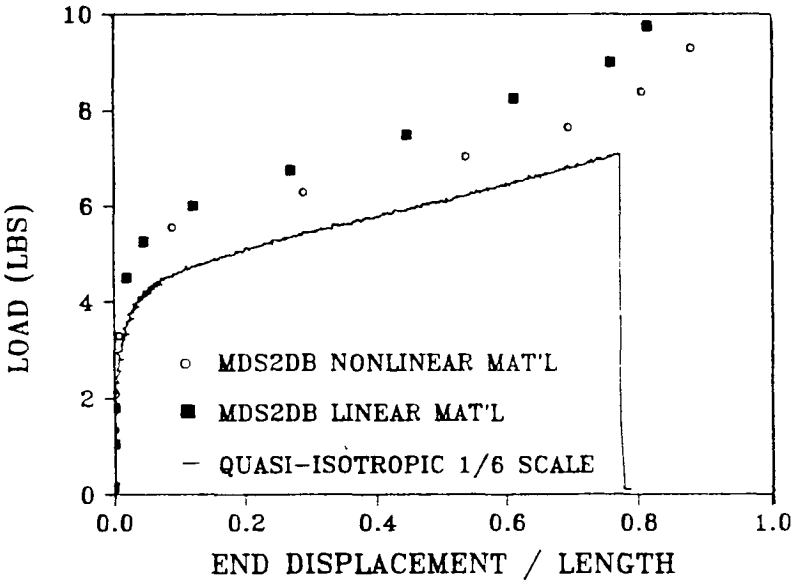

Figure 6-32. Comparison of MDS2DB analysis with quasi-isotropic 1/6 scale model beam load-displacement experimental response.

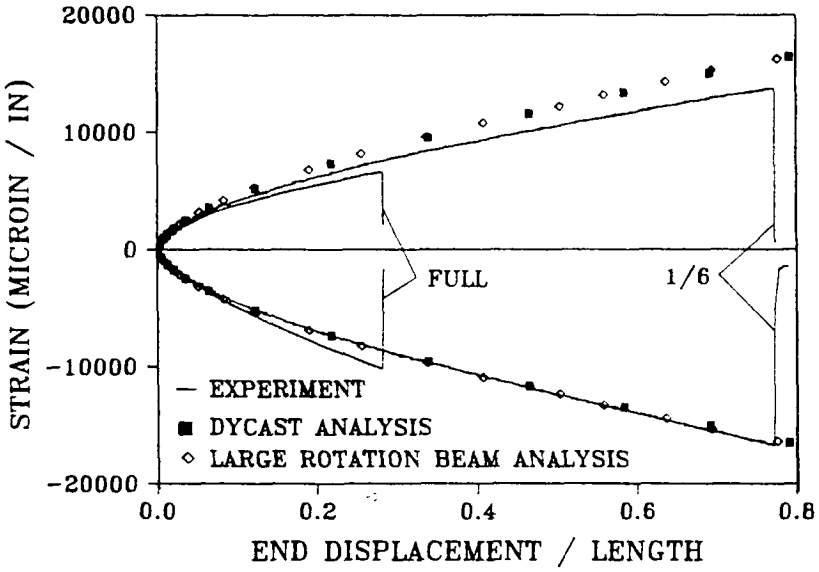

Figure 6-33. Comparison of large deflection beam analysis and DYCAST strain-displacement predictions with quasi-isotropic 1/6 and full scale beam experimental response

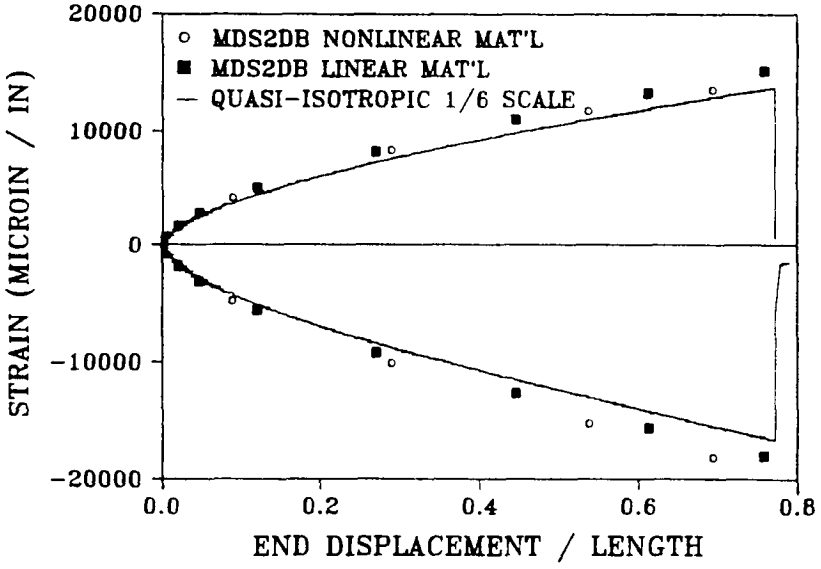

Figure 6-34. Comparison of MDS2DB analysis with quasi-isotropic 1/6 scale model beam strain-displacement experimental response.

difference between tensile and compressive strain magnitudes as shown in Figure 6-30. At failure, the tensile strain magnitude predicted by the analyses is 18% greater than the experimental value. Figure 6-34 shows the strain response predictions from the MDS2DB analysis using both linear and nonlinear material properties plotted with the 1/6 scale quasi-isotropic strain data. The MDS2DB analyses overpredict both the tensile and compressive strain response. Little difference is observed in the strain response predictions due to the inclusion of nonlinear material properties. As indicated in Figure 6-29, the strain responses for the various scale model quasi-isotropic beams do not scale for large end displacement ratios. Consequently, the strain response predicted by any of the three analysis techniques falls within the range of strain behavior observed for the scale model quasi-isotropic beams.

6.4.4 Failure Mechanisms

The quasi-isotropic beams failed through a combination of matrix cracking, delamination, and some fiber failures, as shown in Figure 6-35 which contains a photograph of the three replicate 1/3 scale beams tested statically to failure. Matrix cracks developed in the 45 degree layers and grew along lines parallel to the fibers. Delaminations were observed between the outer 45 degree plies and the adjacent 0 degree plies. Also, some fiber fractures were evident in the failed 1/3 scale beams. Although the photograph in Figure 6-35 does not give a good indication, the damaged quasi-isotropic beams were highly curved. The sequence of failure events occurred such that the outer 45 degree plies on the tensile side of the laminate peeled away from the 0 degree plies. This meant that the portion of the beam left intact was unsymmetric which resulted in the observed curvature. Figure 6-35 indicates that the three replicate 1/3 scale beams experienced the same mode of failure. Figure 6-36 shows a photograph containing a failed quasi-isotropic beam of each scaled size. The same failure mechanisms described for the 1/3 scale

Figure 6-35. Photograph of failed quasi-isotropic 1/3 scale beams, three replicates.

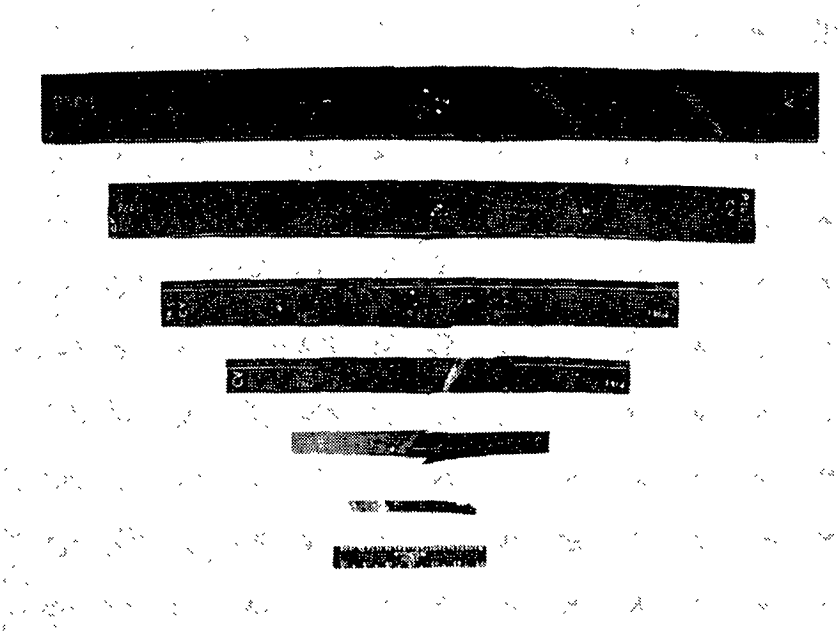

Figure 6-36. Photograph of a set of failed quasi-isotropic beams 1/6 through full scale.

beams are also evident for the larger and smaller scale beams. However, the 1/6, 1/3, and 1/2 scale model beams appear to have sustained more damage. The outer 45 degree plies are completely separated for these laminates and there is evidence of fiber fractures not seen in the larger beams. The failed smaller scale beams exhibited more curvature and twist than the larger beams.

6.5 Summary of Static Test Results

A comprehensive static testing program was performed to investigate scaling effects in the large deflection response and failure of graphite-epoxy composite beams. Experimental load-deflection and strain-deflection results were presented for each of the unidirectional, angle ply, cross ply, and quasi-isotropic laminate families tested. In addition, the experimental results were compared to a large deflection beam analysis and two finite element techniques. The observed failure mechanisms were described for each of the laminate families. The significant findings from the static testing program are highlighted in the following list.

(1). Success in achieving scaled load and strain response is highly dependent on the laminate stacking sequence and, in particular, is a function of the number of 0 degree plies in the laminate. No scaling effects were observed in the load and strain response of the unidirectional and cross ply laminates, even under severe deformations and rotations. However, the angle ply and quasi-isotropic laminates deviated from scaled response due to damage events which altered the beam stiffness. The effect was especially dramatic for the angle ply laminates which contain no 0 degree plies.

(2). A significant scale effect in strength was observed for all laminate families studied in this investigation. In general, the normalized loads, end displacements, and strains at failure increased as the size of the beam decreased from the full scale prototype to the 1/6 scale model. The scale effect in strength was particularly large

for the cross ply laminate family in which the 1/6 scale beam failed at a load ratio 1 1/2 times the value for the full scale beam, and at an end displacement ratio 10 times greater than the full scale beam. The importance of this result and a discussion of current techniques to predict the scale effect in failure are the subject of Chapter 8.

(3). Only the cross ply laminates exhibited a scale effect in failure mechanism, defined as a transition in failure mode based on the size of the beam. For the case of the cross ply laminates, the transition consisted of fiber fractures seen in the smaller scale model beams which were not evident in the larger scale model beams. The transition occurred between the 1/3 and 1/2 scale model beams and resulted in a large gap in the failure locations for these beams in the load-deflection data. No scale effect in failure mode was observed for the unidirectional, angle ply, and quasi-isotropic laminates.

(4). The one dimensional, large deflection beam analysis which was developed based on the "elastica" problem and the DYCAST finite element analysis predicted the load-deflection response well for the unidirectional, cross ply, and quasi-isotropic laminates. The angle ply laminates experienced damage which caused a reduction in beam stiffness. Neither the large deflection beam solution or DYCAST is capable of modeling the effect of progressive damage on beam stiffness and, thus, both analyses overpredicted the load response. In general, the strain response was well predicted by the analyses for all laminate families.

(5). The finite element code developed by Sensmeier [38] was used to investigate the importance of including width-wise degrees of freedom and nonlinear material properties in predicting the load and strain response of the laminates. The MDS2DB code consistently overpredicted the load response. However, the strain predictions using the nonlinear material capabilities of the code agreed well with experiment. The MDS2DB analysis was able to model the large difference in strain magnitudes between the tensile and compressive sides of the beam.

Chapter 7 - Dynamic Test Results

Results of the dynamic testing program are presented for the scale model unidirectional, angle ply, cross ply, and quasi-isotropic beams which were subjected to eccentric axial impact loads using an experimental procedure described in Chapter 3. Due to limitations of the test hardware, it was not possible to test all of the scaled sizes of beams. Consequently, tests were performed on 1/2, 2/3, 3/4, 5/6, and full scale beams only. The number of replicate tests which were conducted for each size and type of beam varied from as many as three to a single test. Consistency of the results between the replicates was good and a single, representative test was chosen for each size and type of beam for presentation of results.

In the following section, the load-time and strain-time histories for each of the laminate families are examined to identify scaling effects in the dynamic response. Also, a DYCAST finite element analysis is compared with experimental results. The DYCAST model was also used to predict the deformed shapes of the beam during impact. A qualitative damage assessment of the beams is made to characterize scaling effects in the mode of failure. Finally, the strain responses obtained from the dynamic tests are compared with results from the static tests for beams of the same size and laminate family.

7.1 Comparison of Full Scale and Scale Model Load Response

The prediction of prototype load response from the scale model experimental data is plotted with the actual full scale experimental data for each of the laminates tested in Figures 7-1 through 7-4. The scaling law derived in Chapter 2 indicates that impact force scales as λ^2 and that time scales as λ. Therefore, the scale model data were multiplied by the appropriate scale factors and plotted on the same graph with the full scale experimental data. Thus, the matching technique used to determine the beam bending stiffnesses was not

applied for the dynamic tests and the load data were not normalized by the Euler load. Results for the unidirectional, angle ply, cross ply, and quasi-isotropic laminates are shown in Figures 7-1 through 7-4, respectively.

Agreement between the unidirectional scale model load predictions and the full scale response is excellent, as shown in Figure 7-1. The scale model beams accurately predict load spikes, pulse duration, and sustained load. Results for the angle ply laminates are, in general, not as good. The 3/4 scale angle ply beam overpredicts the load spike by a factor of three, whereas the 1/2 scale beam underpredicts the load spike by approximately the same amount, as shown in Figure 7-2. The 2/3 scale angle ply test gives the best prediction of full scale load response, including initial load spike and pulse duration. The angle ply beams failed almost immediately on impact which made it difficult to determine a failure load or an accurate time for the failure event.

Figure 7-3 shows the load response results for the cross ply laminates. Typically, the cross ply scale model beams overpredict the prototype load spike, by as much as 25% for the 1/2 scale test. The 3/4 scale beam gives the best prediction of the full scale load spike. All scale model tests accurately predict the pulse duration. In general, however, the scale model beams exhibit a high second load peak following the initial load spike which is not seen in the full scale load response. The 1/2 and 2/3 scale model cross ply beams also exhibit a sustained load prior to failure which is not seen in the 3/4, 5/6, and full scale load responses. This behavior is indicative of a scale effect in strength since under scaled impact conditions the larger scale model beams (greater than 3/4 scale) fail upon impact while the smaller scale model beams are capable of sustaining the load prior to failure.

Results for the quasi-isotropic scale model beams are presented in Figure 7-4. The 1/2 and 5/6 scale model beams overpredict the full scale load spike by approximately 25%, however the 2/3 scale beam test underpredicts the full scale load spike value. The pulse

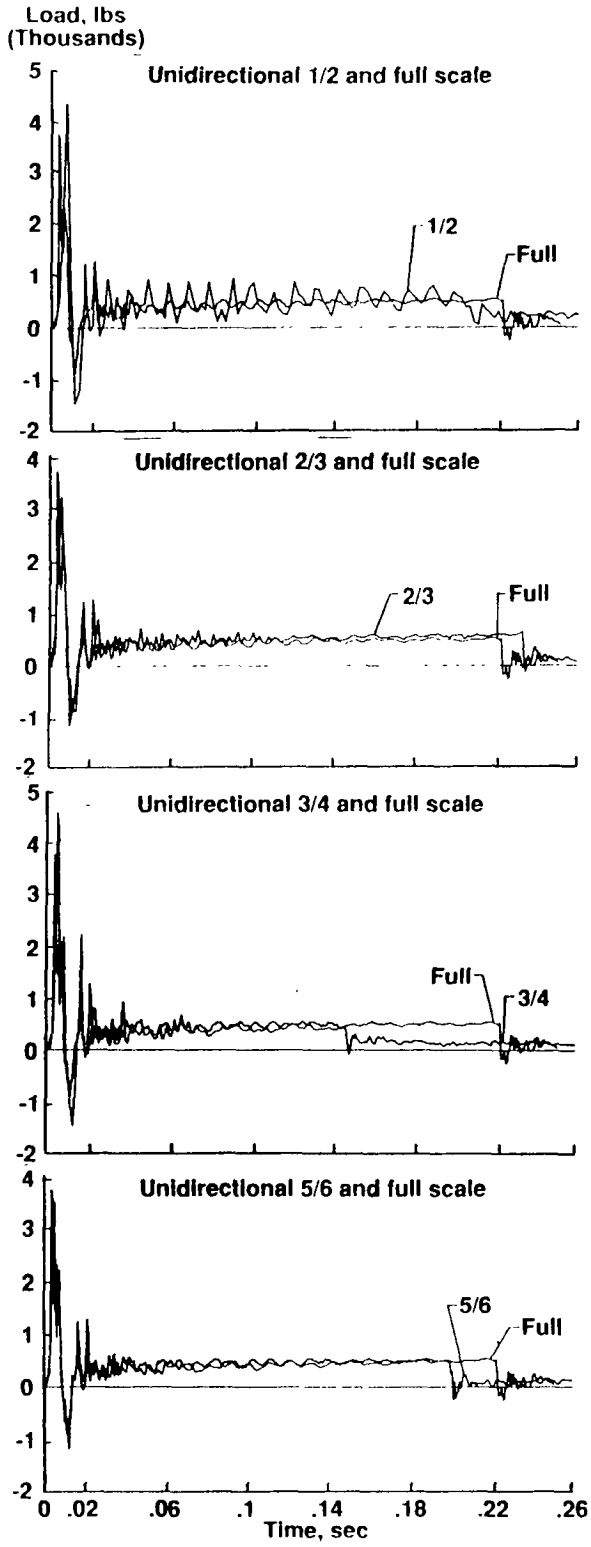

Figure 7-1. Load versus time plots for comparison of scale model predictions of full scale behavior of unidirectional beams.

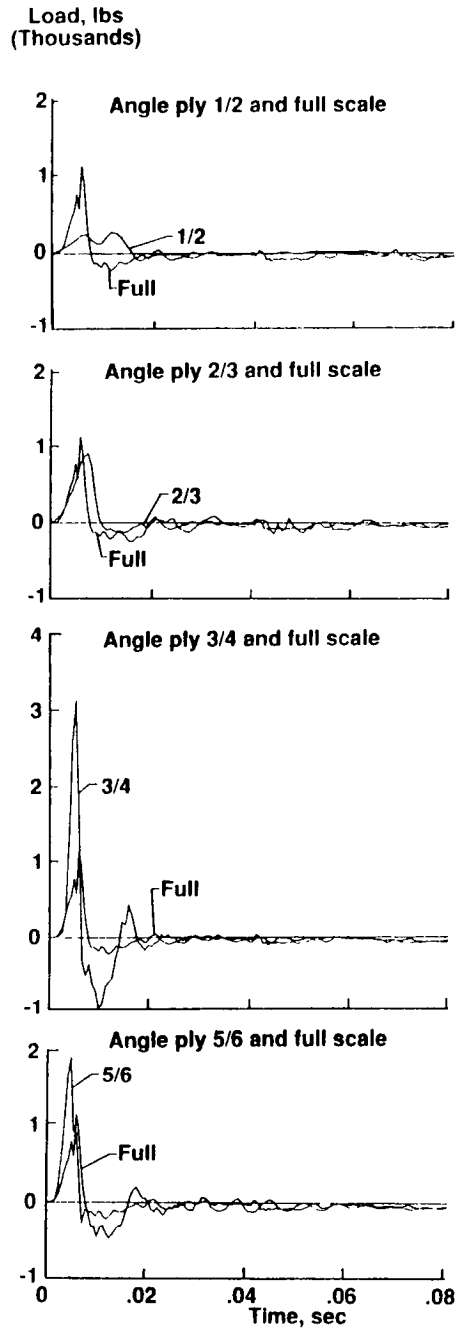

Figure 7-2. Load versus time plots for comparison of scale model predictions of full scale behavior of angle ply beams.

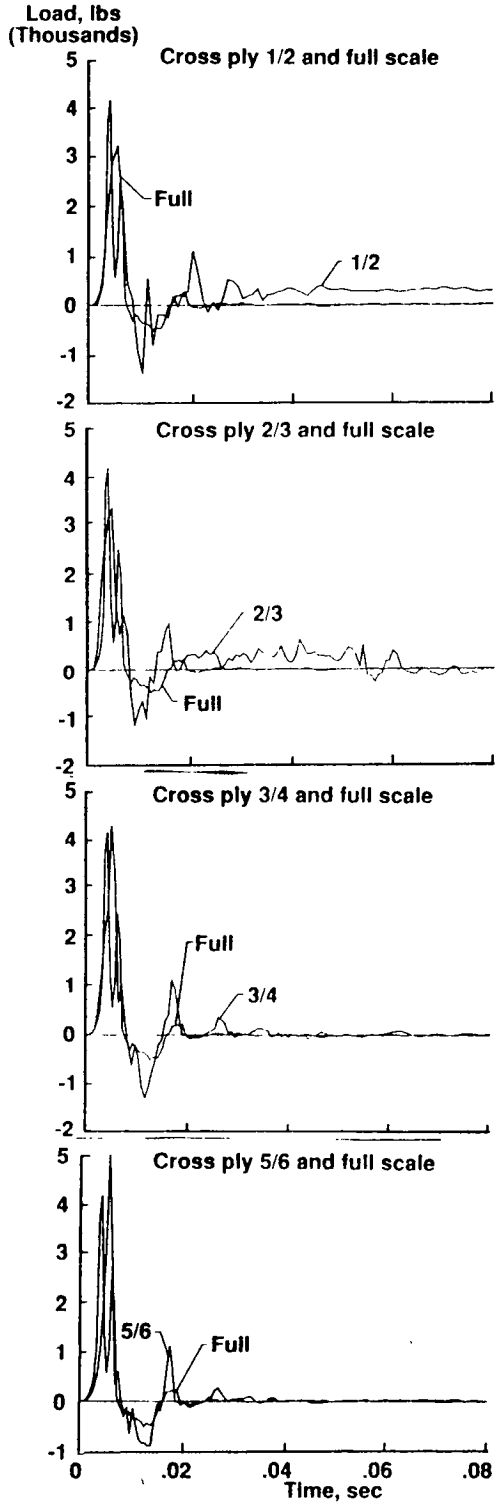

Figure 7-3. Load versus time plots for comparison of scale model predictions of full scale behavior of cross ply beams.

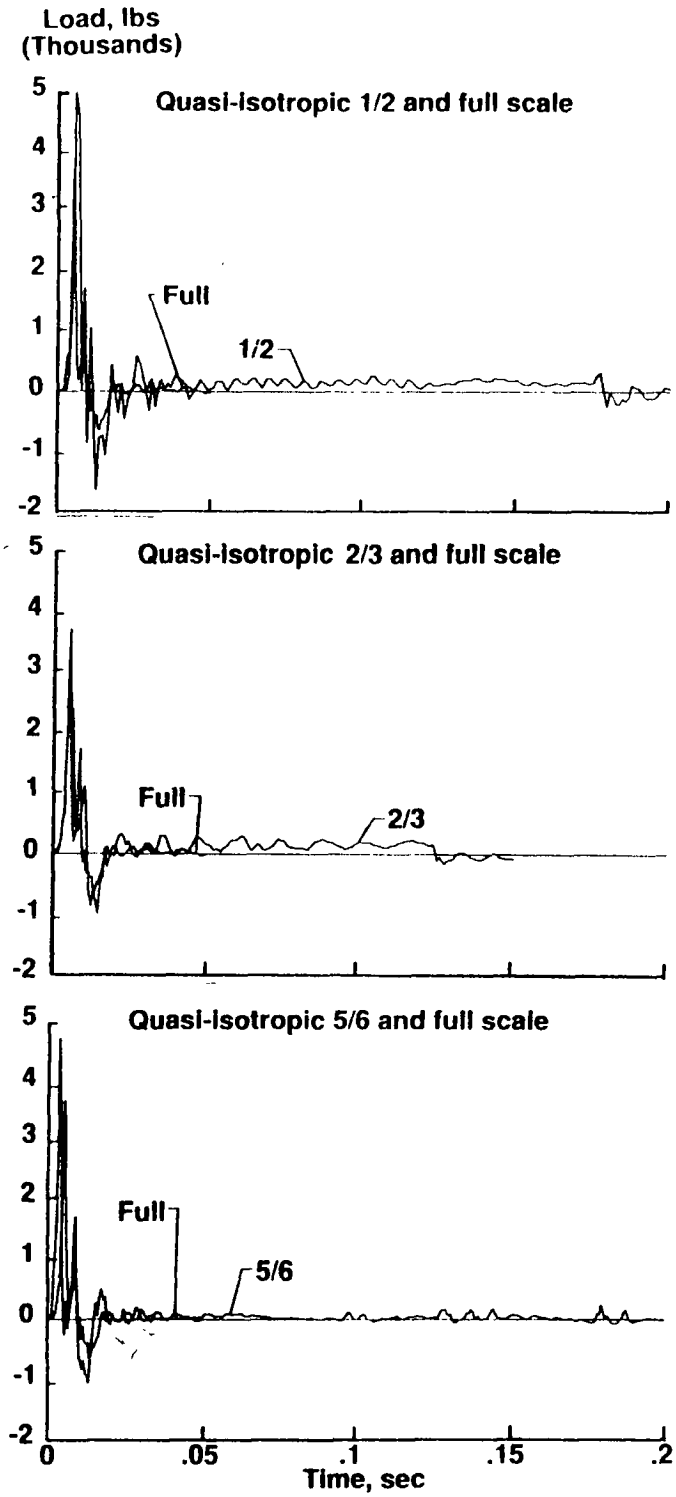

Figure 7-4. Load versus time plots for comparison of scale model predictions of full scale behavior of quasi-isotropic beams.

duration is well predicted by the scale model tests. For the 1/2 and 2/3 scale model quasi-isotropic beams, a sustained load response is observed which is not seen for the 5/6 or full scale beam. Apparently, the 5/6 and full scale beams fail catastrophically on impact whereas the 1/2 and 2/3 scale model beams are able to sustain the load prior to failure. This finding is similar to the behavior seen for the cross ply laminates and indicates a scale effect in strength for the quasi-isotropic laminates.

7.2 Comparison of Full Scale and Scale Model Strain Response

Figures 7-5 through 7-8 are plots comparing the midpoint longitudinal surface strain versus time of the scale model experimental data with the full scale beam response for the unidirectional, angle ply, cross ply, and quasi-isotropic laminates, respectively. Strain is a nondimensional quantity and, thus, scales as unity. Therefore, the strain state in the model beams should be the same as that of the prototype under scaled loading conditions. The scale law requires that time scale as λ. Consequently, the scale model time data were multiplied by the appropriate scale factor to compare with the full scale experimental data.

Results of the unidirectional scale model and full scale strain responses are plotted in Figure 7-5. The full scale strain gages failed prematurely so the failures indicated by the tensile and compressive gages do not represent actual failure of the full scale beam. It is evident from these plots that the strain response scales according to the scale law. Agreement between the scale model and full scale strain response is excellent. The dynamic strain response observed for the unidirectional scale model beams is similar to that reported by Derian [37] and Sensmeier [38]. Initially the tensile gage indicates compressive strain, and the compressive gage indicates tensile response. This effect is observed because the beam takes on the third vibration mode shape, similar to a "w" shape, before deforming

into the curved bending shape. Also, at any given instant of time the magnitude of the compressive strain is greater than the tensile strain, a phenomenon which was also observed for the static strain response. Figure 7-9 contains a plot of the absolute value of the compressive strain plotted with the tensile strain as a function of time for the unidirectional 1/2 scale beam. The data shown in Figure 7-9 indicate that only a difference in strain magnitude is observed. No phase shift or change in the frequency of oscillation is noted. At failure, the percentage difference in strain magnitudes is approximately 14%, which is similar to the value seen in the static unidirectional test. Derian [37] attributed this effect to a shift in the neutral axis of the beam due to bimodular material behavior. Sensmeier [38] also observed the difference in tensile and compressive strain magnitudes and modeled the effect by including nonlinear material properties and width-wise degrees of freedom in his finite element analysis. The MDS2DB code which Sensmeier developed was written to model the static problem so the effect of these parameters on the dynamic response could not be investigated using his code. Another important observation is that failure strain levels and time of failure are similar between scale models. The failure loads, end displacement ratios, and strains are listed in Table 7-1 for each of the scaled beams tested dynamically to failure within the four laminate families. The data for the unidirectional beams, although limited due to gage failures for the 2/3 and full scale beams, indicates that the large scale effect in strength which was observed in the static tests is not seen in the impact failure response.

The strain responses for scale model and prototype angle ply beams are plotted in Figure 7-6. As expected from the poor scaling of the load response, the strain response also exhibits poor scaling. With exception of the 2/3 scale beam, the angle ply scale model beams do not predict the strain magnitudes or general shape of the strain response of the prototype beam. The failure data listed in Table 7-1 for the angle ply beams show that a large scale effect in strength is not observed.

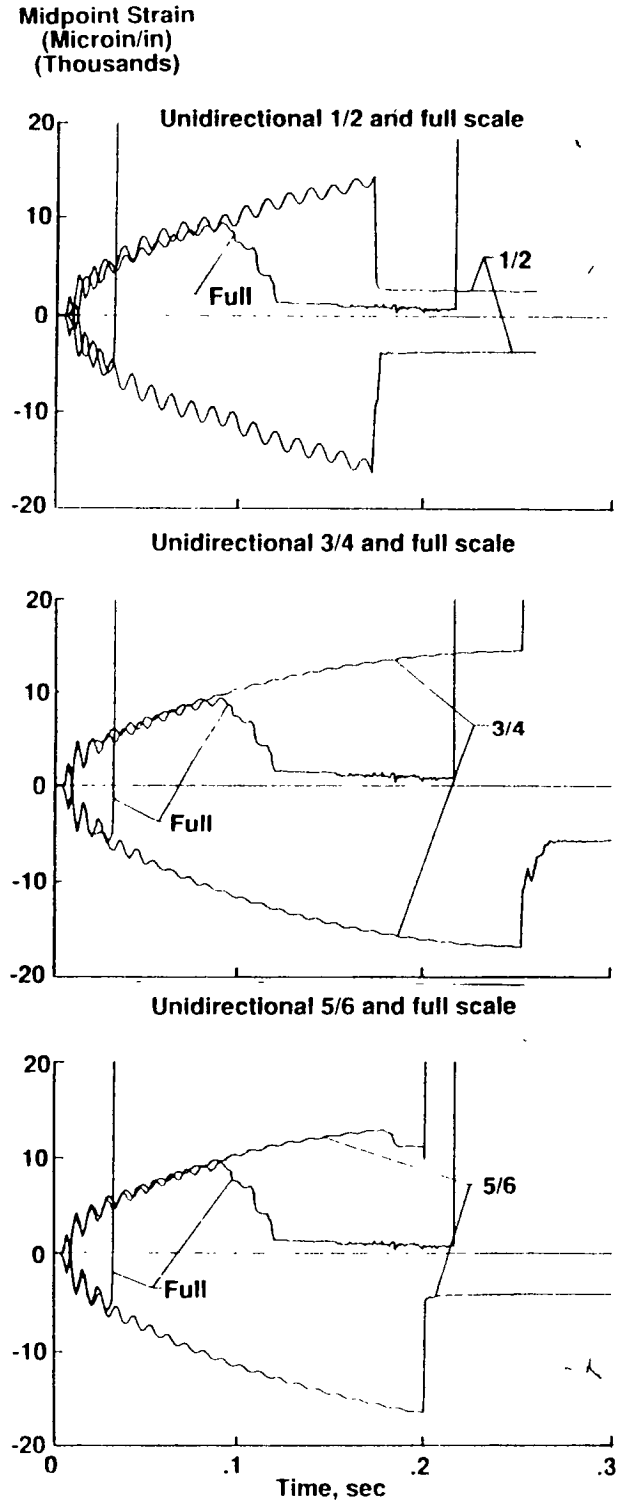

Figure 7-5. Strain versus time plots for comparison of scale model predictions of full scale behavior of unidirectional beams.

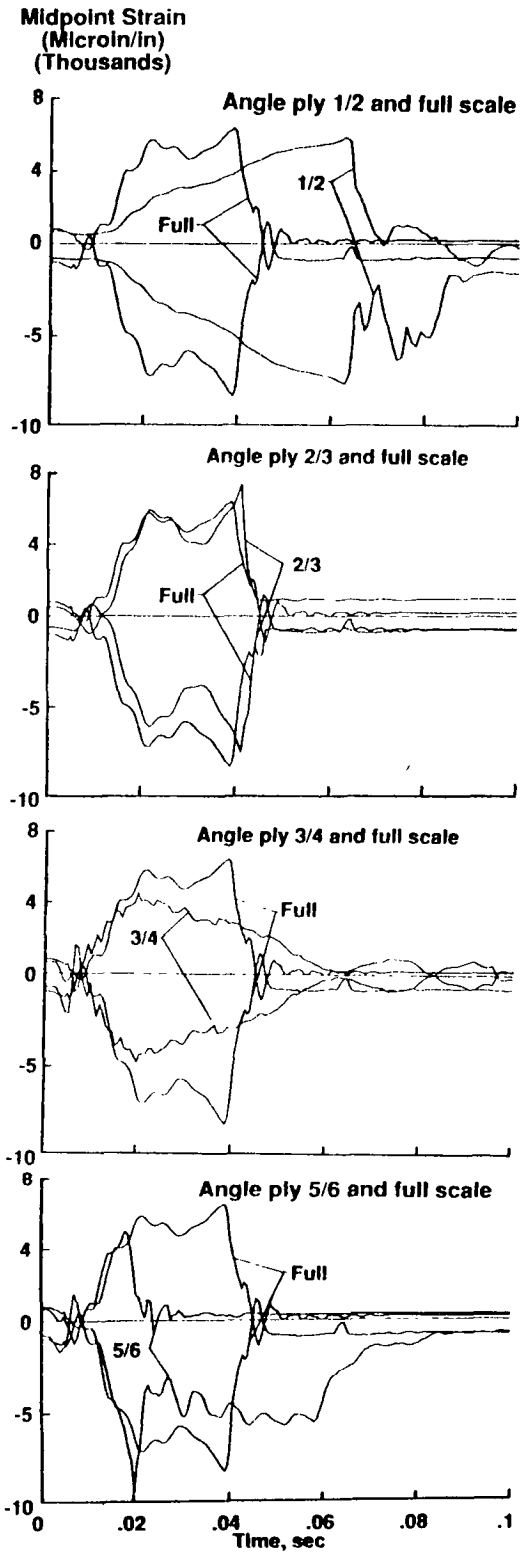

Figure 7-6. Strain versus time plots for comparison of scale model predictions of full scale behavior of angle ply beams.

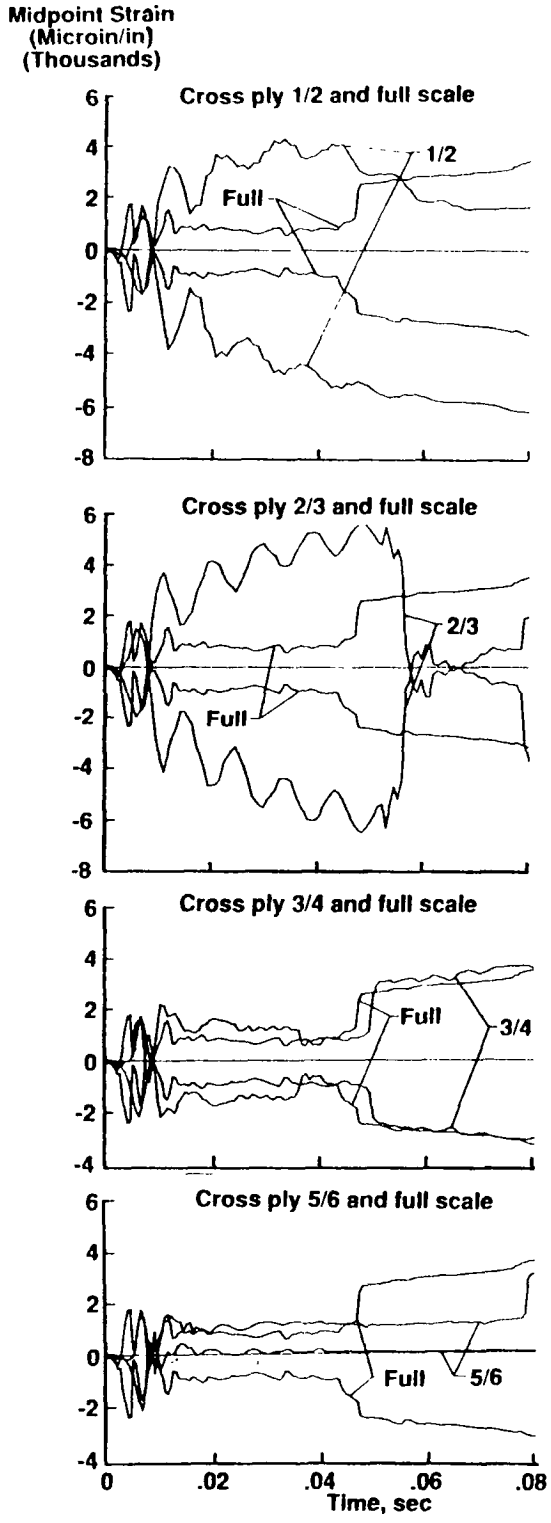

Figure 7-7. Strain versus time plots for comparison of scale model predictions of full scale behavior of cross ply beams.

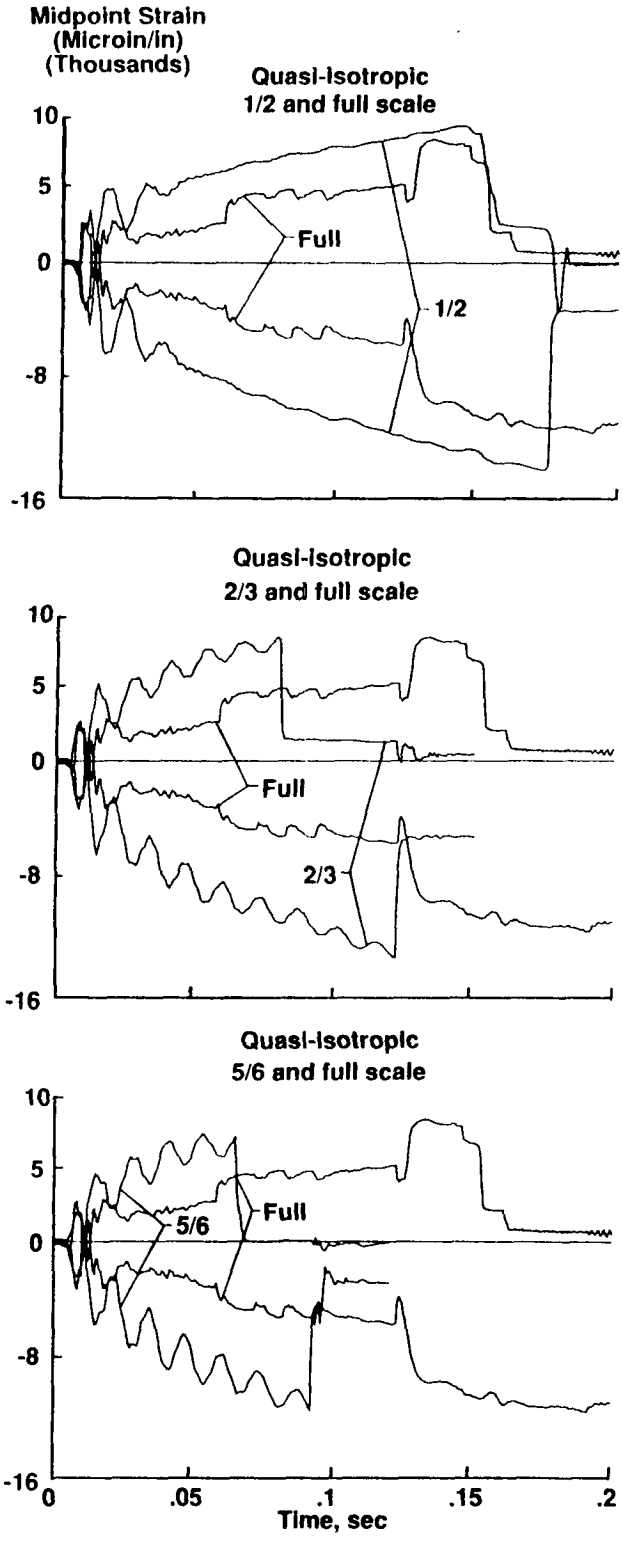

Figure 7-8. Strain versus time plots for comparison of scale model predictions of full scale behavior of quasi-isotropic beams.

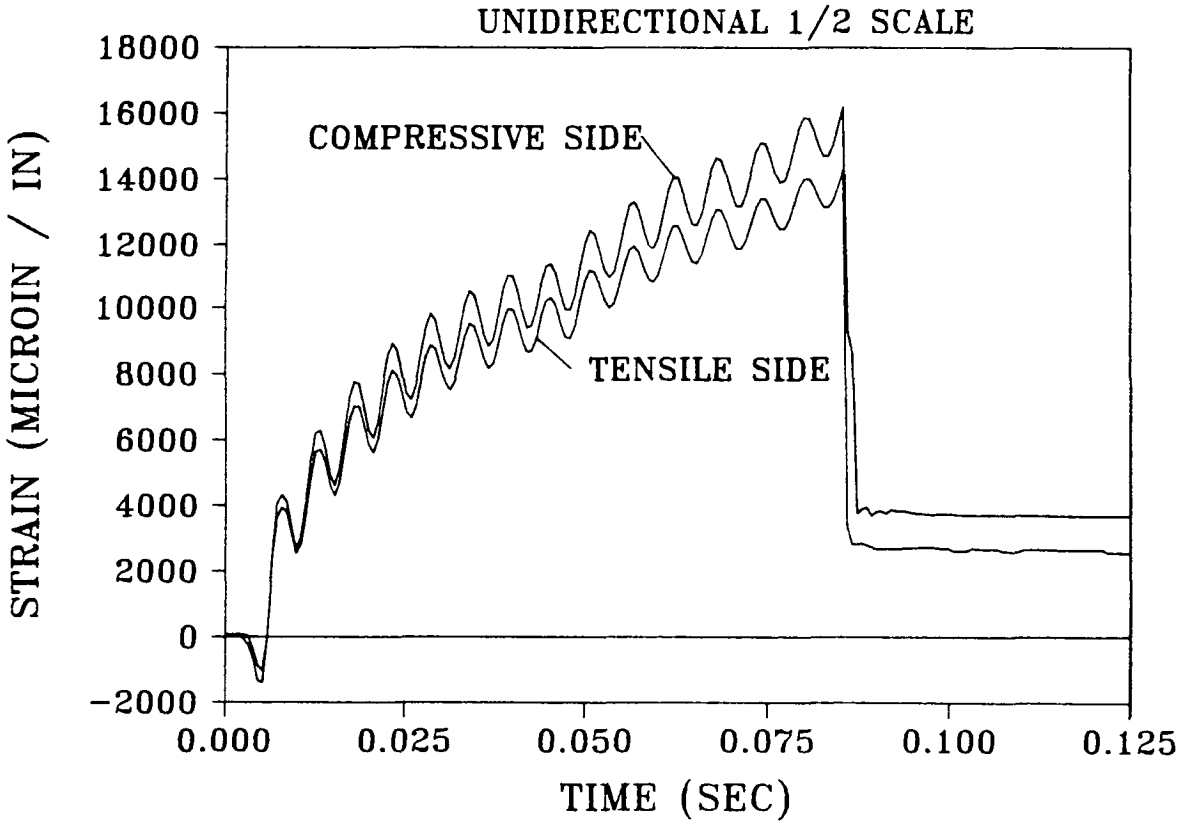

Figure 7-9. Comparison of tensile and compressive strain magnitudes for unidirectional 1/2 scale unidirectional strain-time response.

Table 7-1. Failure loads, end displacement ratios, and strains for scale model beams tested dynamically. (Note: * indicates either premature gage failures or difficulty in determining a value from the experimental data.)

Laminate	Scale Factor	Scaled Failure Load (lbs)	End Displacement Ratio	Failure Strain Tensile (microin/in)	Failure Strain Compressive (microin/in)
Unidirectional	1/2	609.6	0.76	14293	-16324
	2/3	669.8	0.79	*	*
	3/4	503.8	0.73	14476	-16834
	5/6	495.8	0.81	11196	-16533
	FULL	537.0	0.61	*	*
Angle Ply	1/2	48.9	0.22	5875	-7680
	2/3	39.3	0.16	7333	-7564
	3/4	*	0.28	4466	-4987
	5/6	*	0.26	5000	-9800
	FULL	*	0.21	6392	-8349
Cross Ply	1/2	*	*	*	*
	2/3	516.8	0.16	5599	-6440
	3/4	1125.3	0.07	1074	-1224
	5/6	1104.5	0.07	1500	*
	FULL	*	0.06	1475	-1467
Quasi-Isotropic	1/2	318.8	0.53	9333	-14040
	2/3	196.4	0.48	8000	-13300
	5/6	161.2	0.62	7500	-11469
	Full	*	0.82	6735	-10656

Figure 7-7 depicts the strain responses for the scale model and full scale cross ply beams. The 1/2 and 2/3 scale beams predict the full scale strain response initially, but then exhibit an increasing strain response which deviates from the prototype beam. However, the prototype strain response is predicted well by the 3/4 and 5/6 scale beams. The strain response shown in Figure 7-7 and the failure data listed in Table 7-1 indicate a scale effect in strength for the cross ply laminates. The transition occurs between the 2/3 and 3/4 scale model beams. The end displacement ratio at failure for the 2/3 scale beam is approximately twice the value for the 3/4 scale model beam, and the failure strains are 5 times higher for the 2/3 scale model beam than the 3/4 scale beam. However, the failure strains and end displacement ratios are similar for the 3/4, 5/6, and full scale cross ply beams.

The strain responses for scale model and prototype quasi-isotropic beams are plotted in Figure 7-8. None of the scale model beams predict the full scale strain response accurately. However, the strain responses of the 1/2, 2/3, and 5/6 scale model beams agree well. This finding implies that either a scale effect in strain response exists between the full scale and scale model beams, or that the observed strain response for the full scale quasi-isotropic beam is anomalous. Since only one full scale quasi-isotropic beam was tested dynamically, no additional data were available to confirm a scale effect.

7.3 Comparison of DYCAST Analysis and Experiment

Prediction of the strain response by the DYCAST finite element structural analysis program is plotted with the 1/2 scale experimental data for the unidirectional beam in Figure 7-10. The plot shows good agreement between the DYCAST analysis and the experimental response. The analysis predicts the inversion of the tensile and compressive strains which was observed immediately following impact. The DYCAST analysis tends to underpredict both

the tensile and compressive strain response prior to beam failure. Figure 7-11 shows the DYCAST strain prediction for the quasi-isotropic 1/2 scale beam. Excellent agreement is shown for the compressive strain response; however, the DYCAST analysis overpredicts the tensile strain response.

DYCAST also was used to predict the deflected shape of the unidirectional beam. Figure 7-12 depicts a progression of the beam deflected shapes for increasing time increments. The deflected shape at time 0.00225 seconds illustrates the third vibration mode shape which gives rise to the initial inverted strain measurements. By time 0.00475 seconds, the beam has already begun to assume the characteristic curved bending shape. These deformed shapes indicate the severe rotations and deformations experienced by the beams during impact.

7.4 Comparison of Static and Dynamic Results

Plots of load and midpoint strain versus end displacement ratio are shown in Figures 7-13 through 7-16 for a representative beam from each laminate family to compare the static and dynamic test results. As shown in Figure 7-13(a) for the 3/4 scale unidirectional beam, the difference between the static and dynamic load responses is the large load spike due to the impact event. Following the initial spike, the dynamic response exhibits oscillations about the static response. The value of load and end displacement ratio at failure is approximately the same for the beams tested statically and dynamically. The only difference between the static and dynamic strain responses, shown in Figure 7-13(b) for the unidirectional 3/4 scale beam, is the inversion seen in the dynamic data for small end displacement ratios. As previously discussed, this strain inversion is due to the initial mode shape of the beam at impact. Once the beam assumes its curved flexural shape the dynamic strain response

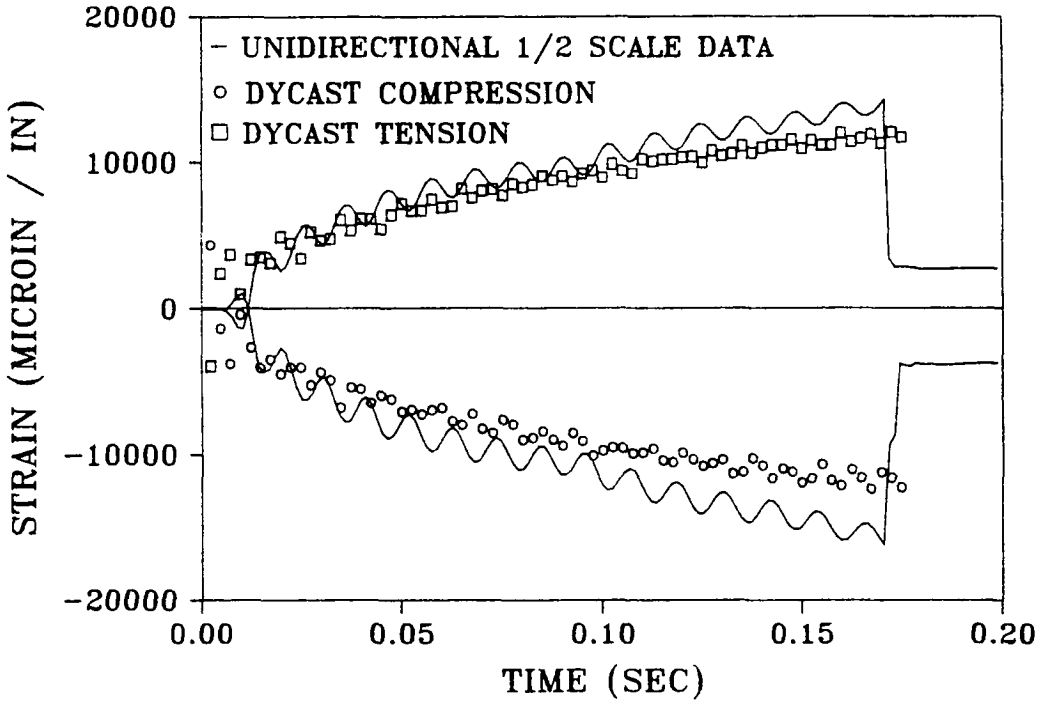

Figure 7-10. Comparison of DYCAST finite element model results with 1/2 scale unidirectional strain-time response.

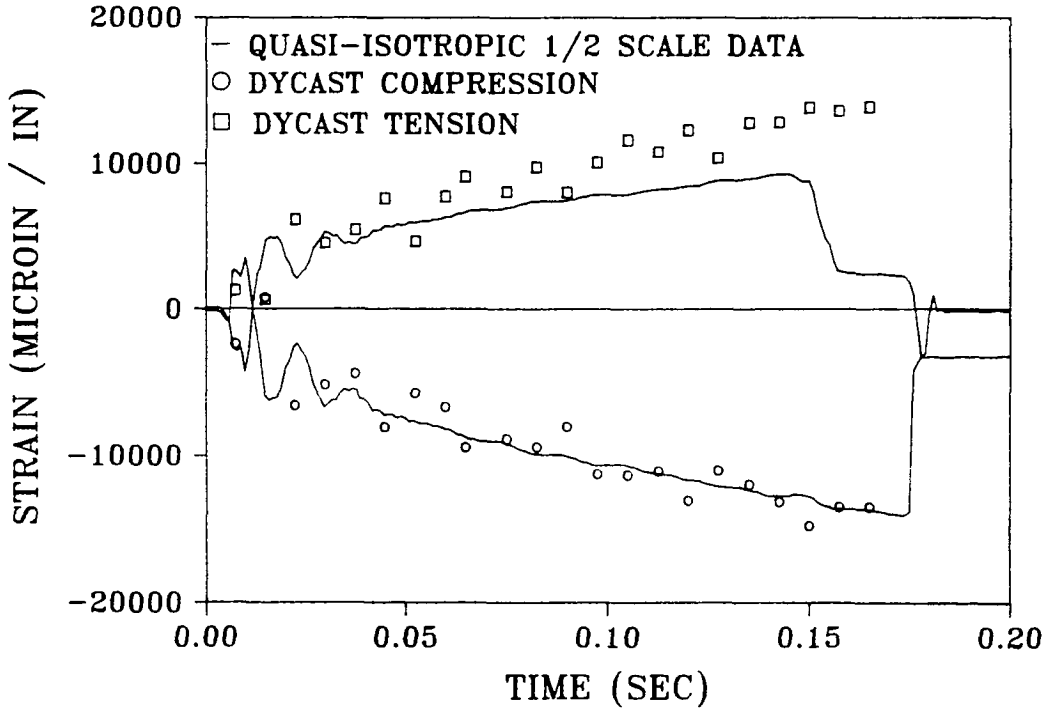

Figure 7-11. Comparison of DYCAST finite element model results with 1/2 scale quasi-isotropic strain-time response.

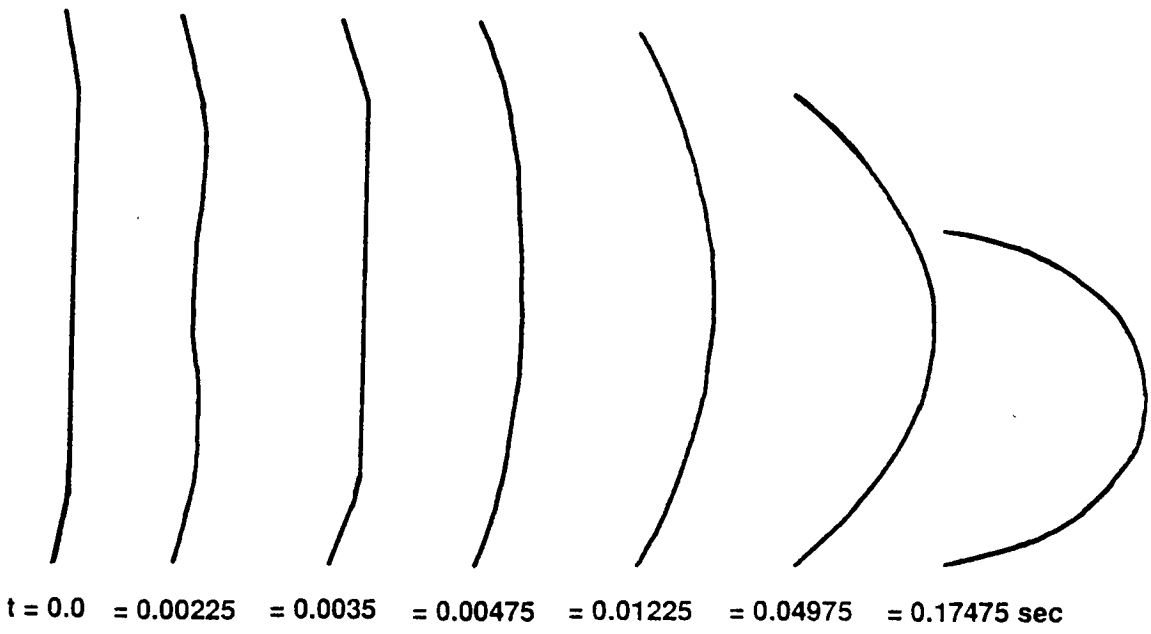

Figure 7-12. DYCAST predictions for deflected shapes of full scale unidirectional beam subjected to impact.

simply oscillates about the static strain response. Failure strains are similar for both the statically and dynamically tested beams.

Figure 7-14 shows the comparison of load and strain responses for 2/3 scale angle ply beams tested under static and dynamic conditions. The dynamic load response for the angle ply beam also exhibits a high load spike and then oscillates about the static response. However, the failure event is not as pronounced for the angle ply beam and is overshadowed in the load response by vibrations and secondary impacts of the drop tower. A better indication of the failure location is seen in the strain response, shown in Figure 7-14(b). Agreement between the static and dynamic strain response is excellent for the angle ply 2/3 scale model beam. As was observed for the unidirectional laminates, the dynamic strain response oscillates about the static response. Failure occurs at approximately the same end displacement ratio for both static and dynamic tests.

Results from static and dynamic tests on 2/3 scale cross ply beams are show in Figure 7-15. The load response from the dynamic test shows the large initial load spike and then follows the static load response somewhat erratically. Agreement between the static and dynamic strain response is more consistent. However, the 2/3 scale cross ply beam which was tested dynamically failed at a lower end displacement ratio than the beam which was tested statically.

Figure 7-16 illustrates a comparison between the static and dynamic data for the 1/2 scale quasi-isotropic scale model beams. The dynamic load response agrees well with the static load response following the initial load spike. Similar agreement is seen between the static and dynamic strain responses following the initial strain inversion phenomenon. Failure events occur at nearly identical end displacement ratios for both the statically and dynamically tested beams.

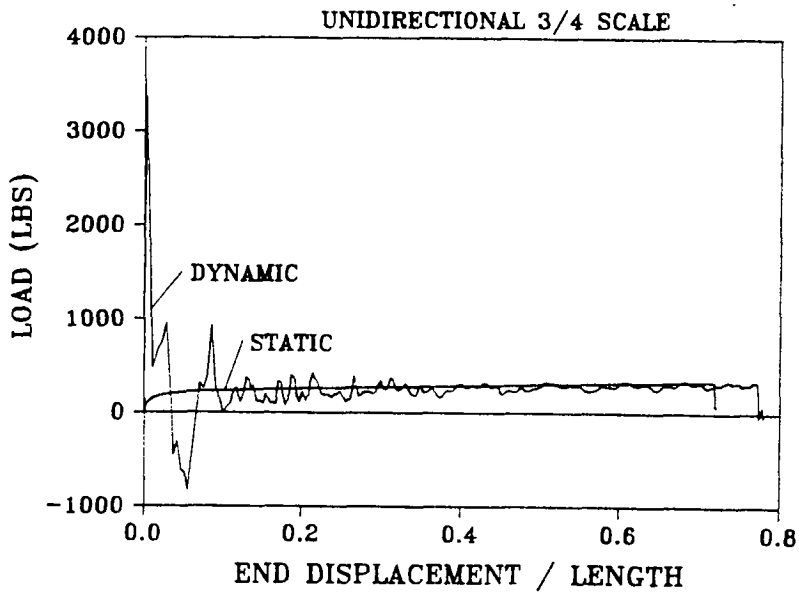

(a) Comparison of static and dynamic load versus end displacement response for a 3/4 scale unidirectional beam.

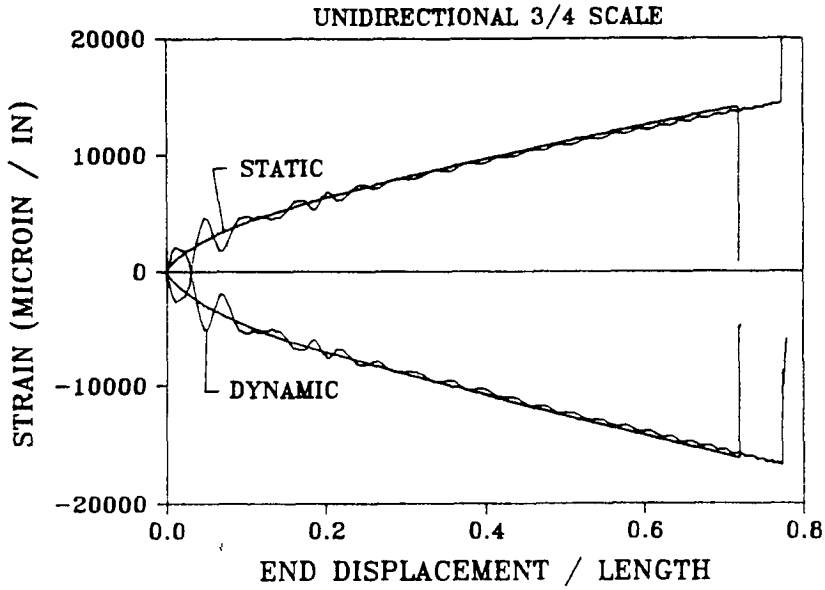

(b) Comparison of static and dynamic strain versus end displacement response for a 3/4 scale unidirectional beam

Figure 7-13. Comparison of static and dynamic load and strain response for unidirectional 3/4 scale beam.

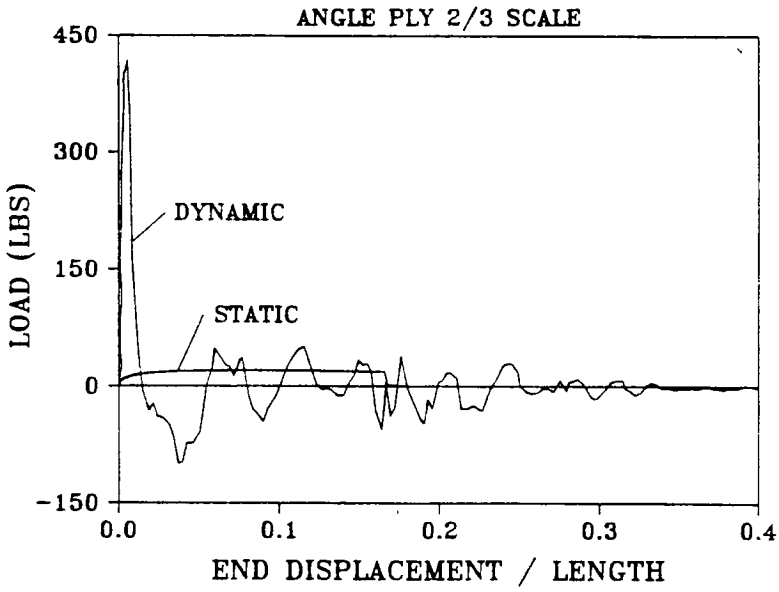

(a) Comparison of static and dynamic load vs. end displacement response for 2/3 scale angle ply beam.

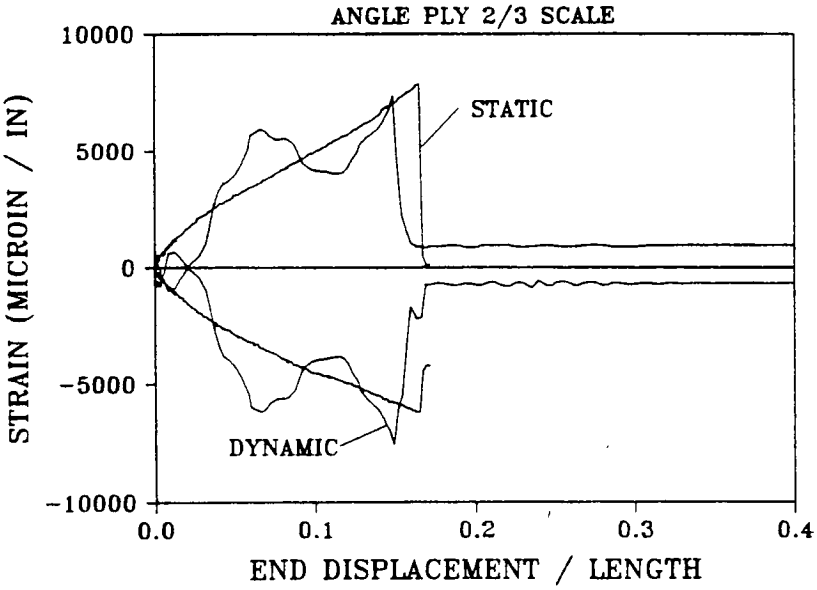

(b) Comparison of static and dynamic strain vs. end displacement response for 2/3 scale angle ply beam

Figure 7-14. Comparison of static and dynamic load and strain response for angle ply 2/3 scale beam.

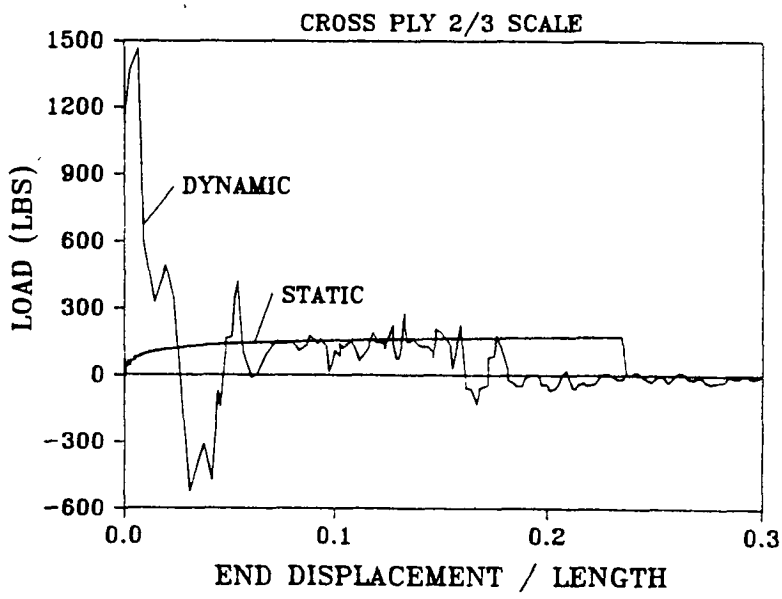

(a) Comparison of static and dynamic load versus end displacement response for a 2/3 scale cross ply beam.

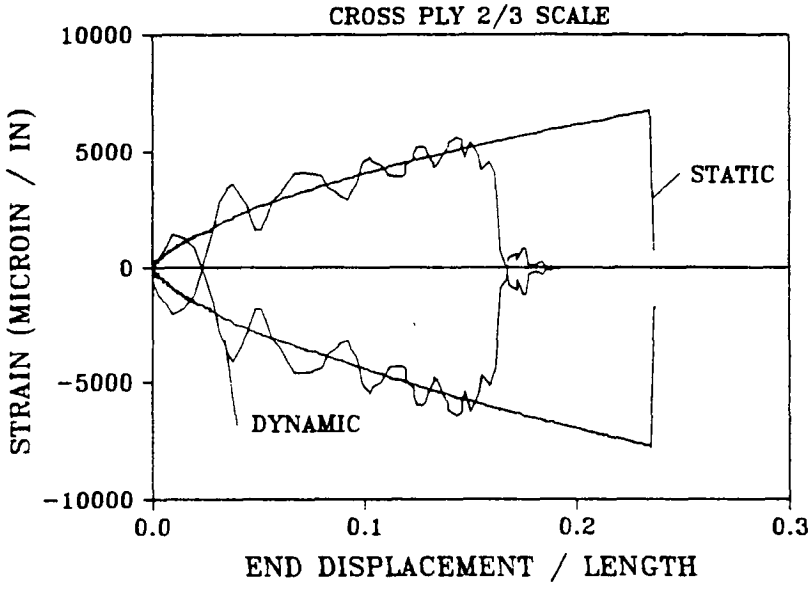

(b) Comparison of static and dynamic strain versus end displacement response for a 2/3 scale cross ply beam

Figure 7-15. Comparison of static and dynamic load and strain response for cross ply 2/3 scale beam.

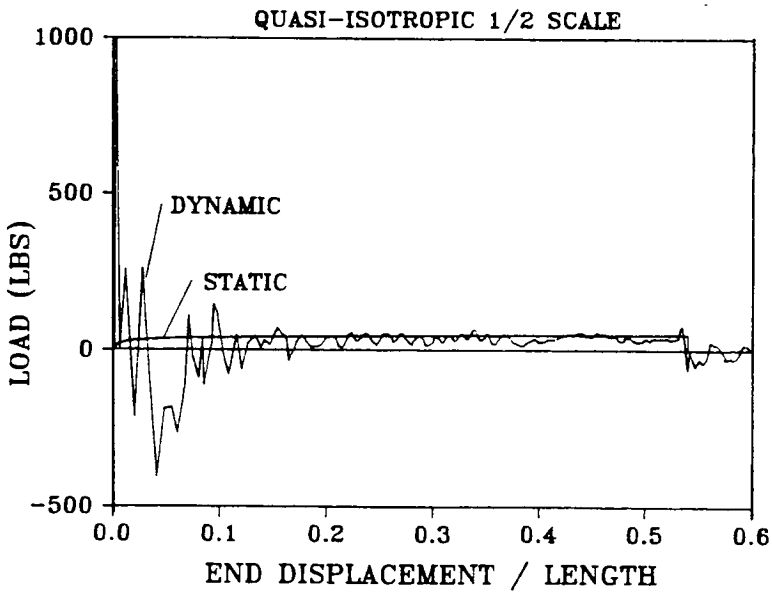

(a) Comparison of static and dynamic load vs. end displacement response for 1/2 scale quasi-isotropic beam.

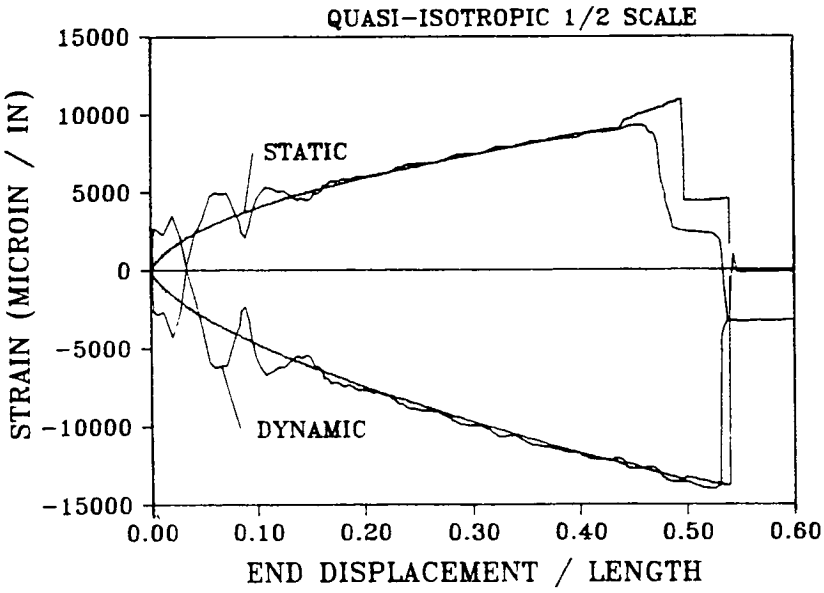

(b) Comparison of static and dynamic strain vs. end displacement response for 1/2 scale quasi-isotropic beam.

Figure 7-16. Comparison of static and dynamic load and strain response for quasi-isotropic 1/2 scale beam.

7.5 Failure Mechanisms

The photographs shown in Figures 7-17 through 7-20 illustrate a failed half and full scale beam for each of the unidirectional, angle ply, cross ply, and quasi-isotropic laminates which were included in the impact tests. Although the failure mechanisms of the four laminate types are different from each other, results of the impact tests indicate that the mechanisms are similar between scaled beams within a laminate family. Thus, failure modes appear to be independent of specimen size. However, for some of the laminate families, more damage was observed in the smaller scale model beams than in the prototype.

The unidirectional beams, shown in Figure 7-17, failed by fiber fracture near the midpoint of the beam and by splitting along the longitudinal axis of the beam. This failure mode is typical of all the unidirectional beams 1/2 through full scale. Figure 7-21 shows a unidirectional full scale beam following impact but before the beam has been removed from the drop tower. Fiber fractures and longitudinal splitting are evident in the photograph.

Failure of the angle ply beams occurred by transverse matrix cracking along the 45 degree fiber lines. There was no evidence of fiber fracture, as shown in Figure 7-18.

The cross ply laminates exhibited combined failure mechanisms of transverse matrix cracking and delamination, as shown in Figure 7-19. The photograph indicates that, unlike the other laminates which failed at the beam midpoint where the maximum moment occurred, the cross ply beam failures were initiated at the hinge connection. A large transverse matrix crack developed at the point of attachment of the beam with the hinge in the 90 degree core of the laminate. This crack split the 90 degree core and initiated a delamination between the 90 degree and 0 degree plies on the compression side of the beam. The delamination completely separated the laminate into two sections which then responded independently of one another. As shown in Figure 7-19,

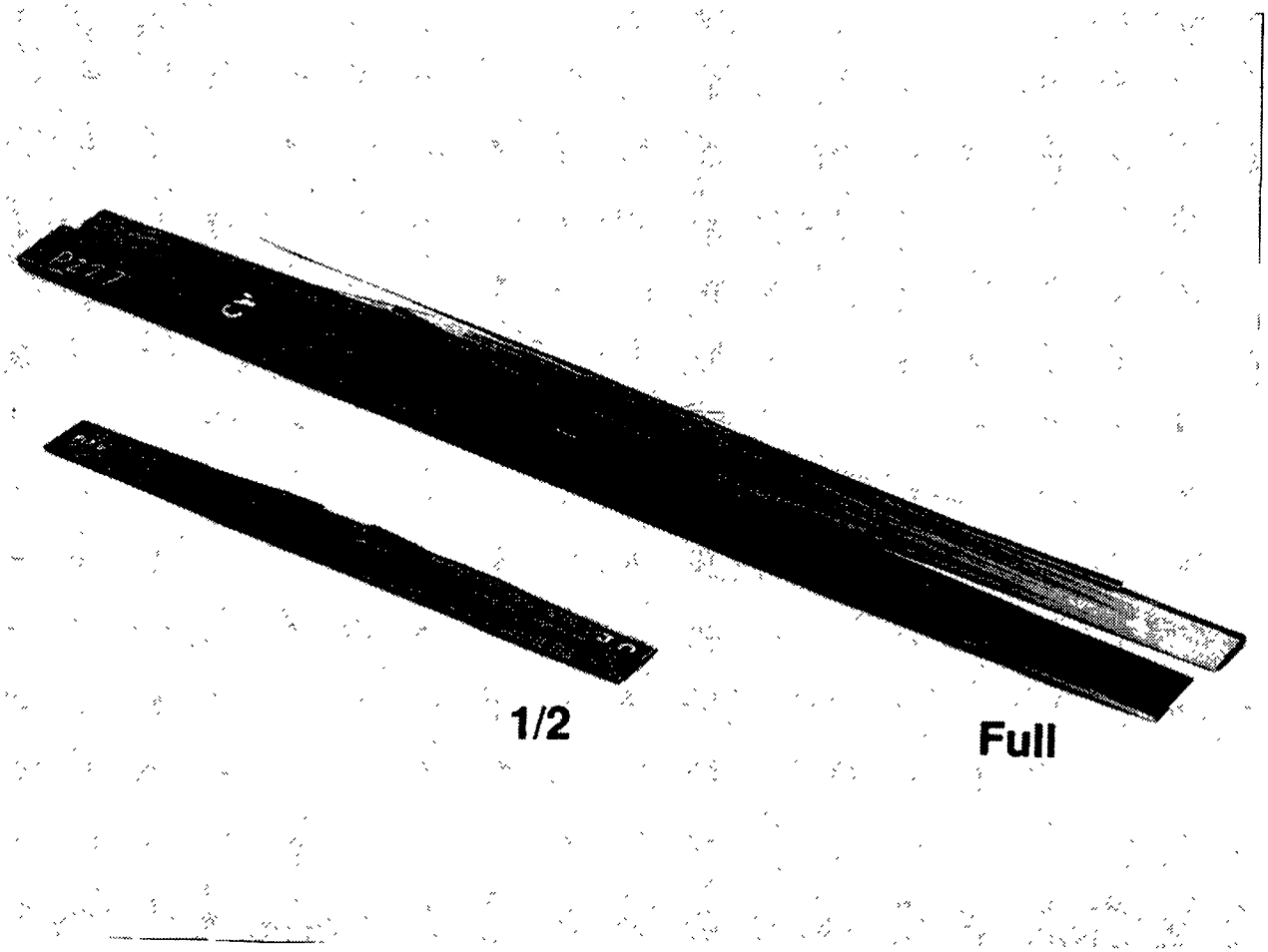

Figure 7-17. Photograph of failed 1/2 and full scale unidirectional beams tested dynamically.

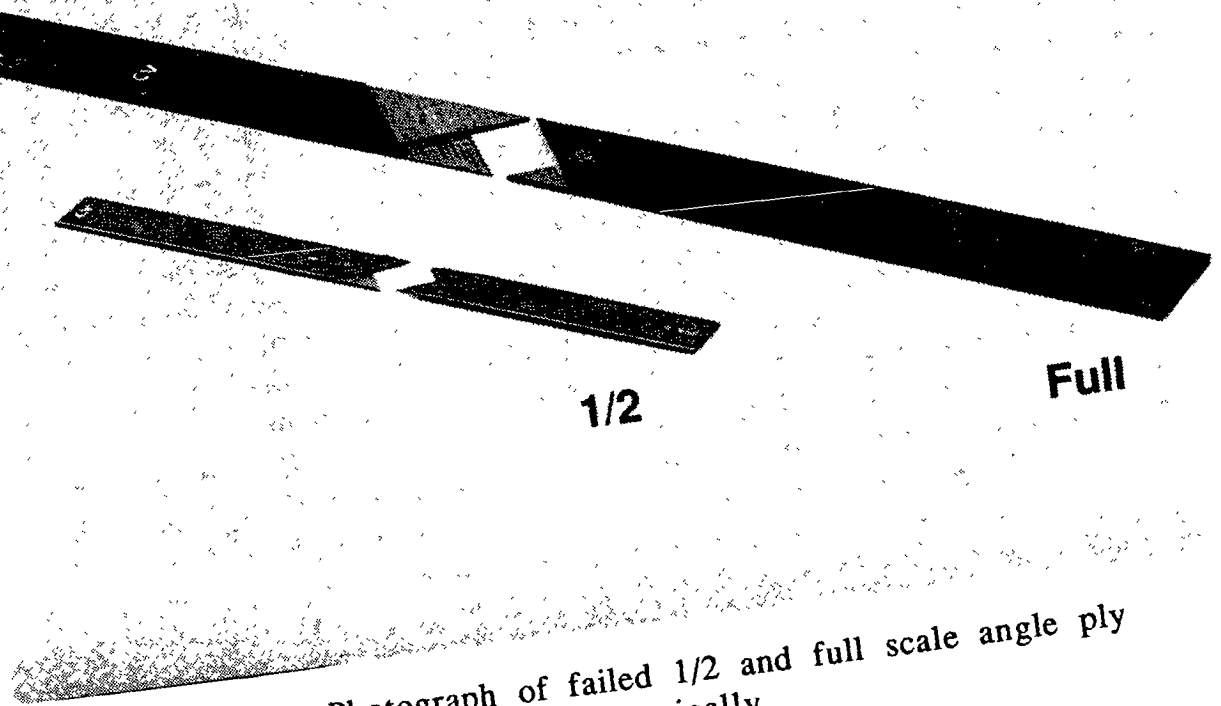

Figure 7-18. Photograph of failed 1/2 and full scale angle ply beams tested dynamically.

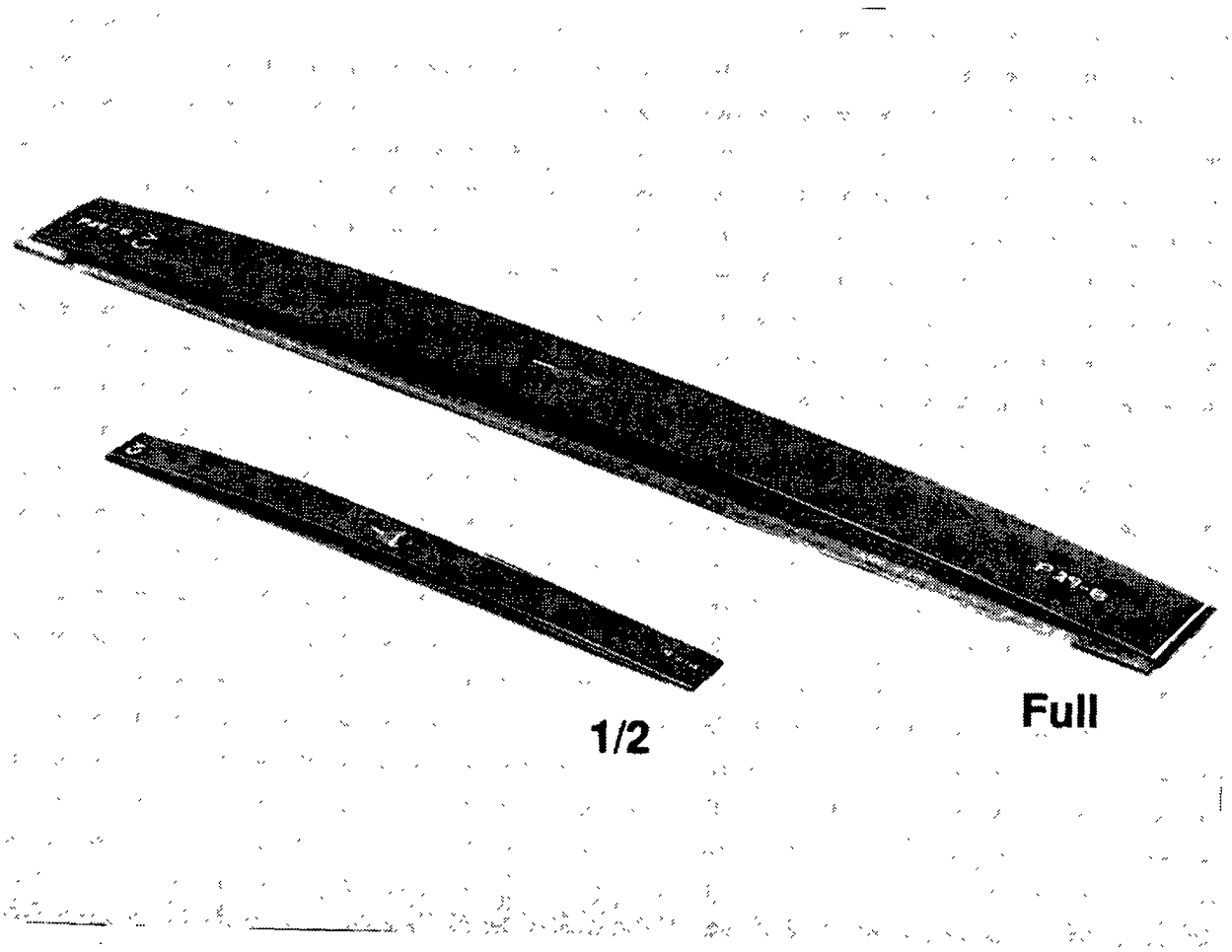

Figure 7-19. Photograph of failed 1/2 and full scale cross ply beams tested dynamically.

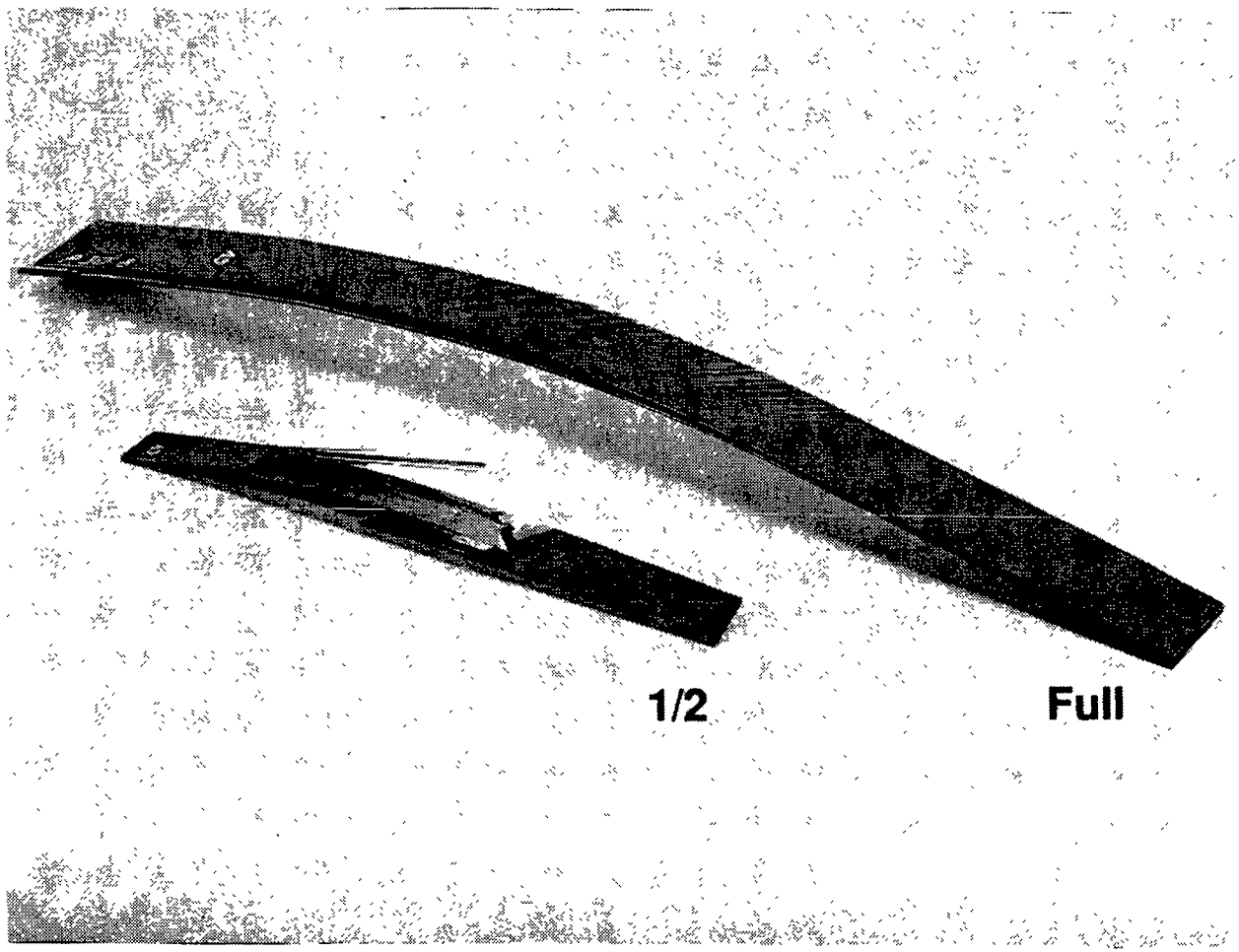

Figure 7-20. Photograph of failed 1/2 and full scale quasi-isotropic beams tested dynamically.

Figure 7-21. Photograph of a full scale unidirectional beam following impact testing in the drop tower.

this failure mode was seen in both the half and full scale beams, and was typical of the other scaled cross ply laminates as well.

The quasi-isotropic beams failed through a combination of matrix cracking, delamination, and some fiber fracture. The photograph of the half and full scale beams, shown in Figure 7-20, indicates that more severe damage occurred in the half scale beam than in the full scale beam. Transverse matrix cracks are seen in both beams in the 45 degree plies. Also, matrix cracks developed in the 90 degree plies which resulted in delaminations between the adjoining layers. The half scale beam exhibits some fiber fractures in the 0 degree plies near the midpoint of the beam which are not seen in the full scale beam. In addition, a section of the outer 45 degree layer has completely delaminated from the half scale beam. The full scale beam has a series of cracks in the outer 45 degree layer along fiber directions which have initiated at the free edge and grown across the width of the beam.

7.6 Summary of Dynamic Test Results

Scaling effects in the large deflection dynamic response of graphite-epoxy composite beams subjected to impact were investigated. A series of tests on scale model composite beams having unidirectional, angle ply, cross ply, and quasi-isotropic laminate stacking sequences were conducted. The beams were loaded under an eccentric axial compressive load to promote large bending deformations and global failure. Plots comparing load and strain time histories for each of the scale model beams within a laminate family were presented to validate the model law. Also, the nonlinear structural analysis computer program DYCAST was used to model the dynamic beam response.

Significant findings from the dynamic testing program are:

(1) Load and strain responses for the unidirectional beams scaled according to the scale law. Tests on scale model beams

accurately predicted the full scale beam behavior. However, scaling of the load and strain responses for the angle ply, cross ply, and quasi-isotropic laminates was inconsistent. The load and strain responses for the cross ply and quasi-isotropic laminates indicated a scale effect in strength.

(2) Experimental results indicate that failure modes between scale model beams and the prototype are similar, i.e., failure mechanisms do not appear to be a function of specimen size. However, the smaller scale model quasi-isotropic beams were more severely damaged than the larger scale model beams.

(3) The DYCAST computer code successfully modeled the strain response of the 1/2 scale unidirectional and quasi-isotropic beam. Plots of the deformed shape of the beam during loading showed that the inversion of the tensile and compressive strains was due to the initial third mode vibratory response of the beam.

(4) Comparisons between static and dynamic test data from beams of the same laminate family and scaled size indicate similar load and strain responses. Following the initial load spike, the dynamic load response oscillates about the static response for all of the laminate types. Also, following the initial strain inversion, agreement between the static and dynamic strain response is excellent. With the exception of the cross ply beam, the failure locations for the static and dynamic beams were nearly identical. This finding implies that important information on the global, dynamic response of structures subjected to impact loads can be found from simple static testing.

Chapter 8 - Investigation of Failure

The experimental results presented in Chapters 6 and 7 indicate that scale model testing is a practical and efficient alternative to full scale testing for determining the structural response of most laminates. However, if the testing involves damage or failure of the structure, then the absolute size of the specimen will have a tremendous influence on the failure behavior and ultimate strength of the structure. Composite materials are often used to build thin, high stiffness, "minimum gage" structures which routinely operate under large deflections and high design loads. If tests on subscale specimens are used to determine ultimate loads for these types of designs, then the strength of prototype structures may be seriously overestimated due to the scale effect in failure. Additional research is needed to study and isolate the factors responsible for scaling effects in strength of composite laminates so that reliable predictions can be made from scale model tests.

The large difference in failure loads, strains, and end displacement ratios between scale models of the eccentrically loaded beam-column demonstrates the magnitude of the size effect on strength. The size effect in strength which is observed on the macroscopic level is the result of damage on the microscopic level which initiates within the laminate and develops in a certain manner under the applied load. The accumulation of damage and interaction of failure mechanisms eventually result in ultimate failure of the structure. A detailed investigation of the effect of test specimen size on failure needs to be addressed on a material level before the phenomenon can be understood on the macroscopic level. A research effort of this type is beyond the scope of the current study. Instead, the focus of this chapter will be to apply commonly used failure criteria including maximum stress, maximum strain, and Tsai-Wu tensor polynomial, to the composite beam-column, and to demonstrate the inability of these criteria to predict the scale effect in strength. The use of statistical approaches and fracture mechanics

theories for predicting the scale effect in strength will be discussed and applied to the eccentrically loaded beam-column problem.

8.1 Failure Analysis

The one dimensional, large deflection beam solution which was described in Chapter 4 and Appendix B is used to predict first ply failure of the static beam-column problem for each of the laminate families. At each load step, a value of axial compressive load (N_x) and moment (M_x) is computed and a stress analysis is performed to determine ply stresses in the material directions. Then, the maximum stress, maximum strain, and Tsai-Wu tensor polynomial theories are applied to predict first ply failure. These criteria are described by Jones in Reference [53]. The criteria require that five material strength properties be known including tensile fiber-direction strength (X_t), compressive fiber-direction strength (X_c), tensile transverse strength (Y_t), compressive transverse strength (Y_c), and inplane shear strength (S). The values of failure strain are found by dividing the strengths by the corresponding moduli. The strength values were determined for the AS4/3502 graphite-epoxy material system by Sensmeier from a series of material characterization tests. His test methods and procedures are presented in Reference [38] and the mean failure strength values are listed in Table 8-1.

Results of the failure analysis for the unidirectional laminates indicate that failure occurs at the midspan of the beam on the compression side at a load ratio of 0.505 and an end displacement ratio of 0.1834. All three failure criteria predict that failure will occur at that load and end displacement ratio. The maximum stress and strain criteria indicate that the compressive stress and strain in the fiber direction exceeds the compressive strength and ultimate compressive strain in the 0 degree ply on the outer surface. The beam analysis indicating the predicted load and end displacement ratios at failure is plotted with the 1/4 and full scale unidirectional

Table 8-1. Summary of failure stresses from material characterization tests on AS4/3502 graphite-epoxy composite material.

Strength	Mean Failure Stress (Ksi)
Tensile fiber-direction, X_T	178.10
Compressive fiber-direction, X_C	-132.40
Tensile transverse, Y_T	7.46
Compressive transverse, Y_C	-32.30
Inplane Shear, S	12.50

experimental load-displacement data in Figure 8-1. As shown in the figure, the predicted failure is conservative. This result is typical of the findings by Derian [37] and Sensmeier [38]. In fact, Sensmeier realized that the failure strains he observed from bending tests on unidirectional 30 ply beams were twice as high as the failure strains he measured from standard material characterization tests. Consequently, he replaced the failure strains determined from uniaxial tensile tests with the flexural values to perform the failure analysis.

It is important to note that the failure load and end displacement ratios for the unidirectional beams (shown in Figure 8-1), are independent of the scaled size. The elementary approach to scaling discussed in Chapter 2 indicates that stress and strain scale as unity. Therefore, for geometrically similar beams, any failure criteria based solely on stress or strain will predict a single failure load ratio, independent of the absolute size of the beam.

Figure 8-2 shows a plot of the normalized load-displacement response up to failure for the angle ply laminate from the beam analysis with the 1/6 and full scale experimental load-displacement data. The Tsai-Wu criterion was used to predict the first ply failure which occurred in the outer 45 degree ply on the tensile side of the beam at a load ratio of 0.517 and an end displacement ratio of 0.202. The maximum stress and maximum strain criteria predict failure at a higher load ratio of 0.565 and an end displacement ratio of 0.36. Both predict a shear failure of the outer 45 degree ply on the compression side of the beam. As shown in the figure, the analysis overpredicts the load response. Consequently, the predicted load ratio at failure is higher than the experimentally observed values, even though the end displacement ratio at failure falls between the 1/6 and full scale end displacement ratios at failure.

The maximum stress and maximum strain criteria predict first ply failure of the cross ply laminates to occur at a load ratio of 0.525 and an end displacement ratio of 0.236. A compressive failure is predicted in the outer 0 degree ply of the beam. The Tsai-Wu

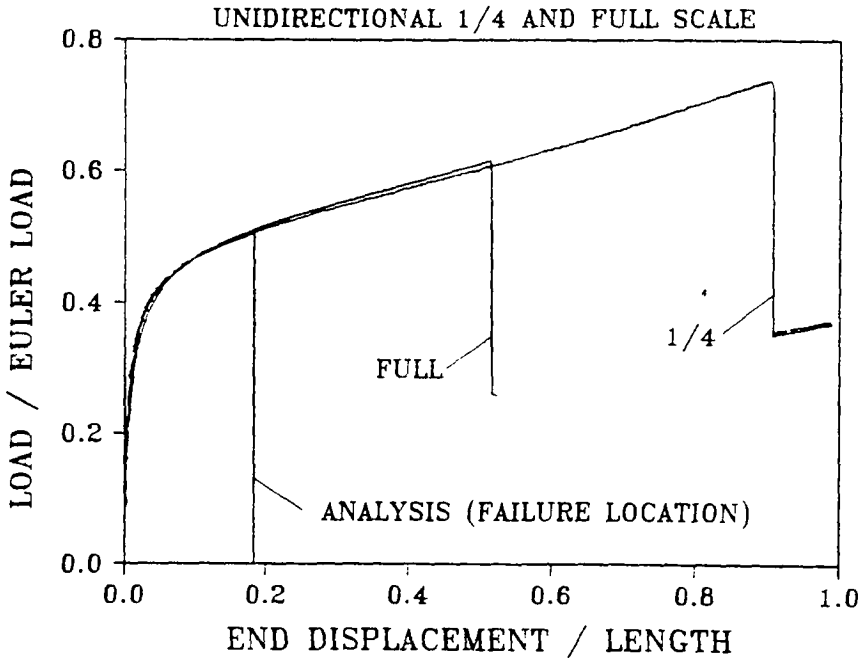

Figure 8-1. Predicted failure location for unidirectional laminates.

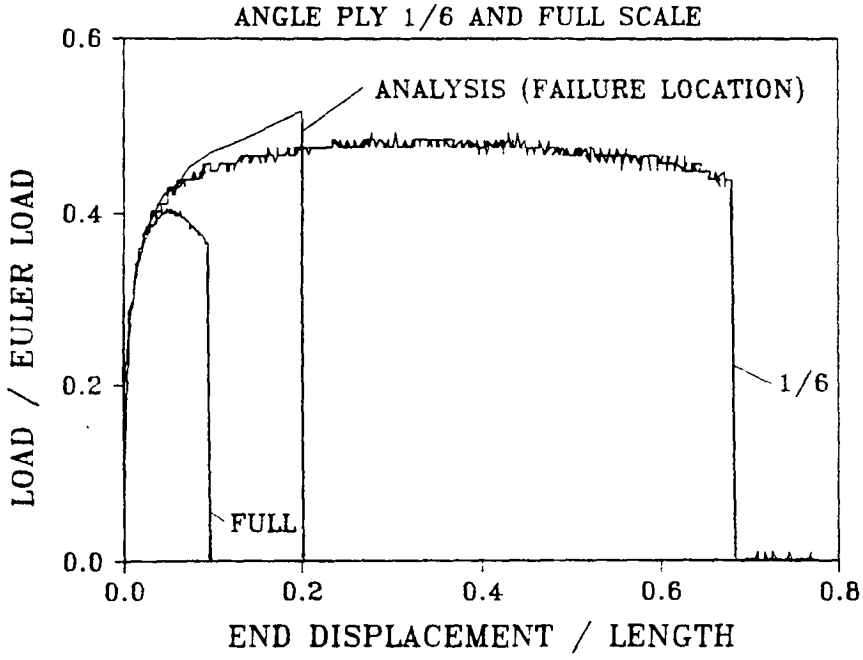

Figure 8-2. Predicted failure location for angle ply laminates.

criterion is exceeded at a higher load ratio of 0.545 and an end displacement ratio of 0.29 in the outer 0 degree ply on the compressive side of the beam. The failure predicted by the maximum stress and maximum strain criteria is plotted with the experimental load response for the 1/4 and full scale cross ply beams in Figure 8-3. The analytical failure prediction overestimates the full scale beam failure and is too conservative of the 1/4 scale failure.

The Tsai-Wu failure criterion predicts that first ply failure occurs in the 0 degree ply in compression for the quasi-isotropic laminates at a load ratio of 0.517 and an end displacement ratio of 0.2. This failure location is shown in Figure 8-4 along with the load-displacement response for the 1/6 and full scale quasi-isotropic beams. The predicted failure load ratio is close to the value observed for the full scale beam, but conservative for the 1/6 scale beam value. The predicted end displacement ratio at failure is conservative for both beams. The maximum stress and maximum strain criteria also predict that the first ply failure will occur in the 0 degree ply on the compressive side of the beam, but at a higher load ratio (0.549) and end displacement ratio (0.297).

8.2 Discussion of Failure Theories Capable of Predicting the Scale Effect in Strength

Results of applying maximum stress, maximum strain, and Tsai-Wu tensor polynomial failure criteria to the eccentrically loaded beam-column problem have demonstrated that these failure criteria cannot predict a difference in strength based on the absolute size of the specimen. To illustrate the magnitude of the scale effect in strength, the failure data listed in Tables 6-1 through 6-4 for the four laminate families have been normalized by the full scale value and plotted versus scale factor. The results are shown in Figures 8-5 through 8-8 for load ratio, end displacement ratio, tensile and compressive strains at failure, respectively. If no scale effect in

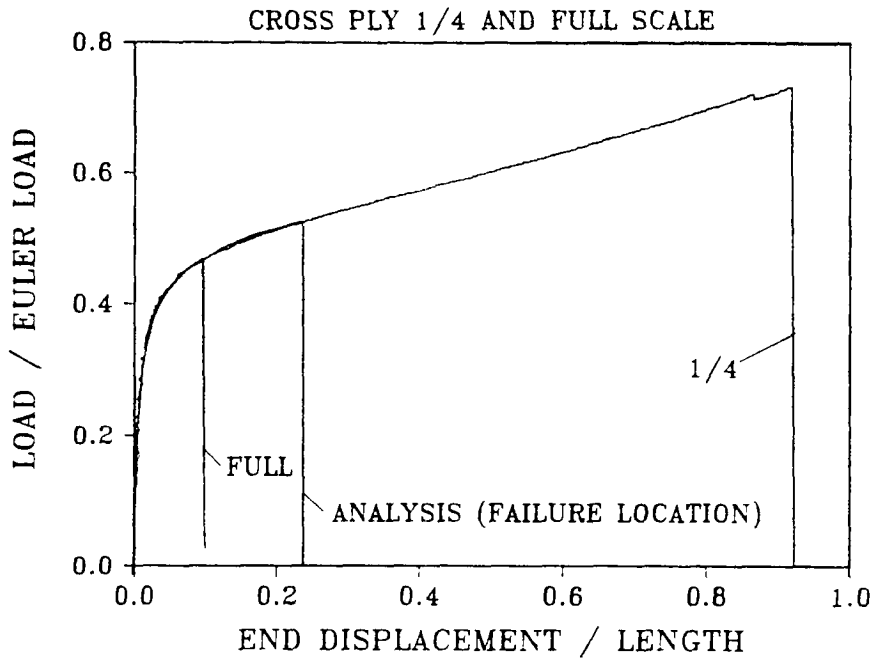

Figure 8-3. Predicted failure location for cross ply laminates.

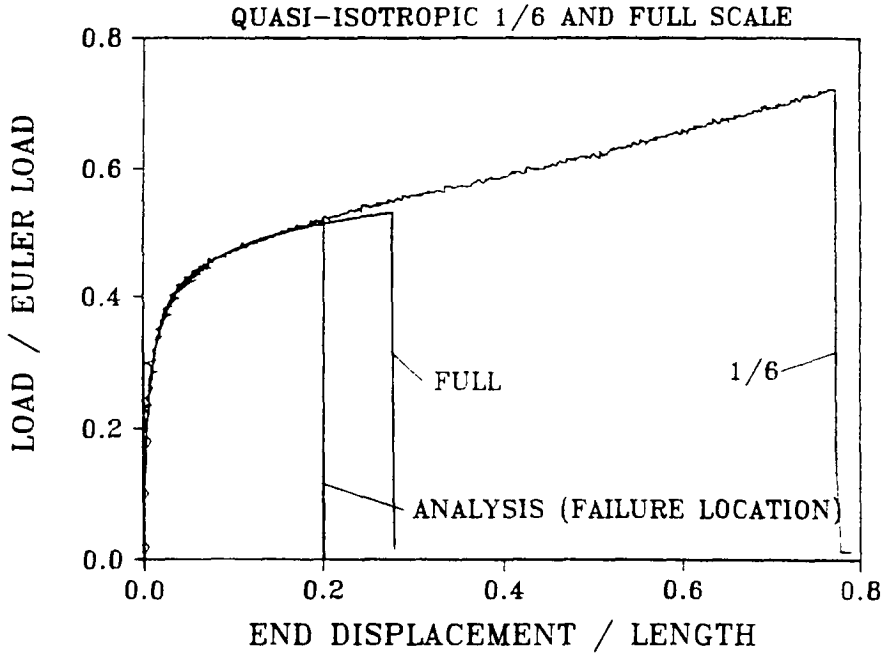

Figure 8-4. Predicted failure location for quasi-isotropic laminates

strength was present, then all of the data would fall on the line drawn at 1.0. These plots indicate that a scale effect is evident even between the full and 5/6 scale beams. The effect increases as the size of the beams decreases. In general, the cross ply laminate family exhibits the largest scale effect in strength among the laminates tested. The unidirectional laminates appear to be least sensitive to the size effect in strength, although the effect is still observed.

Previous researchers have attempted to model the scale effect in strength of fiber-reinforced composite structures using either a statistical approach or a fracture mechanics model. A discussion of these methods and their application to the eccentrically loaded beam-column problem will be presented in the next two sections.

8.2.1 Statistical Approaches

The application of statistical techniques for modeling the size effect in strength of brittle materials is based on the observation that these materials are flaw-sensitive. And, since the presence of imperfections can be statistical in nature, it is reasonable to assume that larger specimens will exhibit a lower strength simply because the probability is higher that a strength-critical flaw, such as a void or crack, is present in a greater volume of material. Typically, two approaches are defined to model the size effect. Weakest link theory assumes that a structure consists of a number of individual elements arranged in series. When one of these elements fails, the entire component fails. In contrast, bundle theory models a structure as a parallel arrangement of elements. When an element fails, the load is redistributed among the remaining elements. Final failure occurs when all of the elements have failed. Weibull statistical theory has been applied to both the weakest link and bundle theories to develop mathematical models for predicting the scale effect in strength. The ultimate failure of individual graphite fibers and fiber bundles has been successfully modeled using Weibull statistics based on the

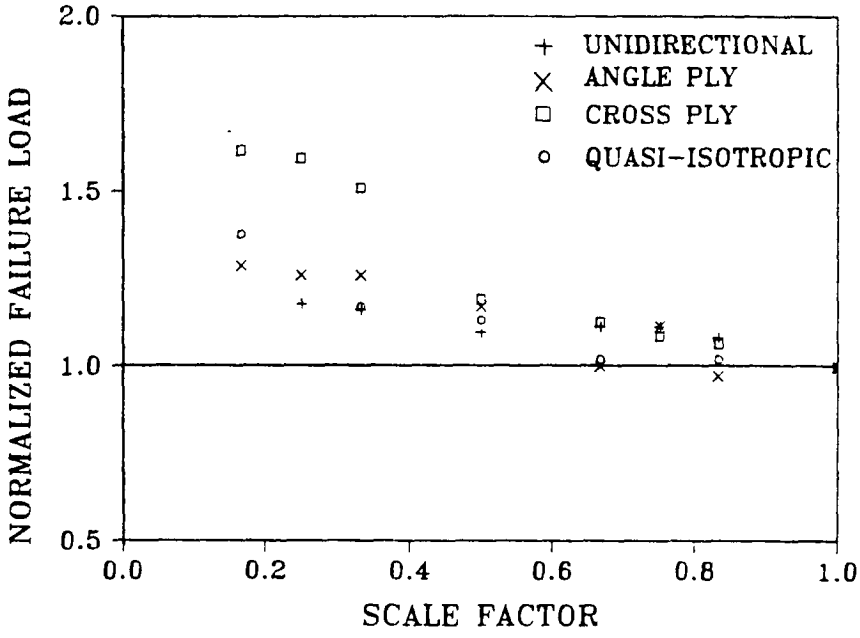

Figure 8-5. Normalized failure load ratio versus scale factor.

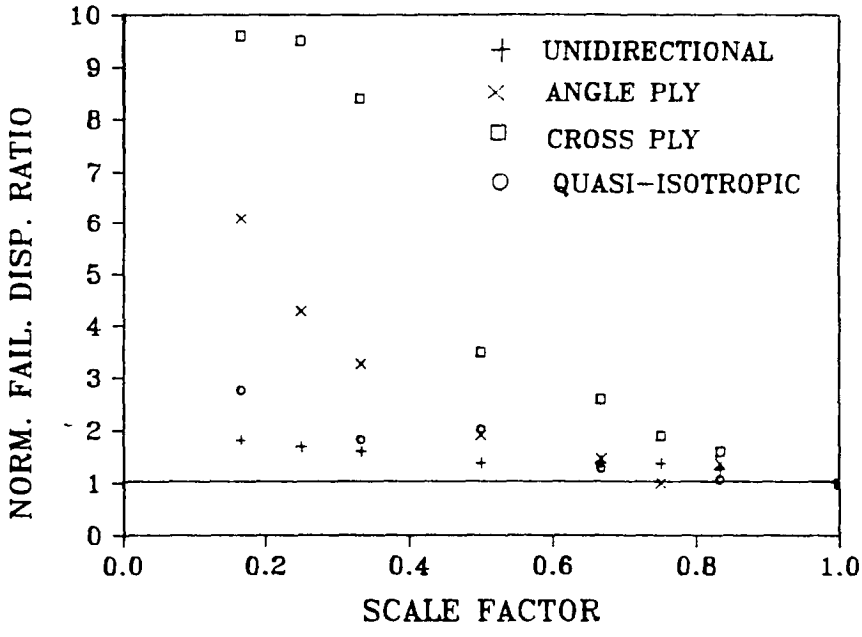

Figure 8-6. Normalized failure end displacement ratio versus scale factor.

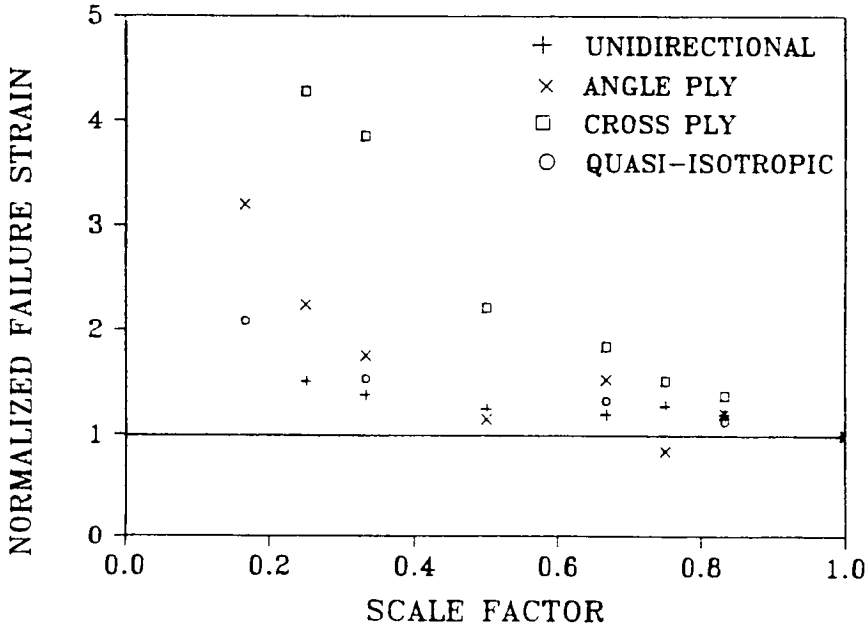

Figure 8-7. Normalized failure tensile strain versus scale factor.

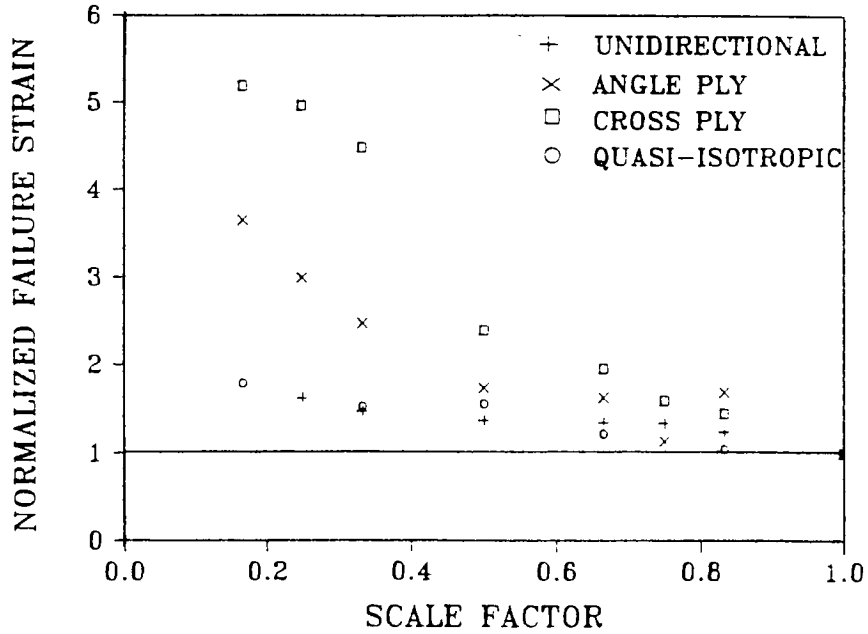

Figure 8-8. Normalized failure compressive strain versus scale factor.

weakest link theory [64,65]. Consequently, this model has been applied by other researchers to investigate the scale effect in strength of composite test specimens.

Statistical analysis has been used to explain the higher strength seen in composite coupons tested in flexure over those tested in uniaxial tension [66,67]. Using Weibull theory, Bullock [67] found that the probability that a specimen containing a distribution of flaws throughout its volume could survive an applied stress distribution, $\sigma(x,y,z)$, is:

$$S = \exp\left\{-\int_V \left[\frac{\sigma(x,y,z) - \sigma_u}{\sigma_o}\right]^{\beta}\right\} dx\ dy\ dz \tag{8.1}$$

where

- β is the flaw-density exponent which characterizes the scatter of strength data for the material
- σ_o is the normalizing scale parameter which locates the strength distribution
- σ_u is the threshold stress (usually assumed to be zero), and
- V is the volume of the specimen.

For uniform tensile loading conditions and σ_u assumed to be zero, Eq. 8.1 becomes:

$$S_t = \exp\left[-V_t\left(\frac{\sigma_t}{\sigma_o}\right)^{\beta}\right] \tag{8.2}$$

where the subscript t is used to identify tensile loading. For the case of three-point bending loading conditions the stress distribution is nonuniform and Equation 8.1 gives:

$$S_f = \exp\left\{-V_f\left(\frac{\sigma_f}{\sigma_o}\right)^{\beta}\left[\frac{1}{2(\beta+1)^2}\right]\right\} \tag{8.3}$$

where the subscript f is used to identify flexural loading. For two geometrically similar specimens (a model and a prototype) of volumes V_m and V_p, either Equation 8.2 or 8.3 can be used to derive the ratio of ultimate strengths for a given probability of failure:

$$\frac{\sigma_m}{\sigma_p} = \left(\frac{V_p}{V_m}\right)^{\frac{1}{\beta}} \tag{8.4}$$

It is interesting to note that the probability of failure of a specimen is dependent on the stress distribution which is determined by the loading conditions. However, the ratio of ultimate strengths for two specimens of different sizes is the same regardless of whether the specimens were tested under uniaxial tension or flexure. The ratio of median failure stress in three-point flexure to that in tension is found by setting S_t equal to S_f in Equations 8.2 and 8.3;

$$\frac{\sigma_f}{\sigma_t} = \left[2(\beta+1)^2\,\frac{V_t}{V_f}\right]^{\frac{1}{\beta}} \tag{8.5}$$

If two specimens of equal volume are tested in flexure and in tension, then by Equation 8.5, the flexural strength will be greater than the tensile strength by the factor:

$$\sigma_f = \left[2(\beta+1)^2\right]^{\frac{1}{\beta}} \sigma_t \qquad (8.6)$$

Bullock applied the statistical analysis presented in Equations 8.1 through 8.6 to predict the strength behavior of graphite-epoxy (T300/5208) composite specimens. Tests were conducted on fiber tows, and tensile and flexural specimens to verify the analysis. An important finding from Bullock's research is that the flaw-density exponent, β, which must be determined empirically, was found to be a material constant. For the composite material system he tested, the value of flaw-density exponent was determined to be approximately 24. Bullock showed good agreement between experiment and analysis and concluded that less expensive flexural specimens which are easier to test can be used to estimate ultimate tensile stresses of composite materials.

While Bullock's results show promise for predicting the ultimate strength of specimens which are tested under different loading conditions, the volume term was found to overestimate the actual volume effect for specimens of greatly different sizes. A limitation of the method includes the requirement that the flaw-density exponent be found empirically for each material system. Also, no data were presented to indicate how well the model would perform for laminates containing off-axis plies. The flaw-density exponent, β, would likely be influenced by the laminate stacking sequence, especially for laminates in which failure mechanisms were matrix dominated and not governed by fiber fractures.

The volumetric model given by Equation 8.4 is used to predict the scale effect in strength observed in the failure response of the eccentrically loaded beams tested in this investigation. The model is applied even though the static test data were not intended to provide a significant number of samples for a thorough statistical analysis. The flaw-density exponent was calculated from results reported by Sensmeier [38] from his material characterization tests on the

AS4/3502 graphite-epoxy composite material. Sensmeier found the longitudinal tensile strength to be 178.1 ksi. However, he observed that the failure strains of the eccentrically loaded beams were much higher than the failure strains determined from material tests on beams loaded in uniaxial tension. Consequently, he used the flexural failure strains to calculate a new longitudinal tensile strength which he determined to be 340.0 ksi. These values are used in Equation 8.6 to solve for the flaw-density exponent, $\beta = 7.75$. Results of the volumetric ratio as calculated from Equation 8.4 are plotted in Figure 8-9 with the experimental data for each of the laminate families. The failure stress ratios were calculated from the strain ratios listed in Tables 6-1 through 6-4 for the four laminate types. As shown in Figure 8-9, the volumetric ratio predicts the scale effect in tensile strength fairly well for the unidirectional and quasi-isotropic laminates. However, agreement between the volumetric ratio and the angle ply and cross ply laminates is not good. This is not unexpected since the failure mechanisms for the angle ply and cross ply laminates are characterized by transverse matrix cracking; but, the flaw-density exponent was determined based on tests of unidirectional laminates which fail by fiber fracture. Obviously, the volumetric ratio is sensitive to the failure mode and should only be applied for laminates which exhibit similar failure mechanisms.

In summary, results indicate that the Weibull statistical model based on the weakest link theory does predict a scale effect in strength due to volumetric differences, and provides good agreement on a material level in predicting the behavior of fiber tows and unidirectional tensile coupons. The model also predicts the observed scale effect in tensile strength for the eccentrically loaded unidirectional and quasi-isotropic beam-columns. However, the model lacks the sophistication needed to predict the difference in magnitude of the scale effect in strength for laminates which do not fail predominantly by fiber fracture.

As a final note, more advanced statistical models have been developed using a two parameter Weibull distribution to analyze the

scale effect in strength and fatigue response of composite structures [68,69]. These models have been successful in predicting scale effects; however, they rely heavily on empirical data to determine the Weibull shape and scale parameters. In addition, the methods have not been applied specifically to replica models. Instead, the effect of varying specimen width, or length, independently of the other specimen dimensions has been studied. When the results are examined for replica models, no noticeable strength variations are found.

8.2.2 Fracture Mechanics Theories

Some of the basic principles of linear elastic fracture mechanics (LEFM) have been applied to model the scale effect in strength of composite laminates. Atkins and Caddell [10] derived a new dimensionless group based on the mechanics of crack propagation and fracture to scale ice-breaking resistance from tests conducted on model ships in ice-towing tanks. And, Carpinteri and Bocca [70] explained the transition from slow crack growth to rapid propagation using strain energy density theory and dimensional analysis. These are just two examples of some of the research which has been conducted to explain the size effect in material strength.

A thorough analysis of the eccentrically loaded beam-column problem using fracture mechanics techniques was not attempted. However, one of the advantages of dimensional analysis is that some insight into a problem may be gained without a rigorous or complete mathematical solution. The stresses in the region near a sharp crack in a body have been derived by Irwin [71] and Williams [72] and have the general form:

$$\sigma_{ij} = \frac{K}{\sqrt{2\pi r}} f_{ij}(\theta) \tag{8.7}$$

where K is the crack tip stress intensity factor, r and θ are polar coordinates to locate a point in the stress field beyond the crack tip, and f_{ij} is a nondimensional function of the variable θ. Irwin [71] and Williams [72] showed that this crack tip stress field is independent of the loading. Thus, all cracks will have the same stress field and will only differ by the intensity factor, K, from one problem to the next. The form of the stress intensity factor is found by performing an elastic stress analysis of the particular problem. Many of the functional forms for K have been calculated and tabulated. However, the exact form of the stress intensity factor is not required to understand how it contributes to the scale effect in strength. A theory of fracture mechanics states that a crack will become unstable when the crack tip stress intensity factor reaches the critical value, K_Q. The critical stress intensity factor is assumed to be a material constant and may be found experimentally through standard materials tests. K_Q was included in the list of parameters used to perform a dimensional analysis for the beam-column impact problem in Chapter 2. From that analysis, a scaling conflict was found since it was impossible to scale stress as unity and have K_Q scale as unity at the same time. If K_Q is assumed to be a material constant ($\lambda_{K_Q} = 1$), then stress must scale as $\lambda^{-1/2}$.

Predicted failure stresses using the fracture model are depicted in Figure 8-10 along with the experimental data for each of the four laminate types. The fracture ratio tends to overpredict the scale effect in strength for the smaller scale model unidirectional and quasi-isotropic laminates, and underpredicts the effect for the angle ply and cross ply laminates. The cross ply laminate response deviates from the fracture ratio model by the largest amount, especially for the smaller scale model beams. In general, the fracture ratio is capable of predicting a scale effect in strength; but, like the volumetric model, the fracture model does not predict any variation in the scale effect due to differences in laminate stacking sequence. Results presented in Figure 8-10 show that a model which

predicts the scale effect in strength must incorporate some measure of the failure mechanism of the laminate to be successful.

Results presented in this section have shown that the scale effect in strength cannot be explained simply by statistical models or fracture mechanics theories. However, research by Crossman [73], Wang [74], and Laws [75] on the effects of transverse matrix cracking on the final fracture of cross ply laminates suggests that a model which incorporates both theories is needed. A statistical approach is used to determine which microflaws within the 90 degree core of the laminate will coalesce to form a transverse matrix crack given a random distribution of flaws and flaw sizes. Once a crack has formed, fracture mechanics theories are applied to determine the stability of the crack given the loading condition. The progression of crack formation and stability are continually monitored for increased loading conditions. In addition, the model developed by Laws [75] will predict loss of stiffness as a function of crack density. A model of this type has been used to successfully predict the ultimate tensile failure of cross ply laminates in which the number of 90 degree plies was varied from 2 to 16. These laminates are not replica models since the number of 0 degree plies was not adjusted in the same proportion as the number of 90 degree plies. However, the success of the model indicates that it may be able to accurately predict the scale effect in strength for laminates of varying sizes and stacking sequences.

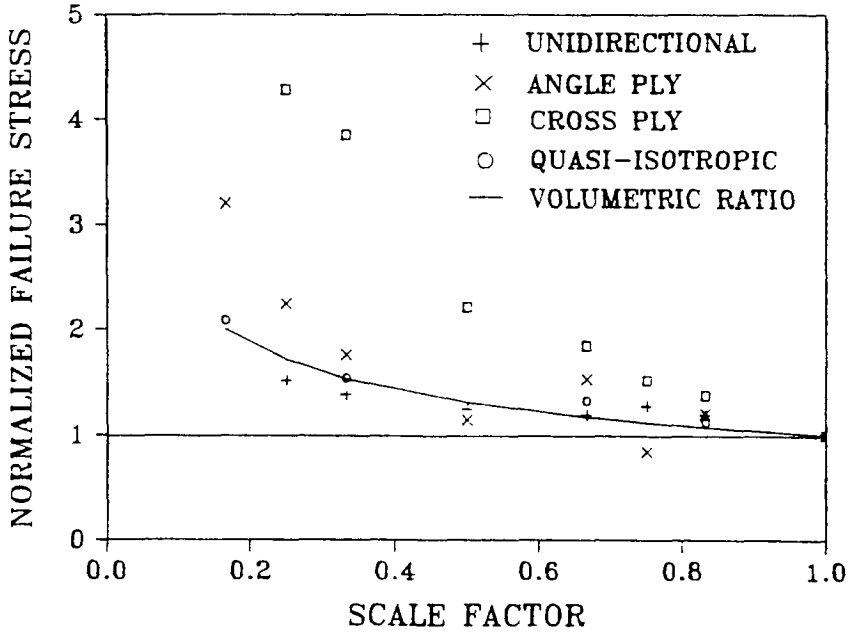

Figure 8-9. A comparison of the volumetric ratio prediction of normalized failure tensile stress versus scale factor and experimental results.

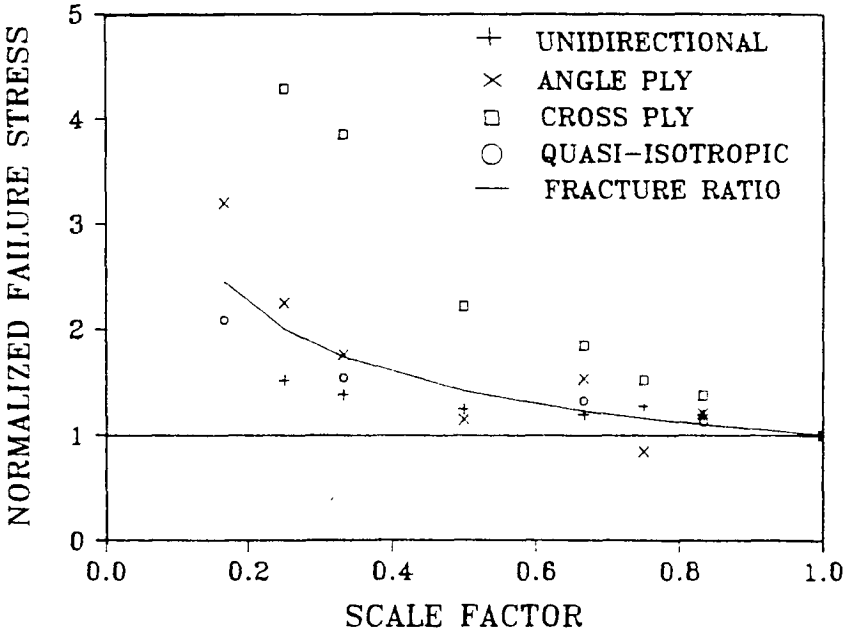

Figure 8-10. A comparison of the fracture ratio prediction of normalized failure tensile stress versus scale factor and experimental results.

Chapter 9 - Summary and Recommendations

The objective of this study was to characterize scaling effects in the static and dynamic large deflection response and failure of graphite-epoxy composite beam-columns. To accomplish this objective, a comprehensive testing program was conducted on a wide range of scale model beams and a variety of laminate stacking sequences representing different stiffnesses and failure modes. The scale model beams were tested under an eccentric axial compressive load designed to produce large bending deflections and global failure. Both static and impulsive loading conditions were applied. A dimensional analysis was performed on the composite beam-column loading configuration to determine a model law governing the system response. The model beams were loaded under scaled test conditions until catastrophic failure. Comparisons of the load and strain data for the scale model beams were made to identify scaling effects in the beam response. Also, a qualitative assessment of the damaged beams was made to determine if beam size influenced the mode of failure.

Various analysis techniques were used to model the eccentrically loaded beam-column. For the static case, a one-dimensional, large deflection beam solution was derived based on the "elastica" problem. The beam solution assumes linear elastic material properties and incorporates the exact expression for beam curvature. The nonlinear structural analysis finite element program DYCAST (DYnamic Crash Analysis of STructures) was used to model the beam-column under both static and impulsive loading conditions. Finally, a finite element analysis which was developed specifically for the beam-column problem was used to study the importance of including width-wise degrees of freedom and nonlinear material properties on the beam response. A stress analysis was incorporated into the large deflection beam solution to apply failure criteria including maximum stress, maximum strain, and Tsai-Wu tensor polynomial to predict beam failure. Statistical approaches and fracture mechanics theories

were also discussed as possible methods for predicting the observed scale effect in strength.

The major findings from this investigation are summarized and suggestions for further work are discussed in the following sections of this chapter.

9.1 Summary of Research

Major conclusions and findings from the experimental and analytical study which was conducted to characterize scaling effects in the large deflection static and dynamic response of composite beam-columns are listed below.

(1.) No scaling effects were observed in the static load and strain response of the unidirectional and cross ply laminates, even for very large deflections and rotations. However, the angle ply and quasi-isotropic laminates deviated from scaled response due to damage events which altered the beam stiffness. These results indicate that the success of achieving scaled response is dependent on the laminate stacking sequence with the best results seen for laminates with a large percentage of 0 degree plies.

(2.) Lamination theory predictions of effective bending stiffnesses based on material properties of the AS4/3502 system were found to be in error by as much as 25 percent. Consequently, the Euler load for each of the scale model beams was calculated using an effective bending stiffness which was determined semi-empirically. The bending stiffnesses were found by matching the analysis and experimental data in the small deflection response region. A comparison of the normalized bending stiffnesses for each of the scaled model beams indicated that no scale effect exists in elastic behavior for the unidirectional, cross ply, and quasi-isotropic laminates. However, a significant scale effect was seen for the angle ply laminates in which the smaller scale model beams were much stiffer than the full scale beam.

(3.) A scale effect in strength was observed for all four laminate types (unidirectional, angle ply, cross ply, and quasi-isotropic) tested under static loading conditions. In general, the failure loads, end displacement ratios, and strains increased as the scale factor decreased. This result implies that data generated from tests on scale model specimens will overestimate ultimate loads of prototype structures.

(4.) In general, the failure mechanisms of the laminates tested were independent of the specimen size. The one exception was the cross ply laminate family which exhibited a transition in failure mechanism between the 1/3 and 1/2 scale model beams. The smaller scale model beams contained fiber fractures not seen in the beams of 1/2 scale or larger. The transition in failure mechanism was evident in the load and strain response.

(5.) Both the large deflection beam solution and DYCAST finite element analysis predicted the load-deflection response well for the unidirectional, cross ply, and quasi-isotropic laminates. The angle ply laminates experienced damage which caused a reduction in beam stiffness and affected the load response. Neither the beam solution or DYCAST analysis could model the partially damaged beam and, thus, overpredicted the load behavior.

(6.) The finite element analysis developed by Sensmeier which includes the effect of width-wise degrees of freedom and nonlinear material properties consistently overpredicted the load response for each of the laminates tested. However, the analysis was able to predict the difference in compressive and tensile strain magnitudes which was observed in the experimental strain response for the four laminate families tested.

(7.) The unidirectional beams tested under impulsive loading conditions showed excellent scaled response. However, inconsistent results were obtained for the angle ply, cross ply, and quasi-isotropic laminates. A scale effect in strength was also evident under dynamic loading conditions. The mode of failure between scaled beams within a laminate family was independent of beam size; however, the

smaller scale model quasi-isotropic beams appeared to be more severely damaged.

(8.) The DYCAST finite element model successfully predicted the dynamic strain response of the unidirectional and quasi-isotropic 1/2 scale model beams, including the initial inversion of tensile and compressive strains, upon impact. In addition, the DYCAST code provided valuable plots of the deformed shape of the beams during loading.

(9.) Comparisons between the dynamic and static data for beams of the same scaled size and laminate type indicated similar responses following the initial load spike and strain inversion due to the impact. This finding implies that valuable insight into the global, dynamic response of structures subjected to impact can be found from tests under static loading conditions.

(10.) Analysis of beam failure using maximum stress, maximum strain, and Tsai-Wu tensor polynomial criteria showed that these theories cannot predict the scale effect in strength.

(11.) The scale effect in strength which was observed for the eccentrically loaded beam-columns cannot be explained by simple statistical models based on Weibull distributions of flaw-densities and the weakest link approach, or by fracture mechanics models based on the critical stress intensity factor. Both of these approaches can predict a scale effect in strength, but do not account for variations in the magnitude of the scale effect due to differences in laminate stacking sequences.

9.2 Recommendations for Future Research

Results of this investigation show that tests on scale model composite structures can provide valuable information on the response of prototype structures. However, if the testing involves failure or damage to the laminate, then scale model data will overpredict the strength of the full scale structure based on the observed size effect in strength. Consequently, any failure criteria

used to predict strength of a composite structure should allow for the size effect. As discussed in Chapter 8, the failure models which incorporate both statistical and fracture mechanics theories possess the capabilities to successfully analyze the size effect and should be applied to this problem.

The scale model beams tested in this investigation were fabricated to achieve scaling on a ply level by increasing the number of plies at each orientation in the laminate stacking sequence. However, in some cases it may not be possible to construct an exact scale model of a composite laminate on a ply level. For example, in this study it was not possible to fabricate a 1/4 or 3/4 scale model quasi-isotropic beam. In other cases, it may not be necessary to test an exact replica model as long as the stiffness is scaled. Composites which are scaled on a sub-laminate level may be acceptable for such cases. Tests on composite laminates which are not scaled on a ply-by-ply basis should be conducted to identify scaling issues for these types of models.

In general, the results of the experimental program indicate that no scaling effects are present in the elastic response. This finding implies that the elastic moduli are not a function of specimen size. However, to verify this observation, a series of material characterization tests should be performed on replica model coupon specimens.

The impact tests which were performed as part of this investigation were conducted under conditions to ensure failure of the beams. As such, it was difficult to study the effects of impact on the initiation and growth of damage in the scale model beams. A testing program in which dynamic loads are applied to produce an elastic response, and then gradually increased to promote beam failure, should be performed. A systematic approach such as this would provide more detailed information on the size effect in strength of laminates under impact loading conditions.

The angle ply laminates were included in this study primarily for academic interest since most structural composite laminates

contain some 0 and 90 degree plies. However, the poor agreement between the analyses and experimental load-deflection results for these laminates illustrates that analytical models need to include stiffness reduction schemes when transverse matrix cracking occurs. The DYCAST finite element code, in particular, is currently being upgraded to incorporate laminated composite elements and will include partial ply failure capabilities.

Finally, the composite beam-column under eccentric axial compressive load was chosen for study because it represented a simple structural configuration, yet possessed some interesting features such as large deflections, combined tensile and compressive loading, and global failures. If a more complex system had been studied, it would have been difficult to isolate size effects from the effects of other structural details. However, the benefits of scale model technology must be demonstrated for real engineering structures. Thus, research of this type should be expanded to include other structural elements with increasing levels of complexity.

Chapter 10 - REFERENCES

1. Freeman, W. T.: "Innovation, Damage Tolerance, and Affordability- NASA's New Thrust for Composites Research." presentation at the 1989 General Aviation Aircraft Meeting and Exposition, sponsored by the SAE, Wichita, Kansas, April 13, 1989.

2. Davies, I. L.: "Studies of the Response of Reinforced Concrete Structures to Short Duration Dynamic Loads." *Design For Dynamic Loading, The Use of Model Analysis*, G. S. T. Armer and F. K. Garas (eds.) London: Construction Press, 1982.

3. Murayama, Y.; and Noda, S.: "Study on Small Scale Model Tests for Reinforced Concrete Structures- Small Scale Model Tests by Using 3MM Diameter Deformed Re-bars." Kajima Institute of Construction Technology, Tokyo, Feb. 1983.

4. Pletta, D. H.; and Frederick, D.: "Model Analysis of a Skewed Rigid Frame Bridge and Slab." *Journal of the American Concrete Institute*, Vol. 26, No. 3, Nov. 1954, pp. 217-230.

5. Pletta, D. H.; and Frederick, D. : "Experimental Analysis." *Proceedings ASCE*, Vol. 79, No. 224, 1953.

6. Haritos, G. K.; Hager, J. W.; Amos, A. K.; Salkind, M. J.; and Wang, A. S. D.: "Mesomechanics: The Microstructure-Mechanics Connection." AIAA Paper 87-0726, *A Collection of Technical Papers Part 1*, 28th Structures, Structural Dynamics and Materials Conference, April 1987, pp. 812-818.

7. Booth, E.; Collier, D.; and Miles, J.: "Impact Scalability of Plated Steel Structures." *Structural Crashworthiness*. Jones and Wierzbicki, eds., London: Butterworths, 1983, pp. 136-174.

8. Duffey, T. A.: "Scaling Laws For Fuel Capsules Subjected to Blast, Impact, and Thermal Loading." *Proceedings of the 1971 Intersociety Energy Conversion Engineering Conference*, Boston, Mass., August 1971, pp. 775-786.

9. Jones, N.: "Scaling of Inelastic Structures Loaded Dynamically." *Structural Impact and Crashworthiness*, Davies, ed., Vol. 1 Keynote Lectures, London: Elsevier Applied Science Publishers, 1984, pp. 46-71.

10. Atkins, A. G.; and Caddell, R. M.: "The Laws of Similitude and Crack Propagation." *International Journal of Mechanical Sciences*, Vol. 16, 1974, pp. 541-548.

11. Ehrlich, I. R.: "Some New Approaches to Scale Modeling." *Journal of Terramechanics*, Vol. 22, No. 1, 1985, pp. 3-16.

12. Baker, W. E.; Westine, P. S.; and Dodge, F. T.: *Similarity Methods in Engineering Dynamics.* Rochelle Park, N.J.: Hayden Book Company, 1973.

13. Langhaar, H. L.: *Dimensional Analysis and Theory of Models.* New York: John Wiley and Sons, Inc., 1951.

14. Murphy, G.: *Similitude in Engineering.* New York: Ronald Press, 1950.

15. Sedov, L. I.: *Similarity and Dimensional Methods in Mechanics.* trans. by Morris Friedman, ed., Maurice Holt, New York: Academic Press, 1959.

16. Bridgman, P. W.: *Dimensional Analysis.* New Haven: Yale University Press, 1922.

17. Buckingham, E.: "On Physically Similar Systems; Illustrations of the Use of Dimensional Equations." *Physical Review*, Series II-4, Oct. 1914, pp.345-376.

18. Macagno, E. O.: "Historical-Critical Review of Dimensional Analysis." *Journal of the Franklin Institute*, Special Issue Modern Dimensional Analysis, Vol. 292, No. 6, Dec. 1971, pp. 391-402.

19. Brooks, G.: "Principles and Practices for Simulation of Structural Dynamics of Space Vehicles." VPI Conference on the

Role of Simulation and Space Technology, Blacksburg, VA., August 1964.

20. Gronet, M. J.; Pinson, E. D.; Voqui, H. L.; Crawley, E. F.; and Everman, E. R.: "Preliminary Design, Analysis, and Costing of a Dynamic Scale Model of the NASA Space Station." NASA CR 4068, July 1987.

21. Hanks, B. R.; and Pinson, L. D.: "Large Space Structures Raise Testing Challenges." *Astronautics and Aeronautics*, Oct. 1983, pp. 34-40.

22. Hanks, B. R.; and Stephens, D.: "The Mechanisms and Scaling of Damping in a Practical Structural Joint." presented at 36th Shock and Vibration Symposium, Los Angeles, CA., Oct. 1966.

23. Jaszlics, I. J.; and Park, A. C.: "Use of Dynamic Scale Models to Determine Launch Vehicle Characteristics: Final Report Vol.I. Analytical Investigation." NASA CR 102272, August 1969.

24. Regier, A.: "The Use of Scaled Dynamic Models in Several Aerospace Vehicle Studies." presented at *ASME Colloquium on the Use of Models and Scaling in Simulation of Shock and Vibration*, Philadelphia, PA., Nov. 1963.

25. Armer, G. S. T.; and Garas, F. K. (eds.): *Design for Dynamic Loading: The Use of Model Analysis.* New York: Construction Press, 1982.

26. Baker, W. E.: "Scaling and Prediction of Impact Puncture of Shipping Casks For Radioactive Materials." *The Shock and Vibration Bulletin*, Bulletin 48, 1978, pp. 143-152.

27. Emori, R. I.: "Scale Models of Automobile Collisions with Breakaway Obstacles." *Experimental Mechanics*, Feb. 1973, pp. 64-69.

28. Gustafson, A. J.; Ng, G. S.; and Singley, G. T.: "Impact Behavior of Fibrous Composites and Metal Substructures." USAAVRADCOM TR-82-D-31, 1982.

29. Tennyson, R. C.; Hansen, J. S.; Teichman, H.; Cicci, F.; and Ioannou, M.: "Crashworthiness Tests on Model Aircraft Fuselage Structures." AIAA Paper No. 79-0688, 1979.

30. Holmes, B. S.; and Sliter, G.: "Scale Modeling of Vehicle Crashes-Techniques, Applicability, and Accuracy; Cost Effectiveness." SAE Paper 740586, 1974.

31. Church, J. W.; and Andrews, J.: "A Model for the Simulation of Wave Impact Loads and Resulting Transient Vibration of a Naval Vessel." *Use of Models and Scaling in Shock and Vibration*, W. E. Baker, ed., New York: ASME, Nov 1963, pp. 16-28.

32. Sperrazza, J.: "Modeling of Air Blast." *Use of Models and Scaling in Shock and Vibration*, W. E. Baker, ed., New York: ASME, Nov 1963, pp. 65-70.

33. McCullers, L. A.; and Naberhaus, J. D.: "Automated Structural Design and Analysis of Advanced Composite Wing Models." *Computers and Structures,* Vol. 3, 1973, pp. 925-937.

34. Verderaime, V. S.: "Scaling Phenomena of Graphite-Epoxy Wound Cases." *Proceedings of the Seventh Conference on Fibrous Composites in Structural Design*, AFWAL-TR-85-3094, June 1985.

35. Fairfull, A. H.: "Scaling Effects in the Energy Absorption of Axially Crushed Composite Tubes." Ph.D. dissertation, University of Liverpool, 1986.

36. Morton, J.: "Scaling of Impact-Loaded Carbon-Fiber Composites." *AIAA Journal* , Vol. 26, No. 8, August 1988, pp. 989-994.

37. Derian, E. J.; and Hyer, M. W.: "Large Deformation Dynamic Bending of Composite Beams." NASA CR 4006, August 1986.

38. Sensmeier, M. D.; Griffin, O. H.; and Johnson, E. R.: "Static and Dynamic Large Deflection Flexural Response of Graphite-Epoxy Beams." NASA CR 4118, March 1988.

39. Fasanella, E. L.; Hayduk, R. J.; and Widmayer, E.: "Analysis of a Fuselage Section Drop Test." NASA CR 2335, June 1984.

40. Pifko, A. B.; Winter, R.; and Ogilvie, P.: "DYCAST- A Finite Element Program for the Crash Analysis of Structures." NASA CR 4040, January 1987.

41. Shames, I.H.: *Mechanics of Fluids.* McGraw-Hill Book Company: New York, 1962.

42. Barr, D. I.: "Consolidation of Basics of Dimensional Analysis." *Journal of Engineering Mechanics.* Vol. 110, No. 9, September, 1984, pp.1357- 1376.

43. Barr, D. I.: "A Survey of Procedures for Dimensional Analysis." *International Journal of Mechanical Engineering Education.* Vol. 11, No. 3, September 1982, pp. 147-159.

44. Barr, D. I.: "Echelon Matrices in Dimensional Analysis." *International Journal of Mechanical Engineering Education.* Vol. 7, No. 2, 1979, pp. 85-89.

45. Barr, D. I.: "Consolidation of the Webb and Fryer Procedure for Dimensional Analysis." *International Journal of Mechanical Engineering Education.* Vol. 10, No. 4, 1982, pp. 279-286.

46. Carden, H. D.: "Impact Dynamics Research on Composite Transport Structures." NASA Technical Memorandum 83691, March 1985.

47. Jackson, K. E.: "Scaling Effects in the Static Large Deflection Response of Graphite-Epoxy Beam-Columns." *Proceedings of the Third Technical Conference on Composite Materials*, Seattle, Washington, September 1988, pp. 655-666.

48. Jackson, K. E.; and Fasanella, E. L.: "Scaling Effects in the Static Large Deflection Response of Graphite-Epoxy Composite Beams." *Proceeding of the American Helicopter Society National Technical Specialists' Meeting on Advanced Rotorcraft Structures*, October 1988, Williamsburg, Virginia.

49. Boitnott, R. L.; Fasanella, E. L.; Calton, L. E.; and Carden, H. D.: "Impact Response of Composite Fuselage Frames." SAE Technical Paper 871009, presented at General Aviation Aircraft Meeting and Exposition, Wichita, Kansas, April 28-30, 1987.

50. Fasanella, E. L.; Widmayer, E.; and Robinson, M. P.: "Structural Analysis of the Controlled Impact Demonstration of a Jet Transport Airplane." *Journal of Aircraft*, Vol. 24, No. 4, April 1987, p. 274.

51. Simitses, G. J.: *An Introduction to the Elastic Stability of Structures*. Robert E. Krieger Publishing Co.: Malabar, Florida, 1986.

52. Whitney, J. M. : *Structural Analysis of Laminated Anisotropic Plates.* Lancaster: Technomic Publishing Co., 1987.

53. Jones, R. M. : *Mechanics of Composite Materials.* Washington, D.C.: Scripta Book Co., 1975.

54. Timoshenko, S. P. : *History of Strength of Materials.* New York: Dover Publications, Inc. 1983.

55. Bickley, W. G.: "The Heavy Elastica." *Philosophical Magazine*, Vol. 17, 1934, pp. 603-622.

56. Bisshopp, K. E.; and Drucker, D. C.: "Large Deflection of Cantilever Beams." *Quarterly of Applied Mathematics.* Vol. III, No. 3, October 1945, pp. 272-275.

57. Saelman, B.: "Some Formulas for the Large Deflections of Beam Columns." *Journal of the Franklin Institute*, Vol. 257, Jan-Jun 1954, pp. 125-132.

58. McComb, H. G., Jr.: "Large Deflections of a Cantilever Beam Under Arbitrarily Directed Tip Load." NASA TM 86442, May 1985.

59. Frisch-Fay, R.: *Flexible Bars.* Washington, D.C.: Butterworth and Co. Publishers, 1962.

60. Timoshenko, S. P.; and Gere, J. M.: *Theory of Elastic Stability.* New York: McGraw-Hill Book Company, 1961.

61. Sathyamoorthy, M.: "Nonlinear Analysis of Beams Part 1: A Survey of Recent Advances." *Shock and Vibration Digest,* Vol.14, No. 8, August 1982, p. 19-35.

62. Jackson, K. E.; and Fasanella, E. L.: "Scaling Effects in the Static Large Deflection Response of Graphite-Epoxy Composite Beams." NASA TM 101619, June 1989.

63. Whitney, J. M.; Browning, C. E.; Mair, A.: "Analysis of the Flexure Test for Laminated Composite Materials." *Composite Materials: Testing and Design (Third Conference),* ASTM STP, American Society for Testing and Materials, pp. 30-45, 1974.

64. Korabel'nikov, Y. G.; Tamuzh, V. P.; Siluyanov, O. F.; Bondarenko, V. M.; and Azarova, M. T.: "Scalar Effect of Fiber Strength and Properties of Unidirectional Composites Based on Them." Translation of "Masshtabnyy effekt prochnosti volokon i svoustva odnonapravlennykh kompozitov na ikh osnove." In:Mekhanika Kompozitnykh Materialov, 1984, March-April, No. 2, pp.195-200.

65. Lanza, F.; and Burg, H.: "Investigation of the Volume Effect on Mechanical Properties of Various Industrial Graphites." *Proceedings of the 11th Biennial Conference on Carbon.* Gatlinburg, Tn., June, 1973, pp. 223-224.

66. Zweben, C.: "The Effect of Stress Nonuniformity and Size on the Strength of Composite Materials." *Composites Technology Review,* Vol. 3, No. 1, 1981, pp. 23-26.

67. Bullock, R. E.: "Strength Ratios of Composite Materials in Flexure and Tension." *Journal of Composite Materials,* Vol. 8, April 1974, pp. 200-206.

68. Wang, A. S. D.; Tung, R. W.; and Sanders, B. A.: "Size Effect on Strength and Fatigue of a Short Fiber Composite Material." *Emerging Technologies in Aerospace Structures, Design,*

Structural Dynamics and Materials, ASME, August 1980, pp. 37-52.

69. Chou, P. C.; and Croman, R.: "Scale Effect in Fatigue of Composite Materials." *Journal of Composite Materials*, Vol. 13, July 1979, pp. 178-194.

70. Carpinteri, A.; and Bocca, P.: "Transferability of Small Specimen Data to Full-Size Structural Components." *Composite Material Response: Constitutive Relations and Damage Mechanisms*, G. C. Sih, G. F. Smith, I. H. Marshall, and J.J. Wu (eds.) London: Elsevier Applied Science, 1987.

71. Irwin, G. R.: "Analysis of Stresses and Strains Near the End of a Crack Transversing a Plate." *Journal of Applied Mechanics*, June 1957.

72. Williams, M. L.: "On Stress Distribution as the Base of a Stationary Crack." *Journal of Applied Mechanics*, March 1957.

73. Crossman, F. W.; Warren, W. J.; and Wang, A. S. D.: "Influence of Ply Thickness on Damage Accumulation and Final Fracture." *Advances in Aerospace Structures, Materials, and Dynamics: A Symposium on Composites*, ASME Publication AD-06, 1983, pp. 215-226.

74. Wang, A.S.D.; Chou, P.C.; and Lei, S.C.: "A Stochastic Model for the Growth of Matrix Cracks in Composite Laminates." *Advances in Aerospace Structures, Materials, and Dynamics: A Symposium on Composites*, ASME Publication AD-06, 1983, pp. 7-16.

75. Laws, N.; and Dvorak, G.J.: "Progressive Transverse Cracking in Composite Laminates." *Journal of Composite Materials*, Vol. 22, October 1988, pp. 900-916.

Appendix A. Dimensional Analysis of Beam-Column Impact Problem

A stepwise approach for determining the Pi terms, or nondimensional parameters, which form the scaling law for the beam-column impact problem, depicted in Figure 1-1, is presented. More complete details of the procedure are outlined in Baker, et al [12].

The first step involves listing the variables associated with the problem, along with a symbol for the variable and its dimension in either the M-L-T or F-L-T system. The list for the beam-column impact configuration is given in Table 2-1. Next, the statement of dimensional homogeneity is written.

$$M^0L^0T^0 \equiv l^{a_1}\, b^{a_2}\, h^{a_3}\, \eta^{a_4}\, A_{11}^{a_5}\, D_{eff}^{a_6}\, \nu^{a_7}\, e^{a_8}\, F^{a_9}\, v^{a_{10}}\, E^{a_{11}}\, \sigma^{a_{12}}\, \varepsilon^{a_{13}}\, M^{a_{14}}\, t^{a_{15}}\, \Delta^{a_{16}}\, g^{a_{17}}\, x^{a_{18}}\, \omega^{a_{19}}\, w^{a_{20}}\, a^{a_{21}}\, \dot{\varepsilon}^{a_{22}}\, \tau^{a_{23}}\, K_Q^{a_{24}} \qquad (A.1)$$

Substituting the dimensional equivalent of each variable symbol into Equation A.1 yields;

$$\begin{aligned} M^0L^0T^0 \equiv\ & (L)^{a_1}\,(L)^{a_2}\,(L)^{a_3}\,(M)^{a_4}\,(M/T^2)^{a_5}\,(ML^2/T^2)^{a_6}(1)^{a_7} \\ & (L)^{a_8}\,(ML/T^2)^{a_9}\,(L/T)^{a_{10}}\,(ML^2/T^2)^{a_{11}}\,(M/LT^2)^{a_{12}} \\ & (1)^{a_{13}}\,(ML^2/T^2)^{a_{14}}\,(T)^{a_{15}}\,(T)^{a_{16}}\,(L/T^2)^{a_{17}}\,(L)^{a_{18}} \\ & (1/T)^{a_{19}}\,(L)^{a_{20}}\,(L/T^2)^{a_{21}}\,(1/T)^{a_{22}}\,(T)^{a_{23}}\,(M/T^2L^{1/2})^{a_{24}}. \end{aligned} \qquad (A.2)$$

The right hand side of Equation A.2 may be rearranged by grouping the exponents of the length, mass and time dimensions together. Using this procedure it is now possible to equate the exponents of mass, length, and time on both sides of Equation A.2. The following three equations result.

$$M: \qquad a_4 + a_5 + a_6 + a_9 + a_{11} + a_{12} + a_{14} + a_{24} = 0 \qquad (A.3)$$

L: $$a_1 + a_2 + a_3 + 2a_6 + a_8 + a_9 + a_{10} + a_{11} - a_{12} + 2a_{14} + a_{17} + a_{18} + a_{20} + a_{21} - 1/2a_{24} = 0 \quad (A.4)$$

T: $$-2a_5 - 2a_6 - 2a_9 - a_{10} - 2a_{11} - 2a_{12} - 2a_{14} + a_{15} + a_{16} - 2a_{17} - a_{19} - 2a_{21} - a_{22} + a_{23} - 2a_{24} = 0 \quad (A.5)$$

This system of equations may be solved for any three of the coefficients, a_i, in terms of the others. In this case, coefficients a_1, a_6, and a_{15} are chosen to be eliminated. This choice is fairly arbitrary since other coefficients could have been eliminated with equally acceptable results. However, it is required that the three equations (A.3 - A.5) be independent; otherwise, additional Pi terms must be formed. One check to verify this is to require that the determinant of the coefficient matrix for the three coefficients chosen to be eliminated be nonzero. For the coefficients a_1, a_6, and a_{15} this requirement is met as shown in equation A.6.

$$\det \begin{vmatrix} 0 & 1 & 0 \\ 1 & 2 & 0 \\ 0 & -2 & 1 \end{vmatrix} = -1(1-0) = -1 \quad (A.6)$$

Solving for a_1, a_6, and a_{15} from Equations A.3 - A.5 yields;

$$a_1 = -a_2 + -a_3 + 2a_4 + 2a_5 + a_9 + 3a_{12} - a_8 - a_{10} - a_{17} - a_{18} - a_{20} - a_{21} + 5/2a_{24} \quad (A.7)$$

$$a_6 = -[a_4 + a_5 + a_9 + a_{11} + a_{12} + a_{14} + a_{24}] \quad (A.8)$$

and,

$$a_{15} = -2a_4 + a_{10} - a_{16} + 2a_{17} + a_{19} + 2a_{21} + a_{22} - a_{23} \quad (A.9)$$

Equations A.7 - A.9 are substituted into the equation of dimensional homogeneity, Equation A.1.

$$M^0L^0T^0 \equiv l^{[-a_2 + -a_3 + 2a_4 + 2a_5 + a_9 + 3a_{12} - a_8 - a_{10} - a_{17} - a_{18} - a_{20} - a_{21} + 5/2a_{24}]}$$
$$b^{a_2}\, h^{a_3}\, \eta^{a_4}\, A_{11}^{a_5}\, D_{eff}^{-[a_4 + a_5 + a_9 + a_{11} + a_{12} + a_{14} + a_{24}]}$$
$$\nu^{a_7}\, e^{a_8}\, F^{a_9}\, \nu^{a_{10}} E^{a_{11}}\, \sigma^{a_{12}}\, \varepsilon^{a_{13}}\, M^{a_{14}}$$
$$t^{[-2a_4 + a_{10} - a_{16} + 2a_{17} + a_{19} + 2a_{21} + a_{22} - a_{23}]}$$
$$\Delta^{a_{16}}\, g^{a_{17}}\, x^{a_{18}}\, \omega^{a_{19}}\, w^{a_{20}}\, a^{a_{21}}\, \dot{\varepsilon}^{a_{22}}\, \tau^{a_{23}}\, K_Q^{a_{24}} \qquad \text{(A.10)}$$

The equation above is now rearranged by collecting the variables having the same exponent.

$$M^0L^0T^0 \equiv \left[\frac{b}{l}\right]^{a_2} \left[\frac{h}{l}\right]^{a_3} \left[\frac{l^2\eta}{D_{eff}}\right]^{a_4} \left[\frac{l^2 A_{11}}{D_{eff}}\right]^{a_5} [\nu]^{a_7} \left[\frac{e}{l}\right]^{a_8} \left[\frac{Fl}{D_{eff}}\right]^{a_9}$$
$$\left[\frac{v\,t}{l}\right]^{a_{10}} \left[\frac{E}{D_{eff}}\right]^{a_{11}} \left[\frac{\sigma l^3}{D_{eff}}\right]^{a_{12}} [\varepsilon]^{a_{13}} \left[\frac{M}{D_{eff}}\right]^{a_{14}}$$
$$\left[\frac{\Delta}{t}\right]^{a_{16}} \left[\frac{gt^2}{l}\right]^{a_{17}} \left[\frac{x}{l}\right]^{a_{18}} [\omega t]^{a_{19}} \left[\frac{w}{l}\right]^{a_{20}}$$
$$\left[\frac{t^2 a}{l}\right]^{a_{21}} [\dot{\varepsilon} t]^{a_{22}} \left[\frac{\tau}{t}\right]^{a_{23}} \left[\frac{K_Q l^{5/2}}{D_{eff}}\right]^{a_{24}} \qquad \text{(A.11)}$$

The Pi terms are the groups enclosed inside each bracket, and are listed separately in Chapter 2 as Equation 2.1.

The model law for the beam-column problem can be developed from the nondimensional parameters by equating the Pi term for the model with the Pi term for the prototype. The notation for the scale factor for a particular variable is given by λ with a subscript which identifies the variable. As an example, the scale factor for the bending stiffness is given by,

$$\lambda_{D_{eff}} = \frac{D_{eff\ (model)}}{D_{eff\ (prototype)}} = \frac{D_{eff\ m}}{D_{eff\ p}} \qquad (A.12)$$

Examining the Pi terms systematically in this manner gives;

Π_1: $$\frac{b_m}{l_m} = \frac{b_p}{l_p} \quad \Rightarrow \quad \lambda_b = \lambda_l \qquad (A.13)$$

Π_2: $$\frac{h_m}{l_m} = \frac{h_p}{l_p} \quad \Rightarrow \quad \lambda_h = \lambda_l \qquad (A.14)$$

Π_3: $$\frac{l_m^2 \eta_m}{D_{eff\ m}\, t_m^2} = \frac{l_p^2 \eta_p}{D_{eff\ p}\, t_p^2} \quad \Rightarrow \quad \lambda_l^2 \lambda_\eta = \lambda_{D_{eff}} \lambda_t^2 \qquad (A.15)$$

Π_4: $$\frac{l_m^2 A_{11m}}{D_{eff\ m}} = \frac{l_p^2 A_{11p}}{D_{eff\ p}} \quad \Rightarrow \quad \lambda_l^2 \lambda_{A_{11}} = \lambda_{D_{eff}} \qquad (A.16)$$

Π_5: $$\nu_m = \nu_p \quad \Rightarrow \quad \lambda_\nu = 1 \qquad (A.17)$$

Π_6: $$\frac{e_m}{l_m} = \frac{e_p}{l_p} \quad \Rightarrow \quad \lambda_e = \lambda_l \qquad (A.18)$$

Π_7: $$\frac{F_m l_m}{D_{eff\ m}} = \frac{F_p l_p}{D_{eff\ p}} \quad \Rightarrow \quad \lambda_F \lambda_l = \lambda_{D_{eff}} \qquad (A.19)$$

Π_8: $$\frac{\nu_m t_m}{l_m} = \frac{\nu_p t_p}{l_p} \quad \Rightarrow \quad \lambda_\nu \lambda_t = \lambda_l \qquad (A.20)$$

Π_9: $$\frac{E_m}{D_{eff\ m}} = \frac{E_p}{D_{eff\ p}} \quad \Rightarrow \quad \lambda_E = \lambda_{D_{eff}} \qquad (A.21)$$

$$\Pi_{10}: \quad \frac{\sigma_m l_m^3}{D_{eff\ m}} = \frac{\sigma_p l_p^3}{D_{eff\ p}} \quad \Rightarrow \quad \lambda_\sigma \lambda_l^3 = \lambda_{D_{eff}} \tag{A.22}$$

$$\Pi_{11}: \quad \varepsilon_m = \varepsilon_p \quad \Rightarrow \quad \lambda_\varepsilon = 1 \tag{A.23}$$

$$\Pi_{12}: \quad \frac{M_m}{D_{eff\ m}} = \frac{M_p}{D_{eff\ p}} \quad \Rightarrow \quad \lambda_M = \lambda_{D_{eff}} \tag{A.24}$$

$$\Pi_{13}: \quad \frac{\Delta_m}{t_m} = \frac{\Delta_p}{t_p} \quad \Rightarrow \quad \lambda_\Delta = \lambda_t \tag{A.25}$$

$$\Pi_{14}: \quad \frac{g_m t_m^2}{l_m} = \frac{g_p t_p^2}{l_p} \quad \Rightarrow \quad \lambda_g \lambda_t^2 = \lambda_l \tag{A.26}$$

$$\Pi_{15}: \quad \frac{x_m}{l_m} = \frac{x_p}{l_p} \quad \Rightarrow \quad \lambda_x = \lambda_l \tag{A.27}$$

$$\Pi_{16}: \quad \omega_m t_m = \omega_p t_p \quad \Rightarrow \quad \lambda_\omega = 1/\lambda_t \tag{A.28}$$

$$\Pi_{17}: \quad \frac{w_m}{l_m} = \frac{w_p}{l_p} \quad \Rightarrow \quad \lambda_w = \lambda_l \tag{A.29}$$

$$\Pi_{18}: \quad \frac{a_m t_m^2}{l_m} = \frac{a_p t_p^2}{l_p} \quad \Rightarrow \quad \lambda_a \lambda_t^2 = \lambda_l \tag{A.30}$$

$$\Pi_{19}: \quad \dot{\varepsilon}_m t_m = \dot{\varepsilon}_p t_p \quad \Rightarrow \quad \lambda_{\dot{\varepsilon}} = 1/\lambda_t \tag{A.31}$$

$$\Pi_{20}: \quad \frac{\tau_m}{t_m} = \frac{\tau_p}{t_p} \quad \Rightarrow \quad \lambda_\tau = \lambda_t \tag{A.32}$$

$$\Pi_{21}: \quad \frac{K_{Qm} l_m^{5/2}}{D_{eff\ m}} = \frac{K_{Qp} l_p^{5/2}}{D_{eff\ p}} \quad \Rightarrow \quad \lambda_{K_Q} \lambda_l^{5/2} = \lambda_{D_{eff}} \tag{A.33}$$

The equations A.13 through A.33 form the basis of the model law. To validate the model law an experiment was designed in which the geometric scale factor, λ_l, was chosen to have discrete values of 1/6, 1/4, 1/3, 1/2, 2/3, 3/4, 5/6, and 1. Typically the geometric scale factor, λ_l, is designated as simply λ. The experiment was performed using the same material system for the prototype beams as for the models. These requirements of the experiment, namely that geometry scales according to λ and material properties scale as 1, force the following scale factors to become fixed.

$$\lambda_{D_{eff}} = \lambda^3$$

$$\lambda_{A_{11}} = \lambda \qquad \text{(A.34)}$$

$$\lambda_\eta = \lambda^3$$

$$\lambda_l = \lambda$$

The known scale factors given in A.34 can now be used to fully derive the scaling law based on Equations A.13 through A.33.

	Pi Term	Scale Law
Π_1:	$\lambda_b = \lambda_l = \lambda$	$\lambda_b = \lambda$
Π_2:	$\lambda_h = \lambda_l = \lambda$	$\lambda_h = \lambda$
Π_3:	$\lambda_l^2 \lambda_\eta = \lambda_{D_{eff}} \lambda_t^2$ $\lambda^2 \lambda^3 = \lambda^3 \lambda_t^2$ $\lambda_t^2 = \lambda^2$	$\lambda_t = \lambda$
Π_4:	$\lambda_l^2 \lambda_{A_{11}} = \lambda_{D_{eff}}$	no new info.

Π_5:	$\lambda_\nu = 1$	$\lambda_\nu = 1$
Π_6:	$\lambda_e = \lambda_l = \lambda$	$\lambda_e = \lambda$
Π_7:	$\lambda_F \lambda_l = \lambda_{D_{eff}}$	$\lambda_F = \lambda^2$
Π_8:	$\lambda_\nu \lambda_t = \lambda_l = \lambda$	$\lambda_\nu = 1$
Π_9:	$\lambda_E = \lambda_{D_{eff}} = \lambda^3$	$\lambda_E = \lambda^3$
Π_{10}:	$\lambda_\sigma \lambda_l^3 = \lambda_{D_{eff}}$	$\lambda_\sigma = 1$
Π_{11}:	$\lambda_\varepsilon = 1$	$\lambda_\varepsilon = 1$
Π_{12}:	$\lambda_M = \lambda_{D_{eff}}$	$\lambda_M = \lambda^3$
Π_{13}:	$\lambda_\Delta = \lambda_t$	$\lambda_\Delta = \lambda$
Π_{14}:	$\lambda_g \lambda_t^2 = \lambda_l = \lambda$	$\lambda_g = 1/\lambda$
Π_{15}:	$\lambda_x = \lambda_l = \lambda$	$\lambda_x = \lambda$
Π_{16}:	$\lambda_\omega = 1/\lambda_t$	$\lambda_\omega = 1/\lambda$
Π_{17}:	$\lambda_w = \lambda_l$	$\lambda_w = \lambda$
Π_{18}:	$\lambda_a \lambda_t^2 = \lambda_l = \lambda$	$\lambda_a = 1/\lambda$
Π_{19}:	$\lambda_{\dot{\varepsilon}} = 1/\lambda_t$	$\lambda_{\dot{\varepsilon}} = 1/\lambda$
Π_{20}:	$\lambda_\tau = \lambda_t$	$\lambda_\tau = \lambda$
Π_{21}:	$\lambda_{K_Q} \lambda_l^{5/2} = \lambda_{D_{eff}}$	$\lambda_{K_Q} = \lambda^{1/2}$

Appendix B. Large Deflection "Exact" Solution Development

This appendix presents more complete details of the development of the large deflection beam analysis which is outlined in section 4.2. Variable definitions are given in Table 4-2. The appendix is divided into three sections which are: (1) development of the governing equation, (2) development of the boundary conditions, and (3) solution development.

B.1 Development of the Governing Equation

Writing the summation of moments about point O in Figure 4-2 gives,

$$\sum M_o = M + P\,y + P\sqrt{e^2 + \delta^2}\,\sin(\phi + \alpha) = 0 \qquad \text{(B.1)}$$

Substituting the constitutive relation $M = EI\ d\theta/ds$ gives,

$$EI\frac{d\theta}{ds} + P\,y + P\sqrt{e^2 + \delta^2}\,\sin(\phi + \alpha) = 0 \qquad \text{(B.2)}$$

Differentiating this expression with respect to s yields:

$$EI\frac{d^2\theta}{ds^2} + P\frac{dy}{ds} = 0 \qquad \text{(B.3)}$$

From the geometry of a differential beam segment $dy/ds = \sin\theta$. Also, the notation for the buckling coefficient, $k^2 = P/EI$, is now introduced. The resulting second order differential equation becomes,

$$\frac{d^2\theta}{ds^2} + k^2\sin\theta = 0 \qquad \text{(B.4)}$$

Equation B.4 may be integrated with respect to θ to reduce the order of the differential equation.

$$\int \frac{d^2\theta}{ds^2}\left(\frac{d\theta}{ds}\right) ds = \int -k^2 \sin\theta \, d\theta \tag{B.5}$$

$$\frac{1}{2}\left(\frac{d\theta}{ds}\right)^2 = k^2\cos\theta + C \tag{B.6}$$

resulting in the final form of the governing differential equation

$$\frac{d\theta}{ds} = \pm\sqrt{2}\,\sqrt{k^2\cos\theta + C} \tag{B.7}$$

where C is a constant of integration which must be found by application of boundary conditions. The necessary boundary condition is derived in the next section.

B.2 Derivation of Boundary Condition

The boundary condition is found by solving for the moment at the hinge-beam connection point, or s = 0. At this point, y = 0 and $\theta = \phi + \alpha$.

$$M(s=0) = - P \sin(\phi + \alpha)\sqrt{e^2 + \delta^2} \tag{B.8}$$

Expanding the sine term gives;

$$M(0) = - P \sqrt{e^2 + \delta^2}\left[\sin\phi\cos\alpha + \cos\phi\sin\alpha\right] \tag{B.9}$$

But, from the hinge geometry, the $\sin\phi$ and $\cos\phi$ terms are given by,

$$\sin\phi = \frac{e}{\sqrt{e^2 + \delta^2}} \qquad \text{and} \qquad \cos\phi = \frac{\delta}{\sqrt{e^2 + \delta^2}} \tag{B.10}$$

Substituting these relations into Equation B.9 gives,

$$M(0) = - P \sqrt{e^2 + \delta^2} \left[\frac{e \cos\alpha}{\sqrt{e^2 + \delta^2}} + \frac{\delta \sin\alpha}{\sqrt{e^2 + \delta^2}} \right] \tag{B.11}$$

Simplifying,

$$M(0) = - P \left[e \cos\alpha + \delta \sin\alpha \right] \tag{B.12}$$

The moment is expressed in terms of the beam curvature through the constitutive relationship resulting in,

$$M(s=0) = EI \left[\frac{d\theta}{ds} \right]_{\theta = \alpha} = - \left[P\, e \cos\alpha + P\, \delta \sin\alpha \right] \tag{B.13}$$

Dividing by the flexural rigidity gives the boundary condition in final form:

$$\left[\frac{d\theta}{ds} \right]_{\theta = \alpha} = - k^2 e \cos\alpha - k^2 \delta \sin\alpha \tag{B.14}$$

B.3 Solution Development

The boundary condition given by Equation B.14 can be applied to the governing differential equation, Equation B.7, to solve for the constant of integration, C.

$$\left[\frac{d\theta}{ds} \right]_{\theta = \alpha} = \pm\sqrt{2}\, \sqrt{k^2 \cos\alpha + C} = - k^2 e \cos\alpha - k^2 \delta \sin\alpha \tag{B.15}$$

Squaring both sides of the equation and solving for C yields,

$$C = \frac{1}{2} \left[k^2 \left(e \cos\alpha + \delta \sin\alpha \right) \right]^2 - k^2 \cos\alpha \tag{B.16}$$

Substituting for C into the governing equation, B.7, gives,

$$\frac{d\theta}{ds} = \pm\sqrt{2}\, \sqrt{k^2 \cos\theta - k^2 \cos\alpha + \frac{1}{2} \left[k^2 \left(e \cos\alpha + \delta \sin\alpha \right) \right]^2} \tag{B.17}$$

Rearranging and expanding some of the terms in Equation B.17 gives,

$$\frac{d\theta}{ds} = -\sqrt{2}\, k \sqrt{\cos\theta - \cos\alpha + \frac{1}{2} k^2 \left(e\cos\alpha + \delta\sin\alpha\right)^2} \tag{B.18}$$

Substituting the trigonometric relationship,

$$\cos\theta = 1 - 2\sin^2\frac{\theta}{2} \tag{B.19}$$

into Equation B.18 gives,

$$\frac{d\theta}{ds} = -2\, k \sqrt{\sin^2\frac{\alpha}{2} - \sin^2\frac{\theta}{2} + \frac{1}{4} k^2 \left(e\cos\alpha + \delta\sin\alpha\right)^2} \tag{B.20}$$

A transformation of variables is introduced to simplify the solution of Equation B.20.

Define,

$$\sin\frac{\theta}{2} = \sqrt{\sin^2\frac{\alpha}{2} + \frac{1}{4} k^2 \left(e\cos\alpha + \delta\sin\alpha\right)^2}\ \sin\psi \tag{B.21}$$

where

$$\sqrt{\sin^2\frac{\alpha}{2} + \frac{1}{4} k^2 \left(e\cos\alpha + \delta\sin\alpha\right)^2} = A \tag{B.22}$$

Thus,

$$\sin\frac{\theta}{2} = A\sin\psi \tag{B.23}$$

Substituting the change of variables into the governing equation, B.20, gives,

$$\frac{d\theta}{ds} = -2k\sqrt{\left[\sin^2\frac{\alpha}{2} + \frac{1}{4}k^2\left(e\cos\alpha + \delta\sin\alpha\right)^2\right]\left(1 - \sin^2\psi\right)} \tag{B.24}$$

$$\frac{d\theta}{ds} = -2kA\sqrt{1 - \sin^2\psi} = -2kA\cos\psi \tag{B.25}$$

Equation B.25 may be inverted to solve for the differential beam segment length, ds,

$$ds = \frac{-d\theta}{2kA\cos\psi} \tag{B.26}$$

This expression cannot be integrated until $d\theta$ is written in terms of the new variable ψ. That relationship is found by taking the differential of Equation B.23,

$$d\left[\sin\frac{\theta}{2} = A\sin\psi\right] \tag{B.27}$$

to give

$$\frac{1}{2}\cos\frac{\theta}{2}d\theta = A\cos\psi\, d\psi \tag{B.28}$$

Finally, $d\theta$ is expressed in terms of ψ in the following manner,

$$d\theta = \frac{2A\cos\psi}{\cos\frac{\theta}{2}}d\psi \tag{B.29}$$

Substituting the expression for $d\theta$ (B.29) into the differential equation for beam length, Equation B.26, gives

$$ds = \frac{-d\psi}{k\cos\frac{\theta}{2}} \tag{B.30}$$

Solving for the $\cos\theta/2$ in terms of the variable, ψ,

$$\cos\frac{\theta}{2} = \sqrt{1 - \sin^2\frac{\theta}{2}} = \sqrt{1 - A^2\sin^2\psi} \tag{B.31}$$

Substituting this expression into Equation B.30 gives,

$$ds = \frac{-\,d\psi}{k\sqrt{1 - A^2\sin^2\psi}} \tag{B.32}$$

The total length of the beam is found by integrating ds from $\theta = \alpha$ to $\theta = -\alpha$,

$$L = \int_{\theta=\alpha}^{\theta=-\alpha} ds \tag{B.33}$$

Substituting Equation B.32 for ds gives,

$$L = \int_{\theta=\alpha}^{\theta=-\alpha} ds = \int_{\theta=\alpha}^{\theta=-\alpha} \frac{-\,d\psi}{k\sqrt{1 - A^2\sin^2\psi}} \tag{B.34}$$

Using symmetry conditions yields,

$$L = \frac{2}{k}\int_{\theta=0}^{\theta=\alpha} \frac{d\psi}{\sqrt{1 - A^2\sin^2\psi}} \tag{B.35}$$

The upper and lower limits of the above integral must be expressed is terms of the variable, ψ, before the integral can be solved. By considering Equation B.23, it is found that at $\theta = 0$, $\psi = 0$. Substituting $\theta = \alpha$ in Equation B.23 establishes the upper limit:

at $\theta = \alpha$,

$$\sin^2\frac{\alpha}{2} = \left[\sin^2\frac{\alpha}{2} + \frac{1}{4}k^2\,(e\cos\alpha + \delta\sin\alpha)^2\right]\sin^2\psi \tag{B.36}$$

or

$$\sin\psi = \frac{\sin\frac{\alpha}{2}}{A} \tag{B.37}$$

Let ψ_α be the notation for the value of ψ when $\theta = \alpha$. Thus,

$$\psi_\alpha = \sin^{-1}\left(\frac{\sin\frac{\alpha}{2}}{A}\right) \tag{B.38}$$

Substituting the limits of integration into Equation B.35 gives the final result:

$$\int_{\theta=\alpha}^{\theta=-\alpha} ds = L = \frac{2}{k}\int_{\psi=0}^{\psi=\psi_\alpha} \frac{d\psi}{\sqrt{1 - A^2\sin^2\psi}} \tag{B.39}$$

The integral of equation B.39 is the complete elliptic integral of the first kind and is denoted as;

$$\frac{k\,L}{2} = F(A,\psi_\alpha) \tag{B.40}$$

The solution for the midpoint deflection comes from consideration of the geometry of a beam segment. From Figure 2 of section 3.2, it can be shown that

$$\frac{dy}{ds} = \sin\theta = 2\sin\frac{\theta}{2}\cos\frac{\theta}{2} \tag{B.41}$$

Substituting Equation B.23 for the $\sin\theta/2$ term and Equation B.31 for the $\cos\theta/2$, allows the above equation to be written in terms of the new variable, ψ.

$$dy = 2\ A\ \sin\psi\ \sqrt{1 - A^2\sin^2\psi}\ ds \tag{B.42}$$

Substituting Equation B.32 for ds gives

$$dy = \frac{-\ 2\ A\ \sin\psi\ d\psi}{k} \tag{B.43}$$

This equation may be integrated from $\theta = \alpha$ to $\theta = 0$ to give the midpoint displacement.

$$y_{mid} = \int_{\theta=\alpha}^{\theta=0} dy = \int_{\theta=0}^{\theta=\alpha} \frac{2\ A\ \sin\psi\ d\psi}{k} \tag{B.44}$$

The limits on integration are expressed in terms of the variable, ψ, such that at θ equal 0, $\psi = 0$; and at $\theta = \alpha$, $\psi = \psi_\alpha$, where ψ_α is given by Equation B.38. The integral for the midpoint displacement becomes,

$$y_{mid} = \int_{\psi=0}^{\psi=\psi_\alpha} \frac{2A}{k} \sin\psi\ d\psi \tag{B.45}$$

Integrating Equation B.45 gives

$$y_{mid} = \frac{2A}{k}\left[-\cos\psi\right]_0^{\psi_\alpha} = \frac{2A}{k}\left[1 - \cos\psi_\alpha\right] \tag{B.46}$$

Based on the definition given in Equation B.38, the $\cos\psi_\alpha$ is found to be,

$$\cos\psi_\alpha = \frac{\sqrt{A^2 - \sin^2\frac{\alpha}{2}}}{A} \tag{B.47}$$

Thus, in final form, the midpoint transverse displacement is,

$$y_{mid} = \frac{2A}{k}\left[1 - \frac{\sqrt{A^2 - \sin^2\frac{\alpha}{2}}}{A}\right] \tag{B.48}$$

The solution for the total axial shortening of the beam is found by integrating the differential displacement, dx, along the length of the beam. From Figure 2 of section 3.2, it can be shown that,

$$\frac{dx}{ds} = \cos\theta = -1 + 2\cos^2\frac{\theta}{2} \tag{B.49}$$

or,

$$dx = \left(-1 + 2\cos^2\frac{\theta}{2}\right) ds \tag{B.50}$$

Substituting Equation B.30 for ds yields,

$$dx = \frac{d\psi}{k\cos\frac{\theta}{2}} - \frac{2}{k}\cos\frac{\theta}{2}\, d\psi \tag{B.51}$$

Rewriting the $\cos\theta/2$ in terms of the $\sin\theta/2$ gives,

$$dx = \frac{d\psi}{k\sqrt{1 - \sin^2\frac{\theta}{2}}} - \frac{2}{k}\sqrt{1 - \sin^2\frac{\theta}{2}}\, d\psi \tag{B.52}$$

Substituting Equation B.23 for the $\sin\theta/2$ in terms of the new variable, ψ, gives,

$$dx = \frac{d\psi}{k\sqrt{1 - A^2\sin^2\psi}} - \frac{2}{k}\sqrt{1 - A^2\sin^2\psi}\, d\psi \tag{B.53}$$

The total axial shortening, x_{total}, is found by integrating Equation B.53 from $\theta = \alpha$ to $\theta = -\alpha$. By symmetry, this operation is equivalent to multiplying the integral by 2 and integrating from $\psi = 0$ to $\psi = \psi_\alpha$.

$$x_{total} = -\frac{2}{k}\int_{\psi=0}^{\psi=\psi_\alpha} \frac{d\psi}{\sqrt{1 - A^2\sin^2\psi}} + \frac{4}{k}\int_{\psi=0}^{\psi=\psi_\alpha} \sqrt{1 - A^2\sin^2\psi}\, d\psi \tag{B.54}$$

The first integral of Equation B.54 has the form of the complete elliptic integral of the first kind and may be simplified by substituting Equation B.40. The second integral has the form of the complete elliptic integral of the second kind and is denoted by $E(A,\psi_\alpha)$. Thus, the equation for x_{total} becomes,

$$x_{total} = -L + \frac{4}{k}E(A,\psi_\alpha) \tag{B.55}$$

Appendix C. Static Load and Strain Deflection Experimental Results

This appendix contains load- and strain- displacement response plots from static tests of unidirectional, angle ply, cross ply, and quasi-isotropic scale model beams. Data from three replicate tests for each scaled size and laminate type are presented. Load data have been normalized by the Euler load which was determined empirically by the matching technique described in Chapter 5.

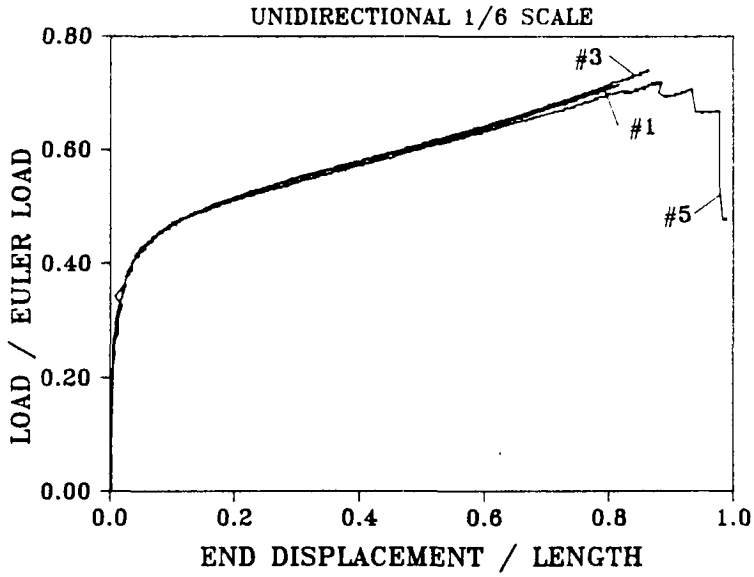

Figure C-1(a). Normalized load versus end displacement.

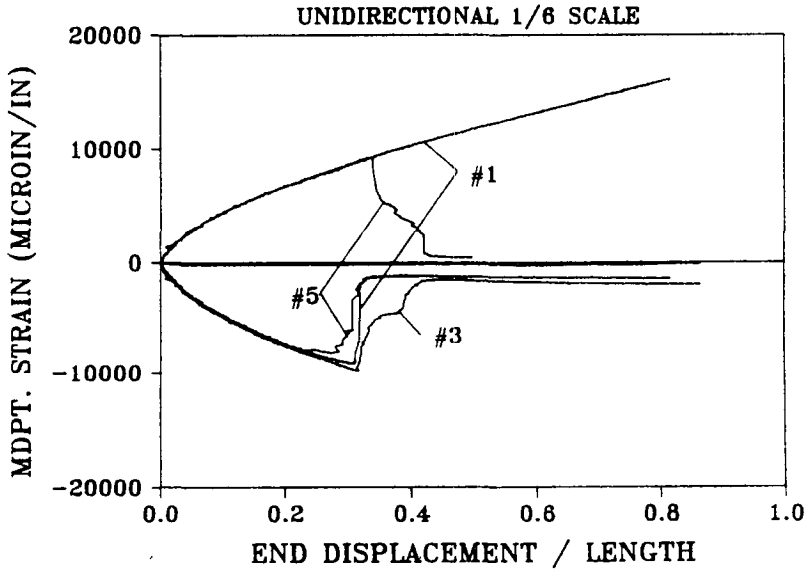

Figure C-1(b). Midpoint strain versus normalized end displacement.

Figure C-1. Static load-deflection and strain-deflection experimental results for 1/6 scale model unidirectional beams, 3 replicate tests.

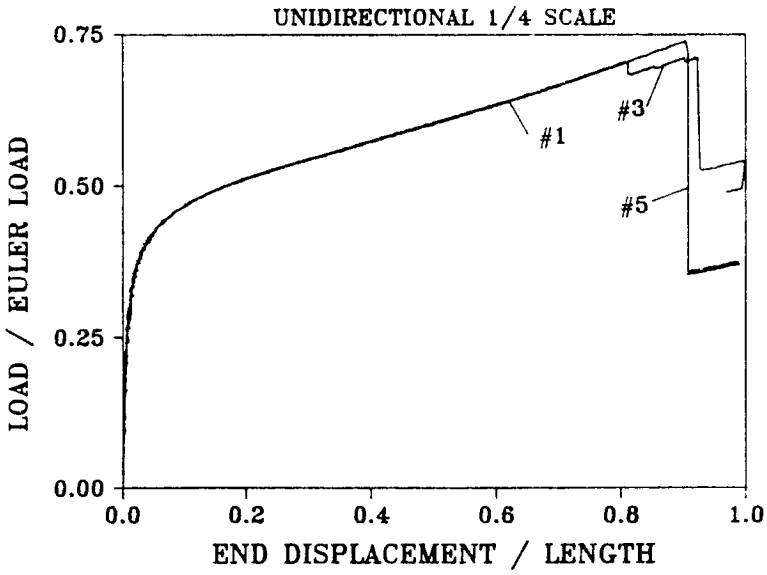

Figure C-2(a). Normalized load versus end displacement.

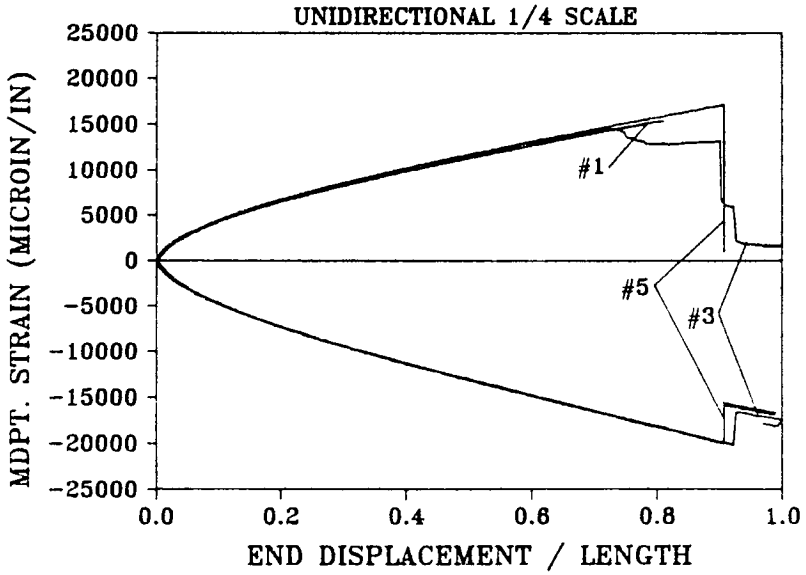

Figure C-2(b). Midpoint strain versus normalized end displacement.

Figure C-2. Static load-deflection and strain-deflection experimental results for 1/4 scale model unidirectional beams, 3 replicate tests.

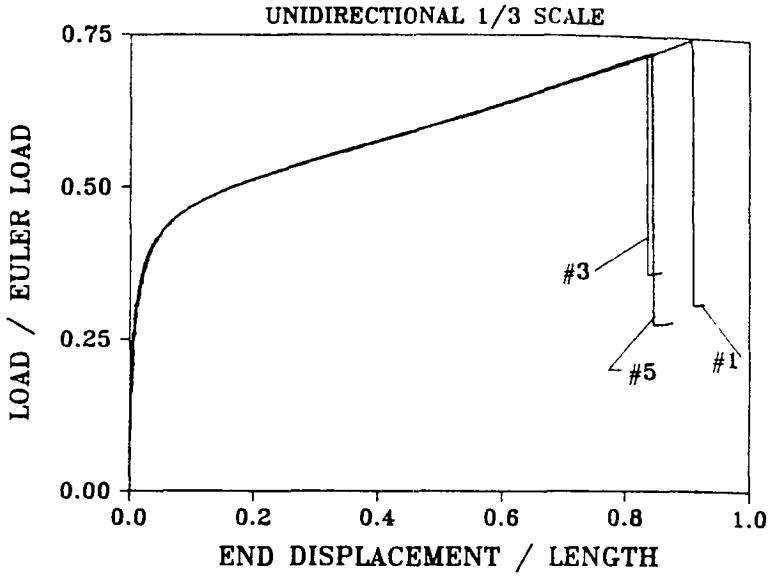

Figure C-3(a). Normalized load versus end displacement.

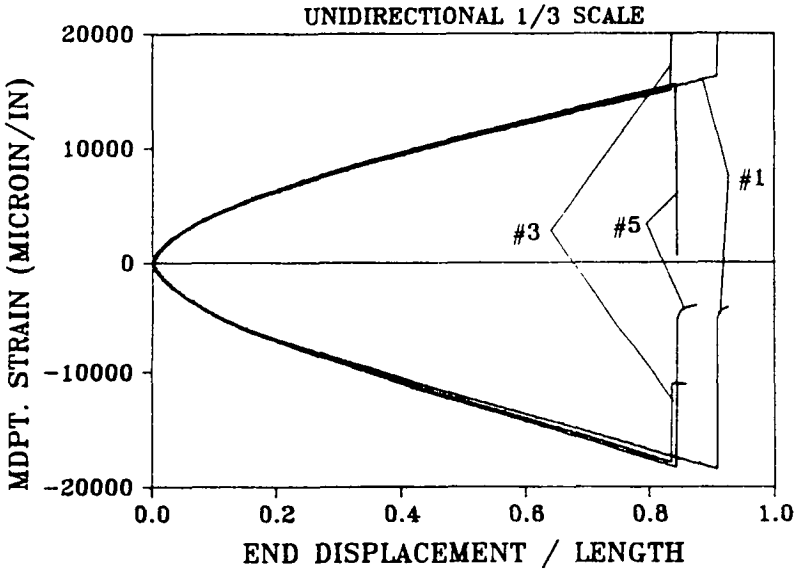

Figure C-3(b). Midpoint strain versus normalized end displacement.

Figure C-3. Static load-deflection and strain-deflection experimental results for 1/3 scale model unidirectional beams, 3 replicate tests.

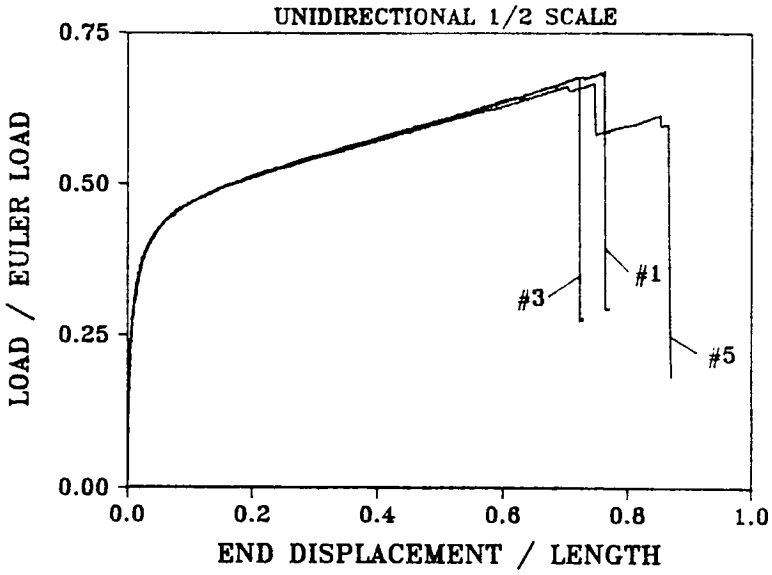

Figure C-4(a). Normalized load versus end displacement.

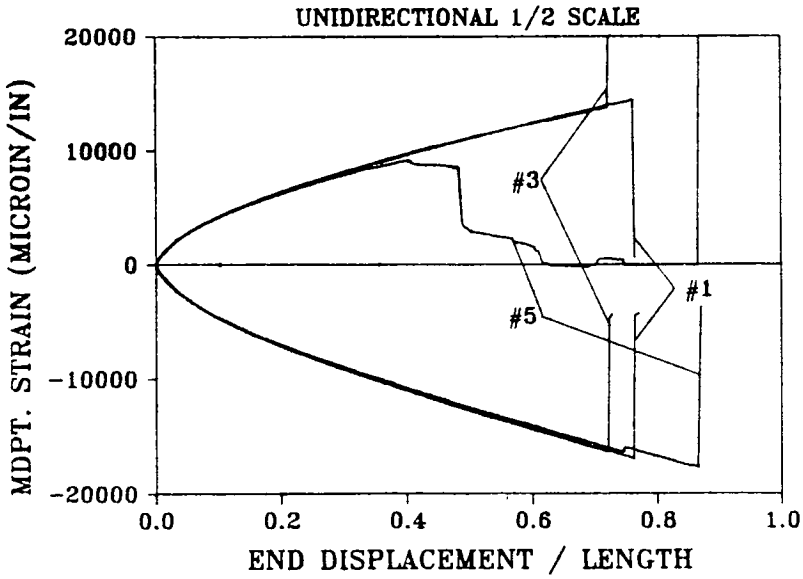

Figure C-4(b). Midpoint strain versus normalized end displacement.

Figure C-4. Static load-deflection and strain-deflection experimental results for 1/2 scale model unidirectional beams, 3 replicate tests.

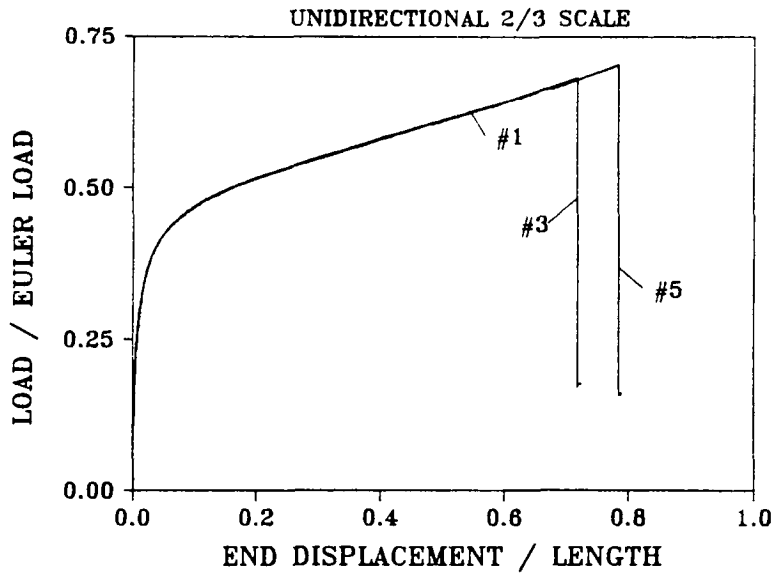

Figure C-5(a). Normalized load versus end displacement.

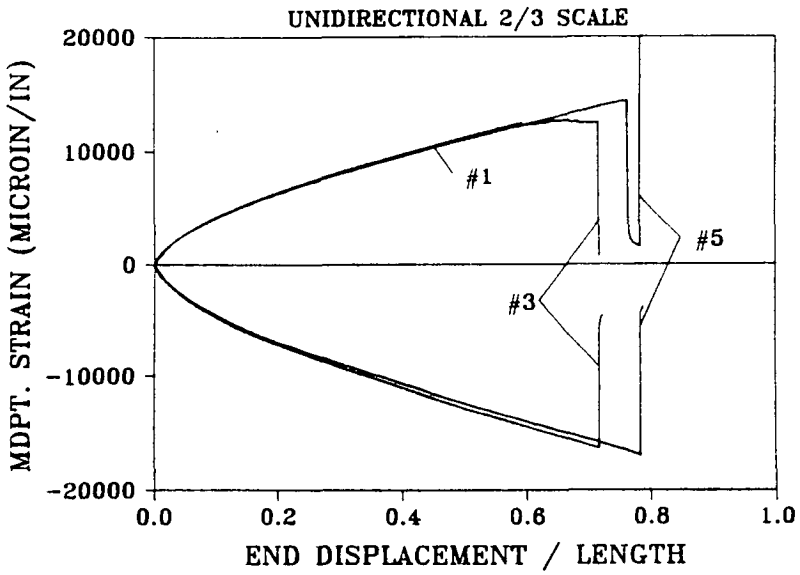

Figure C-5(b). Midpoint strain versus normalized end displacement.

Figure C-5. Static load-deflection and strain-deflection experimental results for 2/3 scale model unidirectional beams, 3 replicate tests.

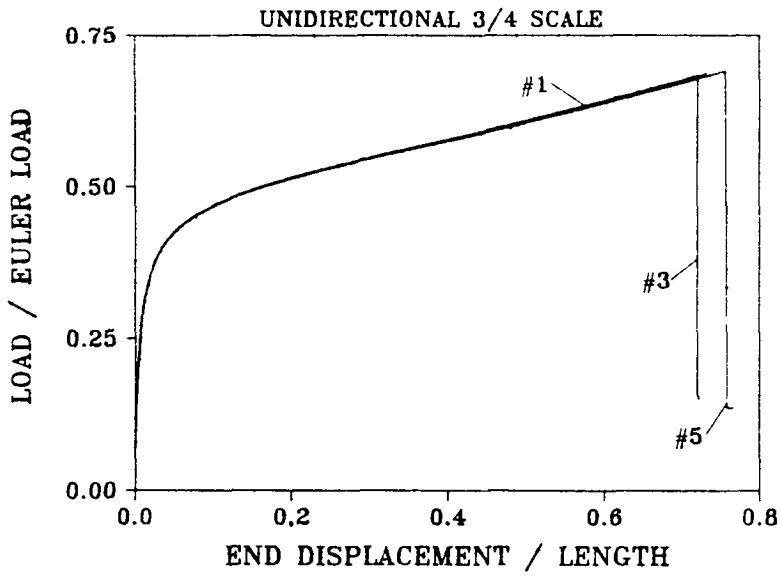

Figure C-6(a). Normalized load versus end displacement.

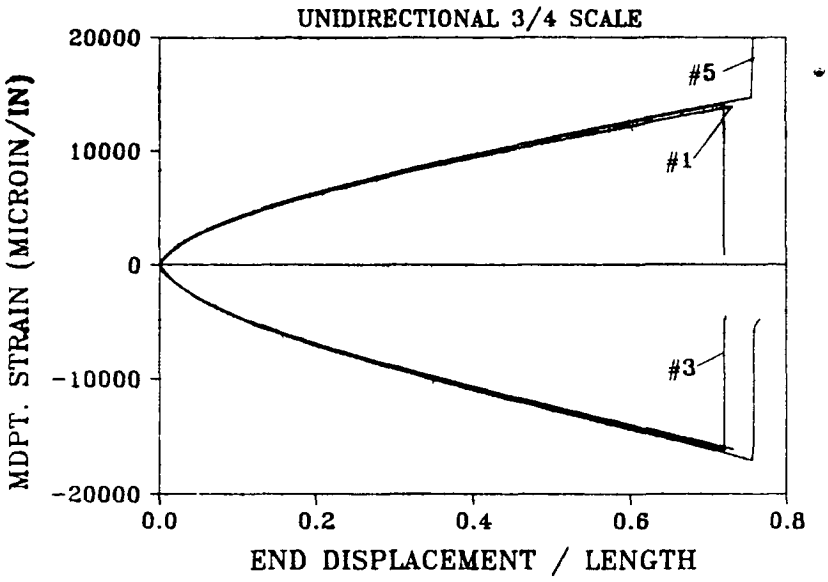

Figure C-6(b). Midpoint strain versus normalized end displacement.

Figure C-6. Static load-deflection and strain-deflection experimental results for 3/4 scale model unidirectional beams, 3 replicate tests.

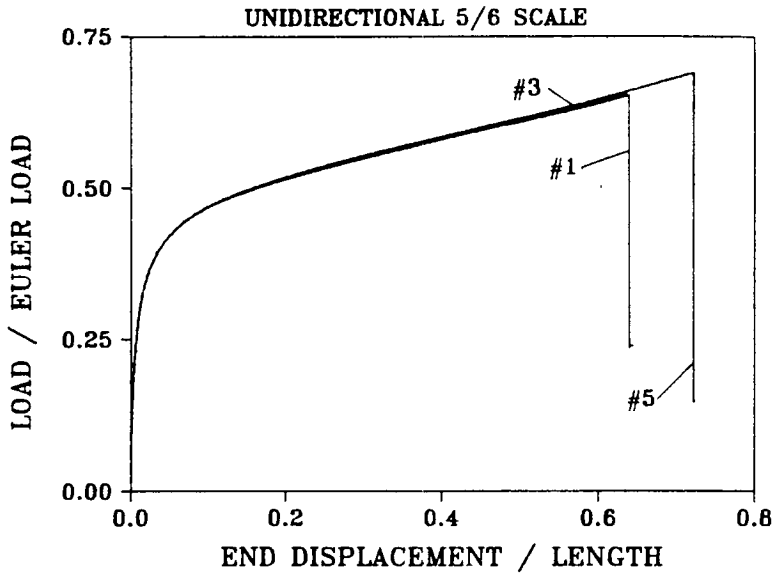

Figure C-7(a). Normalized load versus end displacement.

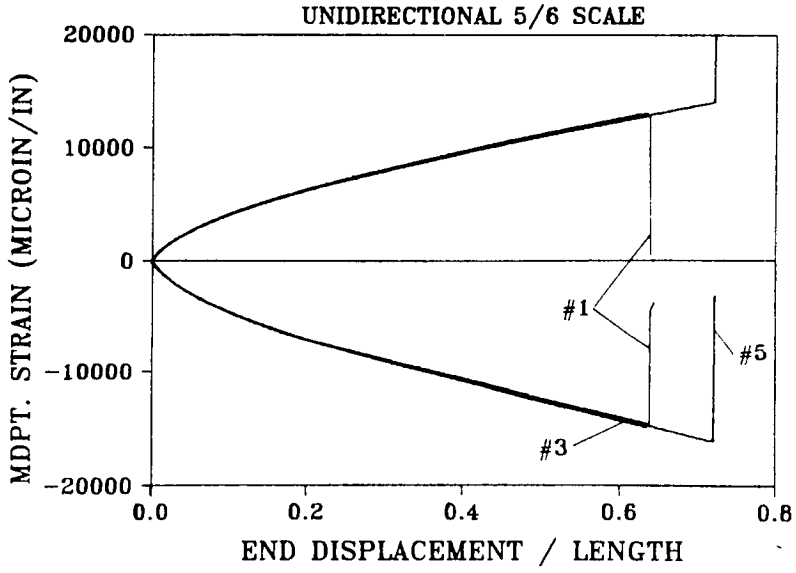

Figure C-7(b). Midpoint strain versus normalized end displacement.

Figure C-7. Static load-deflection and strain-deflection experimental results for 5/6 scale model unidirectional beams, 3 replicate tests.

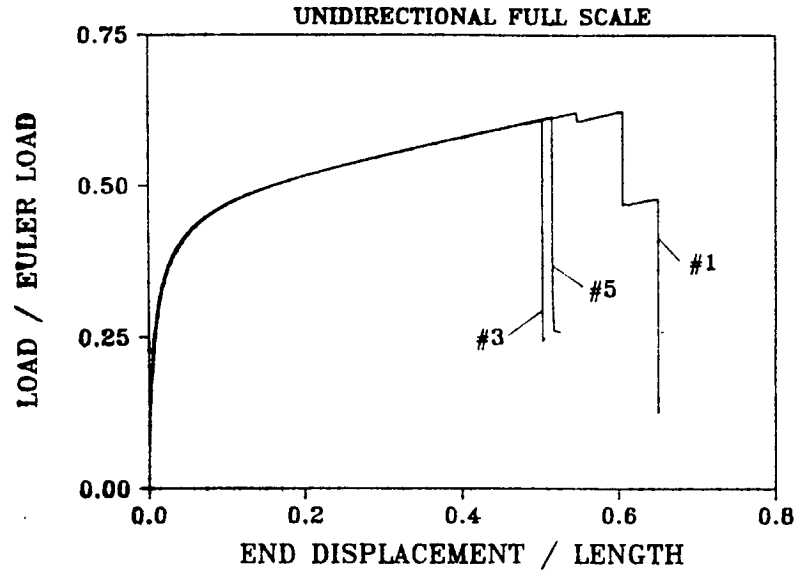

Figure C-8(a). Normalized load versus end displacement.

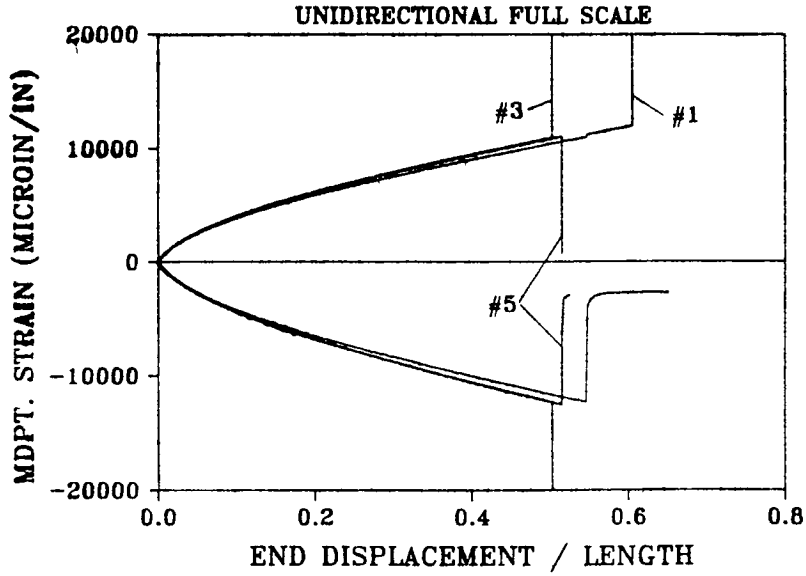

Figure C-8(b). Midpoint strain versus normalized end displacement.

Figure C-8. Static load-deflection and strain-deflection experimental results for full scale model unidirectional beams, 3 replicate tests.

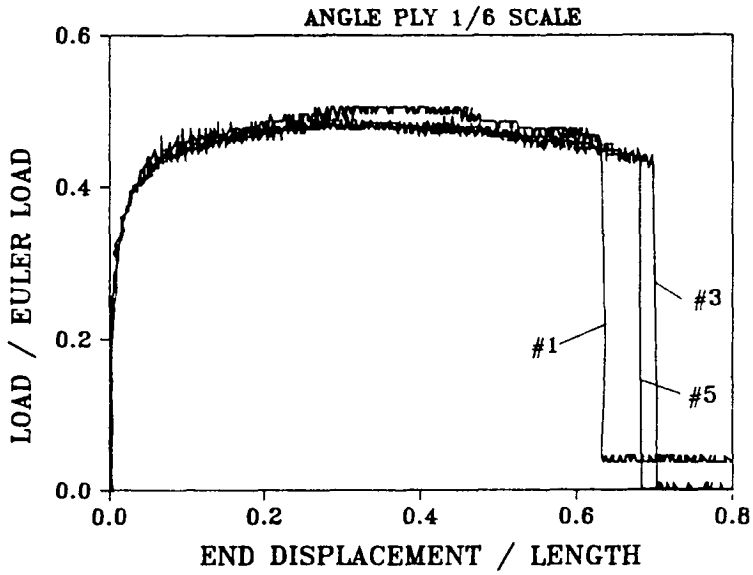

Figure C-9(a). Normalized load versus end displacement.

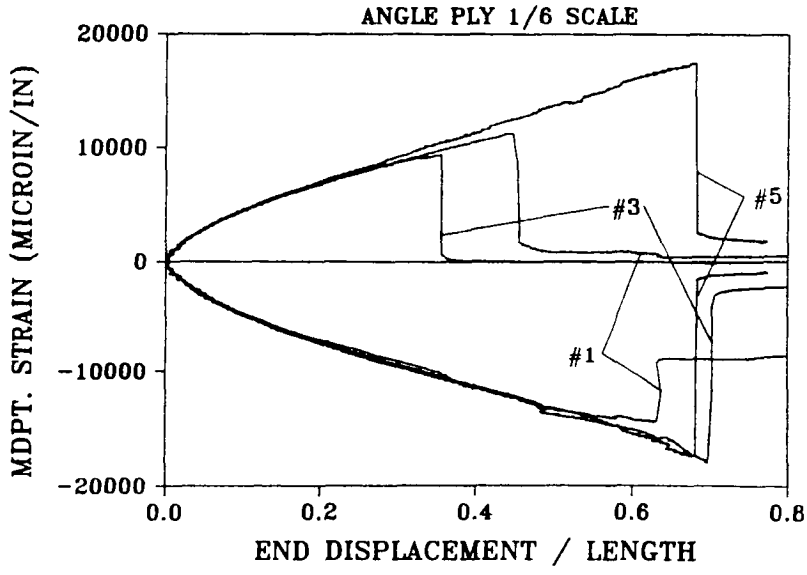

Figure C-9(b). Midpoint strain versus normalized end displacement.

Figure C-9. Static load-deflection and strain-deflection experimental results for 1/6 scale model angle ply beams, 3 replicate tests.

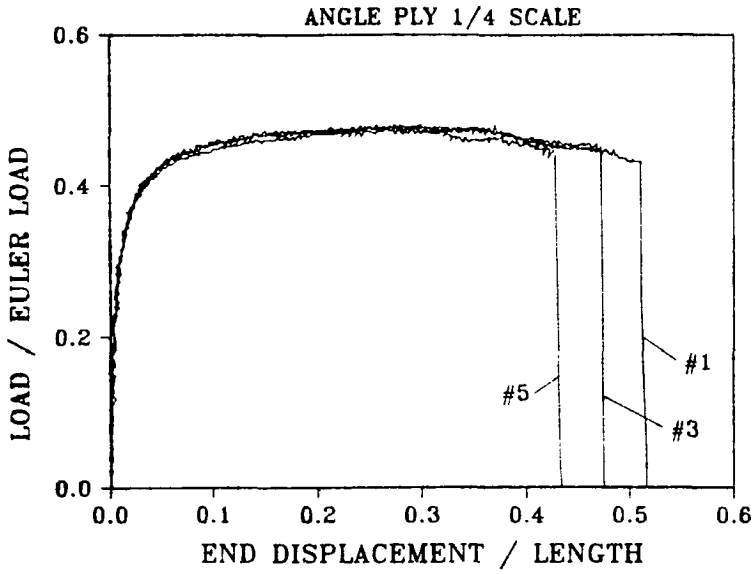

Figure C-10(a). Normalized load versus end displacement.

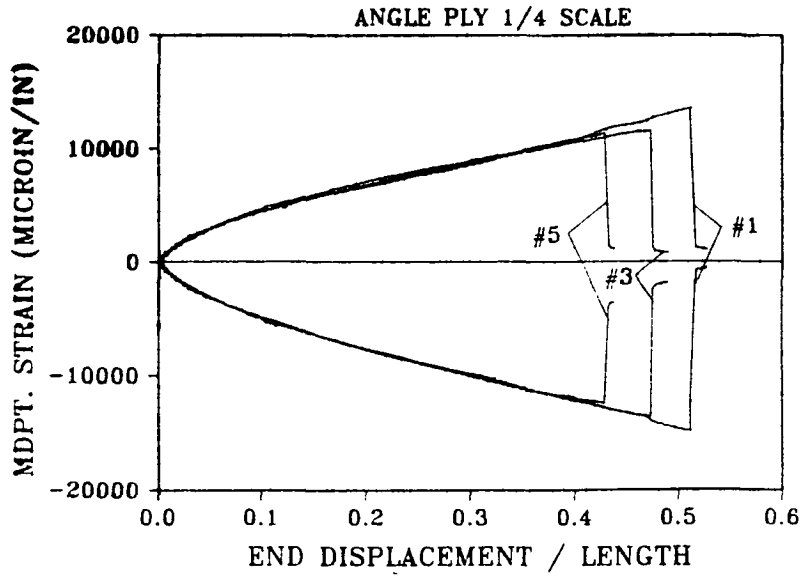

Figure C-10(b). Midpoint strain versus normalized end displacement.

Figure C-10. Static load-deflection and strain-deflection experimental results for 1/4 scale model angle ply beams, 3 replicate tests.

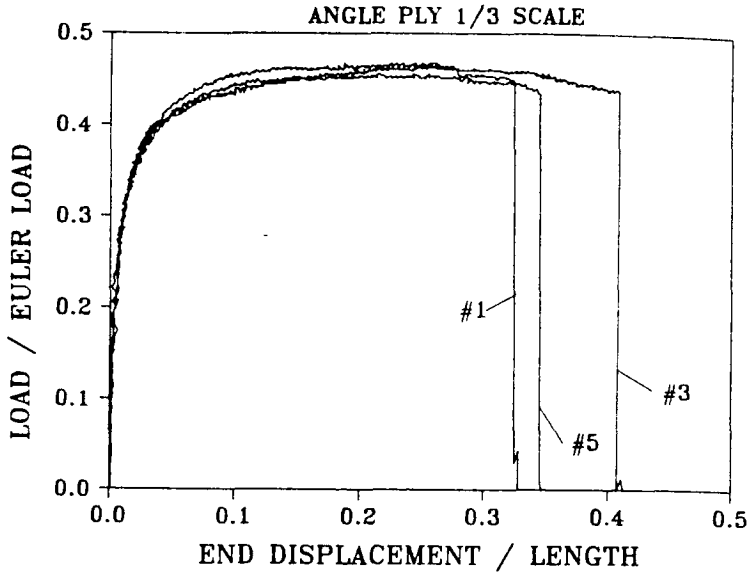

Figure C-11(a). Normalized load versus end displacement.

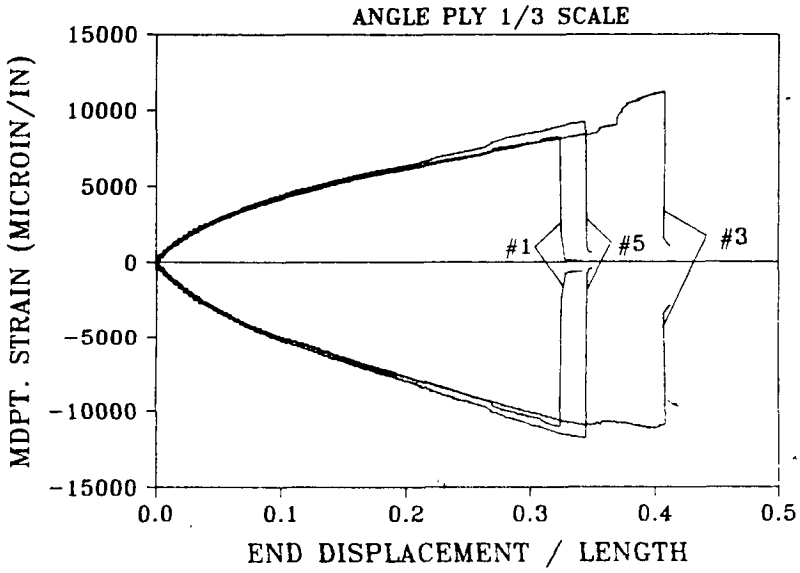

Figure C-11(b). Midpoint strain versus normalized end displacement.

Figure C-11. Static load-deflection and strain-deflection experimental results for 1/3 scale model angle ply beams, 3 replicate tests.

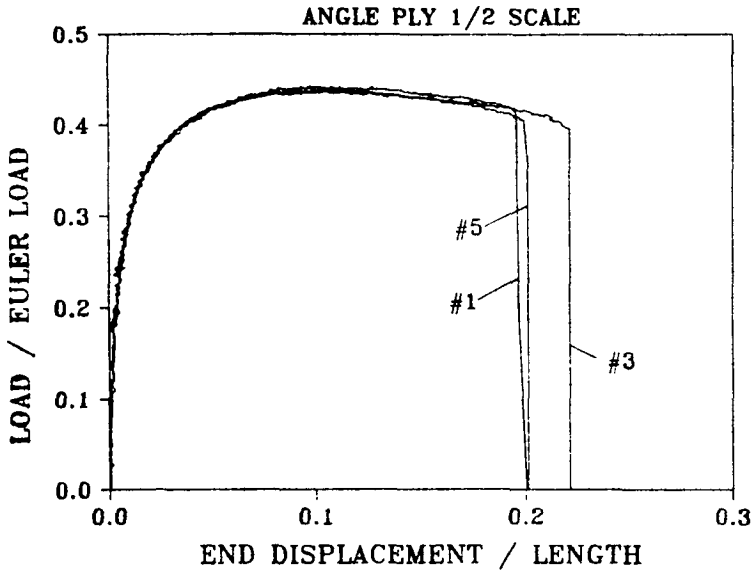

Figure C-12(a). Normalized load versus end displacement.

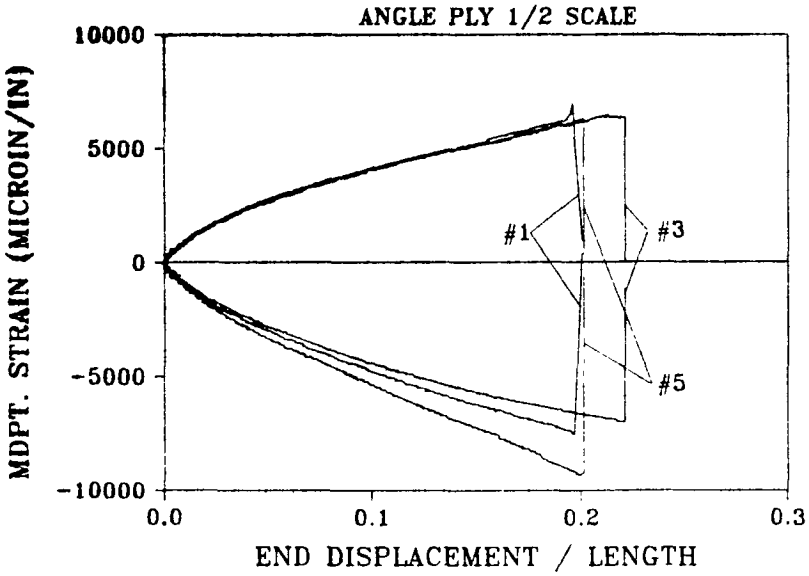

Figure C-12(b). Midpoint strain versus normalized end displacement.

Figure C-12. Static load-deflection and strain-deflection experimental results for 1/2 scale model angle ply beams, 3 replicate tests.

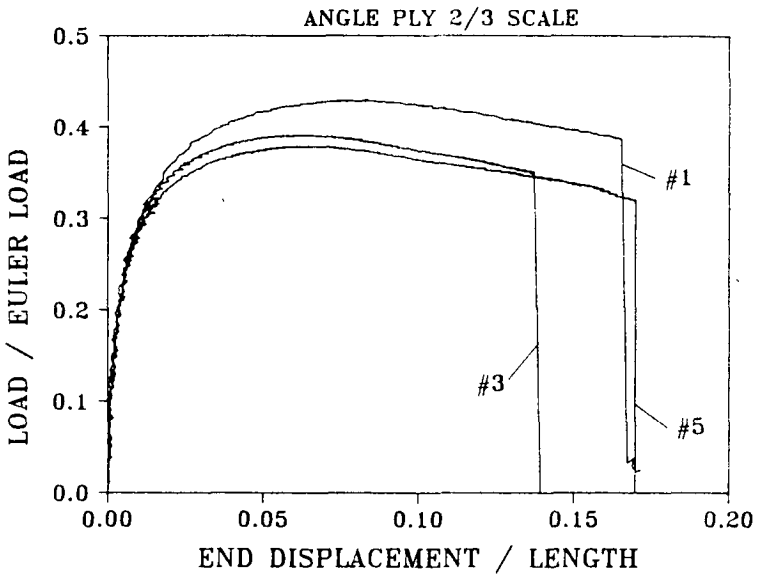

Figure C-13(a). Normalized load versus end displacement.

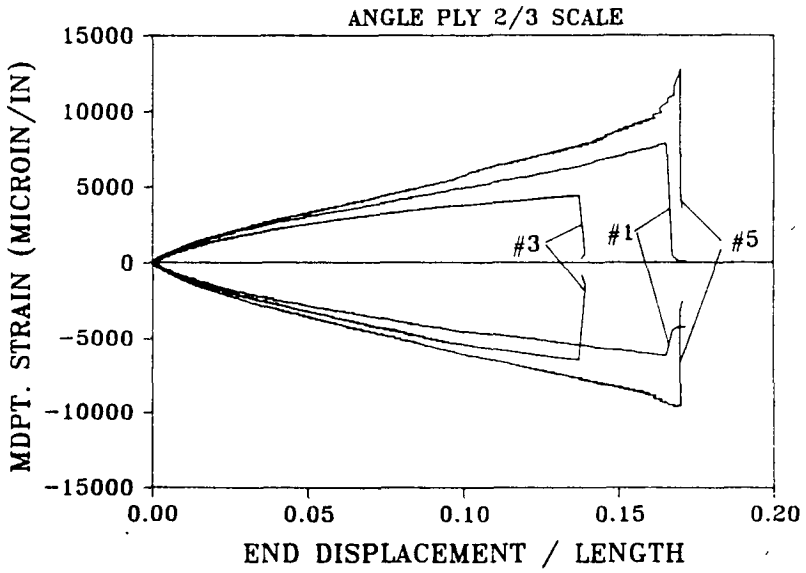

Figure C-13(b). Midpoint strain versus normalized end displacement.

Figure C-13. Static load-deflection and strain-deflection experimental results for 2/3 scale model angle ply beams, 3 replicate tests.

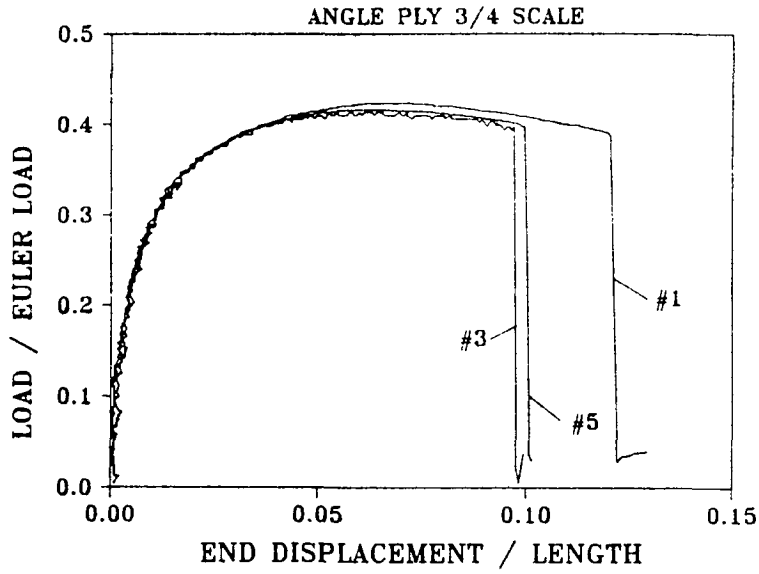

Figure C-14(a). Normalized load versus end displacement.

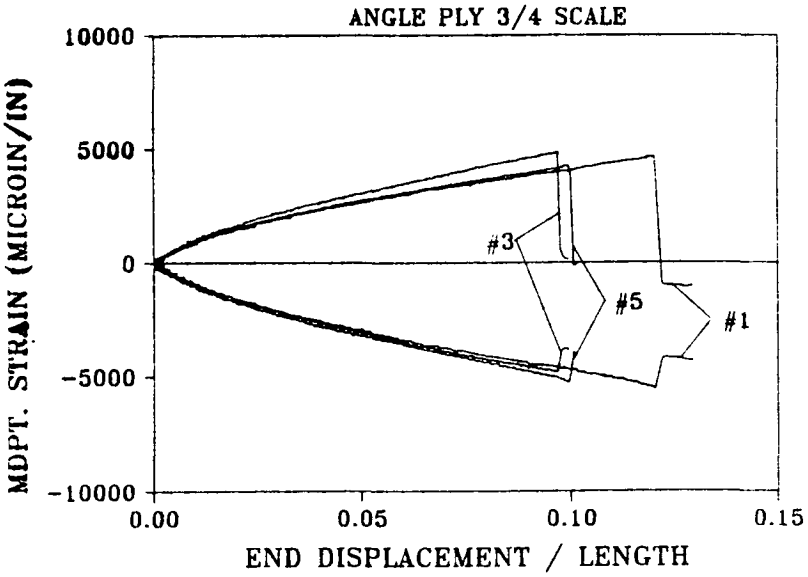

Figure C-14(b). Midpoint strain versus normalized end displacement.

Figure C-14. Static load-deflection and strain-deflection experimental results for 3/4 scale model angle ply beams, 3 replicate tests.

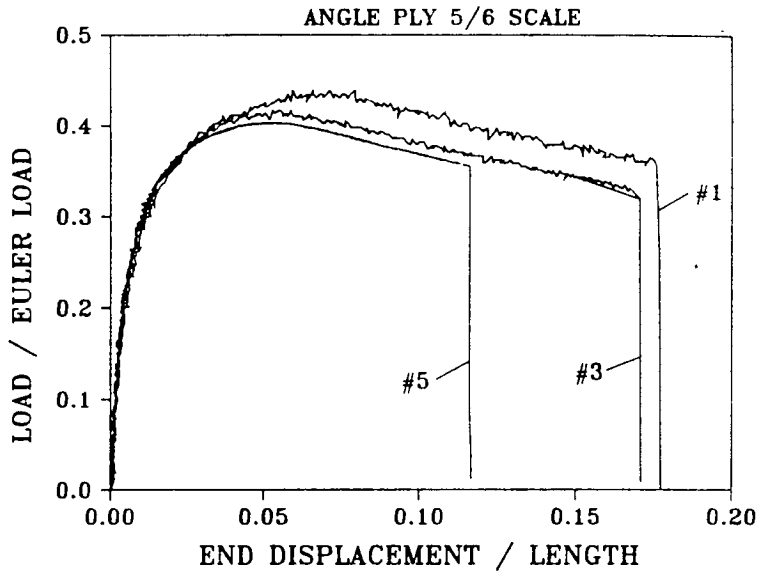

Figure C-15(a). Normalized load versus end displacement.

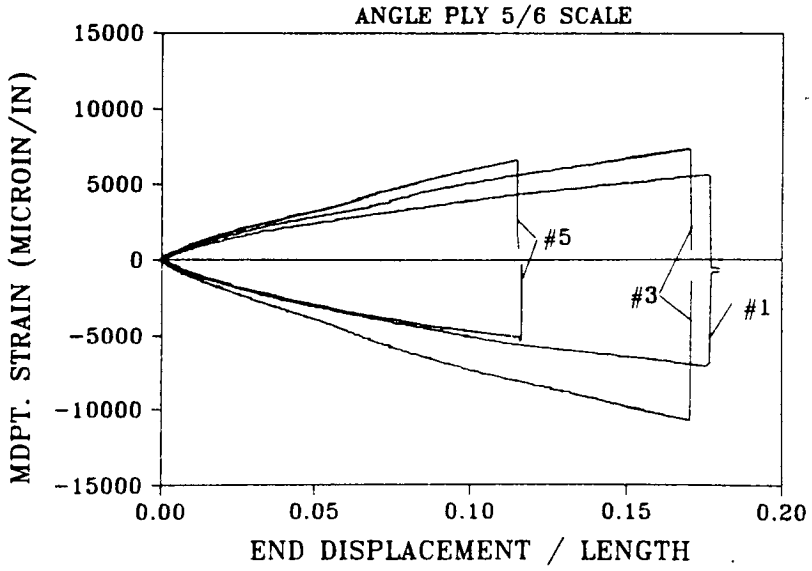

Figure C-15(b). Midpoint strain versus normalized end displacement.

Figure C-15. Static load-deflection and strain-deflection experimental results for 5/6 scale model angle ply beams, 3 replicate tests.

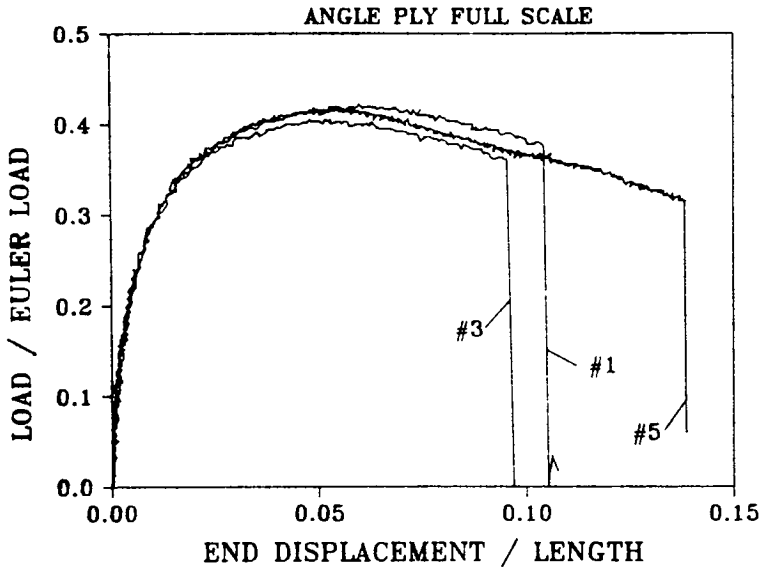

Figure C-16(a). Normalized load versus end displacement.

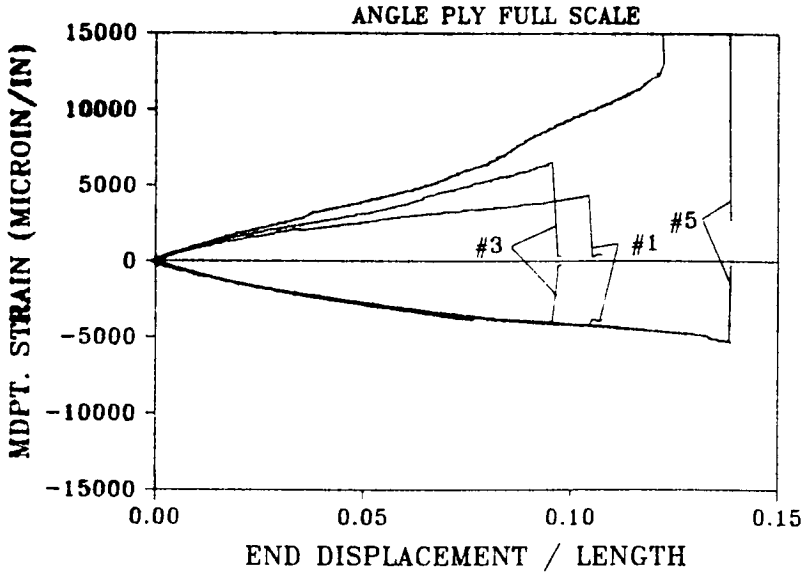

Figure C-16(b). Midpoint strain versus normalized end displacement.

Figure C-16. Static load-deflection and strain-deflection experimental results for full scale model angle ply beams, 3 replicate tests.

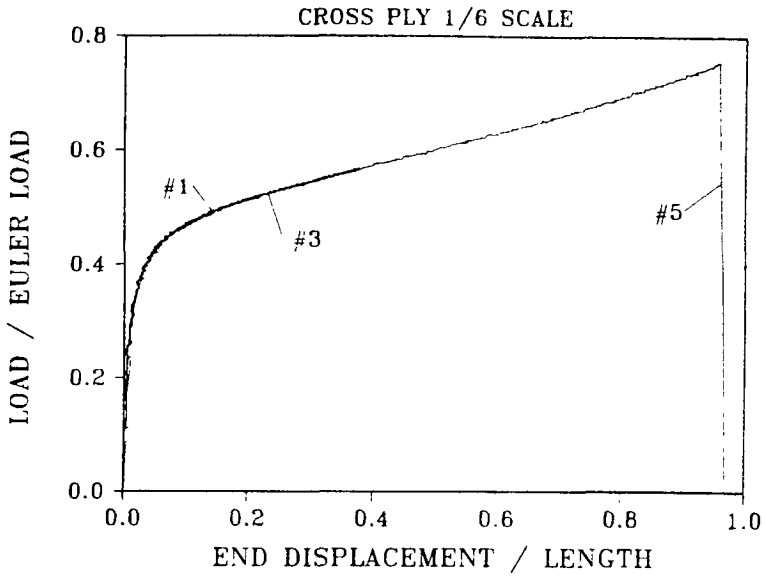

Figure C-17(a). Normalized load versus end displacement.

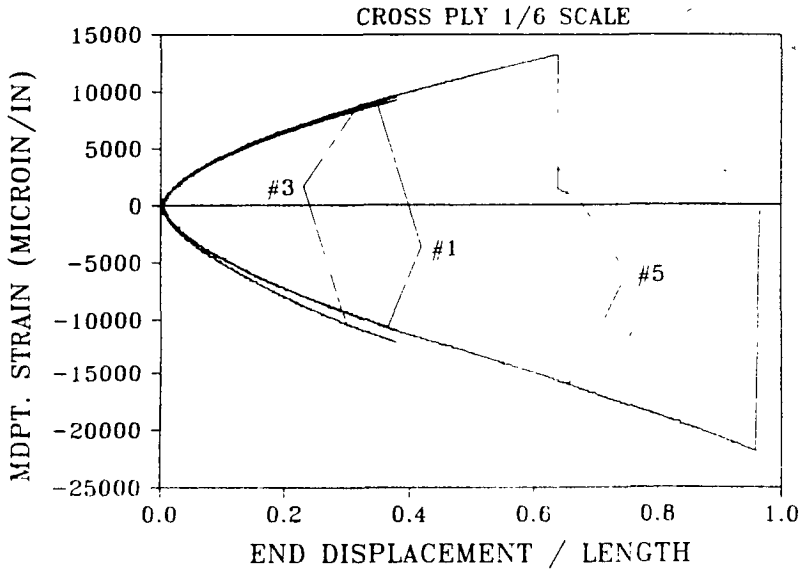

Figure C-17(b). Midpoint strain versus normalized end displacement.

Figure C-17. Static load-deflection and strain-deflection experimental results for 1/6 scale model cross ply beams, 3 replicate tests.

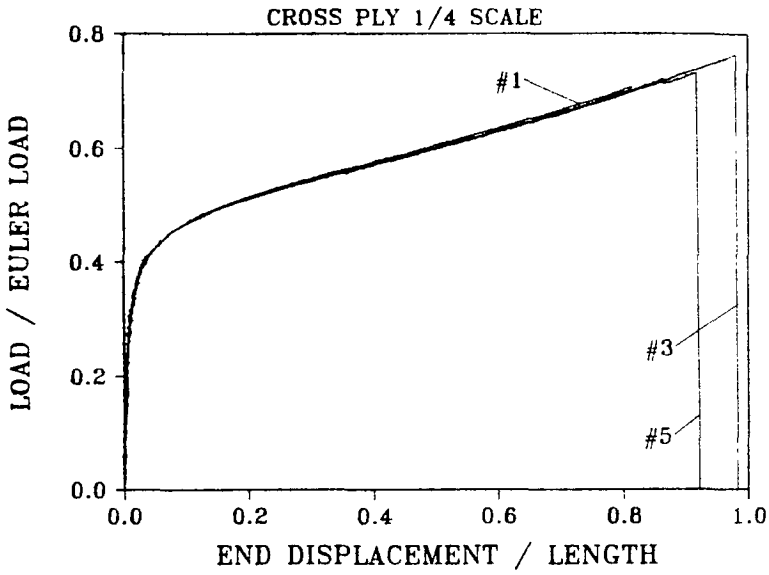

Figure C-18(a). Normalized load versus end displacement.

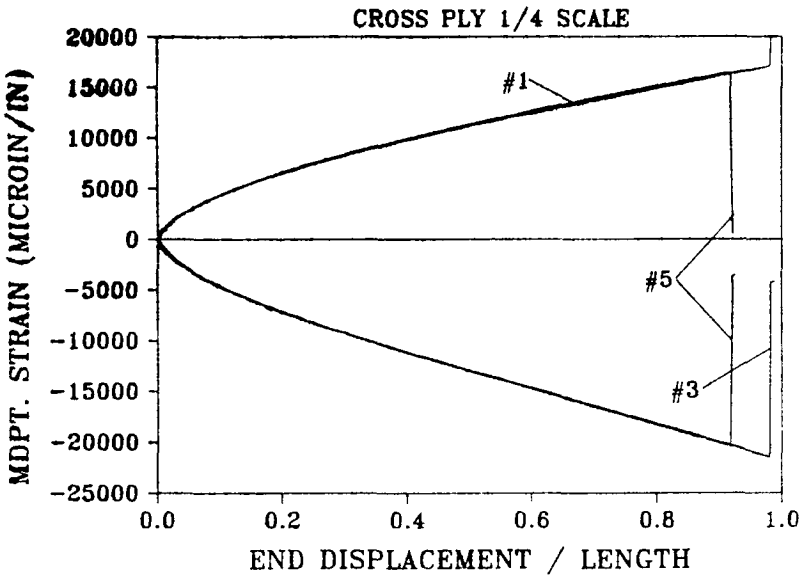

Figure C-18(b). Midpoint strain versus normalized end displacement.

Figure C-18. Static load-deflection and strain-deflection experimental results for 1/4 scale model cross ply beams, 3 replicate tests.

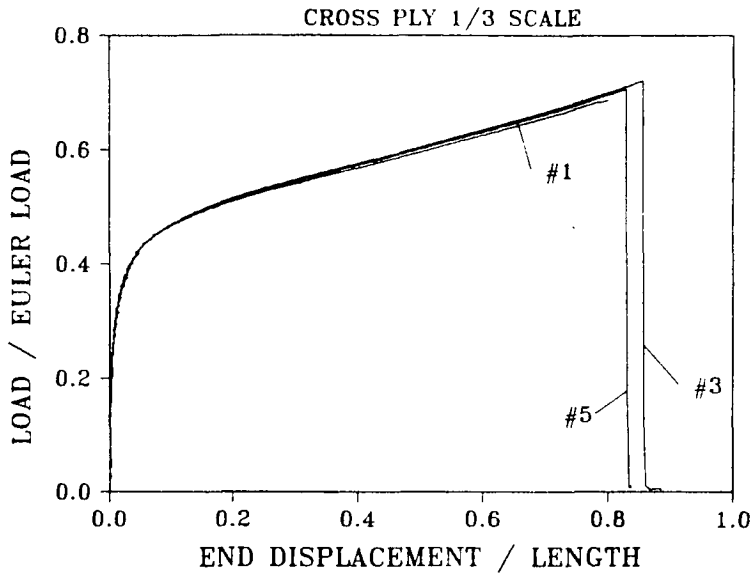

Figure C-19(a). Normalized load versus end displacement.

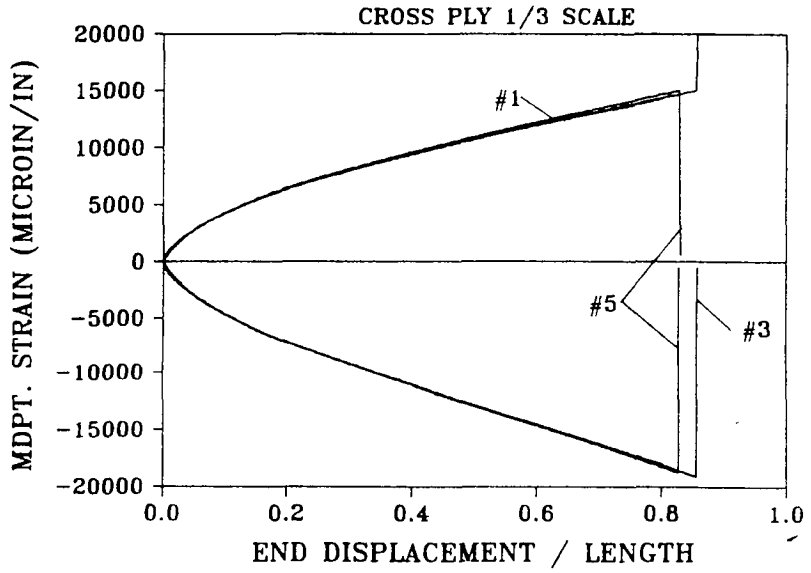

Figure C-19(b). Midpoint strain versus normalized end displacement.

Figure C-19. Static load-deflection and strain-deflection experimental results for 1/3 scale model cross ply beams, 3 replicate tests.

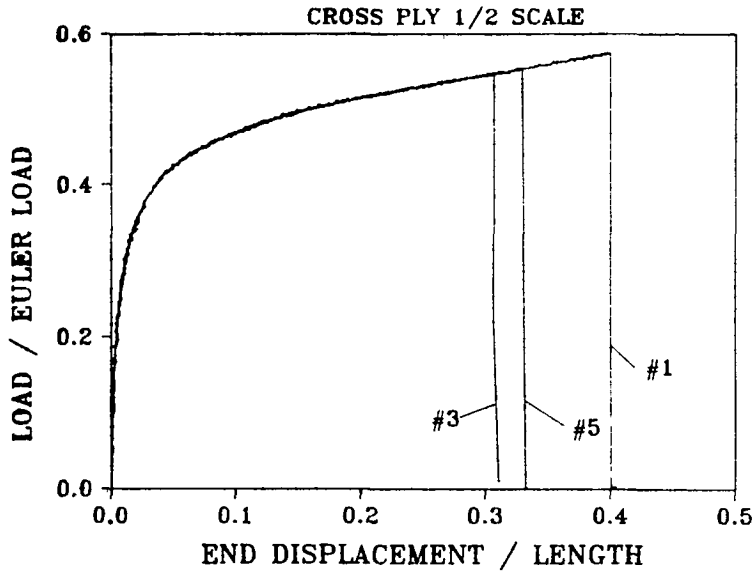

Figure C-20(a). Normalized load versus end displacement.

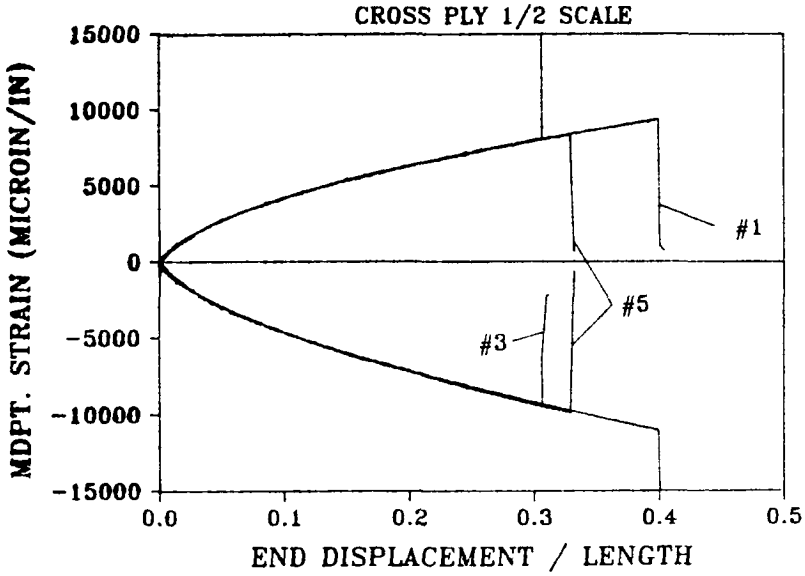

Figure C-20(b). Midpoint strain versus normalized end displacement.

Figure C-20. Static load-deflection and strain-deflection experimental results for 1/2 scale model cross ply beams, 3 replicate tests.

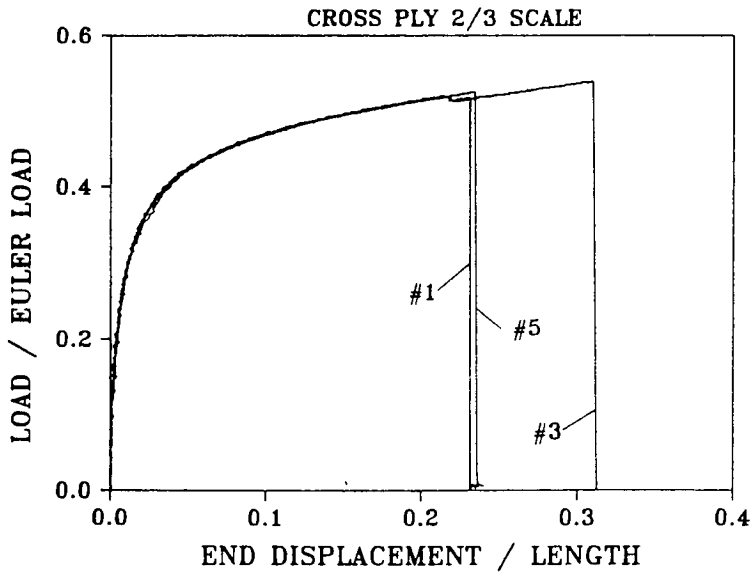

Figure C-21(a). Normalized load versus end displacement.

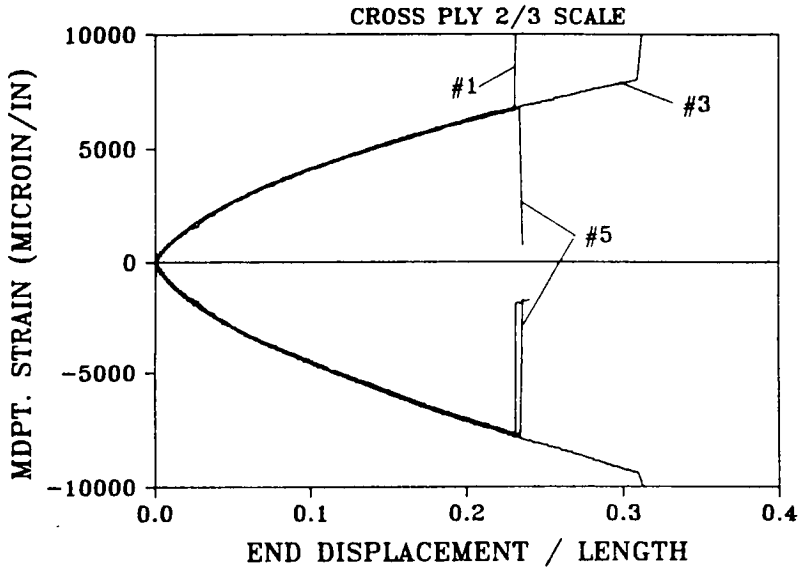

Figure C-21(b). Midpoint strain versus normalized end displacement.

Figure C-21. Static load-deflection and strain-deflection experimental results for 2/3 scale model cross ply beams, 3 replicate tests.

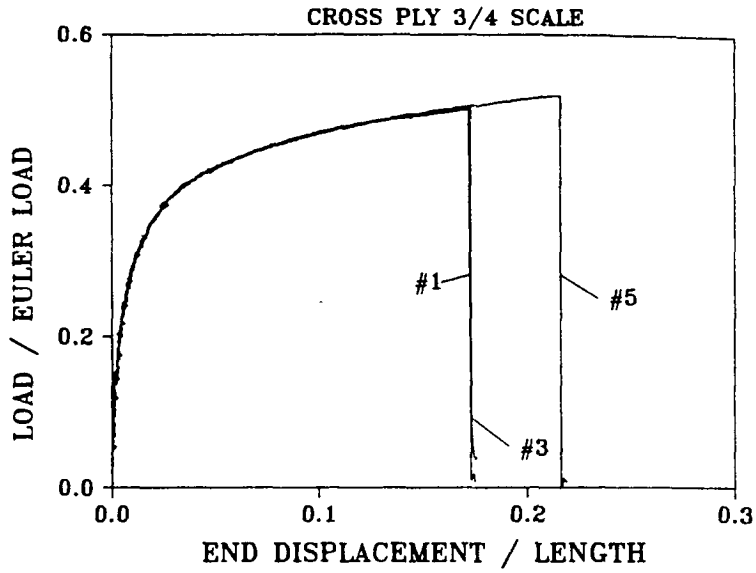

Figure C-22(a). Normalized load versus end displacement.

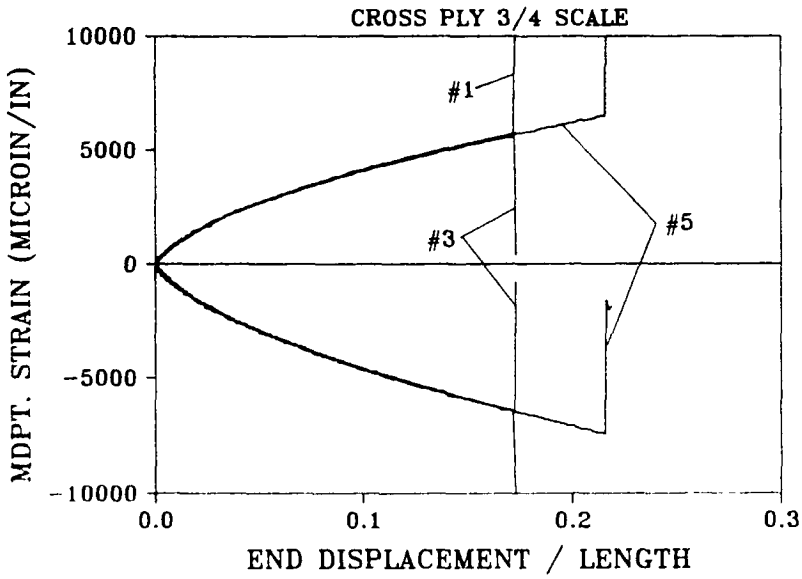

Figure C-22(b). Midpoint strain versus normalized end displacement.

Figure C-22. Static load-deflection and strain-deflection experimental results for 3/4 scale model cross ply beams, 3 replicate tests.

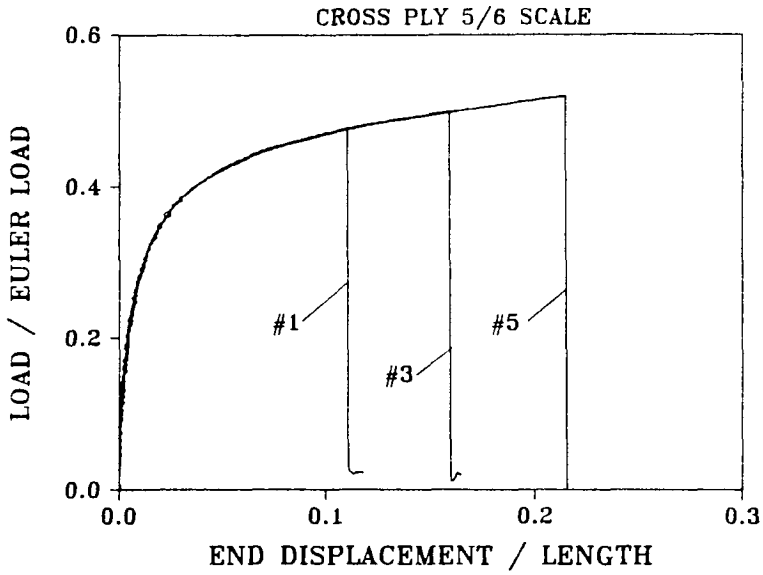

Figure C-23(a). Normalized load versus end displacement.

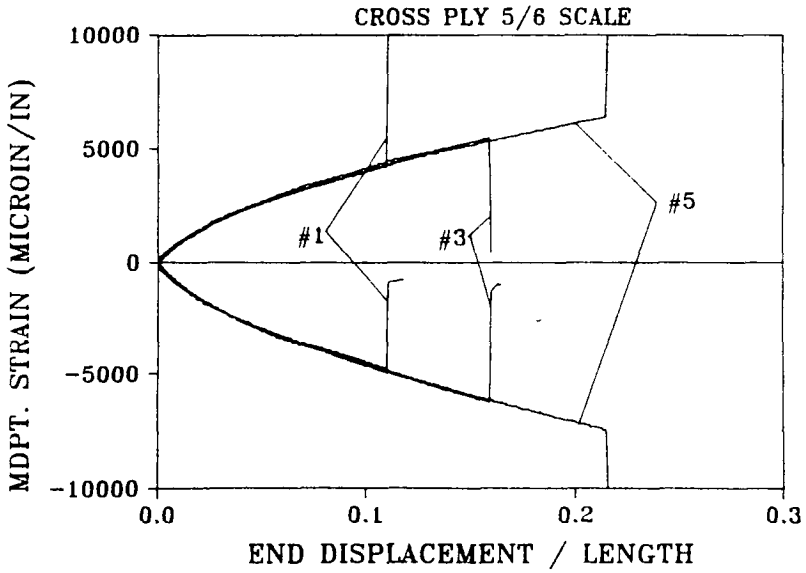

Figure C-23(b). Midpoint strain versus normalized end displacement.

Figure C-23. Static load-deflection and strain-deflection experimental results for 5/6 scale model cross ply beams, 3 replicate tests.

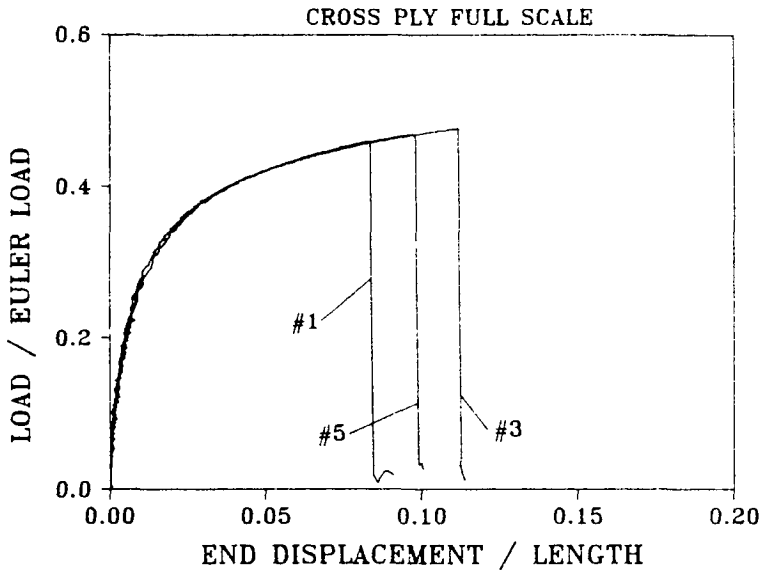

Figure C-24(a). Normalized load versus end displacement.

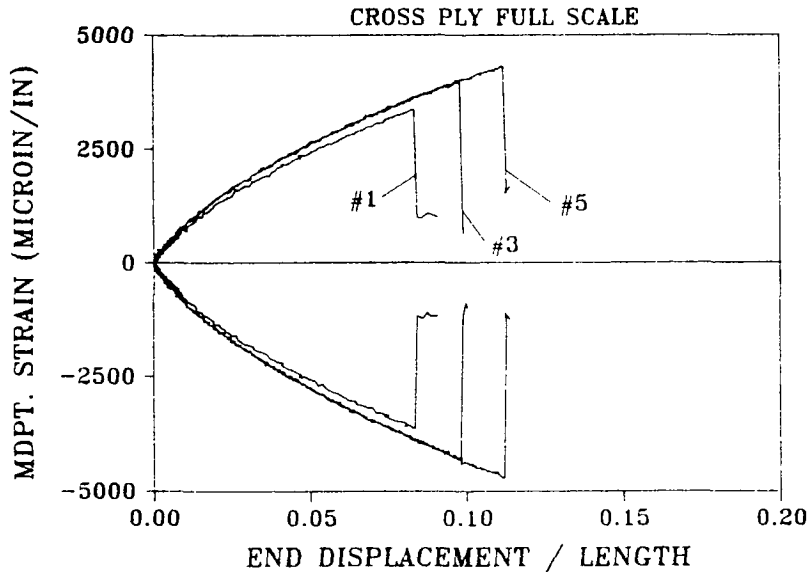

Figure C-24(b). Midpoint strain versus normalized end displacement.

Figure C-24. Static load-deflection and strain-deflection experimental results for full scale model cross ply beams, 3 replicate tests.

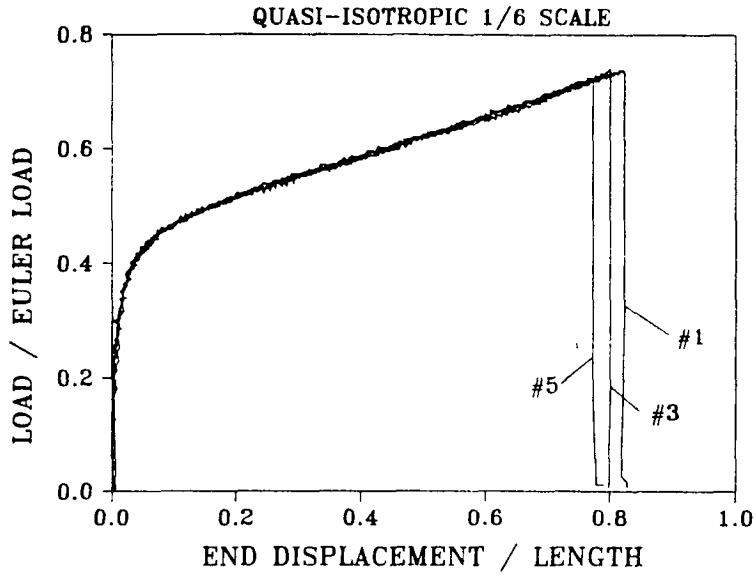

Figure C-25(a). Normalized load versus end displacement.

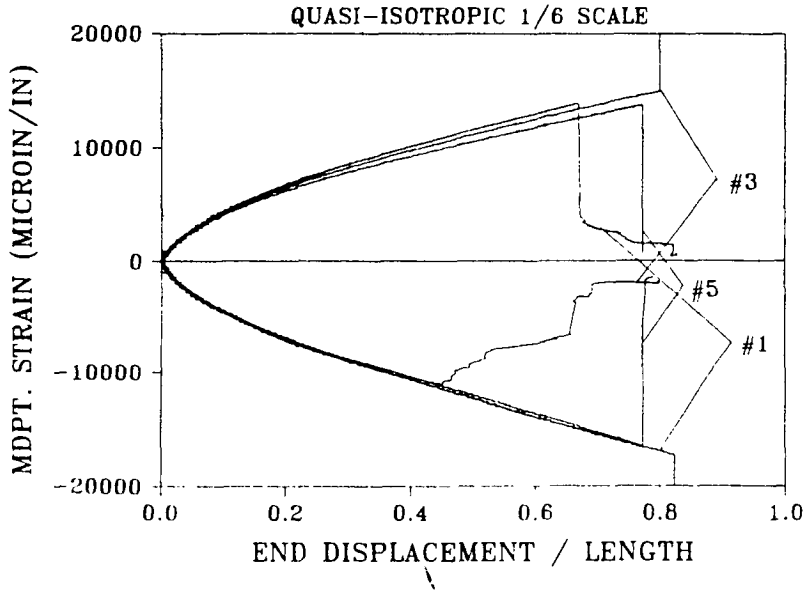

Figure C-25(b). Midpoint strain versus normalized end displacement.

Figure C-25. Static load-deflection and strain-deflection experimental results for 1/6 scale model quasi-isotropic beams, 3 replicate tests.

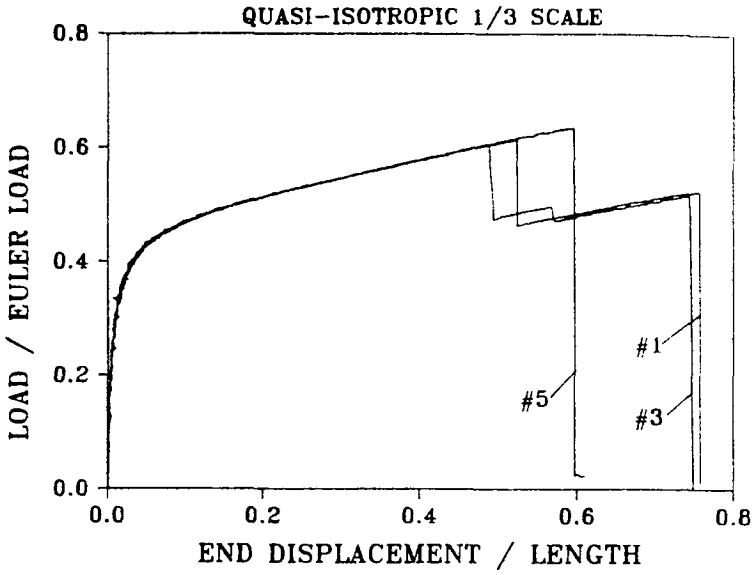

Figure C-26(a). Normalized load versus end displacement.

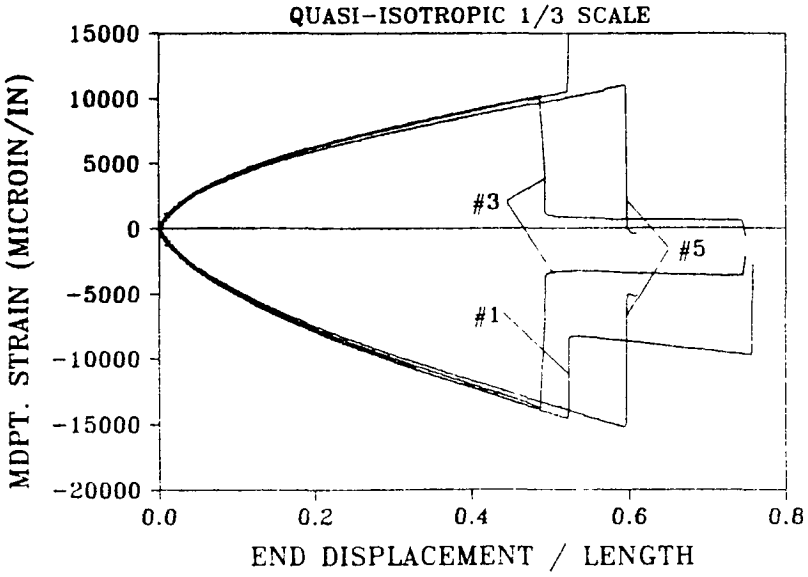

Figure C-26(b). Midpoint strain versus normalized end displacement.

Figure C-26. Static load-deflection and strain-deflection experimental results for 1/3 scale model quasi-isotropic beams, 3 replicate tests.

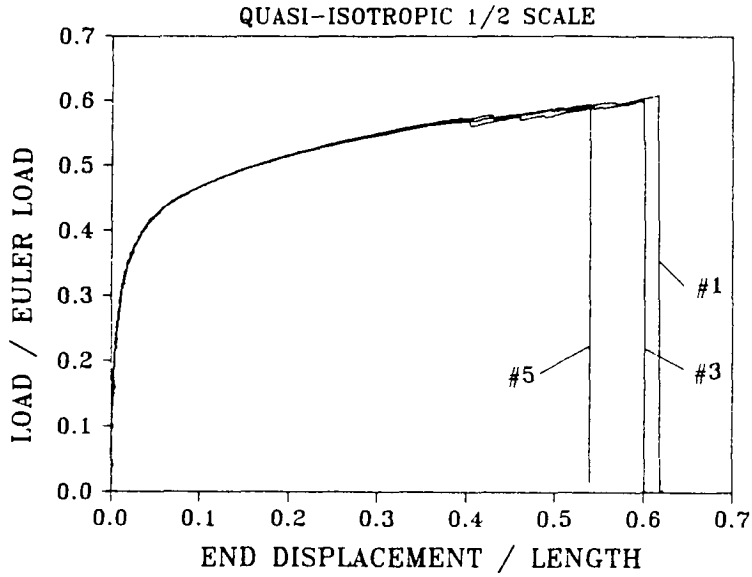

Figure C-27(a). Normalized load versus end displacement.

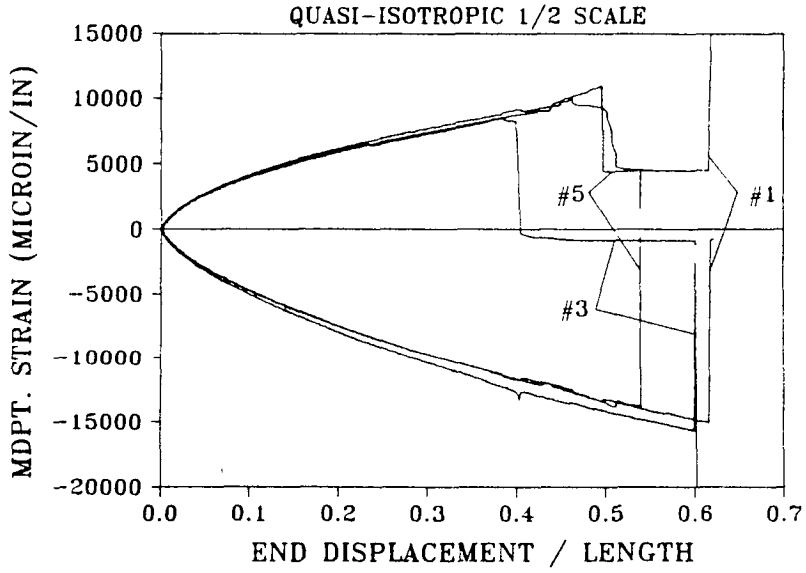

Figure C-27(b). Midpoint strain versus normalized end displacement.

Figure C-27. Static load-deflection and strain-deflection experimental results for 1/2 scale model quasi-isotropic beams, 3 replicate tests.

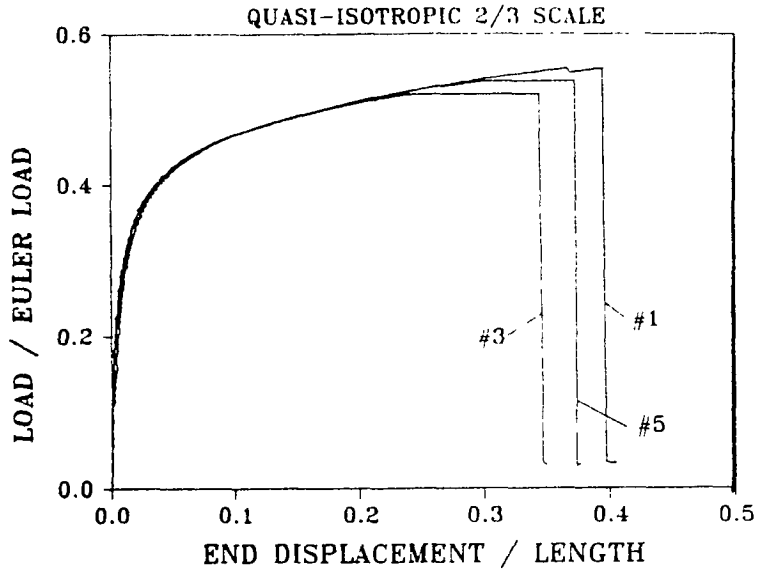

Figure C-28(a). Normalized load versus end displacement.

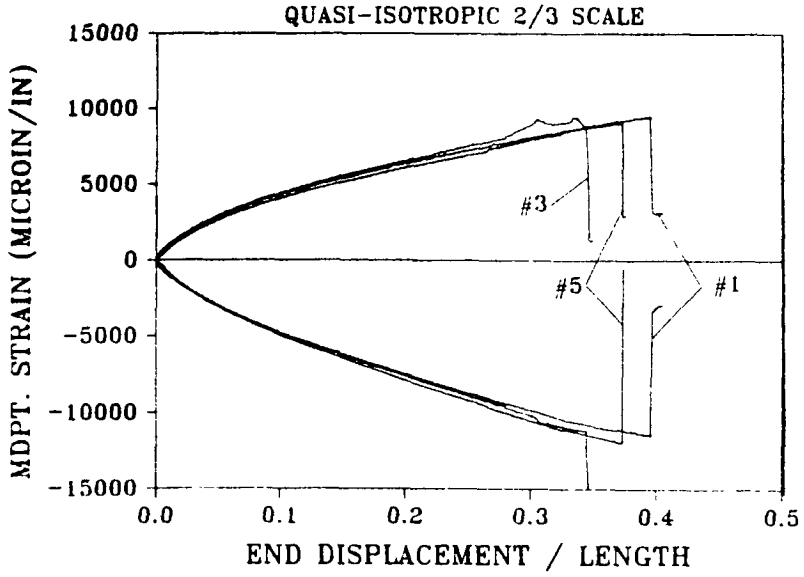

Figure C-28(b). Midpoint strain versus normalized end displacement.

Figure C-28. Static load-deflection and strain-deflection experimental results for 2/3 scale model quasi-isotropic beams, 3 replicate tests.

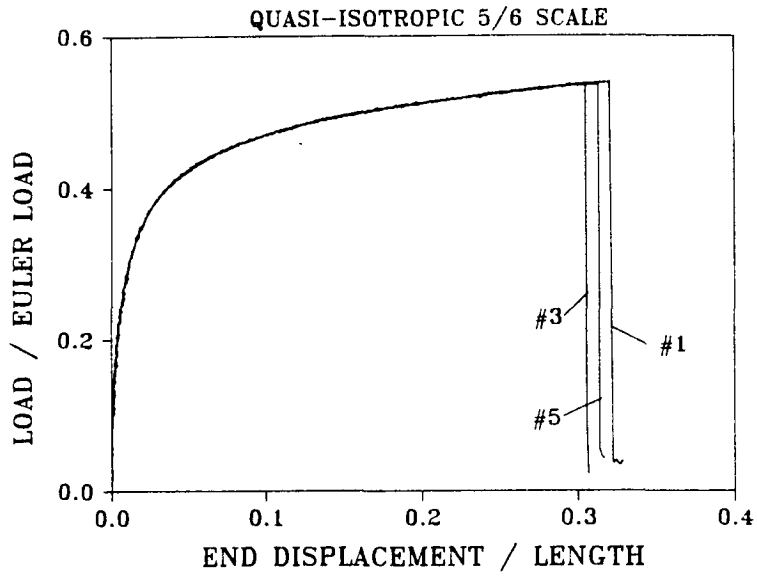

Figure C-29(a). Normalized load versus end displacement.

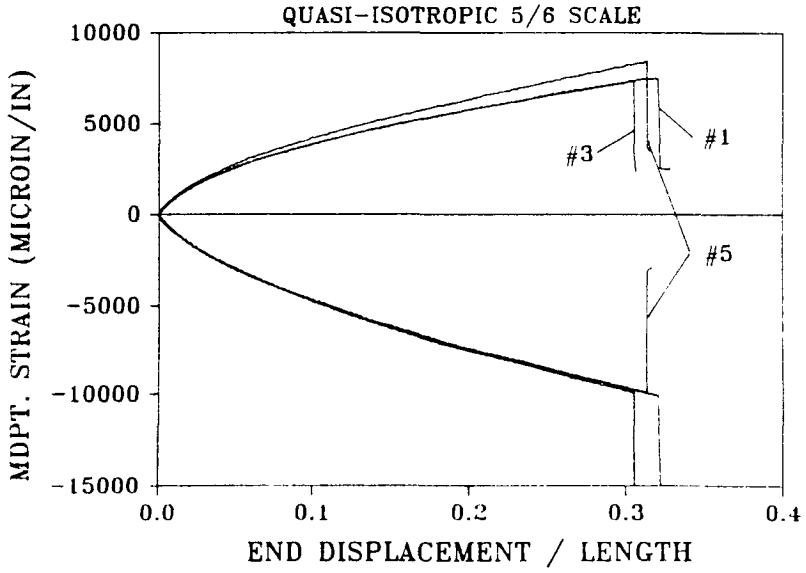

Figure C-29(b). Midpoint strain versus normalized end displacement.

Figure C-29. Static load-deflection and strain-deflection experimental results for 5/6 scale model quasi-isotropic beams, 3 replicate tests.

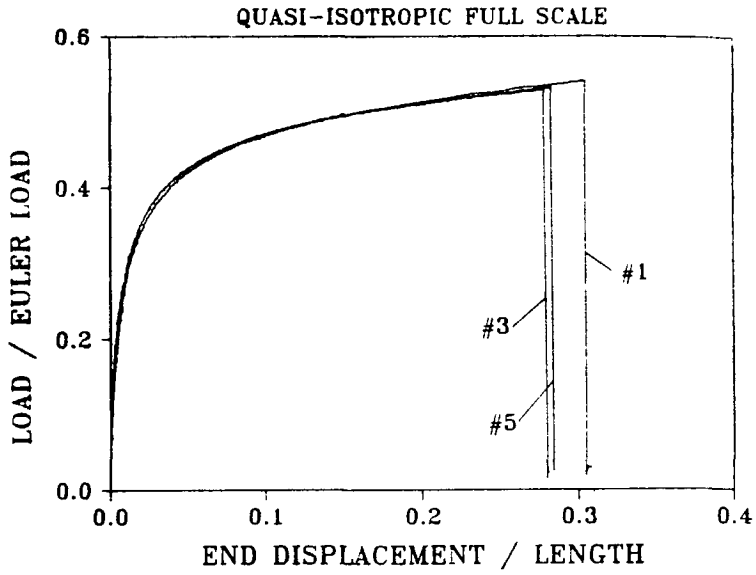

Figure C-30(a). Normalized load versus end displacement.

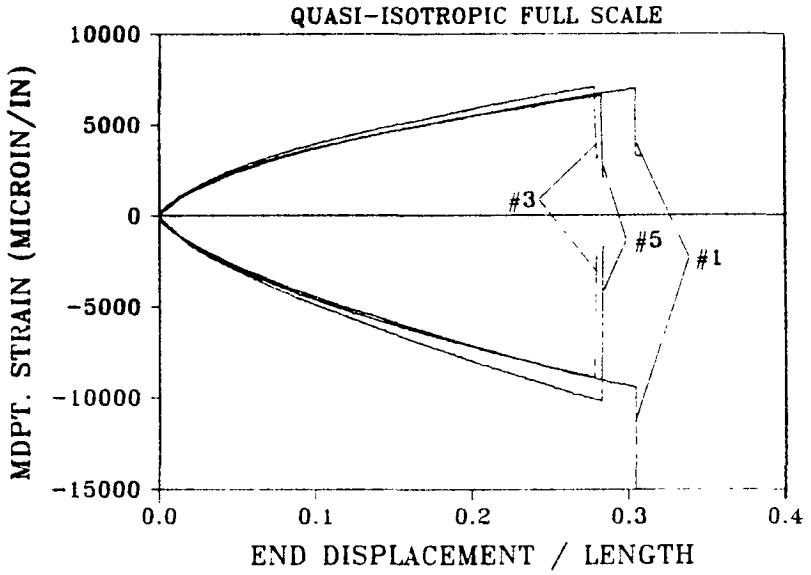

Figure C-30(b). Midpoint strain versus normalized end displacement.

Figure C-30. Static load-deflection and strain-deflection experimental results for full scale model quasi-isotropic beams, 3 replicate tests.

NASA National Aeronautics and Space Administration

Report Documentation Page

1. Report No.	2. Government Accession No	3 Recipient's Catalog No
NASA TM-102697 AVSCOM TR-90-B-006		

4. Title and Subtitle	5. Report Date
Scaling Effects in the Static and Dynamic Response of Graphite-Epoxy Beam-Columns	July 1990
	6 Performing Organization Code

7. Author(s)	8 Performing Organization Report No.
Karen E. Jackson	
	10. Work Unit No 505-63-01-11

9. Performing Organization Name and Address	11. Contract or Grant No
NASA Langley Research Center Aerostructures Directorate USAARTA-AVSCOM Hampton, VA 23665-5225	
	13. Type of Report and Period Covered Technical Memorandum
12. Sponsoring Agency Name and Address National Aeronautics and Space Administration Washington, DC 20546-0001 U.S. Army Aviation Systems Command St. Louis, MO 63120-1798	14. Sponsoring Agency Code

15. Supplementary Notes

Author's Ph.D. Dissertation, Virginia Polytechnic Institute and State University, Blacksburg, VA

16. Abstract

An experimental and analytical investigation was conducted to characterize scaling effects in the large deflection response and failure of graphite-epoxy composite beam-columns. Scale model beams ranging in size from 1/6 to full-scale were tested under static and impulsive conditions with an eccentric, axial compressive load. Unidirectional, angle ply, cross ply, and quasi-isotropic laminates were tested to examine a diversity of composite response and failure modes. A large deflection "exact" beam solution was developed to compare with the static experimental results and to analyze beam failure. The finite element code DYCAST (Dynamic Crash Analysis of Structures) was used to model both the static and impulsive beam response. Results of this investigation show that valuable information can be obtained from testing scale model composite structures. However, a significant scale effect is observed in the strength behavior of composite laminates which cannot be satisfactorially predicted by failure criteria.

17. Key Words (Suggested by Author(s))	18. Distribution Statement
Scaling effects Dimensional Analysis Failure Analysis Composite Materials Large-Deflection Beam Analysis DYCAST	Unclassified - Unlimited Subject Category 39

19. Security Classif. (of this report)	20. Security Classif. (of this page)	21 No of pages	22. Price
Unclassified	Unclassified	279	A13